UNIVERSITAT DE BARCELONA

# Developing supramolecular polymers for drug delivery

Edgar Fuentes Fuentes

Doctoral Thesis

# Developing supramolecular polymers for drug delivery

Edgar Fuentes Fuentes

Thesis co-supervisors:

Dr. Sílvia Pujals & Dr. Lorenzo Albertazzi


UNIVERSITAT DE BARCELONA

# Developing supramolecular polymers for drug delivery

Memòria presentada per optar al grau de doctor per la Universitat de Barcelona

Programa de doctorat en Nanociències

**Autor:** Edgar Fuentes Fuentes

**Directors:** Sílvia Pujals & Lorenzo Albertazzi

**Tutor:** Dr. Gabriel Gomila Lluch

Barcelona, 2022


UNIVERSITAT DE BARCELONA

# Table of contents

# Abstract

A strategy that is being intensively explored to efficiently deliver pharmaceuticals involves drug delivery systems. These carriers should greatly improve the pharmacokinetics of drugs, while providing a selective delivery at the target tissue. Even though great advances are being done in the field, the lack of an effective targeting keeps this strategy away from real application.

Supramolecular polymers could introduce some advantages compared with conventional drug delivery systems. Supramolecular polymers are nanostructures build from self-assembled monomeric units, held together by non-covalent interactions. Thus, it is a modular system in which each monomer can introduce multiple functionalities to the entire structure. Furthermore, their dynamic nature makes them ideal to respond to a stimulus and promote a controlled therapeutic release. Additionally, their characteristic fiber-like shape makes them ideal for seeking and recognition of their target, due to the higher surface-volume ratio and multivalency effect.

In the current thesis, a new family of discotic amphiphiles is especially designed for drug delivery. A benzene-1,3,5-tricarboxamide was selected as the core moiety, followed by an amphiphilic peptide-like wedge. The modification of this sequence modifies completely the behaviour of the supramolecular polymers, allowing to explore their use as drug delivery carriers. Overall, this thesis is an effort to push supramolecular polymers forward in their use for drug delivery, by understanding their behaviour in water, their stability, the potential ability to carry drugs and their potential targeting of cancer tissues.

First, we synthesized a multi-responsive supramolecular polymer, in which assembly/disassembly of nanofibers was triggered by multiple stimuli. In second place, more hydrophobic polymers were synthesized, their stability/responsiveness trade-off was compared, and the stability upon a hypothetical intravenous injection was evaluated. Likewise, two strategies for the encapsulation of biologically active molecules were explored, demonstrating the potential applicability of the system to trigger a biological response upon light- triggered disassembly. Furthermore, the monomer was re-design to explore the potential degradability of the polymer by cancer overexpressed enzymes. In the final chapter, some optical microscopy methods are used to visualize and characterize supramolecular materials in native conditions.

# Resumen en castellano

Actualmente se está haciendo un esfuerzo por mejorar los tratamientos farmacológicos a través de una estrategia denominada liberamiento controlado de fármaco. Para ello, se está explorando el uso de nanopartículas que actúen como transportadores de dichos fármacos en el cuerpo, mejorando su farmacocinética y permitiendo la liberación selectiva del fármaco en el tejido deseado. Si bien se están logrando grandes avances en el campo, aún se requiere de transportadores capaces de liberar el fármaco en el tejido de destino con mayor eficacia.

Los polímeros supramoleculares podrían presentar algunas ventajas en comparación con los sistemas clásicos de administración de fármacos. Los polímeros supramoleculares son nanoestructuras construidas a partir de unidades monoméricas autoensambladas, unidas por interacciones no covalentes. De esta manera, se trata de un sistema modular en el que cada monómero puede aportar múltiples funcionalidades a toda la estructura. Además, su naturaleza dinámica los hace ideales para reaccionar a estímulos específicos y, por ejemplo, promover una liberación controlada y guiada del fármaco. Además, su característica estructura en forma de fibras las hacen ideales para la búsqueda y reconocimiento de su objetivo, debido a la mayor relación superficie-volumen y al efecto de multivalencia.

En esta tesis, una nueva familia de moléculas anfifílicas, llamadas discóticos por su forma circular, se han diseñado especialmente para llevar a cabo la liberación controlada de fármacos. Se seleccionó un benceno-1,3,5-tricarboxamida como estructura central, seguida de tres moléculas anfifílicas de estructura peptídica, creando una molécula con simetría C3. La modificación de esta secuencia peptídica modifica completamente el comportamiento de los polímeros supramoleculares, permitiendo relacionar diferentes variantes de la molécula y sus propiedades con su uso como transportadores de fármacos. En general, esta tesis es un esfuerzo por impulsar el uso de polímeros supramoleculares para la administración de fármacos, mediante la comprensión de su comportamiento en el agua, su estabilidad, la capacidad potencial para transportar fármacos y su posible dirección hacia los tejidos enfermos.

En primer lugar, sintetizamos un polímero supramolecular multi-responsivo, en el que varios estímulos desencadenaron el ensamblaje o el desensamblaje de estas nanofibras. De esta manera, la luz ultravioleta o una acidez o basicidad altas tienden a desensamblar las nanofibras, mientras que la luz visible, una temperatura alta, un pH neutro y una alta fuerza iónica tienden a ensamblar las nanofibras. En segundo lugar, se sintetizaron dos polímeros más hidrofóbicos, se comparó el equilibrio existente entre estabilidad y capacidad de respuesta a estímulos y se evaluó su estabilidad tras una hipotética inyección intravenosa, evaluando como afectan la dilución y la presencia de proteínas. Asimismo, se exploraron dos estrategias para la encapsulación de moléculas biológicamente activas, demostrando la potencial aplicabilidad del sistema para desencadenar una respuesta biológica ante el desensamblaje provocado por la luz. Además, se rediseñó el monómero para explorar la potencial degradabilidad del polímero por acción de enzimas sobre expresadas en cáncer. En el capítulo final, se utilizan algunos métodos de microscopía óptica para visualizar y caracterizar materiales supramoleculares en condiciones nativas.

# Chapter 1 | Background

Nanoscience is an intrinsically interdisciplinary research field that feeds from chemistry, physics, and biology to understand systems with nanoscale dimensions, and it has been central in the technological progress of the past century.[1] Advances in the comprehension and manipulation of nanoscale matter has been a revolution for many fields, where nanotechnological solutions flourished. One of the most successful examples are the continuous scale down of electronic components, like transistors, that brought the computational power to heights never imagined before.

Synthetic nanoscale materials can be prepared by two different approaches: Top-down or Bottom-up. Top-down is centred in the mill of a bulk material into a nanosized or nanostructured material. Milling bulk metal to produce metallic nanoparticles,[2] or the physical etching of a surface to create a nanopattern are examples top-down.[3] It is a very straigh-forward method, easier to scale-up and especially useful to modify surfaces, however the nanoparticles produced have a very limited complexity and often lack of a narrow homogenity.

The bottom-up approach build the nanosctructures from the molecular or atomic units. Examples of this approach can be the formation of metalic nanoparticles from the reduction of the metal salt or the direct synhtesis of a nanosized polymer.[4] These methods are generally more complex, but bring higher levels of complexity and control over the materials properties.

Inorganic nanoparticles have been widely studied, and methods to synthesize them have been greatly improved. However, they possess limited complexity, because they are typically composed of one atom, with one internal structure. The most complex nanoparticles include core-shell, with a bulk interior and a shell changing surface properties,[5] or Janus particles, in which half of the surface is covered by one material and the other half is covered by a second material, providing two different surface chemistries in one particle.[6] Most of the times, functionality is tightly related with the surface chemistry, and the most used strategy to tune it consists of the functionalizing of the surface with specific molecules. These materials are mostly passive, what means that the material cannot change, the nanoparticle must fulfill its function as it is.

This contrast enormously with living systems, which are composed of organic molecules, continuously active, continuously transforming. Essentially, being dynamic. Mimicking this dynamicity is only possible with organic molecules because they relate with the environment using weak and reversible interactions.

## 1.1 Supramolecular chemistry: towards life-like materials

Intermolecular interactions are one of the pillars of life. Biological systems are formed by a vast variety of molecules in water that diffuse, recognise, interact or bind among themselves, without the need to form covalent bonds. While the latter are very energetic (100-900 kJ/mol), supramolecular interactions are not (typically 1-60 kJ/mol), being easily reversible (table 1).[7,8] Nature has evolved to maximize the versatility and reversibility of such interactions to create dynamic systems that, ultimately, create diverse functions.[9]

Table 1. Binding energy by type of interaction.

| *Interaction* | *Energy in kJ/mol* |
|---|---|
| Covalent bond | 100-900 |
| Ion-Ion | 100-350 |
| Ion-Dipole | 50-200 |
| Hydrogen bond | 4-60 |
| Dipole-dipole | 4-50 |
| Van der Waals | 0.5-5 |

Supramolecular interactions can be electrostatic like coulombic interactions, hydrogen bonding (H-bonds), or Van der Waals, as well as solvophobic. All these types of intermolecular bonds differ in terms of energy and directionality and chemists, soon explored how to use them, as nature, to design synthetic systems with specific properties and functions.[9] Donald J. Cram, Jean-Marie Lehn, and Charles J. Pedersen, established the supramolecular chemistry field, and were awarded the Nobel Prize for Chemistry in 1987.[10]

The relentless advances of synthetic chemistry of the XX century,[11] granted access to all kind of molecular structures displaying supramolecular interactions. The challenge slowly shifted from how to build specific molecules, to how to build with those molecules. The molecular self-assembly field have been increasing since then, focusing the efforts in creating molecules that spontaneously assemble into synthetic functional materials, not accessible by traditional means.

## 1.2 Self-assembly

Self-assembly is the spontaneous process by which molecular units aggregate into well-defined structures, using merely supramolecular interactions. The main idea is to design molecular units (monomers) with the ability to recognize themselves and bind, building along the process a stable supramolecular structure. Once monomers are synthesised, complex supramolecular materials can be obtained reproducibly by very simple steps, like dissolving the monomers in an appropriate solvent.

Given the challenge of the task, scientists looked back at the multiple self-assembled systems in nature in seek of inspiration (Fig. 1.1). Protein-protein interactions, DNA condensation, microtubule polymerization, and the lipid bilayer membrane itself are great examples of self-assembly in nature.[12-17] Scientist have created so far a myriad of synthetic self-assembled systems, like spherical or worm-like micelles, vesicles of diverse lamellarity, all kinds of polymersomes, supramolecular polymers or the sophisticated structures of the precise DNA origami.[18] Each type has its own idiosyncrasies; however some characteristics are common among them.

The intrinsic properties of synthetic self-assembled structures often depend on multiple factors, like monomer's shape, polarity, solvent, type and number of functional groups and their location and orientation inside the monomer. All these factors must be considered to shape the self-assembled materials' properties.[19-23] Nevertheless, there must be always a balance between the monomer-monomer interactions and the monomer-solvent interactions.

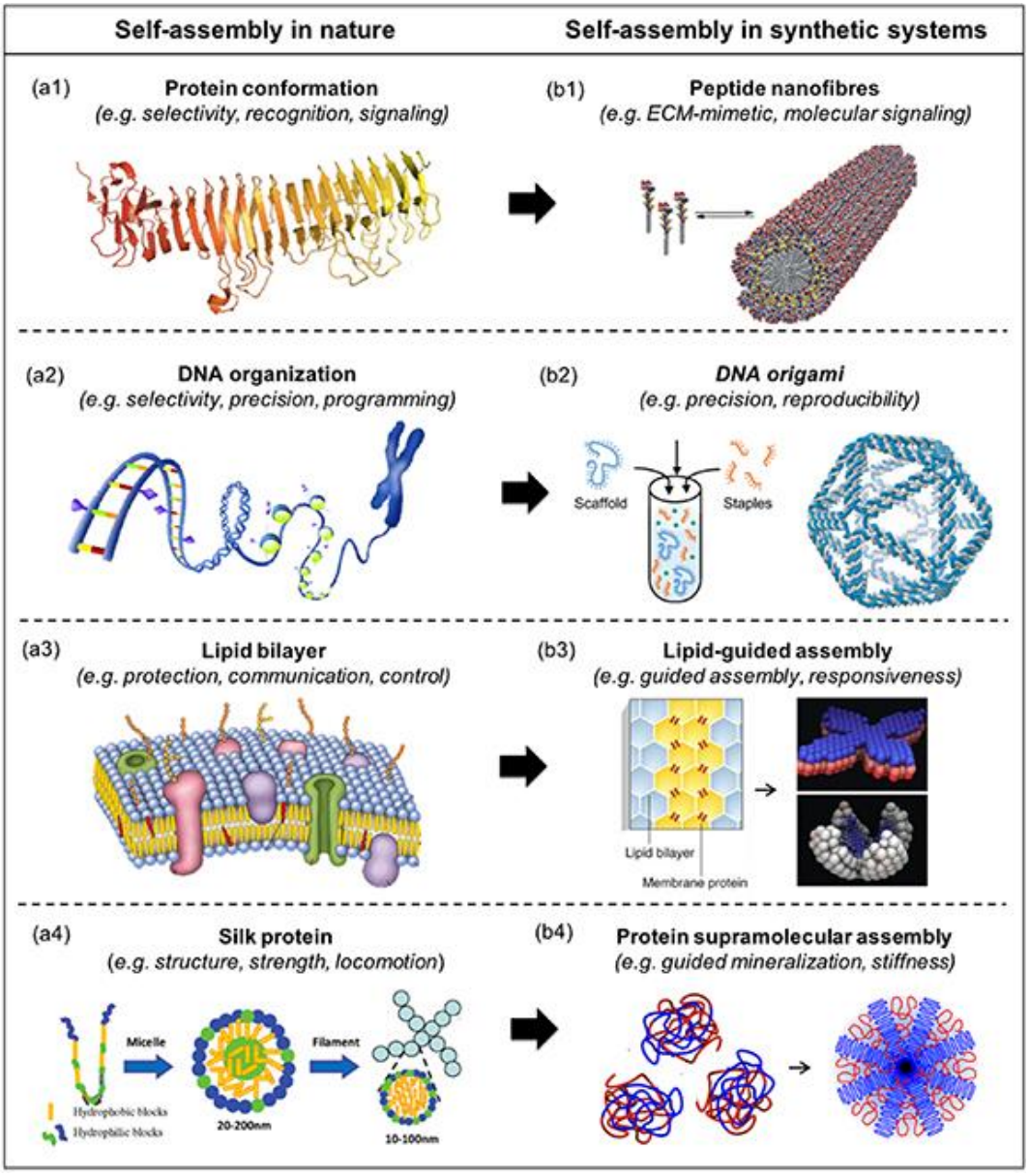


Figure 1.1 illustrated examples of natural (a1 to a4) and synthetic (b1 to b4) self-assembled systems. Reproduced from reference 18. © 2020 IOP Publishing Ltd.

Self-assembled structures are modular by nature. Different monomers (or components) can be designed to display complementarity among them, driving their co-assembly into a multiple component structure.[24] There are plenty of examples showing multicomponent self-assembly, where each component introduces new properties and functionalities.[25] This feature is crucial because it allows to modify the supramolecular material by formulation, and not by molecular design. In other words, the properties of the material can be changed mixing monomers of different types or in different proportions.[26-29]

Self-assembled system can be found in different states depending on their position in the free energy landscape (Fig. 1.2).[30-33] Monomers can be found in a non-dissipative state, that corresponds to the global energy minimum, called thermodynamic equilibrium.

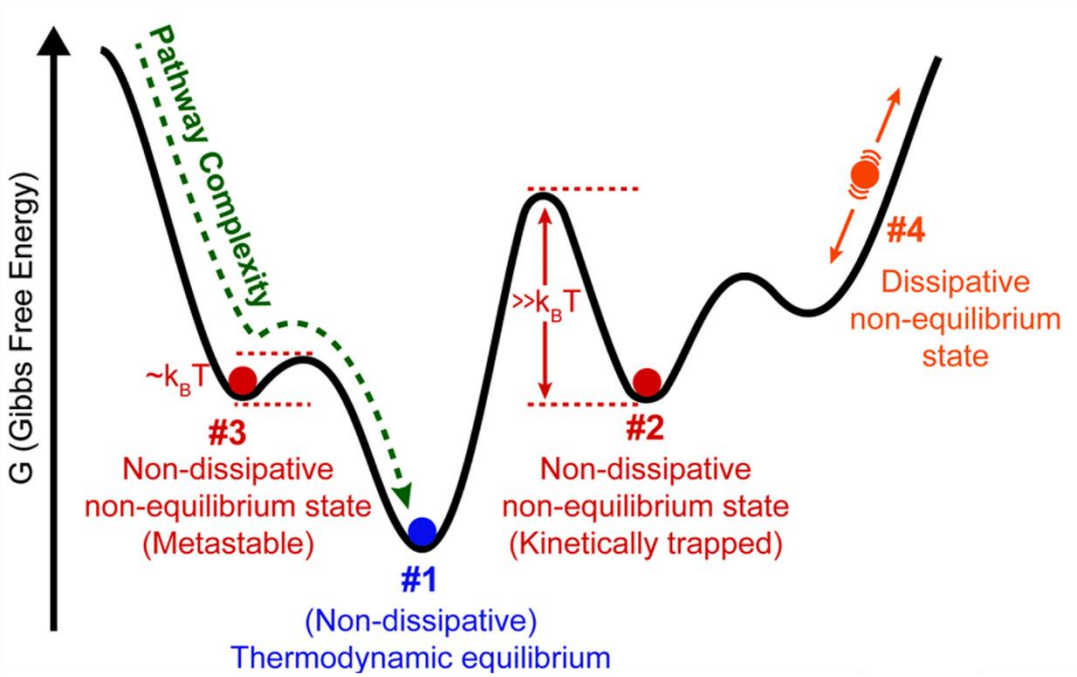


Figure 1.2 Representation of the possible supramolecular states. #1, Thermodynamic equilibrium. It corresponds to the global free energy minimum. #2 and #3, Kinetic controlled states, correspond to local minimums of the energy landscape. They can slowly evolve towards the thermodynamic equilibrium (metastable states) or they can remain in this state (kinetic trap). #4, Dissipative systems, in which the supramolecular state in dynamically maintained by a continuous inflow of energy. Reproduced from Ref 24, © The Royal Society of Chemistry 2017.

Other frequent states are the non-dissipative non-equilibrium states, that correspond to local minimums. They are generally responsible for pathway complexity behaviours. When the energy barrier separating this state from the thermodynamic equilibrium is similar to the thermal energy, it is a transient metastable state that will progress towards the thermodynamic equilibrium. Sorrenti et al. reported this type of behaviour when manually formulating cetyltrimethylammonium bromide together with tetrakis(4-sulfonatophenyl)porphyrin in presence of a chiral surfactant (S)-C16 in water. This produced metastable assemblies with a specific chirality (metastable state), that over the pass of 3 days changed to a different chirality, reaching the thermodynamic equilibrium. This happened because the thermal energy was enough to trigger the transition.[34] In the cases when the energy barrier is much higher than the thermal energy, they are called kinetic traps. The system cannot escape this state without an external input of energy. A clear example was reported by Yamamoto et al., where they reported the self-assembly of hexabenzocoronene derivatives into nanocoils at low temperature (kinetically trapped state), which could transform only upon thermal annealing into nanotubes (thermodynamic equilibrium state).[35] Finally, we can also observe the dissipative states, in which a constant inflow of energy is required to maintain a steady state. Often, they are called out-of-equilibrium systems. Boekhoven et al. smartly reported the use of a dibenzoyl-(L)-cysteine, displaying two negative charges and no self-assembling behaviour. Upon the addition of methyl iodide, acids were alkylated, removing the electrostatic interaction between molecules and allowing for its self-assembly into fibrous aggregates. Monomers became active upon ester formation, but only temporary, until the ester bonds hydrolysed. By these means,

monomers were actively and continuously self-assembling and dissociating until the chemical fuel, the methyl iodide, depleted.[36]

Additionally, self-assembled systems can behave differently depending on the energetic barrier from the assembled monomer to the non-assembled monomers (free). When this energy barrier is comparable to thermal energy, the systems are dynamic, meaning the assembled monomers are in continuous equilibrium with free monomers. In these cases, the net exchange between states is 0 and the free monomer concentration is constant (CAC), determined by the Boltzmann distribution. When the energy barrier is larger than the thermal energy, the systems are static, implying there is no exchange from assembled to free state. This is typically achieved with very high intermolecular forces.

Finally, as monomers are generally held together by weak interactions, they can easily be disassembled with modest energy inputs (stimuli). This feature has been widely used to trigger responses in the material as a response to changes in the surrounding environment like pH or ionic concentration, or as a response to external stimuli like light or solvent composition. The material design together with the stimuli applied determines the transformation of the material that can go from changing shape or size until modifying its surface chemistry or composition.[37,38]

A widely used strategy to design supramolecular structures responsive to the environment consists of the addition of pH sensitive groups. In the work by Mendez-Ardoy et al.[39] it is described the synthesis of a cyclic peptide containing a histidine and a lysine. It is reported that the cyclic peptide is able to self-assemble only upon deprotonation of the imidazole of histidine, when pH increases above 6. Additionally, they mention the enhanced self-assembly upon deprotonation of the lysine, when pH increases above pH 8. In this case, the mechanism of responsiveness is the electrostatic repulsion between positively charged histidines and lysines. When repulsion among histidines is lost, self-assembly is allowed. And when repulsion among lysinies is reduced, self-assembly is enhanced.

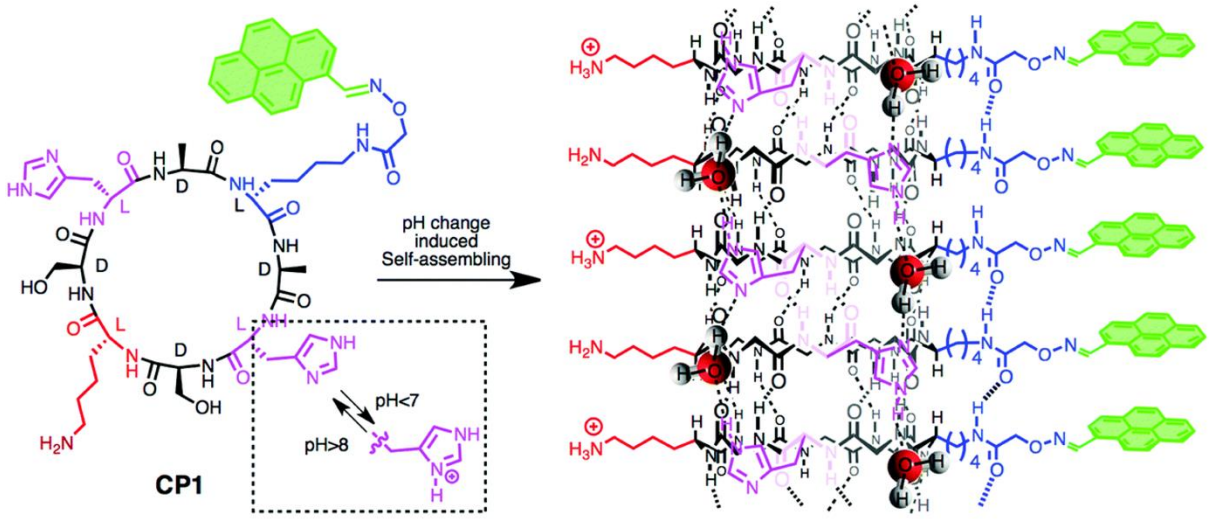


Figure 1.3 Representation of the pH-dependent self-assembly of a cyclic peptide. Reproduced from Ref 30, © The Royal Society of Chemistry 2018.

A general strategy for the external control of self-assembly involves the use of photoswitches.[40,41] Here, azobenzenes occupy a prominent space given their small size, their high versatility, photostability and efficiency.[42] In the group of Yagai, they have smartly exploited the use of azobenzenes to trigger all types of responses on their self-assembled structures. For example, Adhikari et. al. described the preparation of an azobenzene containing monomer, which in methyl cyclohexane self-assembled spontaneously into fibrillar assemblies folded into coiled structures.[43] Interestingly, by photo-isomerizing the azobenzene group, they could trigger the transition from a helical structure to a liner structure and vice versa. Using light, they could control at will the folding of the supramolecular structures.

## 1.3 On the stability-responsiveness trade-off

Typically, supramolecular stability refers to the ability to resist environmental perturbations (e.g. dilution). However, from the supramolecule point of view, there is a very little difference between the stimuli mentioned above, and environmental perturbations. In other words, it is extremely challenging to make your assemblies responsive to some stimuli (e.g. pH) but not others (e.g. dilution). For hence, exists an inverse relationship between the supramolecular response to stimuli, and the supramolecular stability against the perturbation. For example, increasing the supramolecular stability against dilution will reduce at the same time the responsiveness to pH. For this reason, designing structures with enough stability to remain assembled but sufficiently responsive to disassemble upon certain stimuli is very challenging.

## 1.4 Supramolecular polymers

As suggested by its name, supramolecular polymers (SP) are the supramolecular counterparts of conventional polymers. They are defined as linear structures formed by repeating molecular units, linked through intermolecular interactions instead of covalent ones. For this reason, they are self-assembled systems that possess all their advantages. Additionally, they offer the possibility to control their size and copolymerization microstate (Figure 1.3).[44-47]

SP's architectural, dynamic and structural properties can be modified by kinetic control, this is, directing the self-assembling pathway towards specific states. It is often called pathway complexity and it has been observed in a variety of systems, controlling the helicity, the folding or the morphology affecting at the same time the dynamics of the system.[32,48-56]

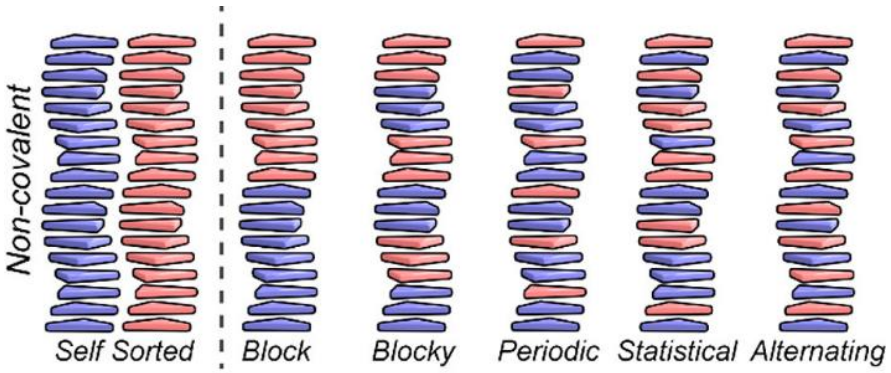


Figure 1.3 Representation of the possible copolymerization microstructures. Microstructures are ordered from no inter-reactivity (self-sorted polymerization) to high inter-reactivity (alternate copolymers). Adapted from reference 46, © 2019 American Chemical Society.

Different strategies have been used to build supramolecular polymers.[44-46] Important niches in the field are built around H-bonding arrays (e.g. ureidopyrimidinone), peptide amphiphiles, π-conjugated systems, host-guest systems and discotic molecules like hexabenzocoronene or benzene-1,3,5-tricarboxamides (BTA).

BTA's have been widely studied over the last decades and have demonstrated a remarkable versatility.[57] BTA is a C3-symmetric small motif, that drives aggregation into well-ordered columnar stacks via 3-fold H-bonding (Fig. 1.4). BTA's can be extended with three sidechains, accepting a wide range of groups and modifications. These sidechains are crucial for the final properties of the self-assembled stacks, like for example a preferred helicity.

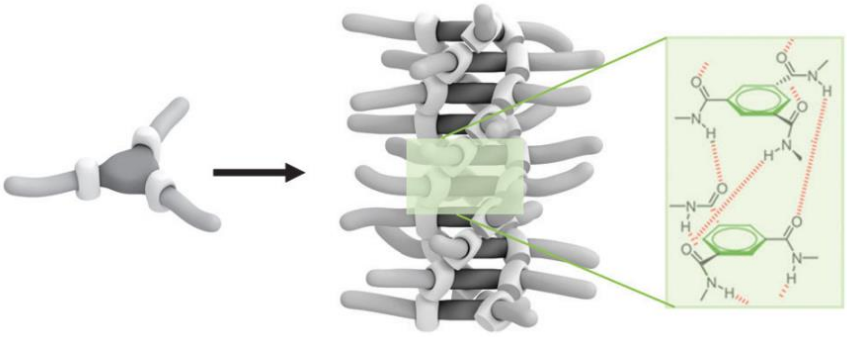

Figure 1.4 Schematic representation of BTA based self-assembly into columnar stacks. Self-assembly is driven by the threefold H-bonding, displaying a specific rotation that grants the structure of helicity. Reproduced from reference 57, © The Royal Society of Chemistry 2012.

Initially it was conceived as an H-bonding moiety for driving self-assembly in organic solvents. However, there has been an effort to translate these systems to aqueous solvents. BTA's were modified to contain a hydrophobic core, that shields the H-bonding from surrounding water, and a hydrophilic shell that provides water solubility to the whole structure. The Meijer Lab demonstrated for the first time that BTA's can be functional in water, by extending the core with a fluorinated L-phenylalanine and an aminobenzoate spacer, placing a M(III) coordinating

complex as the hydrophilic group.[58] Additionally, as Gd (III) was complexed, supramolecular polymers could potentially be used as a contrast agent for magnetic resonance imaging.

The next significant aqueous BTA design of the Meijer Lab was reported by Leenders et al. in which the BTA were extended by different alkyl spacers followed by tetraethylene glycol chains.[59] The different hydrophobic spacers were systematically studied to understand their self-assembly in water. It was demonstrated that both hydrogen bonding and hydrophobic effects are necessary for the formation of SP's. Additionally, they demonstrated how small changes in the hydrophilic-hydrophobic balance can lead to dramatical changes in self-assembly.[60]

The Besenius lab, also showed that BTA's can be extended with multiple L-amino acids, that assist the self-assembly by β-sheet formation or extra coulombic interactions or introduce functionalities. These works are a great inspiration because they demonstrate that amino acids can be successfully incorporated in the sidechain and add extra functionalities that were synthetically more complex to introduce before.[53,61,62] The group has also exploited the benefits of Solid Phase Peptide Synthesis (SPPS, Figure 1.5) to prepare the amino acid sequences on one side, and then couple to the hydrophilic chains and core.

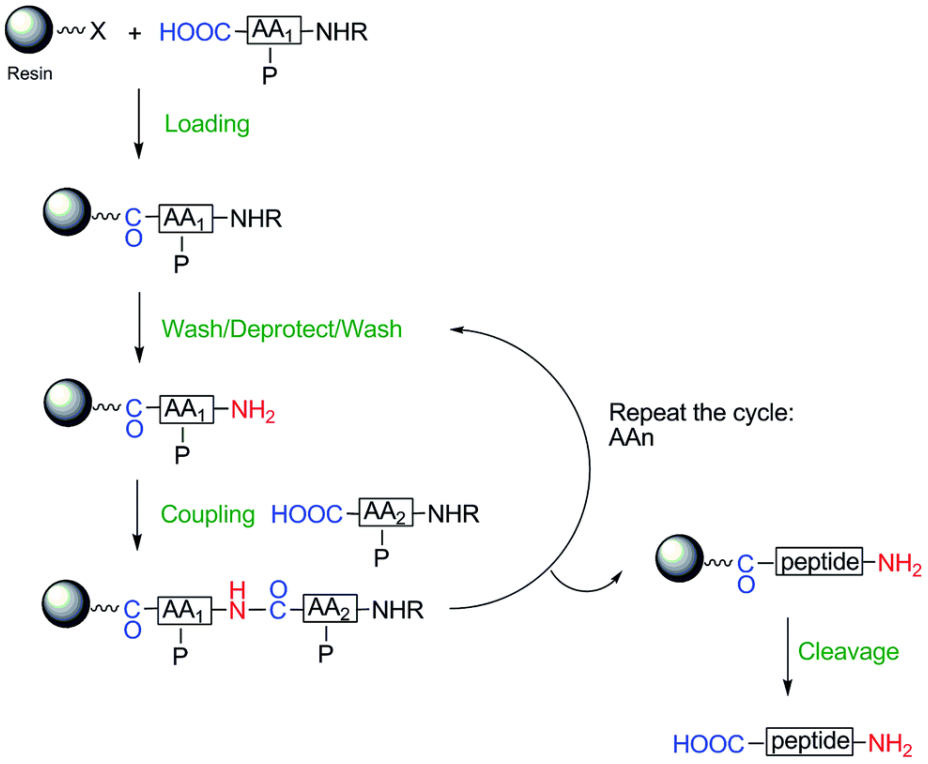


Figure 1.5. Schematic representation of a solid phase peptide synthesis strategy. Reproduced from reference 63, © The Royal Society of Chemistry 2014.

SPPS is a method in which peptides are gown sequentially from a polymeric support by following a series of steps repeated in cycles. Basically, properly protected amino acids are loaded on the insoluble resin and excess of reagents are washed out by filtration. Synthesis is followed by the selective deprotection of the (typically) amino group, and subsequently washed by filtration. Finally, the following amino acid is coupled to the on-resin amino acid. This cycle is repeated until completion of peptide sequence. The last step consists of the cleavage from resin, that normally triggers at the same time the deprotection of the side chains. The only thing that changes between

cycles is the amino acid used, but the reactions are always the same and the purification is always made by filtration. These make SPPS a simple, robust and very high-throughput method for the synthesis of challenging polymeric molecules like peptides, DNA or RNA.

In recent advances, SPPS was pushed to its full potential in the complete synthesis of C3-symmetric molecules, were the C3-symmetric core was coupled directly on resin.[64] In spite of the fact of the low yields obtained for different rigid cores, the advance towards high-throughput molecular screening is very valuable in the self-assembly field.

## 1.5 Advances in nanomedicine

Nanomedicine is an effervescent area in which supramolecular polymers are being investigated too. The strategy behind nanomedicine consists of tacking advantage of nanotechnologies to tackle medical challenges. These advantages arise from the reduced size of the materials, which modify interaction with tissues, cells and proteins, increase surface-to-volume ratio, are highly tuneable in terms of modularity and functionality and can be made responsive.

The most interesting nanotechnological solutions can be found in the field of medical imaging, biomolecular sensing,[65,66] and medical treatments.[67] A recent example in the use of nanoparticles for improving cancer diagnosis was reported by Fang-ju et al. In this work, they showed the development of a platform based on a core-shell fluorescent nanoparticles for the sensing of micro-RNA-141, which is a biomarker of prostate cancer.[68] By functionalizing the nanoparticles with a complementary RNA strand, linked to a florescence quencher, they could detect the hybridization of the analyte.

On the side of the medical treatments, there are also astonishing improvements. Biomaterials for regenerative therapies and drug delivery are the two biggest families inside this category. Biomaterials for regenerative medicine are designed to interact with living systems assisting the healing process. An interesting recent example is described in Perez-Amodio et al., where they prepare a composite of poly(lactic acid) and calcium-releasing ceramic nanoparticles. When applied to chronic bounds in mice, this material accelerated wound closure, promoted vascularization, granulation tissue formation, and collagen deposition.[69]

In the biomaterials field, there is also an increasing interest in the development of SP, given their tendency to aggregate into 1D-structures and form physical hydrogels, a network of entangled fibres with a high content of water. Interestingly, these materials resemble the ones find in the body, reason why they integrate more easily into a biological environment.[70] It is remarkable the effort of the Stupp lab in the development of peptide amphiphile materials for regenerative medicine, allowing for cell growth and mineralization.[71-74]

In a recent contribution, Álvarez et al. designed supramolecular fibril scaffolds build from peptide amphiphiles displaying two peptide sequences for promoting nerve regeneration. In this work, peptide amphiphiles serve not only as a scaffold but as a bio-stimulating player too, and the intrafibre mobility of peptides demonstrated to be related with a higher axon regrowth. They

hypothesise that the mobility of peptide sequences fosters their correct location and interaction with the receptors.[75]

BTA's display very interesting features that make them very promising biomaterials too.[76,77] They can be easily functionalized to display specific ligands on their surface, controlling protein binding or interacting directly with specific cells.[78-81] And this is appealing not only for regenerative therapies, but also for improving pharmacological treatments.

In addition to the biomaterials, nanotechnology has been applied to improve pharmacological treatments, what is commonly known as drug delivery. One of the most studied modalities consists of the encapsulation of therapeutics into nanosized carriers, in order to overcome the typical problems of small molecules, like poor solubility, lack of specificity, rapid clearance and inability to cross biological barriers.[82] Hence, drug carriers must encapsulate a drug, be soluble and stable in time, avoid unspecific interaction with tissues and proteins and have the ability to reach the target tissue and deliver the drug. These are not minor challenges and nanostructures have the right size to overcome them. However, success cases have been scarce.

In 1995, Doxil was the first nanoformulation commercially approved by the US Food and Drug Administration. It consisted of a doxorubicin, a widely used drug used for treating breast and ovary cancer, formulated inside PEGylated liposomes. The encapsulation of doxorubicin increased circulation times and reduced acute cardiac toxicity, among others. However, it did not demonstrate an increase in the survival rate of the patients.[83,84] Since then, around 50 different drug nanoformulations successfully passed clinical trials and are commercially available.[85] However, their formulation into nanoparticles usually offers a reduced toxicity rather than improved efficacy.[86] It is worth to mention that of approved nanoformulations, around 30% correspond to nanocrystals, 60 % correspond to organic nanoparticle carriers and only 10 % correspond to inorganic nanoparticles (Fig. 1.6). Interestingly, this 10% corresponds only to iron formulations to treat iron deficiency in chronic kidney disease.[85]

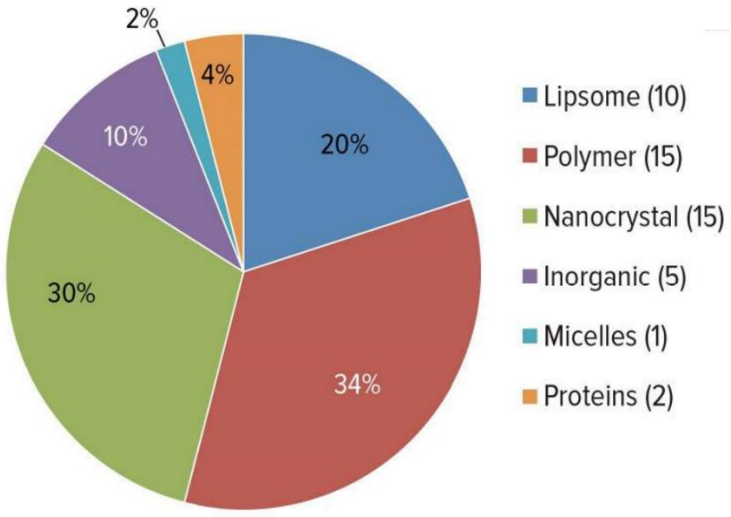


Figure 1.6 Nanoformulated drugs approved by types of nanoparticle. Reproduced from reference 85, under the Creative Commons Attribution License, 2017.

In the same time frame, thousands of scientific contributions have developed a myriad of nanoparticles and strategies for drug delivery, however the immense majority failed in preclinical trials.[86] This high contrast highlights the difficult of the enterprise.

The translation of nanocarriers from the bench to the market is challenging due to poorly understood behaviour in complex systems, often including unspecific interactions with biomolecules, cells and tissues, leading to lack of safety, biocompatibility and effectiveness.[87] Furthermore, the manufacturing of the nanocarriers should be scalable to improve the overall cost-effectiveness comparing with current therapies. Very crucial as well is the weak extrapolation of data from in animal models to humans. Basically, the animal models of human diseases cannot capture crucial information that make nanoformulations succeed. For example, there are biochemical, physiological and proteomic differences and disease heterogeneities are not well represented in the animal models.[86,87]

Because of all these reasons, there is a need for understanding the journey of nanomedicines in the body as well as exploring more complex and functional carriers, different from the classical spherical drug delivery systems.

## 1.6 Towards cancer drug delivery

Cancer is a complex disease that nowadays is the second leading cause of death worldwide. It is characterized by the uncontrolled cell division, leading to organ mal function. It can develop in any tissue of the body, and it can invade any other tissue as well. For these reasons, there are many types of cancer displaying a substantial variety of phenotypes.[88] Cancer is generally treated by a combination of therapies like surgery, radiotherapy and chemotherapy, the combination depends on the type and stage of the cancer. Chemotherapies are generally potent cytotoxic drugs than affects cells in division. They are specially interesting given their systemic availability and potency, however the lack of specificity of these drugs usually leads to severe side effects. As cancer cells are very similar to healthy cells, it is considerably difficult to produce drugs only effective on cancer cells. For this reason, nanoformulations have received an immense attention for the improvement of chemotherapy.[89]

In this context, there are only 15 nanoformulations approved for cancer. It is estimated that 52 % of nanoformulations fail in phase II of clinical trials and only 14% of the nanoformulations succeed in phase III.[90] In most of the cases, failure is due to lack of efficacy, originated from the difficulties of nanoparticles to extravasate, reach and accumulate in the cancer tissue.[91]

This slow progression can have several causes. In many cases, drug delivery strategies relied on the enhanced permeation and retention effect (EPR). The fast-pace growing of vasculature around tumours does not allow to acquire the proper physiological architecture, forming leaking vessels allowing the permeation of nanoparticles. Even though this effect works very well in animal models, EPR in humans is very heterogenous among patients and cancers. For this reason, there is a need for creating efficient nanomedicines that can extravasate and accumulate exclusively within the cancer tissue.[91]

In this sense, targeted drug delivery appears as a great solution, exploiting the differences between cancer tissues and healthy tissues to trigger a local accumulation and delivery of the drug. As a recent example, MM-302,[92] a PEGylated liposome encapsulating doxorubicin, functionalized with an anti-human epidermal growth factor receptor 2, overexpressed in some types of breast cancer. This allows a positive and specific interactions between the liposome and the cancer tissue. However, even though the positive results of phase II, it failed in phase III due to the lack of efficacy.[90]

In despite of the remarkable efforts in bringing targeted therapies to the market, no targeted nanoformulation have reached the market yet. In addition to the heterogenic EPR effect, scientist have to consider also every obstacle that nanoparticles can encounter in the body, like for example the accumulation in highly vascularized organs like the liver, the recognition and clearance by the reticuloendothelial system, the change in the surface identity of nanoparticles because of the interaction with biomolecules and the extravasation into cancer tissue. All these factors must be deeply understood to rationalize effective nanoparticle designs,[89] however, they are typically overseen by researchers.

In the recent years, supramolecular polymers are emerging in the drug delivery field too. Their size and fibre-like shape (high surface-volume ratio) could improve extravasation and interaction with cells in comparison with other spherical nanocarriers.[93] The modularity of their composition, the easy formulation and stimuli-responsive behaviour can also be exploited to modify with high precision the functionality of the supramolecular carrier, a very appealing feature for treating cancer.[94,95] Very interesting advances appeared recently demonstrating the potential of supramolecular polymers for carrying and delivering drugs as well.[96,97] Additionally, the Meijer group started exploring the use of BTA's as biomaterials, demonstrating the compatibility between BTA assemblies an four different cell lines, showing very low cytotoxicities.[98]

A recent work by Albertazzi et al. used multicomponent BTA supramolecular polymers to encapsulate a small hydrophobic molecule (NileRed) and complex siRNA on the surface of the nanofibres.[59,99] After demonstrating the efficient loading, they could deliver both cargoes intracellularly. This work is a great proof of concept that exposes the potential applications of BTA's in drug delivery.

Currently, there is a need for improving the fundamental understanding of the supramolecular polymers' behavior in a complex biological environment. Understanding how they interact with proteins, biological barriers, extravasate and deliver the drugs will improve current designs and strategies.

## 1.7 Objectives and thesis content

The purpose of the research described in this thesis is to make a step forward towards the use of supramolecular polymers for drug delivery. We expanded the existing knowledge regarding aqueous supramolecular polymers by creating a new subfamily of supramolecular fibres, responsive to multiple cues, displaying differences in stability and with the ability to carry drugs. They were used to explore key properties for an effective drug delivery performance:

In **chapter 2**, a multi-responsive supramolecular polymer was designed, synthesised, and thoroughly characterized. The monomer design included an azobenzene amino acid, an octaethylene glycol chain and a terminal lysine. Together, these building blocks assembled into fibres and provided them with responsiveness to light, temperature, pH and ionic strength. A combination of solid phase and solution synthesis were successfully used for the monomers synthesis.

In **chapter 3**, the hydrophobic core of the multi-responsive monomer was extended to generate two new supramolecular polymers of different stabilities. The stability-responsiveness was evaluated for these polymers, yielding two completely different regimes. These regimes were then related with the stability upon a hypothetical intravenous injection, understanding how dilution or the interaction with proteins can affect them.

In **chapter 4**, two strategies for loading and delivering biologically active molecules were explored. The first strategy consisted in a co-assembly between two self-assembling monomers with different functions. One served as a scaffold, governing the self-assembly, while the second contained a covalently linked glutamate, that acted as the ligand. The second strategy consisted of the encapsulation of the ligand Iperoxoazo into a supramolecular polymer composed only of one monomer. Interestingly, the first strategy proved more challenging than strategy 2, but also more promising.

In **chapter 5**, the monomer design was modified to increase specificity towards cancer. The strategy consisted of extending the hydrophobic core of the monomer with a specific tetrapeptide, cleavable by Cathepsin B. As cathepsin B is a well-known enzyme overexpressed in certain cancers, this strategy would provide a responsive mechanism specific for cancer.

Finally, in **chapter 6** are described some advances done with different advanced optical microscopy techniques to understand better supramolecular systems, including discrete supramolecular fibres, supramolecular hydrogels and Quatsomes.

## 1.8 References


1. Nouailhat, A. An introduction to nanoscience and nanotechnology. Wiley, 2008.
2. Wang, S.; Gao, L. Chapter 7 - Laser-Driven Nanomaterials and Laser-Enabled Nanofabrication for Industrial Applications. Thomas, S., Grohens, Y., Pottathara, Y. B. Industrial Applications of Nanomaterials. Micro and Nano Technologies; Elsevier, 2019.
3. Pimpin, A.; Srituravanich, W. Review on Micro- and Nanolithography Techniques and Their Applications. Eng. J. 2012, 16 (1), 37–56.
4. Naito, M.; Yokoyama, T.; Hosokawa, K.; Nogi, K. Nanoparticle Technology Handbook - 3rd Edition, Elsevier, 2018.
5. Ghosh Chaudhuri, R.; Paria, S. Core/Shell Nanoparticles: Classes, Properties, Synthesis Mechanisms, Characterization, and Applications. Chem. Rev. 2012, 112 (4), 2373–2433.
6. Zhang, Y.; Huang, K.; Lin, J.; Huang, P. Janus Nanoparticles in Cancer Diagnosis, Therapy and Theranostics. Biomater. Sci. 2019, 7 (4), 1262–1275.

7. Israelachvili, J.N. In Intermolecular and Surface Forces (Third Edition). Academic Press, 2011.
8. Biedermann, F.; Schneider, H.-J. Experimental Binding Energies in Supramolecular Complexes. Chem. Rev. 2016, 116 (9), 5216–5300.
9. Steed, J.W.; Atwood, J. L. Supramolecular Chemistry (Third Edition). Wiley, 2022.
10. Nobel Media, The Nobel Prize in Chemistry 1987 - NobelPrize.org
11. 11. Nicolaou, K. C. Classics in Total Synthesis: Targets, Strategies, Methods. Wiley, 1996.
12. Mouw, J. K.; Ou, G.; Weaver, V. M. Extracellular Matrix Assembly: A Multiscale Deconstruction. Nat. Rev. Mol. Cell Biol. 2014, 15 (12), 771–785.
13. Vale, R. D. The Molecular Motor Toolbox for Intracellular Transport. Cell 2003, 112 (4), 467–480.
14. Sept, D. Microtubule Polymerization: One Step at a Time. Curr. Biol. 2007, 17 (17), R764–R766.
15. Forth, S.; Kapoor, T. M. The Mechanics of Microtubule Networks in Cell Division. J. Cell Biol. 2017, 216 (6), 1525–1531.
16. van den Ent, F.; Amos, L. A.; Löwe, J. Prokaryotic Origin of the Actin Cytoskeleton. Nature 2001, 413 (6851), 39–44.
17. Pollard, T. D.; Cooper, J. A. Actin, a Central Player in Cell Shape and Movement. Science 2009, 326 (5957), 1208–1212.
18. Hedegaard, C. L.; Mata, A. Integrating Self-Assembly and Biofabrication for the Development of Structures with Enhanced Complexity and Hierarchical Control. Biofabrication 2020, 12 (3), 032002.
19. Israelachvili, J. N.; Mitchell, D. J.; Ninham, B. W. Theory of Self-Assembly of Hydrocarbon Amphiphiles into Micelles and Bilayers. J. Chem. Soc. Faraday Trans. 2 Mol. Chem. Phys. 1976, 72 (0), 1525–1568.
20. Thota, B. N. S.; Urner, L. H.; Haag, R. Supramolecular Architectures of Dendritic Amphiphiles in Water. Chem. Rev. 2016, 116 (4), 2079–2102.
21. Parshad, B.; Prasad, S.; Bhatia, S.; Mittal, A.; Pan, Y.; Mishra, P. K.; Sharma, S. K.; Fruk, L. Non-Ionic Small Amphiphile Based Nanostructures for Biomedical Applications. RSC Adv. 2020, 10 (69), 42098–42115.
22. Lombardo, D.; Kiselev, M. A.; Magazù, S.; Calandra, P. Amphiphiles Self-Assembly: Basic Concepts and Future Perspectives of Supramolecular Approaches. Adv. Condens. Matter Phys. 2015, 2015, e151683.
23. Hill, J. P.; Shrestha, L. K.; Ishihara, S.; Ji, Q.; Ariga, K. Self-Assembly: From Amphiphiles to Chromophores and Beyond. Molecules 2014, 19 (6), 8589–8609.
24. Rest, C.; Mayoral, M. J.; Fernández, G. Aqueous Self-Sorting in Extended Supramolecular Aggregates. Int. J. Mol. Sci. 2013, 14 (1), 1541–1565.
25. Li, L.; Sun, R.; Zheng, R. Tunable Morphology and Functionality of Multicomponent Self-Assembly: A Review. Mater. Des. 2021, 197, 109209.
26. Okesola, B. O.; Mata, A. Multicomponent Self-Assembly as a Tool to Harness New Properties from Peptides and Proteins in Material Design. Chem. Soc. Rev. 2018, 47 (10), 3721–3736.
27. Besenius, P.; Goedegebure, Y.; Driesse, M.; Koay, M.; Bomans, P. H. H.; Palmans, A. R. A.; Dankers, P. Y. W.; Meijer, E. W. Peptide Functionalised Discotic Amphiphiles and Their Self-Assembly into Supramolecular Nanofibres. Soft Matter 2011, 7 (18), 7980–7983.

28. Albertazzi, L.; Martinez-Veracoechea, F. J.; Leenders, C. M. A.; Voets, I. K.; Frenkel, D.; Meijer, E. W. Spatiotemporal Control and Superselectivity in Supramolecular Polymers Using Multivalency. Proc. Natl. Acad. Sci. 2013, 110 (30), 12203–12208.
29. Besenius, P. Controlling Supramolecular Polymerization through Multicomponent Self-Assembly. J. Polym. Sci. Part Polym. Chem. 2017, 55 (1), 34–78.
30. Sorrenti, A.; Leira-Iglesias, J.; Markvoort, A. J.; Greef, T. F. A. de; Hermans, T. M. Non-Equilibrium Supramolecular Polymerization. Chem. Soc. Rev. 2017, 46 (18), 5476–5490.
31. Hagan, M. F.; Elrad, O. M.; Jack, R. L. Mechanisms of Kinetic Trapping in Self-Assembly and Phase Transformation. J. Chem. Phys. 2011, 135 (10), 104115.
32. Wang, X.; Guerin, G.; Wang, H.; Wang, Y.; Manners, I.; Winnik, M. A. Cylindrical Block Copolymer Micelles and Co-Micelles of Controlled Length and Architecture. Science 2007, 317 (5838), 644–647.
33. Mattia, E.; Otto, S. Supramolecular Systems Chemistry. Nat. Nanotechnol. 2015, 10 (2), 111–119.
34. Sorrenti, A.; Rodriguez-Trujillo, R.; Amabilino, D. B.; Puigmartí-Luis, J. Milliseconds Make the Difference in the Far-from-Equilibrium Self-Assembly of Supramolecular Chiral Nanostructures. J. Am. Chem. Soc. 2016, 138 (22), 6920–6923.
35. Yamamoto, T.; Fukushima, T.; Yamamoto, Y.; Kosaka, A.; Jin, W.; Ishii, N.; Aida, T. Stabilization of a Kinetically Favored Nanostructure: Surface ROMP of Self-Assembled Conductive Nanocoils from a Norbornene-Appended Hexa-Peri-Hexabenzocoronene. J. Am. Chem. Soc. 2006, 128 (44), 14337–14340.
36. Boekhoven, J.; Brizard, A. M.; Kowlgi, K. N. K.; Koper, G. J. M.; Eelkema, R.; van Esch, J. H. Dissipative Self-Assembly of a Molecular Gelator by Using a Chemical Fuel. Angew. Chem. Int. Ed. 2010, 49 (28), 4825–4828.
37. Yan, X.; Wang, F.; Zheng, B.; Huang, F. Stimuli-Responsive Supramolecular Polymeric Materials. Chem. Soc. Rev. 2012, 41 (18), 6042–6065.
38. Blum, A. P.; Kammeyer, J. K.; Rush, A. M.; Callmann, C. E.; Hahn, M. E.; Gianneschi, N. C. Stimuli-Responsive Nanomaterials for Biomedical Applications. J. Am. Chem. Soc. 2015, 137 (6), 2140–2154.
39. Méndez-Ardoy, A.; Granja, J. R.; Montenegro, J. PH-Triggered Self-Assembly and Hydrogelation of Cyclic Peptide Nanotubes Confined in Water Micro-Droplets. Nanoscale Horiz. 2018, 3 (4), 391–396.
40. Szymański, W.; Beierle, J. M.; Kistemaker, H. A. V.; Velema, W. A.; Feringa, B. L. Reversible Photocontrol of Biological Systems by the Incorporation of Molecular Photoswitches. Chem. Rev. 2013, 113 (8), 6114–6178.
41. Pianowski, Z. L. Recent Implementations of Molecular Photoswitches into Smart Materials and Biological Systems. Chem. – Eur. J. 2019, 25 (20), 5128–5144.
42. Bandara, H. M. D.; Burdette, S. C. Photoisomerization in Different Classes of Azobenzene. Chem. Soc. Rev. 2012, 41 (5), 1809–1825.
43. Adhikari, B.; Yamada, Y.; Yamauchi, M.; Wakita, K.; Lin, X.; Aratsu, K.; Ohba, T.; Karatsu, T.; Hollamby, M. J.; Shimizu, N.; Takagi, H.; Haruki, R.; Adachi, S.; Yagai, S. Light-Induced Unfolding and Refolding of Supramolecular Polymer Nanofibres. Nat. Commun. 2017, 8, 15254.
44. Yang, L.; Tan, X.; Wang, Z.; Zhang, X. Supramolecular Polymers: Historical Development, Preparation, Characterization, and Functions. Chem. Rev. 2015, 115 (15), 7196–7239.
45. Aida, T.; Meijer, E. W.; Stupp, S. I. Functional Supramolecular Polymers. Science 2012, 335 (6070), 813–817.

46. Adelizzi, B.; Van Zee, N. J.; de Windt, L. N. J.; Palmans, A. R. A.; Meijer, E. W. Future of Supramolecular Copolymers Unveiled by Reflecting on Covalent Copolymerization. J. Am. Chem. Soc. 2019, 141 (15), 6110–6121.
47. Aratsu, K.; Takeya, R.; Pauw, B. R.; Hollamby, M. J.; Kitamoto, Y.; Shimizu, N.; Takagi, H.; Haruki, R.; Adachi, S.; Yagai, S. Supramolecular Copolymerization Driven by Integrative Self-Sorting of Hydrogen-Bonded Rosettes. Nat. Commun. 2020, 11 (1), 1623.
48. Ogi, S.; Fukui, T.; Jue, M. L.; Takeuchi, M.; Sugiyasu, K. Kinetic Control over Pathway Complexity in Supramolecular Polymerization through Modulating the Energy Landscape by Rational Molecular Design. Angew. Chem. Int. Ed. 2014, 53 (52), 14363–14367.
49. Dhiman, S.; George, S. J. Temporally Controlled Supramolecular Polymerization. Bull. Chem. Soc. Jpn. 2018, 91 (4), 687–699.
50. Korevaar, P. A.; George, S. J.; Markvoort, A. J.; Smulders, M. M. J.; Hilbers, P. A. J.; Schenning, A. P. H. J.; De Greef, T. F. A.; Meijer, E. W. Pathway Complexity in Supramolecular Polymerization. Nature 2012, 481 (7382), 492–496.
51. Suzuki, A.; Aratsu, K.; Datta, S.; Shimizu, N.; Takagi, H.; Haruki, R.; Adachi, S.; Hollamby, M.; Silly, F.; Yagai, S. Topological Impact on the Kinetic Stability of Supramolecular Polymers. J. Am. Chem. Soc. 2019, 141 (33), 13196–13202.
52. Greciano, E. E.; Matarranz, B.; Sánchez, L. Pathway Complexity Versus Hierarchical Self-Assembly in N-Annulated Perylenes: Structural Effects in Seeded Supramolecular Polymerization. Angew. Chem. 2018, 130 (17), 4787–4791.
53. Kemper, B.; Zengerling, L.; Spitzer, D.; Otter, R.; Bauer, T.; Besenius, P. Kinetically Controlled Stepwise Self-Assembly of AuI-Metallopeptides in Water. J. Am. Chem. Soc. 2018, 140 (2), 534–537.
54. Tidhar, Y.; Weissman, H.; Wolf, S. G.; Gulino, A.; Rybtchinski, B. Pathway-Dependent Self-Assembly of Perylene Diimide/Peptide Conjugates in Aqueous Medium. Chem. – Eur. J. 2011, 17 (22), 6068–6075.
55. Fukushima, T.; Tamaki, K.; Isobe, A.; Hirose, T.; Shimizu, N.; Takagi, H.; Haruki, R.; Adachi, S.; Hollamby, M. J.; Yagai, S. Diarylethene-Powered Light-Induced Folding of Supramolecular Polymers. J. Am. Chem. Soc. 2021, 143 (15), 5845–5854.
56. Suda, N.; Saito, T.; Arima, H.; Yagai, S. Photo-Modulation of Supramolecular Polymorphism in the Self-Assembly of a Scissor-Shaped Azobenzene Dyad into Nanotoroids and Fibers. Chem. Sci. 2022, 13 (11), 3249–3255.
57. Cantekin, S.; Greef, T. F. A. de; Palmans, A. R. A. Benzene-1,3,5-Tricarboxamide: A Versatile Ordering Moiety for Supramolecular Chemistry. Chem. Soc. Rev. 2012, 41 (18), 6125–6137.
58. Besenius, P.; Portale, G.; Bomans, P. H. H.; Janssen, H. M.; Palmans, A. R. A.; Meijer, E. W. Controlling the Growth and Shape of Chiral Supramolecular Polymers in Water. Proc. Natl. Acad. Sci. 2010, 107 (42), 17888–17893.
59. Leenders, C. M. A.; Albertazzi, L.; Mes, T.; Koenigs, M. M. E.; Palmans, A. R. A.; Meijer, E. W. Supramolecular Polymerization in Water Harnessing Both Hydrophobic Effects and Hydrogen Bond Formation. Chem. Commun. 2013, 49 (19), 1963–1965.
60. Leenders, C. M. A.; Baker, M. B.; Pijpers, I. A. B.; Lafleur, R. P. M.; Albertazzi, L.; Palmans, A. R. A.; Meijer, E. W. Supramolecular Polymerisation in Water; Elucidating the Role of Hydrophobic and Hydrogen-Bond Interactions. Soft Matter 2016, 12 (11), 2887–2893.
61. Frisch, H.; Unsleber, J. P.; Lüdeker, D.; Peterlechner, M.; Brunklaus, G.; Waller, M.; Besenius, P. PH-Switchable Ampholytic Supramolecular Copolymers. Angew. Chem. Int. Ed. 2013, 52 (38), 10097–10101.

62. Spitzer, D.; Marichez, V.; Formon, G. J. M.; Besenius, P.; Hermans, T. M. Surface-Assisted Self-Assembly of a Hydrogel by Proton Diffusion. Angew. Chem. 2018, 130 (35), 11519–11523.
63. Palomo, J. M. Solid-Phase Peptide Synthesis: An Overview Focused on the Preparation of Biologically Relevant Peptides. RSC Adv. 2014, 4 (62), 32658–32672.
64. Sanders, A. M.; Kale, T. S.; Katz, H. E.; Tovar, J. D. Solid-Phase Synthesis of Self-Assembling Multivalent π-Conjugated Peptides. ACS Omega 2017, 2 (2), 409–419.
65. Zhang, Y.; Li, M.; Gao, X.; Chen, Y.; Liu, T. Nanotechnology in Cancer Diagnosis: Progress, Challenges and Opportunities. J. Hematol. Oncol.J Hematol Oncol 2019, 12 (1), 137.
66. Chinen, A. B.; Guan, C. M.; Ferrer, J. R.; Barnaby, S. N.; Merkel, T. J.; Mirkin, C. A. Nanoparticle Probes for the Detection of Cancer Biomarkers, Cells, and Tissues by Fluorescence. Chem. Rev. 2015, 115 (19), 10530–10574.
67. Abdel-Mageed, H. M.; AbuelEzz, N. Z.; Radwan, R. A.; Mohamed, S. A. Nanoparticles in Nanomedicine: A Comprehensive Updated Review on Current Status, Challenges and Emerging Opportunities. J. Microencapsul. 2021, 38 (6), 414–436.
68. Jou, A. F.; Lu, C.-H.; Ou, Y.-C.; Wang, S.-S.; Hsu, S.-L.; Willner, I.; Ho, J. A. Diagnosing the MiR-141 Prostate Cancer Biomarker Using Nucleic Acid-Functionalized CdSe/ZnS QDs and Telomerase. Chem. Sci. 2014, 6 (1), 659–665.
69. Perez-Amodio, S.; Rubio, N.; Vila, O. F.; Navarro-Requena, C.; Castaño, O.; Sanchez-Ferrero, A.; Marti-Munoz, J.; Alsina-Giber, M.; Blanco, J.; Engel, E. Polymeric Composite Dressings Containing Calcium-Releasing Nanoparticles Accelerate Wound Healing in Diabetic Mice. Adv. Wound Care 2021, 10 (6), 301-316.
70. Zhang, Y. S.; Khademhosseini, A. Advances in Engineering Hydrogels. Science 2017, 356 (500), 3627.
71. Rajangam, K.; Behanna, H. A.; Hui, M. J.; Han, X.; Hulvat, J. F.; Lomasney, J. W.; Stupp, S. I. Heparin Binding Nanostructures to Promote Growth of Blood Vessels. Nano Lett. 2006, 6 (9), 2086–2090.
72. Mata, A.; Geng, Y.; Henrikson, K. J.; Aparicio, C.; Stock, S. R.; Satcher, R. L.; Stupp, S. I. Bone Regeneration Mediated by Biomimetic Mineralization of a Nanofiber Matrix. Biomaterials 2010, 31 (23), 6004–6012.
73. Hartgerink, J. D.; Beniash, E.; Stupp, S. I. Self-Assembly and Mineralization of Peptide-Amphiphile Nanofibers. Science 2001, 294 (5547), 1684–1688.
74. Hartgerink, J. D.; Beniash, E.; Stupp, S. I. Peptide-Amphiphile Nanofibers: A Versatile Scaffold for the Preparation of Self-Assembling Materials. Proc. Natl. Acad. Sci. U. S. A. 2002, 99 (8), 5133–5138.
75. Álvarez, Z.; Kolberg-Edelbrock, A. N.; Sasselli, I. R.; Ortega, J. A.; Qiu, R.; Syrgiannis, Z.; Mirau, P. A.; Chen, F.; Chin, S. M.; Weigand, S.; Kiskinis, E.; Stupp, S. I. Bioactive Scaffolds with Enhanced Supramolecular Motion Promote Recovery from Spinal Cord Injury. Science 2021, 374 (6569), 848–856.
76. Leenders, C. M. A.; Mes, T.; Baker, M. B.; Koenigs, M. M. E.; Besenius, P.; Palmans, A. R. A.; Meijer, E. W. From Supramolecular Polymers to Hydrogel Materials. Mater. Horiz. 2013, 1 (1), 116–120.
77. Hendrikse, S. I. S.; Su, L.; Hogervorst, T. P.; Lafleur, R. P. M.; Lou, X.; van der Marel, G. A.; Codee, J. D. C.; Meijer, E. W. Elucidating the Ordering in Self-Assembled Glycocalyx Mimicking Supramolecular Copolymers in Water. J. Am. Chem. Soc. 2019, 141 (35), 13877–13886.

78. Müller, M. K.; Brunsveld, L. A Supramolecular Polymer as a Self-Assembling Polyvalent Scaffold. Angew. Chem. Int. Ed. 2009, 48 (16), 2921–2924.
79. Straßburger, D.; Stergiou, N.; Urschbach, M.; Yurugi, H.; Spitzer, D.; Schollmeyer, D.; Schmitt, E.; Besenius, P. Mannose-Decorated Multicomponent Supramolecular Polymers Trigger Effective Uptake into Antigen-Presenting Cells. ChemBioChem, 19 (9), 912-916.
80. Morgese, G.; de Waal, B. F. M.; Varela-Aramburu, S.; Palmans, A. R. A.; Albertazzi, L.; Meijer, E. W. Anchoring Supramolecular Polymers to Human Red Blood Cells by Combining Dynamic Covalent and Non-Covalent Chemistries. Angew. Chem. Int. Ed. 2020, 59 (39), 17229–17233.
81. Wijnands, S. P. W.; Engelen, W.; Lafleur, R. P. M.; Meijer, E. W.; Merkx, M. Controlling Protein Activity by Dynamic Recruitment on a Supramolecular Polymer Platform. Nat. Commun. 2018, 9 (1), 65.
82. Mitchell, M. J.; Billingsley, M. M.; Haley, R. M.; Wechsler, M. E.; Peppas, N. A.; Langer, R. Engineering Precision Nanoparticles for Drug Delivery. Nat. Rev. Drug Discov. 2021, 20 (2), 101–124.
83. Markman, M. Pegylated Liposomal Doxorubicin in the Treatment of Cancers of the Breast and Ovary. Expert Opin. Pharmacother. 2006, 7 (11), 1469–1474.
84. Petersen, G. H.; Alzghari, S. K.; Chee, W.; Sankari, S. S.; La-Beck, N. M. Meta-Analysis of Clinical and Preclinical Studies Comparing the Anticancer Efficacy of Liposomal versus Conventional Non-Liposomal Doxorubicin. J. Controlled Release 2016, 232, 255–264.
85. Ventola, C. L. Progress in Nanomedicine: Approved and Investigational Nanodrugs. Pharm. Ther. 2017, 42 (12), 742–755.
86. Ramos, T. I.; Villacis-Aguirre, C. A.; López-Aguilar, K. V.; Santiago Padilla, L.; Altamirano, C.; Toledo, J. R.; Santiago Vispo, N. The Hitchhiker's Guide to Human Therapeutic Nanoparticle Development. Pharmaceutics 2022, 14 (2), 247.
87. Greish, K.; Mathur, A.; Bakhiet, M.; Taurin, S. Nanomedicine: Is It Lost in Translation? Ther. Deliv. 2018, 9 (4), 269–285.
88. Hassanpour, S. H.; Dehghani, M. Review of Cancer from Perspective of Molecular. J. Cancer Res. Pract. 2017, 4 (4), 127–129.
89. van der Meel, R.; Sulheim, E.; Shi, Y.; Kiessling, F.; Mulder, W. J. M.; Lammers, T. Smart Cancer Nanomedicine. Nat. Nanotechnol. 2019, 14 (11), 1007–1017.
90. He, H.; Liu, L.; Morin, E. E.; Liu, M.; Schwendeman, A. Survey of Clinical Translation of Cancer Nanomedicines—Lessons Learned from Successes and Failures. Acc. Chem. Res. 2019, 52 (9), 2445–2461.
91. Wilhelm, S.; Tavares, A. J.; Dai, Q.; Ohta, S.; Audet, J.; Dvorak, H. F.; Chan, W. C. W. Analysis of Nanoparticle Delivery to Tumours. Nat. Rev. Mater. 2016, 1 (5), 1–12.
92. Miller, K.; Cortes, J.; Hurvitz, S. A.; Krop, I. E.; Tripathy, D.; Verma, S.; Riahi, K.; Reynolds, J. G.; Wickham, T. J.; Molnar, I.; Yardley, D. A. HERMIONE: A Randomized Phase 2 Trial of MM-302 plus Trastuzumab versus Chemotherapy of Physician's Choice plus Trastuzumab in Patients with Previously Treated, Anthracycline-Naïve, HER2-Positive, Locally Advanced/Metastatic Breast Cancer. BMC Cancer 2016, 16 (1), 352.
93. Blanco, E.; Shen, H.; Ferrari, M. Principles of Nanoparticle Design for Overcoming Biological Barriers to Drug Delivery. Nat. Biotechnol. 2015, 33 (9), 941–951.
94. Webber, M. J.; Langer, R. Drug Delivery by Supramolecular Design. Chem. Soc. Rev. 2017.
95. Hossen, S.; Hossain, M. K.; Basher, M. K.; Mia, M. N. H.; Rahman, M. T.; Uddin, M. J. Smart Nanocarrier-Based Drug Delivery Systems for Cancer Therapy and Toxicity Studies: A Review. J. Adv. Res. 2019, 15, 1–18.

96. Bakker, M. H.; Kieltyka, R. E.; Albertazzi, L.; Dankers, P. Y. W. Modular Supramolecular Ureidopyrimidinone Polymer Carriers for Intracellular Delivery. RSC Adv. 2016, 6 (112), 110600–110603.
97. Ma, W.; Su, H.; Cheetham, A. G.; Zhang, W.; Wang, Y.; Kan, Q.; Cui, H. Synergistic Antitumor Activity of a Self-Assembling Camptothecin and Capecitabine Hybrid Prodrug for Improved Efficacy. J. Controlled Release 2017, 263, 102–111.
98. Varela-Aramburu, S.; Morgese, G.; Su, L.; Schoenmakers, S. M. C.; Perrone, M.; Leanza, L.; Perego, C.; Pavan, G. M.; Palmans, A. R. A.; Meijer, E. W. Exploring the Potential of Benzene-1,3,5-Tricarboxamide Supramolecular Polymers as Biomaterials. Biomacromolecules 2020, 21 (10), 4105–4115.
99. Bakker, M. H.; Lee, C. C.; Meijer, E. W.; Dankers, P. Y. W.; Albertazzi, L. Multicomponent Supramolecular Polymers as a Modular Platform for Intracellular Delivery. ACS Nano 2016, 10 (2), 1845–1852.

# Chapter 2 | Designing multi-responsive supramolecular polymers

*This chapter reproduces almost literally the findings reported in: Fuentes, E.; Gerth, M.; Berrocal, J. A.; Matera, C.; Gorostiza, P.; Voets, I. K.; Pujals, S.; Albertazzi, L. An Azobenzene-Based Single-Component Supramolecular Polymer Responsive to Multiple Stimuli in Water. J. Am. Chem. Soc. 2020, 142 (22), 10069–10078.*

## 2.1 Introduction

As introduced in Chapter 1, supramolecular polymers are promising self-assembled structures showing a great potential for medical applications such as drug delivery systems,[1–5] contrast agents[6] or hydrogels for tissue engineering.[7–10]

Inspired by supramolecular polymers existing in nature, e.g. actin filaments, chemists attempt to create synthetic materials with life-like properties. In this framework, the design of dynamic structures capable of mimicking the polymerization-depolymerization equilibrium of biological polymers allows the preparation of functional adaptive materials that change properties in response to a specific stimulus. This responsiveness is interesting at a fundamental level, but is also appealing for a variety of applications. For example, the possibility to disassemble supramolecular drug carriers in a controlled fashion allows for spatio-temporal control over the release of drugs.[11] Many efforts have been carried out to explore new responsive materials and new strategies to impart responsivity into the monomer design. The groups of Besenius, Schmuck and Stupp designed systems using pH as a trigger to change stability and promote disassembly.[12–15] Yagai and co-workers explored the use of light, temperature and ultrasound as triggers to control foldability of supramolecular polymers.[16–18] Lee reported supramolecular nanotubules that undergo a contraction in response to temperature.[19] Voets reported salt triggered changes in dimensions and cooperativity of the self-assembly.[20] Moreover, in light of biological applications, the possibility to obtain response to protein binding and enzyme activity has also been studied.[21–26]

Multi-responsivity, i.e. the ability to independently respond to different cues, in aqueous media proved to be more challenging to implement. Using multiple stimuli appears as a promising strategy to achieve fine control over supramolecular polymers' properties. Moreover, it opens the way to logic-gate assemblies able to generate a response only when two stimuli are simultaneously present, increasing selectivity.[27-29] This is particularly interesting in the case of biological applications where the complex cellular environment provides multiple cues to the administered synthetic material.

Few pioneering examples of multi-responsivity have recently been reported. Besenius and co-workers designed a system responsive to pH and reactive oxygen species, which together with temperature was able to tune the gelating properties of the material.[30] Bhosale and co-workers reported supramolecular ribbons with both pH- and temperature-dependent helicity.[31] Thayumanavan and co-workers showed the possibility to incorporate different responsive moieties into polymeric amphiphiles through a post-polymerization step, enabling response to light, protein and redox environment.[32] Li and co-workers designed a molecule that self-assembled into fibres, responsive to different ions and temperature.[33] However, these interesting properties come at the

price of complex design, either by incorporating multiple components or synthetically challenging building blocks. Using multiple response mechanisms in the same monomer appears as a promising strategy to achieve fine control over supramolecular polymers.

In this chapter we synthesise a single component supramolecular polymer, self-assembled in water which is capable of independently responding to four stimuli, namely light, pH, ionic strength and temperature. This system is designed to offer control over self-assembly through distinct mechanisms, modifying the assembly state in terms of both length and configuration. By a combination of techniques including Transmission Electron Microscopy (TEM), Circular Dichroism (CD), High Performance Liquid Chromatography (HPLC) and Static Light Scattering (SLS), we demonstrate that the assembly/disassembly of supramolecular polymers in water is pursued through controlled stimulations.

The results exposed in this chapter pave the way towards simpler and highly controllable supramolecular polymers, contributing to the fundamental development of self-assembly in water as well as to their biomedical applications.

## 2.2 Results and discussion

### 2.2.1 Molecular design and synthesis

First, a discotic amphiphile was especially designed to self-assemble into supramolecular polymers and exhibit responsiveness to light, temperature, pH and salt concentration. The design was based on the well-studied BTA, bearing three identical amphiphilic wedges. These wedges were designed to be modular, combining natural and non-natural amino acids chosen to induce self-assembly in water as well as to imprint specific responsiveness (Fig. 2.1).

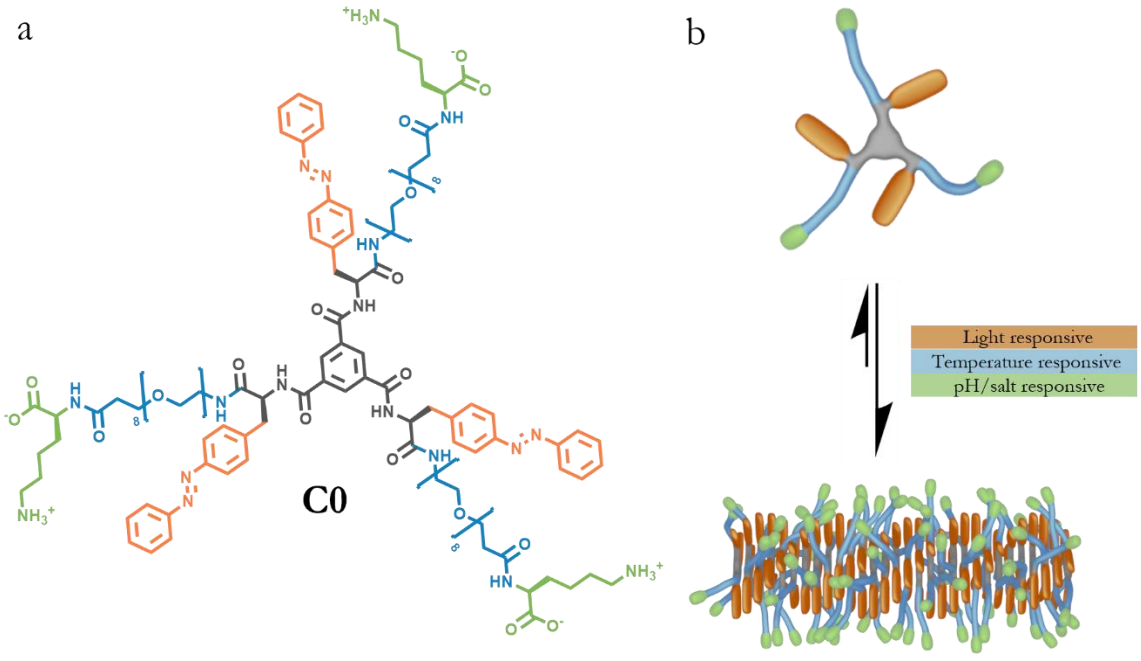


Figure 2.1 (a) Molecular structure of C0. (b) Schematic representation of monomer C0 and its self-assembly into supramolecular fibres. The moieties responsible for responsiveness are highlighted in different colours: Orange: light responsive moiety / Blue: temperature responsive moiety / Green: pH and ionic strength responsive moiety.

BTA was chosen as a core to drive aggregation into columnar stacks due to the well-known H-bonding behaviour (Fig. 2.1 a, highlighted in grey).[34] A non-natural azobenzene amino acid (L-phenylalanine-4'-azobenzene, Fig. 2.1 a, highlighted in orange), was placed as the innermost block of the wedge to enhance self-assembly by increasing hydrophobicity, adding new π-π stacking and by shielding the intermolecular H-bonds of the BTA core from water. At the same time, the azobenzene moiety imparts light-responsivity through the well-known *E*-*Z* isomerization. Azobenzenes are a well-established class of molecular photoswitches in the fields of smart materials and photocontrol of biological systems because of some favourable characteristics, such as design flexibility, ease of synthesis, large changes in geometry upon isomerization, high quantum yields, and low photobleaching rates.[35,36] We hypothesized that the *E* form favours assembly due to its planar hydrophobic nature, while the non-planar and more polar *Z* form will destabilize monomer stacking and increase monomer solubility.[37] The second module of the wedge is an octa(ethylene glycol) amino acid (Fig. 2.1 a, highlighted in blue) that grants flexibility and solubility in water, while it confers thermal responsivity due to its temperature-dependent hydrophilicity.[38–41] Finally, a C-terminal lysine (Fig. 2.1 a, highlighted in green) was added to enhance water solubility owing to the charged groups and induce the ampholytic character of this particular amino acid, which can result in dual pH and ionic strength response. In addition, the free amine gives an ideal anchoring point to do further functionalizations.

The described monomer was designed to be synthesized through standard solid phase peptide synthesis (SPPS), offering a modular and straightforward synthesis (Fig. 2.2). All building blocks are commercially available or are synthesized as Fmoc-protected amino acids allowing to iteratively repeat the same synthetic steps. Following a Fmoc strategy, the wedge is grown sequentially on the resin from C-terminus to N-terminus using the proper Fmoc protected building blocks. Both octa(ethylene glycol) and azobenzene couplings were not standard and were optimized (see methods section). After its completion (steps i to vi, Fig. 2.2), the wedge was cleaved from the resin keeping the Boc protecting group (step vii) and subsequently purified through $H_2O$:DCM extraction.

The final step, consisting of the convergent coupling to form the BTA, was performed in solution. The wedge was reacted with a 1,3,5-benzenetricarbonyl trichloride, thereby forming the Boc-protected C0 (step viii). Boc deprotection was performed and the final product was purified through reversed-phase HPLC (step ix). The purity and molecular weight of the desired product were confirmed using reversed-phase HPLC-MS, MALDI and $^1$H-NMR. Detailed synthetic procedures and material characterizations are provided in the methods section.

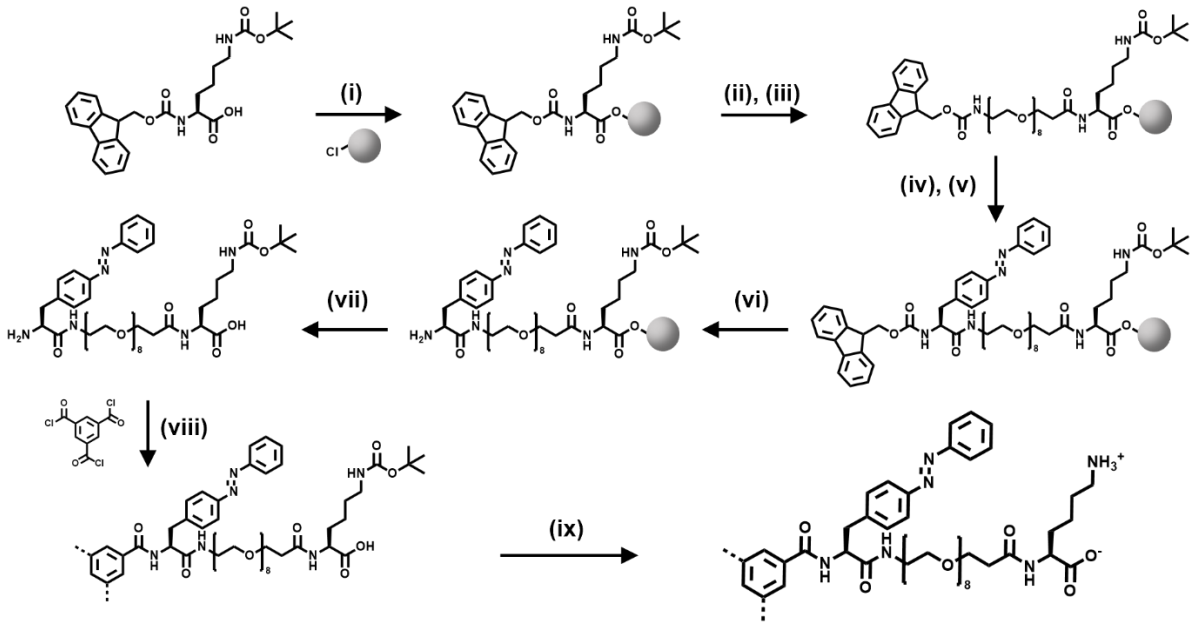


Figure 2.2 Synthesis of C0: i) Coupling of Fmoc-Lys(Boc)-OH to 2-chlorotrityl chloride resin (grey circle), DCM, DIEA, 1h. ii) Fmoc removal, 20% piperidine in DMF. iii) Coupling of Fmoc-octa(ethylene glycol)-OH, DCM:DMF 1:1, PyBOP, DIEA 15h. iv) Fmoc removal, 20% piperidine in DMF. v) Coupling of Fmoc-Azo, DCM:DMF 1:1, PyBOP, DIEA 15h. vi) Fmoc removal, 20% piperidine in DMF. vii) Cleavage, TFA 95% v/v in $H_2O$. viii) Core coupling, 1,3,5-benzenetricarbonyl trichloride, $CHCl_3$, DIEA PyBOP 15h. ix) Boc removal, TFA 95% $H_2O$.

This synthetic strategy allows the facile and precise control over the structure by using standard Solid-Phase Peptide Synthesis (SPPS). The use of properly protected natural and non-natural amino acids reduces the number of necessary purifications in comparison with in-solution synthesis. Moreover, the sequence, the chemical nature and the number of amino acids can be changed without modifying the synthetic procedure. This is a great advantage in light of structure optimization as well as for the generation of libraries of compounds.

## 2.2.2 Self-assembly and spectroscopic behaviour

To investigate the self-assembly behaviour, C0 was first dissolved in DMSO at a concentration of 2.5-10 mM, in which it is molecularly dissolved, eliminating any possible pre-existing aggregates. Next, the concentrated stock solution was diluted with milli Q water to obtain a 25-100 μM of monomer, triggering the self-assembly. Unless stated otherwise, a temperature annealing (70 °C for 1 h + 24 h at rt) was applied to obtain a reproducible equilibrium.

TEM showed the absence of aggregates in DMSO (Fig. 2.3 a), confirming, together with the resolved $^1$H-NMR, the molecularly dissolved state in this solvent. In water, C0 at 100 μM assembled into μm-long and flexible fibres as shown in Fig. 2.3 b. A quantitative analysis of the TEM images reveals a diameter of 6.48 ± 1.15 nm, in good agreement with other reported water-soluble BTAs.[42]

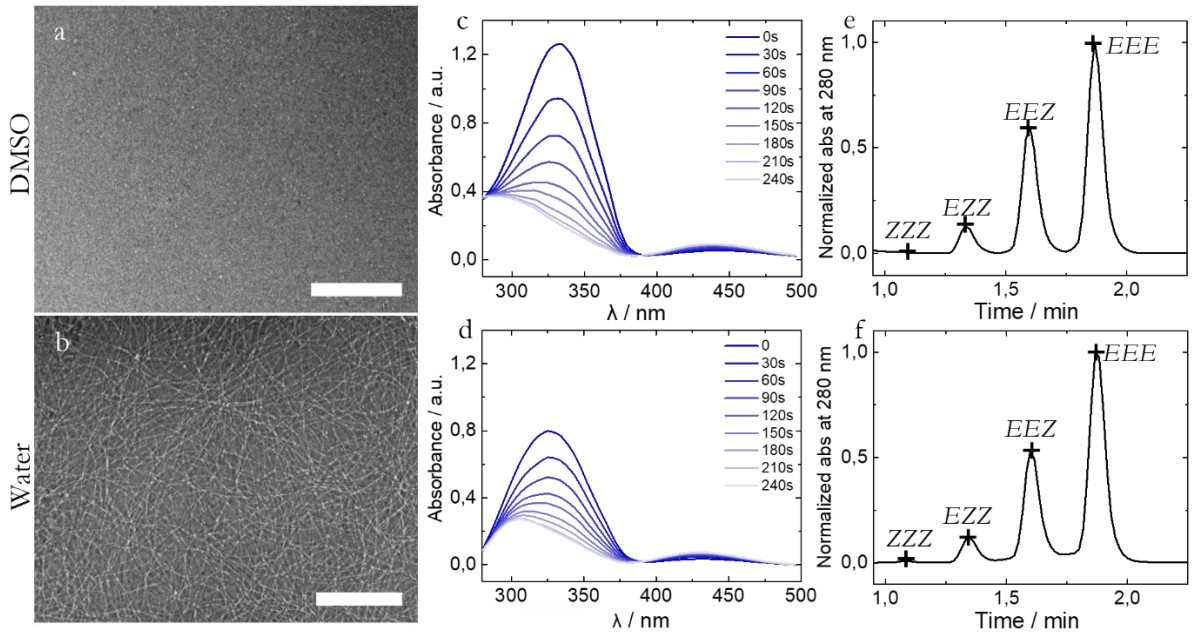


Figure 2.3 TEM image of 100 μM of C0 (a) in DMSO and (b) in water (scale bar: 500 nm). *E-Z* photoisomerization of C0 at 25 μM (c) in DMSO and (d) water, with UV (λ = 365 nm) irradiations of 30s. HPLC chromatogram of C0 (e) in DMSO and (f) water at 280 nm (measured isosbestic point).

In order to characterize the monomer isomerization state and switching ability inside the assemblies we performed UV-Vis spectroscopy and HPLC of C0 prepared in both in DMSO and water (Fig. 2.3 c, d, e and f). Azobenzene has a characteristic absorbance spectrum that allows studying the relative population of the two isomers, namely for the *E* isomer $\lambda_{max}$= 330 nm and for the *Z* isomer $\lambda_{max}$= 430 nm. The UV-Vis spectra were recorded in DMSO (non-stacked monomer) and milli Q (mainly stacked monomer) at different UV irradiation (λ = 365 nm) times (Fig. 2.3 c and d). Initially, one absorbance peak was visible at λ = 330 nm corresponding to the *E*-configured azobenzene, the most stable isomer at standard conditions. Upon UV irradiation, the *E*-azobenzene peak decreases while the *Z*-azobenzene peak at 440 nm appears, resulting in two isosbestic points, at 280 nm and 387 nm, indicating that the isomerization took place.

Interestingly, even though spectroscopically we differentiate two states (*E* and *Z*), the monomer can actually be found in four different configurations. Considering that each monomer has three independent azobenzene moieties, that can be either *E* or *Z*, the monomer can be found as *EEE*, *EEZ*, *EZZ* and *ZZZ*. Indeed, the analysis of C0 in both DMSO and water by HPLC-MS (Fig. 2.3 e, f) displayed four peaks in agreement with previous reports.[42] HPLC also allowed the analysis of the relative distribution in population of the isomers, which is valuable information since the isomers' distribution can have an impact on the self-assembly.[48] As shown in figure 2.3 e, f, monomers start mostly with azobenzenes in the *E* configuration (*EEE*), while a significant population of *EEZ* is present in the non-irradiated state. UV irradiation will change the distribution of these populations, which can be recovered through irradiation with blue light (455 nm).

Additionally, we were able to compare the kinetics of photoisomerization in water and DMSO by plotting the ratio between the peaks at 430 nm and 330 nm of the UV-Vis spectra, which as a first approximation we define as the "*E*/*Z* ratio". This shows an identical curve for water and DMSO,

with a maximum conversion in less than 5 minutes, and concludes that the azobenzene moiety can efficiently isomerize as a free molecule in solution (DMSO) and in the assembled state (water) (Fig. 2.4).

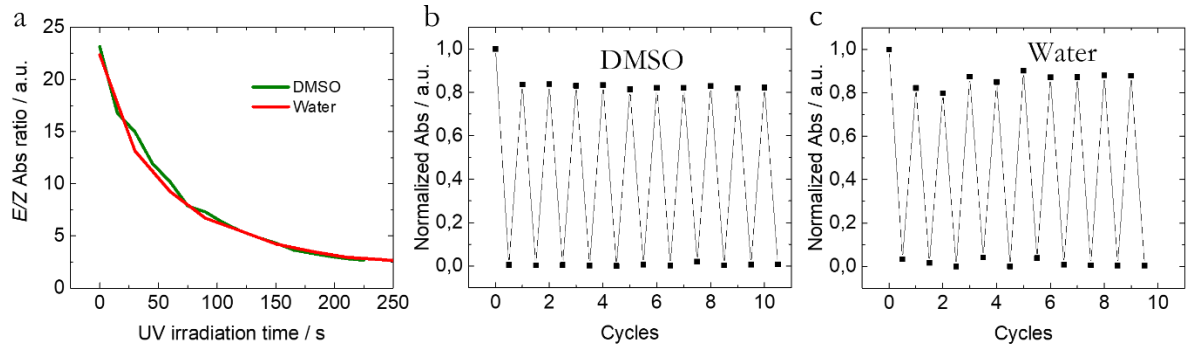


Figure 2.4. (a) *E*-*Z* isomerization kinetics, comparison between DMSO and $H_2O$ for C0 at 25 µM. Photofatigue experiment on C0 at 25 µM, in (a) DMSO and (b) water.

Azobenzenes in *Z* can isomerize back to the *E*-azobenzene by irradiating with blue light (455 nm), and our lab could reproduce 10 isomerization cycles without showing signs of fatigue in both DMSO and water (Fig. 2.4 b, c).

Finally, azobenzenes in *Z* configuration can thermally relax back to the *E*-configuration, and the kinetics of the isomerization depends on the azobenzene design. For this reason, we tested the thermal stability of the *Z* configuration overnight at 25 °C by recording the absorbance spectrum. We could conclude that the *Z* configuration is stable under the experimental conditions (Fig. 2.5) confirming the measured isomer distribution is not affected by the thermal back-isomerization. This is an important feature to consider when using photochromic ligands, especially for functional biological assays.[43,44]

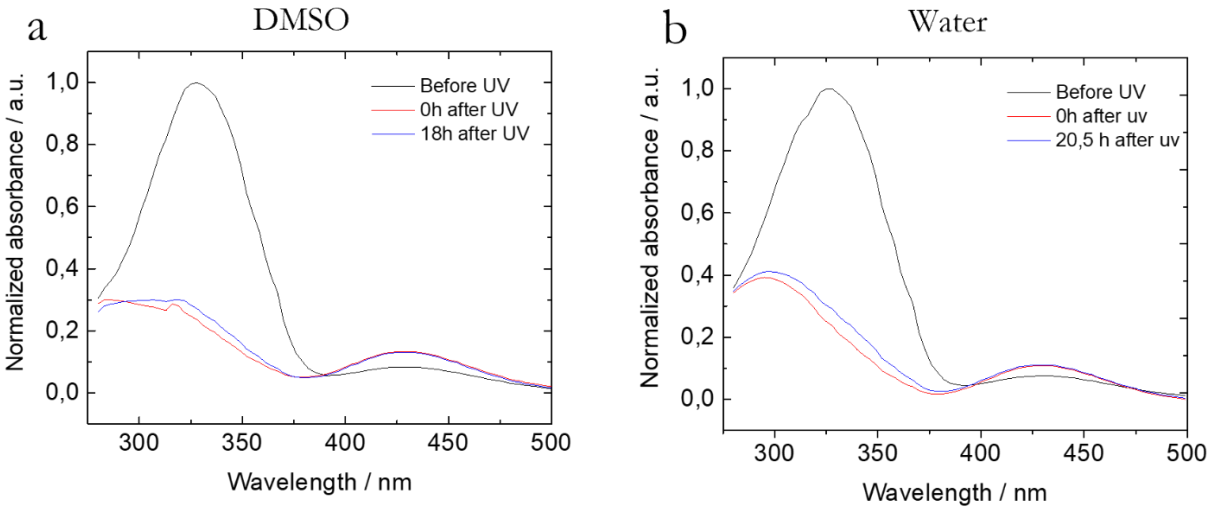


Figure 2.5 Thermal relaxation evaluation of C0 at 25 µM, in (a) DMSO and (b) water. After UV irradiation and measurement, sample was kept in the dark at 25 °C overnight and measured again after.

Altogether, these observations highlight a number of crucial features of our system. Firstly, the azobenzenes can isomerize both in the assembled and non-assembled states. This is far from trivial as the steric hindrance and interactions inside the assembly can prevent isomerization.[45–47]

Secondly, the very slow thermal recovery allows to photocontrol the system in time. Lastly, the system is fully reversible and can undergo multiple photoisomerization cycles. With these premises we proceed in studying the responsive behaviour of these fibres.

### 2.2.3 Light responsive self-assembly

As discussed, we hypothesized that the *E-Z* isomerization of an azobenzene placed close to the BTA would disrupt the self-assembly, due to the decreased propensity of the bent *Z*-azobenzenes to stack and the higher solubility in water.[36, 48] Thus, UV irradiation would result in disassembly of the fibres, and visible irradiation would promote fibre reassembly.

To confirm this hypothesis a combination of HPLC, TEM and CD was used. In Fig. 2.6 (a-i) we report a comparison among samples before/after irradiation with UV light, and after irradiation with blue light, making use of the three different techniques. The pristine sample contains a large fraction of EEE-monomer (about 60%), as indicated by HPLC (Fig. 2.6 a), which results in the assembly of long fibres as observed by TEM (Fig. 2.6 b). Due to the chirality of the azobenzene-containing amino acid, a helical stack with a preferred helicity is formed which can be followed by CD.[50] Fig. 2.6 c shows the CD spectrum of the fibres, revealing a band at 260-380 nm, centred at 330 nm, corresponding to the stacking of the azobenzene moieties.

After UV irradiation several dramatic changes can be observed. Firstly, significant isomerization takes place as shown by HPLC. Before UV treatment the photostationary state is primarily (>90%) composed of *EEE* and *EEZ* monomers, while Z-rich monomers are the majority species (*EZZ* 42% and *ZZZ* 42%) after UV irradiation. This photoisomerization is accompanied by the disappearance of the CD peak at 330 nm (Fig. 2.6 f) indicating loss of helical order, and most strikingly, by the complete disappearance of long fibrillar aggregates in the TEM characterization (Fig. 2.6 e). These observations showed that the *E-Z* isomerization of the azobenzene moieties results in the disassembly of the supramolecular polymers. Notably, after irradiation with blue light, recovery of the initial supramolecular polymers was obtained: HPLC shows that the population of isomers is reverted (Fig. 2.6 g), the CD signal is re-stablished (Fig. 2.6 i) and TEM again shows the presence of fibres of the same length and morphology (Fig. 2.6 h). Therefore, the material designed here is reversibly photo-responsive, and a correlation between monomer configuration and assembly state is established.

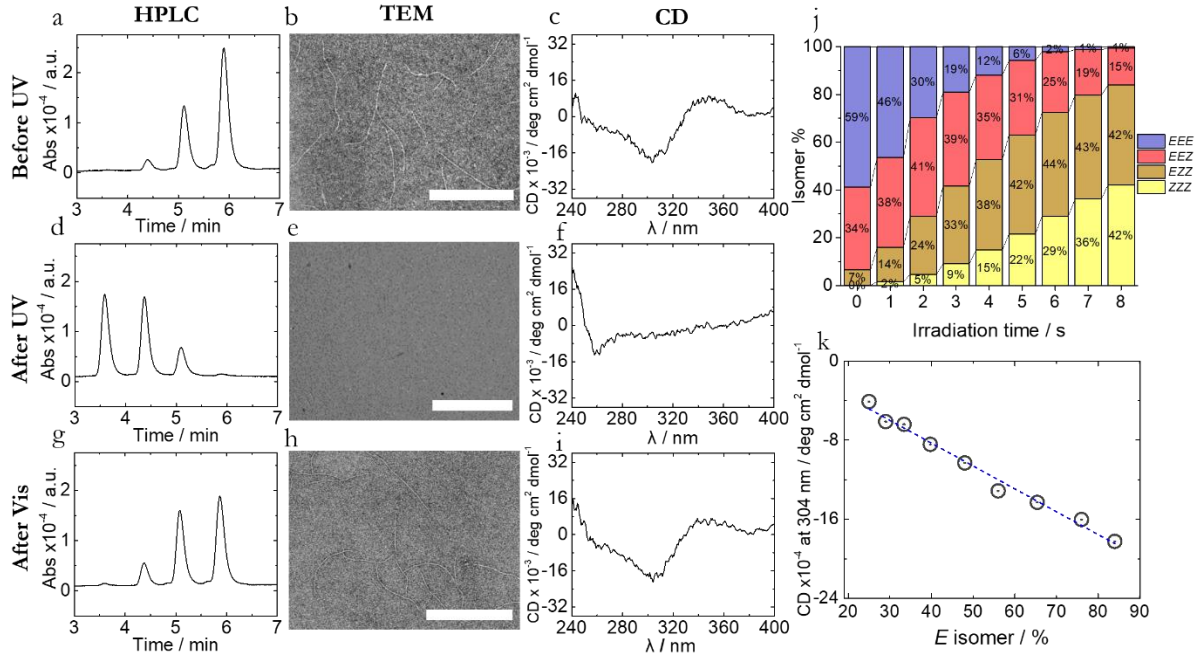


Figure 2.6 HPLC-UV at 280 nm of sample at 25 μM (a) before UV, (b) after UV irradiation (365nm, 8 s 100% at 1000mA of the LED intensity) and (c) after blue light (455 nm, 10 s, 100% at 1000 mA of the LED intensity). TEM of sample at 25 μM (d) be-fore UV, (e) after UV and (f) after blue light irradiation (scale bar: 500nm). CD of sample at 25 μM (g) before UV, (h) after 365 nm irradiation 8 s and (i) after 455 nm irradiation 10 s. (j) HPLC-UV analysis of isomer distribution at different UV irradiation times. (k) CD at 304 nm at different E-isomer % (the line was added to guide the eye).

To demonstrate that this switch is not abrupt but it is gradual and therefore more controllable, we performed a kinetic study to evaluate the isomer distribution and the assembly state at different irradiation times by HPLC and CD. In Fig. 2.6 j a plot of the distribution of isomers after stepwise UV irradiation is presented. Initially, the system contains predominantly monomers in *EEE* configuration while very gradually *Z*-forms are enriched. This shows the potential to precisely control relative abundance of the isomers by irradiation time. Interestingly, the CD signal, and therefore the amount of monomers in a helical fibre, is proportional to the amount of *E*-form of monomers (Fig. 2.6 k). This tendency points out that the crucial feature for the self-assembly of the monomers is the amount of *E* isomers. This indicates that there is a constructive interaction between azobenzenes in E inside the assembly, favouring the stacking of *EEE*, over *EEZ* or *EZZ*.

These results demonstrate a strong relationship between self-assembly and concentration of the *EEE*-isomer, as well as fine-tuning the self-assembly by UV irradiation. By this means, specific degrees of assembly are accessible by controlling the concentration of the *EEE* monomer.

In brief, we demonstrated by a combination of HPLC, TEM and CD that self-assembly in our system can be finely modulated by irradiation with UV and blue light to tune the isomer population distribution.

### 2.2.4 Temperature responsiveness

Due to the weak nature of the non-covalent bonding, supramolecular polymers generally display temperature-dependent behaviour, typically disassembling at high temperatures, a property that is

often used to study the self-assembly mechanism.[51] However, it has also been extensively reported that polyethylene glycol-containing supramolecular structures exhibit a different temperature response in water, showing a transition to an enhanced aggregation state at higher temperatures due to entropic effects.[30,52–55] Aiming to elucidate the temperature responsiveness of our system, we studied the assembly state at different temperatures by TEM, CD and SLS.

First, a temperature cycle (25-75-25 °C) was performed on the sample and TEM images were taken at the three different temperature points. Before heating, TEM showed few fibres per field with a length in the range of 300 nm (Fig. 2.7 a). When increasing the temperature to 75 °C, an increase in both number and length of the fibres can be clearly observed (Fig. 2.7 b). After cooling down and subsequent equilibration for 24 h, the number of fibres decreased again, resembling the situation before heating (Fig. 2.7 c) and strongly suggesting a reversible character of the response. In all cases, the sample preserved the fibre-like shape and diameter, although an increase in number, length and degree of entanglements can be observed at the higher temperature.

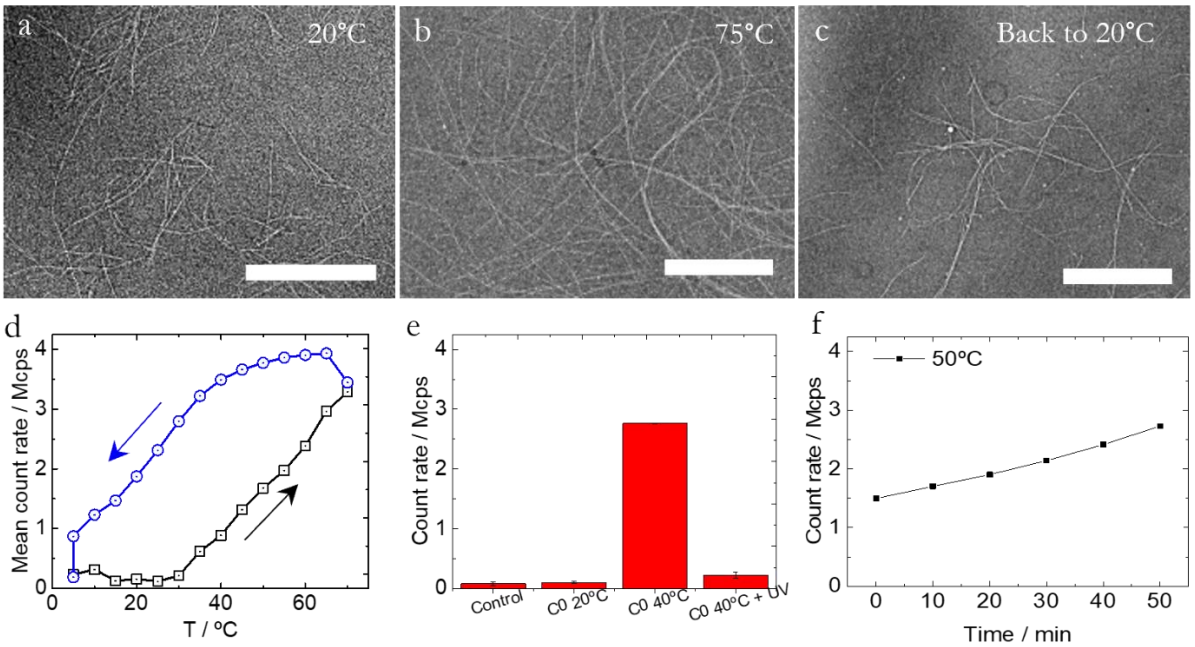


Figure 2.7 TEM of C0 at 20 μM at (a) 20 °C, (b) 75 °C and (c) 20 °C after cooling from 75 °C. (d) SLS temperature cycle on sample at 100 μM at 60 °C/h measuring in steps of 5 °C (the line was added to guide the eye). (e) SLS of C0 25 μM and 40 °C for 1 h, before and after UV irradiation. (e) SLS at 50 °C measured every 10 min for 50 min. All measurements were performed in a low volume Quartz cuvette, which was sealed to prevent solvent evaporation.

To corroborate this, a temperature cycle was performed with SLS (Fig. 2.7 d). We observed a very low scattering intensity (close to the limit of detection) at low temperatures. However, a linear increase was obtained ramping up from 25-30 °C to 70 °C. This trend is also reversible, matching with TEM results, but shows a hysteresis because of the long time required to reach equilibrium. Additionally, we tested this equilibration time by maintaining a sample at 50 °C for 50 min (Fig. 2.7 e). A linear increase is observed and no tendency towards plateau is observed, probably meaning the equilibration time is above 1h.

In order to confirm that the increase in scattering intensity is due to an increase in aggregation and not due to an increase in the refractive index at higher temperatures, we made use of the UV response of the system. We proceeded to warm up the sample at 40 °C and equilibrate, obtaining the increase in scattering, and then we irradiated the sample with UV light. The experiment resulted in a decrease of the scattering signal to detection limits (Fig. 2.7 f), for which the only explanation can be a loss in aggregation. Thus, the UV irradiation can trigger the disassembly even when the polymerization is enhanced.

To further investigate the mechanism of this phenomenon, a temperature cycling experiment was performed also with CD (Fig. 2.8 a), showing two clear transitions. First, a signal inversion for the stacked azobenzene from 5 °C to 40 °C, and second, a decrease in signal intensity above 50 °C (Fig. 2.8 a, b). The spectrum showed a positive Cotton effect between 260 nm and 380 nm (corresponding to the azobenzene absorbance) below rt, that changed to a negative Cotton effect at 20-25 °C. On the contrary the CD signal corresponding of the BTA cores ($\lambda_{max}$ = 220 nm, only peak shoulder can be observed) did not seem altered even though the cut-off wavelength of DMSO prevented a detailed analysis. Therefore, a full helix inversion seems unlikely while a change in the packing and helicity of the azobenzenes along the fibres seems responsible for the observed transition. The signal kept increasing until 50 °C, and then started decreasing in a reversible manner (Fig. 2.8 b). This inflection could imply a "classical" loss in aggregation due to temperature-induced depolymerization.

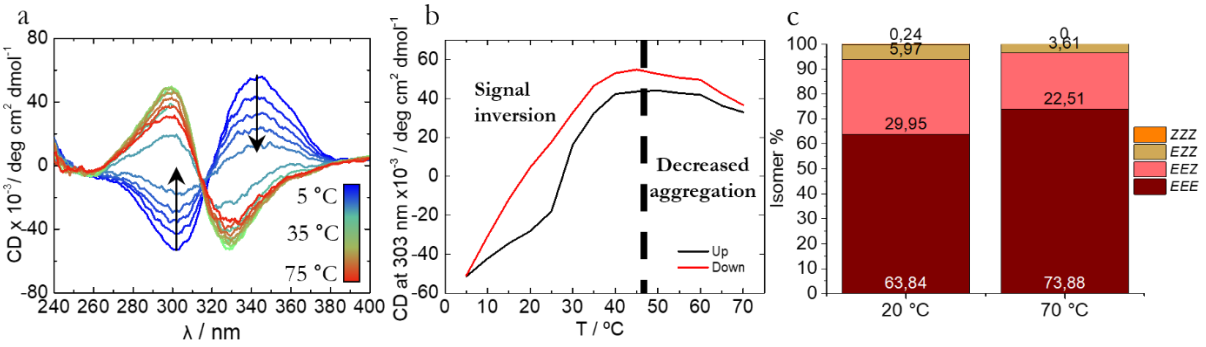


Figure 2.8 CD heating ramp experiment on sample at 25 μM at 60 °C/h, measuring in steps of 5 °C. (Left) HPLC-UV analysis of isomer distribution at 20 °C and 70 °C. (Right) CD at 303 nm recorded during a T cycle. Two transitions can be noticed. From 5 °C to 45-50 °C a signal inversion can be observed. From 50 °C to 70 °C, a loss in chiral assembly can be observed.

Interestingly, this unusual temperature-enhanced polymerization is the consequence from the synergistic response of the azobenzene moiety and the octa(ethylene glycol) chain together. Firstly, temperature modifies the distribution of *E* and *Z* isomers of the azobenzene moiety, favouring the more thermodynamically stable *EEE* isomer at high temperatures (Fig. 2.8 c) and thus increasing aggregation. However, this increase in the concentration (+20%) on its own cannot explain the increased SLS signal (+2000%) or the signal inversion observed in CD spectroscopy. Secondly, octa(ethylene glycol) hydrophobicity is increased upon heating because of loss of solvating water molecules,[39, 41] thereby increasing the driving forces for self-assembly driving forces. We hypothesize that the monomer rearrangement inside the fibres is related to the desolvation of octa(ethylene glycol), because it leads to an increased hydrophobicity and a reduced

steric hindrance between octa(ethylene glycol) chains. Analogous results have been reported before in similar scenarios.[19]

Together, these two effects are amplified. The temperature increases at the same time the hydrophobicity of each monomer and the distribution of azobenzene moieties in the *E*-configuration. Therefore, there are more monomers able to stack than at rt and their hydrophobicity is higher. The sum brings the systems to the highest aggregation state at 40-50 °C.

Summarizing, we have a supramolecular system with a reversible response to temperature, enhancing monomer aggregation above room temperature and changing the internal conformation of the lateral chain packing. Furthermore, even when the polymerization is enhanced, the assemblies remain responsive to light. Considering that the kinetics of the photoisomerization is much faster than the kinetics of the thermal back-isomerization, the light response dominates over the temperature response.

### 2.2.5 pH and ionic strength responsiveness

Previous work highlighted that the stability of supramolecular polymer can be affected by the repulsion between charged monomers.[56] An elegant strategy to design responsive systems using this phenomenon consists of introducing specific groups, whose protonation, and consequently charge, depends on pH.[12] Inspired by this work and aiming for an ampholytic behaviour in a single component, we included a C-terminal lysine in our design, exposing a carboxylic acid and a primary amine at the periphery of the monomer. Considering the pKa's of both amino (10.79) and carboxylic groups (2.20), we can delimit three pH ranges in which the net charge of the discotic monomer undergoes significant variations.

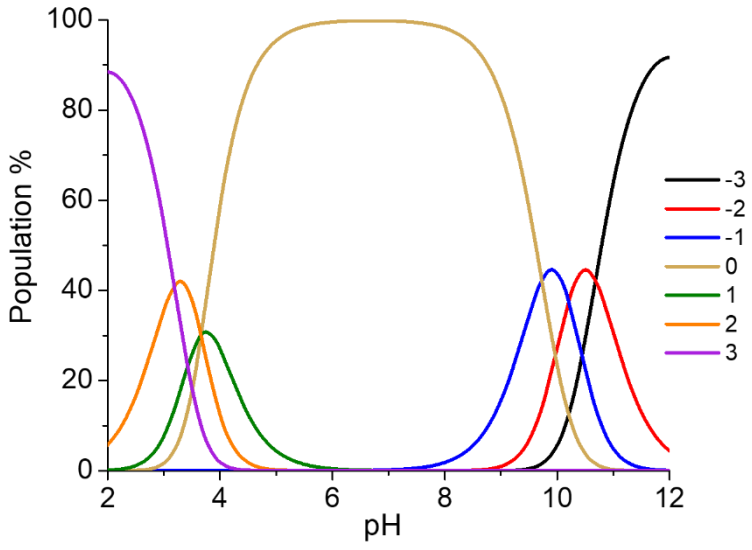


Figure 2.9 Percentage of charged species of C0 at different pH, estimated by MarvinSketch calculators software[57].

Approximately, between pH 3.9 and pH 9.6 monomers are zwitterionic, comprising three carboxylate groups and three ammonium groups, with a net charge of 0 (Fig. 2.9). When

approaching to pH 2.2, the carboxylate groups become protonated, resulting in a net positive charge, which would destabilize the aggregates and promote disassembly. A similar process would happen when approaching to pH 12, when the ammonium moieties are deprotonated, resulting in a net negative charge. Therefore, the system can evolve from a zwitterionic monomer, where the assembly would be favoured through potential ionic bridges between stacked discs, to electrostatic repulsion-induced disassembly.

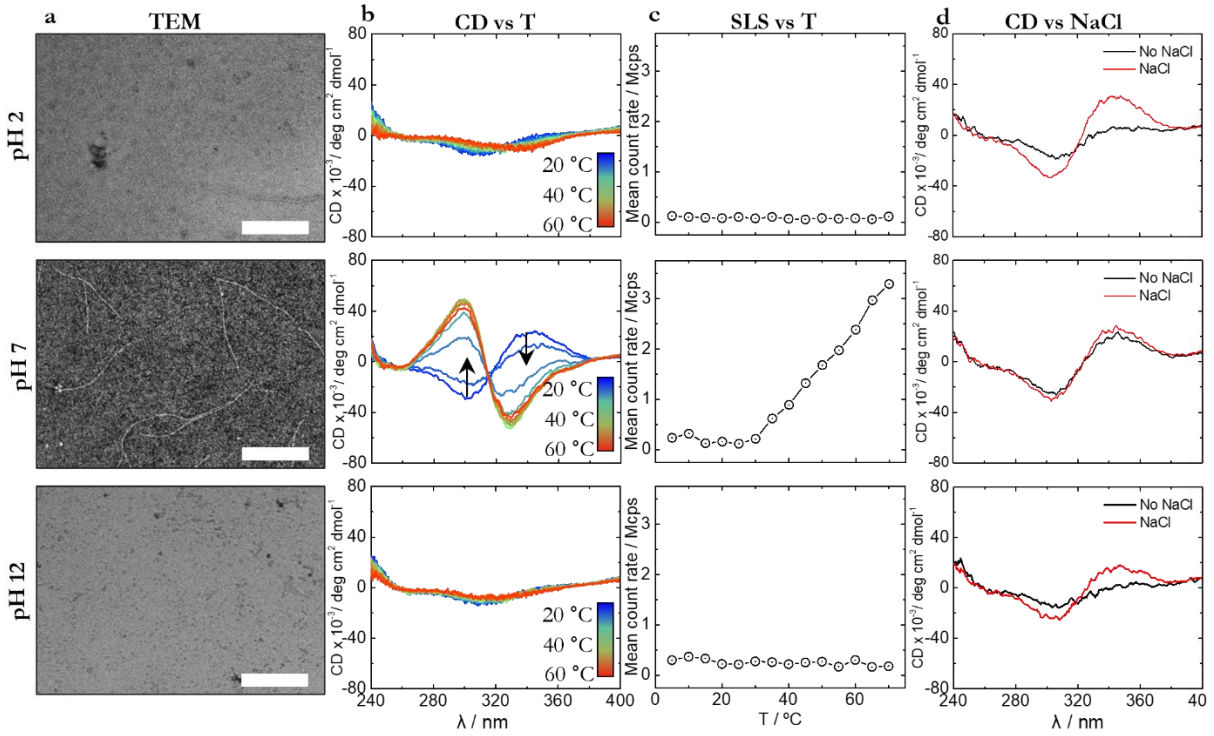


Figure 2.10 TEM image of C0 at 100 μM (a) at pH 2.0 ± 0.2, 7.0 ± 0.2 and 11.6 ± 0.2 (Scale bar: 250 nm). CD heating experiment at 25 μM (b) at pH 2.2 ± 0.2, 7.2 ± 0.8 and 12.0 ± 0.2 (60 °C/h, measuring in steps of 5 °C). SLS heating experiment at 100 μM (c) at pH 2.0 ± 0.2, 7.0 ± 0.2 and 11.6 ± 0.2 (60 °C/h measuring in steps of 5 °C) (the line was added to guide the eye). CD at 5 °C with and without NaCl 150 mM (d) at pH 2.2 ± 0.2, 7.2 ± 0.8 and 12.0 ± 0.2.

In order to demonstrate that this ampholytic behaviour has an impact on self-assembly, we performed a series of experiments including TEM, CD and SLS. We prepared samples at three different pH and compared the self-assembly of zwitterionic monomers (+3/-3 at pH 7.2 ± 0.8) with positively charged monomers (+3 at pH 2.2 ± 0.2) and negatively charged monomers (-3 at pH 12.0 ± 0.2). These pH values were chosen according to the expected maximum of population of each charged species (Fig. 2.9).

TEM revealed the formation of fibres at neutral pH, while very few were observed at low pH and none at high pH (Fig. 2.10 a). This indicates that the repulsion at high and low pH values is sufficient to destabilize the aggregates resulting in monomers or small aggregates. In order to reinforce this result and explore the combination of the temperature and pH responses, a temperature ramping experiment with CD and SLS was performed at the different pH values. Very low signal was obtained for non-zwitterionic samples using CD, showing also a very weak temperature response (Fig. 2.10 b). This can be attributed to the few monomers still zwitterionic and, hence, able to aggregate. SLS showed a low count rate that did not increase upon heating (Fig.

2.10 c), indicating no (significant) aggregation, confirming the TEM and CD results. These indications altogether support the pH responsiveness of our fibres and the existence of three pH windows in which the system´s net charge changes, producing a dramatic change in aggregation. Furthermore, it demonstrated that the temperature effect on the self-assembly at extreme pH's, where the increased hydrophobicity due to desolvation of the octaethylene glycol chain competes against the electrostatic repulsion, is too subtle to make a change. Thus, in this scenario the pH response dominates over the temperature response.

Previous reports have also shown that ionic strength can modulate monomer repulsion through shielding of charges.[55] Here, we tested if our fibres respond to changes in ionic strength in the three pH windows. In particular, we added NaCl at a physiological concentration (150 mM) with the purpose of shielding the charges. In figure 2.10 d we compare CD spectra from samples at pH 2.2, 7.2 and 12.0, with and without salt. In all cases, we observe an increase in CD signal, associated with an increased aggregation. Under the acidic and basic conditions, the influence is more pronounced, because the sample changes from a disassembled to an assembled state.

These results demonstrate that the repulsion can be modified by the ionic strength, confirming the mechanism of the responsiveness to pH and its reversibility, and indicates the temperature response remains.

## 2.3 Conclusions

In conclusion, we synthesised C0 for the first time, proving the possibility to condensate different response mechanisms in single-component supramolecular polymers through a rational monomer design. Following a modular synthesis, we incorporate moieties in the monomer design which, simultaneously, drive the self-assembly and introduce responsiveness to different stimuli. The synthesis introduces advantages in light of structure optimization as well as for the generation of libraries of compounds.

Our system responds in a controlled and reversible fashion to light, temperature, pH and ionic strength modulating the assembly-disassembly equilibrium. By these means, we describe a system with multiple equilibria in which each state is accessible through different pathways, applying the stimuli either orthogonally or in combination, thereby facilitating a sophisticated degree of control (Fig. 2.11).

Our results pave the way towards effective and highly controllable supramolecular materials in which the responsiveness is fully imprinted in a single monomer. This is especially interesting for biological applications, such as drug delivery or tissue engineering, where controlling the material performance in a complex environment is challenging.

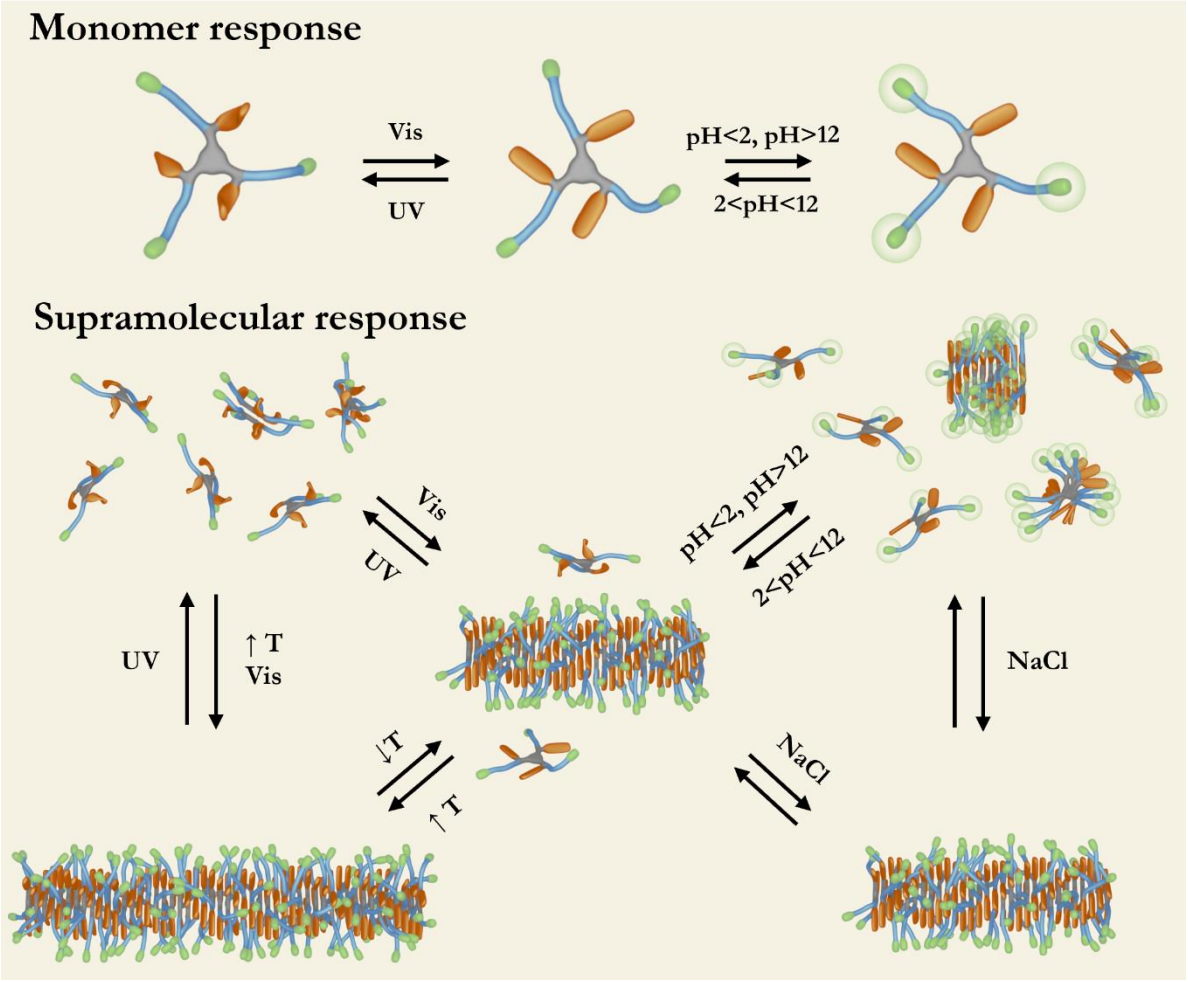


Figure 2.11 Schematic representation of the system. Above, molecular responsiveness to light and pH. Below, supramolecular responsiveness to light, pH, ionic strength and temperature.

## 2.4 Materials and Methods:

### 2.4.1 Materials

Unless stated otherwise, all solvents were obtained from commercial sources in at least analytical quality (a.r.) and were used without further purification. Ultrapure water was obtained from a Milli Pore system from Merck. Lysine and 2-Chlorotrityl chloride resin were obtained from Iris biotech. Fmoc-octa(ethylene glycol) amino acid and HBTU were purchased from Chempep. DIEA, piperidine, formic acid and benzene tricarbonyl chloride were obtained from Sigma-Aldrich.

L-Phenylalanine-4'-azobenzene was synthesised following the procedure reported before.[58,59] Synthesis performed by Dr. José Augusto Berrocal.

[3-(3-aminomethyl)phenylazo]phenylacetic acid (AMPP) was synthesised following the synthesis reported before.[60] Synthesis performed by Dr. Carlo Matera.

### 2.4.2 Instrumentation

**UV-Vis**

Measurements were performed with a Tecan infinite M200Pro microplate reader using a quartz cuvette of 0.5 mL and 1 cm of pathlength. Spectra were taken from 280 nm to 500 nm at every 3 nm.

**Reverse Phase-High Performance Liquid Chromatography**

During synthesis and characterization of monomers C0 and C0-2, measurements were recorded on a HPLC Waters e2695 separation module equipped with Photodiode Array detector Waters 2998 and Mass spectrometer QDA detector Acquity. A XSelect CSH C183.5 μm 4.6x50mm was used. Water 0.1% HCOOH and ACN 0.1% HCOOH were used as eluents. A gradient of 25-45% ACN in water was applied in 3.5 min. The elution speed was kept at 1.6 $ml \cdot min^{-1}$ and the temperature was maintained at 50 °C. The injection volume was 10 μl.

For the rest of the measurements reported in the main text, HPLC analysis was performed on a Shimadzu UFLC XR, equipped with two LC-20 AD XR prominence solvent pumps, a DGU-20A3 degassing unit, a SIL-20A autosampler and SPD-m20A UV detector. A Waters XTerra®MS C18 3.5 μm 2.1×150 mm column was used. A 30-60% gradient of ACN in water was applied in 8 min, with an elution speed of 0.2 $ml \cdot min^{-1}$. The injection volume was 10 μl.

**Transmission Electron Microscopy**

Images were taken with Jeol JEM 1010 MT electron microscope (Japan), operating at 80 kV. Images were obtained on a CCD camera Megaview III (ISIS), MNnster, Germany.

**Negative staining**

Samples were deposited onto C-only grids (pre-treated with glow discharge for 30 s) for 1 min. Then the solution was washed with water for 30 s, and finally it was negatively stained with uranyl acetate 2% during 1 min. The excess of solution was blotted with a filtering paper and the grids were stored in the desiccator.

**Static Light Scattering**

SLS measurements were performed with a Malvern ZetaSizer Nano ZS instrument operating at a light source wavelength of 532 nm and a fixed scattering angle of 173°. SLS was obtained at different temperatures, from 5 °C to 70 °C, measuring every 5 °C with a temperature ramp of 60 °C/h. The average of 3 accumulations is reported at each temperature.

**Circular Dichroism**

spectra was recorded on a Jasco J815 spectrometer, equipped with a PTC-423s/5 Peltier cell holder. A sealable quartz cell with a pathlength of 1 cm was used.

The spectra in Fig. 2.6 e were recorded continuously between 550-200 nm at every 0.5 nm, with a sensitivity of 100 mdeg, at 100 $nm \cdot min^{-1}$. The response time was set to 0.25s. The spectra were recorded at an interval of 5 °C between 5-75 °C at a temperature ramp of 1 $°C \cdot min^{-1}$. The average of 3 accumulations is reported.

The spectra in Fig. 2.6 and 2.8 c, f, i and Figure 2.10 d were recorded continuously between 550-235 nm at every 0.5 nm, with a sensitivity of 100 mdeg, at 200 nm·min$^{-1}$. The response time was set to 0.125s. The average of 3 accumulations is reported. During measurements the sample was kept isothermal at 20 °C, and if reported brought to 5 °C at an uncontrolled rate.

The spectra in Fig. 2.10 b were recorded continuously between 550-230 nm at every 0.2 nm, with a sensitivity of 100 mdeg, at 500 nm·min$^{-1}$. The response time was set to 0.25s. The spectra were recorded at an interval of 5 °C between 5-70 °C at a temperature ramp of 1 °C·min$^{-1}$. The average of 3 accumulations is reported.

**Nuclear magnetic resonance spectrometry (NMR)**

NMR spectra were recorded on a Varian Mercury Vx 400 MHz. Chemical shifts are given in ppm (δ) values relative to tetramethylsilane (TMS). The sample concentration was 2.3 mM.

**Matrix Assisted Laser Desorption Ionization -aldi-TOF**

Spectra were recorded on a Applied Biosystems - 4800 Plus MALDI TOF/TOF™ Analyzer. α-Cyano-4-hydroxycinnamic acid was used as a matrix.

### 2.4.3 Methods

## Chemical synthesis

The synthetic strategy consists of the wedge growth on a polymeric support (Solid Phase Peptide Synthesis), the subsequent cleavage from the solid and the final convergent coupling to the core in solution. The synthesis route described in Fig 2.1 for C0 is identical to the synthesis route followed for C0-2, just changing the synthetic azobenzene amino acid.

Initially, two discotic amphiphiles were synthesized following the same design, differing only in the type of azobenzene amino acid. C0 contains a L-phenylalanine-4'-azobenzene, the azobenzene is placed as a side chain of the wedge. In C0-2 (Fig. 2.18), which comprises a [3-(3-aminomethyl)-phenylazo]phenylacetic acid, the azobenzene is placed as backbone of the wedge. Despite the similar structures of both monomers, C0-2 did not self-assemble under any of the tested conditions of concentration, temperature and light irradiation. We hypothesize that the orientation and proximity to the core of the azobenzene moiety of C0-2 prevent effective stacking.

**Solid-phase peptide synthesis protocol**

**- Resin swelling**

2-chloro-trytil chloride resin (1.6 mmol/g) was transferred to a reaction syringe and swelled first with DCM and next with DMF, following:

I. DCM: x5 washings of 15 mL + 15 mL for 1 h.

II. DMF: x5 washings of 15 mL + 15 mL for 30 min.

III. DCM: x5 washings of 15 mL + 15 mL for 1 h

**- Loading**

Just after swelling, the first aa (Lys) was coupled. 1 eq Fmoc-Lys(Boc)-OH, 3 eq DIEA (N,N-Diisopropylethylamine) in 5 mL DCM for 1 h (manual shaking the first 5 minutes). MeOH (1 mL) was added to the mixture for 10 min. Then, the contents of the syringe were filtered and washed with DCM 15 mL x 3, DMF 15 mL x 3 and DCM 15 mL x 3.

**- Fmoc deprotection**

After each coupling, Fmoc-group deprotection is performed by treating the resin with piperidine in DMF a 20% v/v for 10 min, twice. The resin is then washed with DMF 15 mL 5 times and DCM 15 mL 5 times.

**- Octa(ethylene glycol) coupling**

1.5 eq Fmoc-Octa(ethylene glycol)-OH was preactivated in DCM:DMF 9:1 with 1.5 eq HBTU (Hexafluorophosphate Benzotriazole Tetramethyl Uronium) and 4.5 eq. DIEA. The mixture was transferred to the syringe, rocked for 15 h and shaken for 5 min every hour during the first three hours. Then, the syringe was filtered and washed with DCM 15 mL x 3, DMF 15 mL x 3 and DCM 15 mL x 3.

**- Azobenzene amino acid coupling**

1.5 eq Fmoc-Azo-OH was preactivated in DCM:DMF 1:1 with HBTU 1.5 eq and DIEA 4.5 eq. The mixture was transferred to the syringe, rocked for 15 h and agitated for 5 min every hour during the first three hours. Syringes containing the azobenzene compound were covered with aluminium foil to avoid light exposure. Then, the contents of the syringes were filtered and washed with DCM 15 mL x 3, DMF 15 mL x 3 and DCM 15 mL x 3.

**- Nynhydrin test** (Purchased from Anaspec)

Just after an aa coupling, a ninhydrin test was used in order to identify primary amines, so to check if the coupling is completed. The protocol can be found in the datasheet of the product (AS-25241):

1. 20-30 beads of resin were added in a test tube.

2. Two drops reagent 1, 2 and 3 were added.

3. The test tube was heated at 120 °C for 3-4 min.

The test has three possible results:

a) Blue (positive): Primary amines detected

b) Brown-red: Secondary amines detected

c) Pale yellow (no change of color, negative): no amines detected

In the cases of positive result, a recoupling of the same amino acid was required. If the result was negative, we proceeded to the Fmoc deprotection step.

**- Cleavage**

The resin was filtered and transferred to a 50 mL vessel and treated with 1% TFA in DCM for two minutes and filtrated and dried by a gentle stream of $N_2$. The procedure was performed twice. The product was purified by DCM:$H_2O$ phase extraction and dried in vacuo yielding wedge C0 and wedge C0-2.

Wedge C0

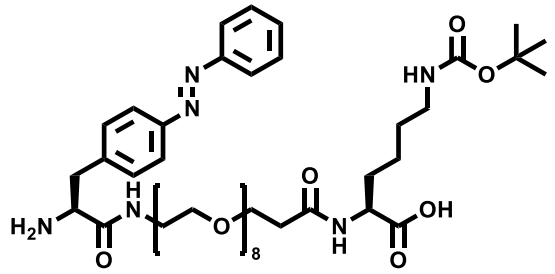

Figure 2.12 Molecular structure of wedge C0.

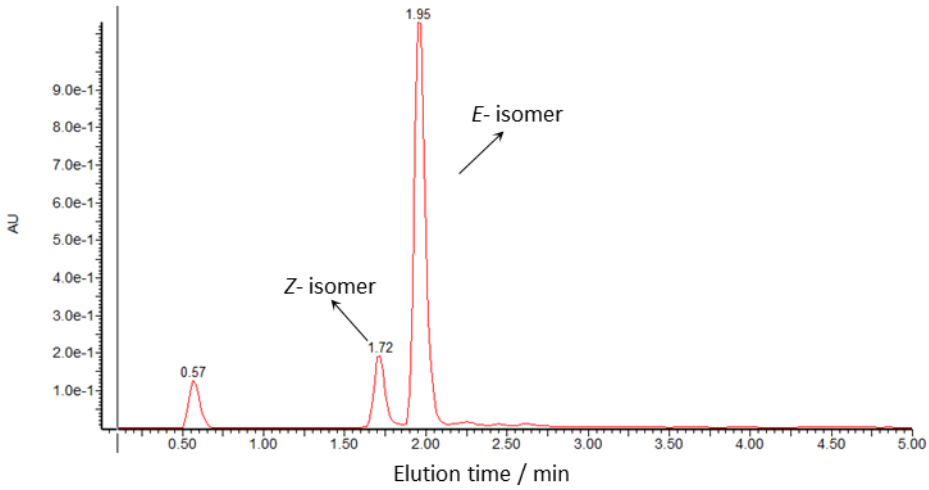


Figure 2.13 Chromatogram of wedge C0. Peak 1.72 corresponds to Z-isomer, peak at 1.96 corresponds to the E-isomer.

ESI(+) of wedge 1. m/z: $[M+H]^+$= 921.5, $[M+2H]^{2+}$= 461.2 m/z Calculated: m/z: $[M+H]^+$=921.5, $[M+2H]^{2+}$= 461.3

Wedge C0-2

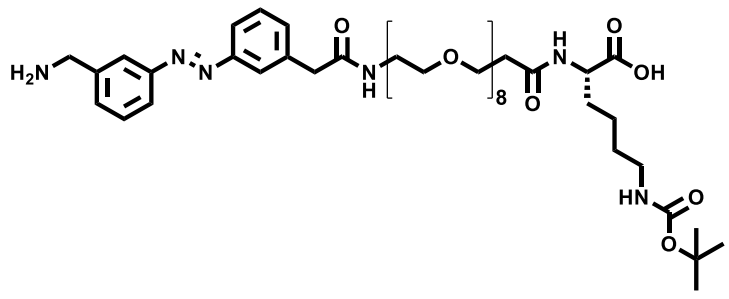

Figure 2.14 Molecular structure of wedge C0-2.

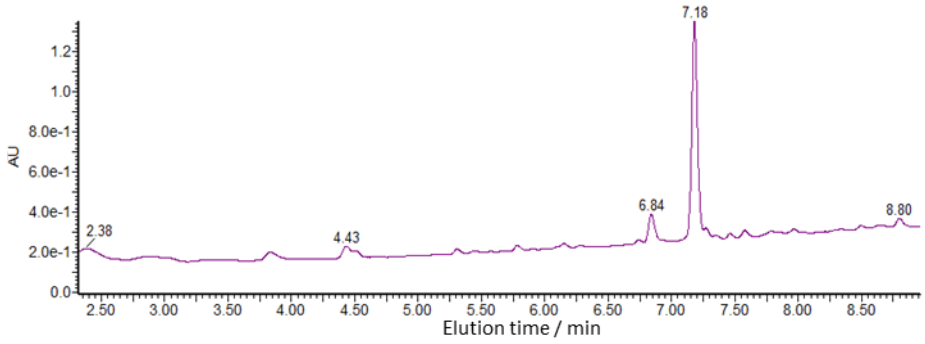


Figure 2.15 Chromatogram of wedge C0-2. The peak at 6.84 min corresponds to the Z-isomer, the peak at 7.18 min corresponds to the E-isomer. In this case a different column was used (SunFire C18 5 µm 4.6x150mm) and a different gradient was applied (linear gradient 5 - 100% ACN in water was applied in 16 min).

ESI(+) of wedge 2. m/z: $[M+H]^+$= 921.6, $[M+2H]^{2+}$= 461.2 m/z Calculated: m/z: $[M+H]^+$=921.5, $[M+2H]^{2+}$= 461.3

**Solution synthesis protocol**

1 eq of wedge (31.7 mg, 34.42 µmol) and 3 eq of triethylamine were dissolved in $CHCl_3$ (0.5 mL) and cooled to 0 °C. 0.25 eq of 1,3,5-benzenetricarbonyl trichloride (2.29 mg, 8.60 µmol) was dissolved in 0.5 mL of $CHCl_3$ and added dropwise to the reaction mixture under stirring. After 15 min at 0 °C, the mixture was stirred another 12 hrs at rt. The mixture was subsequently concentrated in vacuo and the resulting oil was dissolved in $H_2O$:ACN 1:1 and dried in vacuo.

Boc cleavage was performed by treating the product with TFA 95%, 2,5% $H_2O$ and 2.5% TIPS (triisopropyl silane) for 1 h. The product was then dried by a gentle stream of $N_2$, dissolved in $H_2O$:ACN 1:1, purified by reversed-phase HPLC and dried in vacuo yielding C0 and C0-2.

C0 monomer

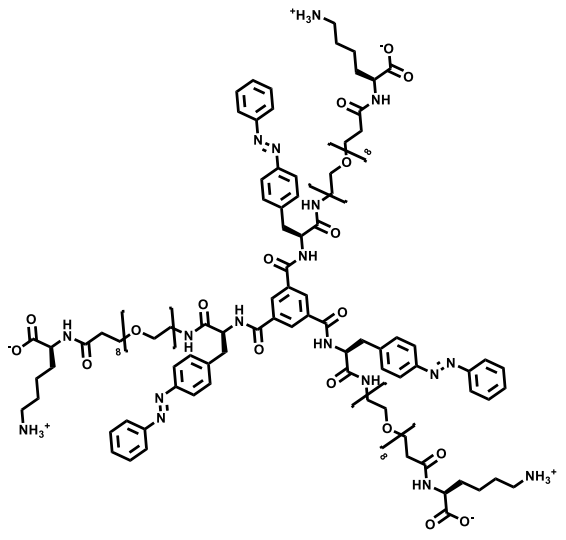

Figure 2.16. Molecular structure of C0. MW: 2619.042.

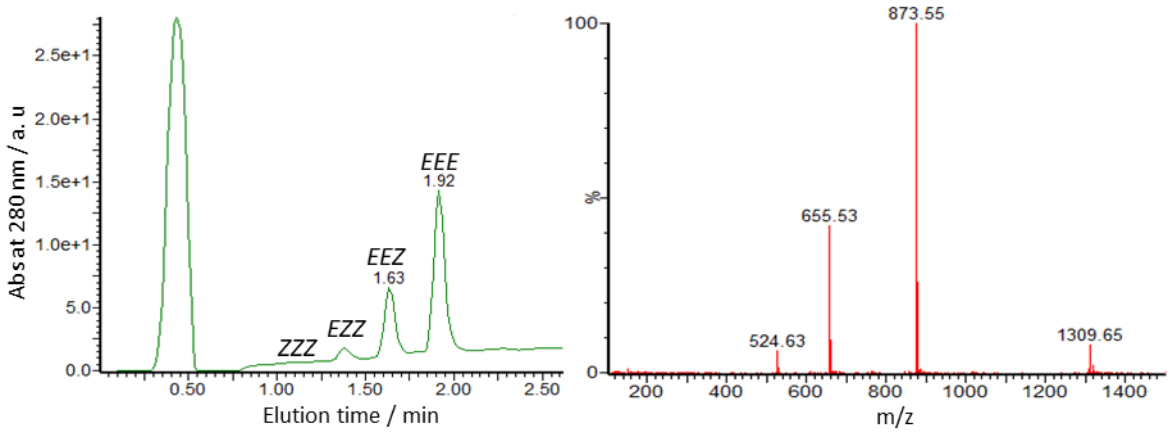


Figure 2.17 (Left) RP-HPLC at 280 nm of C0. (Right) ESI-MS(+): m/z: $[M+2H]^{2+}$= 1309.65, $[M+3H]^{3+}$= 873.55, $[M+4H]^{4+}$= 655.53, $[M+5H]^{5+}$= 524.63 / Calculated m/z: $[M+2H]^{2+}$= 1310.52, $[M+3H]^{3+}$= 874.01, $[M+4H]^{4+}$= 655.85, $[M+5H]^{5+}$= 524.81

MALDI-TOF-MS (α-Cyano-4-hydroxycinnamic acid was used as a matrix): m/z: $[M+H]^{+}$= 2617.1 (Isotopic distribution can be observed).

$^{1}$H NMR (400 MHz, DMSO-d6, *E*/*Z* mixture, signals of the main isomer)

δ /ppm = 9.12 (s, 3H), 8.39 (m, 6H), 8.31 (m, 3H), 7.84-7.76 (m, 12H), 7.62 (m, 3H), 7.55 (m, 6H), 6.68 (m, 3H), 4.81 (m, 3H), 3.96 (m, 3H), 3.65-3.40 (m, 114H, partially hidden by water signal), 2.70 (m, 6H), 2.35 (m, 6H), 1.64 (m, 3H), 1.50 (m, 9H), 1.29 (m, 6H).

C0-2 monomer

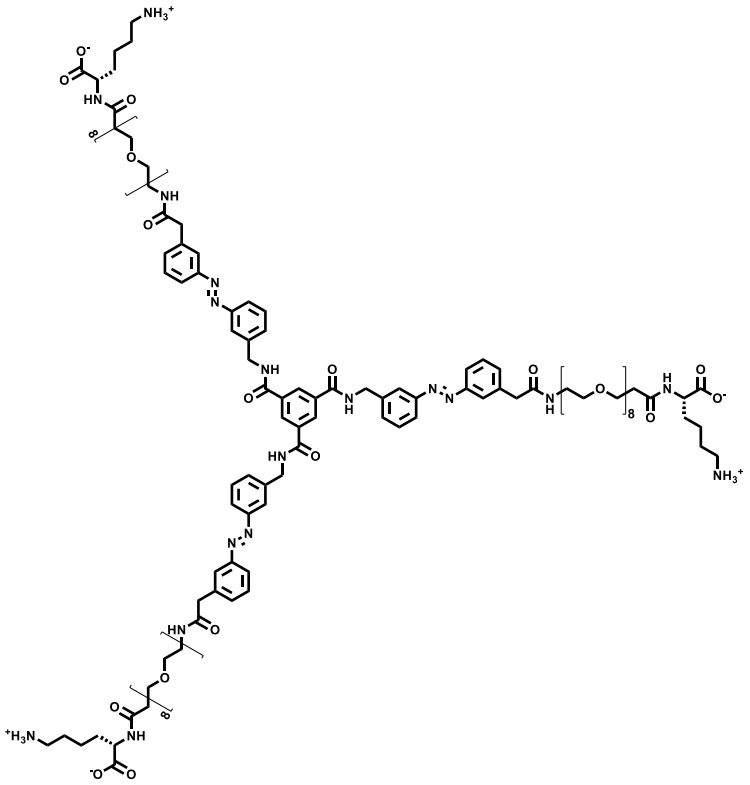

Figure 2.18 Molecular structure of C0-2. MW: 2619.042.

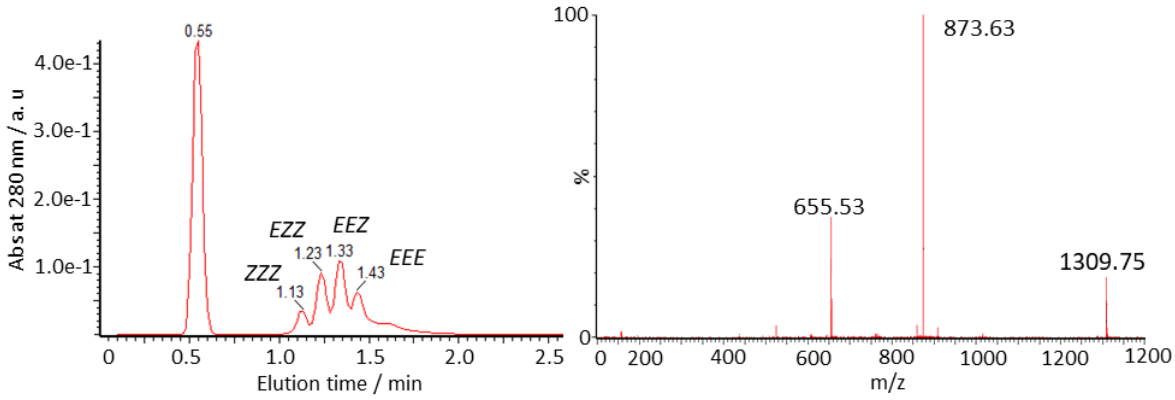


Figure 2.19 (Left) RP-HPLC at 280nm of C0-2. (Right) ESI-MS(+): m/z: $[M+2H]^{2+}$= 1309.75, $[M+3H]^{3+}$= 873.63, $[M+4H]^{4+}$= 655.53 / Calculated m/z: $[M+2H]^{2+}$= 1310.52, $[M+3H]^{3+}$= 874.01, $[M+4H]^{4+}$= 655.85

MALDI-TOF-MS (α-Cyano-4-hydroxycinnamic acid was used as a matrix): m/z: $[M+H]^{+}$= 2619.2 (Isotopic distribution can be observed). Calculated: $[M+H]^{+}$= 2619.04.

## Self-assembly characterization

### Irradiation set up

Vilber Lourmat - VL-6-LC Lamp was used as UV source at 365 nm, and custom LED lamp from FCTecnics was used as blue source at 455 nm. For CD experiments and HPLC of Fig. 2.6 and

2.10, another two LED light sources were used, a Thorlabs M365LP1-C5 was used as UV source at 365 nm, and a Thorlabs M455L3-C5 was used as blue source at 455 nm. Irradiations were performed inside a custom-made black box and with a distance between the sample and the light source of 15 cm.

## Light responsiveness

### Sample preparation

Samples were prepared as explained in the main text. The pH of the samples was measured only for samples used to evaluate the pH and ionic strength responsiveness. For the rest, we assume no significant variations comparing to pH 7 sample, as they were prepared in the same way.

### Irradiation set up

For CD experiments and HPLC of Fig. 2.6, two LED light sources were used, a Thorlabs M365LP1-C5 was used as UV source at 365 nm (irradiation steps of 1s, 100% at 1000 mA of the LED intensity), and a Thorlabs M455L3-C5 was used as blue source at 455 nm (irradiation steps of 10 s, 100% at 1000 mA of the LED intensity). Irradiation occurred on the bench top at rt, with approximately 15 cm distance between the sample and the LED.

### Discussion aggregation

No conclusive evidence of aggregations after UV irradiation were obtained. The CD signal from BTA is very noisy due to the presence of DMSO, however, it looks like this signal does not disappear upon irradiation. Also, a low CD signal coming from *Z*-azobenzene appears in the spectrum, however its behaviour has been mostly unpredictable. TEM images have not revealed any structure after irradiation and other studies with SLS did not show any evidence of aggregates. We hypothesise some small aggregates could be forming, maybe related with the intermediate species *EEZ*, *EZZ*.

## Temperature responsiveness

### Sample preparation

The monomer was dissolved at 2.5 mM DMSO. Then, a 25 μM solution in water was prepared, and the following conditions were applied:

- Temperature experiments with TEM:
- 20 °C: equilibrate at rt for 48 h. (no previous thermal cycle was applied)
- 75 °C: 75 °C for 1 h and perform negative staining.
- Back to 20 °C: 70 °C for 1 h and equilibrate at rt for 48h.

- Temperature experiments with SLS:
- Equilibrate at rt for 24 h after thermal cycle. + heat to 40 °C for 1h.
    - Measure before and after the irradiation with UV

- Equilibrate at rt for 24 h after thermal cycle. Perform a thermal cycle at 60 °C/h and heat to 50 °C for 1h.
    - Measure every 10 min, for 60 min.

- Temperature experiment with HPLC:
- 20 °C: equilibrate at rt for 48 h. (no previous thermal cycle was applied).
- 70 °C: 70 °C for 1 h.

## pH and ionic strength responsiveness

### Sample preparation

C0 dissolved in DMSO at 2.5 mM was diluted in MilliQ brought to the target pH by addition of NaOH or HCl and target salinity by addition of NaCl, reaching a final concentration of 25 μM and 1vol% DMSO. Samples were then heated to 70 °C for 1 h and subsequently equilibrated for 48 hrs at rt. The pH values reported in the manuscript were measured after the spectroscopic measurements.

## 2.5 References


1. Albertazzi, L.; Martinez-Veracoechea, F. J.; Leenders, C. M. A.; Voets, I. K.; Frenkel, D.; Meijer, E. W. Spatiotemporal Control and Superselectivity in Supramolecular Polymers Using Multivalency. Proc. Natl. Acad. Sci. U. S. A. 2013, 110 [30], 12203–12208.
2. Matson, J. B.; Stupp, S. I. Drug Release from Hydrazone-Containing Peptide Amphiphiles. Chem. Commun. 2011, 47 [28], 7962–7964.
3. Bakker, M. H.; Lee, C. C.; Meijer, E. W.; Dankers, P. Y. W.; Albertazzi, L. Multicomponent Supramolecular Polymers as a Modular Platform for Intracellular Delivery. ACS Nano 2016, 10 [2], 1845–1852.
4. Su, H.; Zhang, W.; Wang, H.; Wang, F.; Cui, H. Paclitaxel-Promoted Supramolecular Polymerization of Peptide Conjugates. J. Am. Chem. Soc. 2019, 141, [30], 11997-12004.
5. Su, H.; Wang, F.; Wang, Y.; Cheetham, A. G.; Cui, H. Macrocyclization of a Class of Camptothecin Analogues into Tubular Supramolecular Polymers. J. Am. Chem. Soc. 2019, 141, [43], 17107-17111.
6. Besenius, P.; Heynens, J.L.; Straathof, R.; Niuwenhuizen, M.M.; Bomans, P.; Terreno, E.; Aime, S.; Strijkers, G.; Nicolay, K.; Meijer, E.W. Paramagnetic self-assembled nanoparticles as supramolecular MRI contrast agents. Contrast Media Mol. Imaging. 2012, 7 [3], 356–361.
7. Orbach, R.; Adler-Abramovich, L.; Zigerson, S.; Mironi-Harpaz, I.; Seliktar, D.; Gazit, E. Self-Assembled Fmoc-Peptides as a Platform for the Formation of Nanostructures and Hydrogels. Biomacromolecules 2009, 10 [9], 2646–2651.
8. Mata, A.; Geng, Y.; Henrikson, K. J.; Aparicio, C.; Stock, S. R.; Stacher, R. L.; Stupp, S. I.; Bone regeneration mediated by biomimetic mineralization of a nanofiber matrix. Biomaterials. 2010, 31, [23], 6004–6012.

9. Choe, S.; Bond, C. W.; Harrington, D. A.; Stupp, S. I.; McVary, K. T.; Podlasek, C. A. Peptide Amphiphile Nanofiber Hydrogel Delivery of Sonic Hedgehog Protein to the Cavernous Nerve to Promote Regeneration and Prevent Erectile Dysfunction. Nanomedicine Nanotech-nol. Biol. Med. 2017, 13 [1], 95–101.
10. Saunders, L.; Ma, P. X. Self-Healing Supramolecular Hydrogels for Tissue Engineering Applications. Macromol. Biosci. 2019, 19, 1800313.
11. Blum, A. P.; Kammeyer, J. K.; Rush, A. M.; Callmann, C. E.; Hahn, M. E.; Gianneschi, N. C. Stimuli-Responsive Nanomaterials for Biomedical Applications. J. Am. Chem. Soc. 2015, 137 [6], 2140–2154.
12. Frisch, H.; Unsleber, J. P.; Lüdeker, D.; Peterlechner, M.; Brunklaus, G.; Waller, M.; Besenius, P.; "pH-Switchable Ampholytic Supramolecular Copolymers," Angew. Chem. Int. Ed. 2013, 52 [38], 10097–10101.
13. Gröger, G.; Meyer-Zaika, W.; Böttcher, C.; Gröhn, F.; Ruthard, C.; Schmuck, C. Switchable Supramolecular Polymers from the Self-Assembly of a Small Monomer with Two Orthogonal Binding Interactions. J. Am. Chem. Soc. 2011, 133 [23], 8961–8971.
14. Moyer, T. J.; Finbloom, J. A.; Chen, F.; Toft, D. J.; Cryns, V. L.; Stupp, S. I. pH and Amphiphilic Structure Direct Supramolecular Behavior in Biofunctional Assemblies. J. Am. Chem. Soc. 2014, 136 [42], 14746–14752.
15. Ahlers, P.; Frisch, H.; Holm, R.; Spitzer, D.; Barz, M.; Besenius, P. Tuning the pH-Switch of Supramolecular Polymer Carriers for siRNA to Physiologically Relevant pH. Macromol. Biosci. 2017, 17 [10], 1700111.
16. Adhikari, B.; Yamada, Y.; Yamauchi, M.; Wakita, K.; Lin, X.; Aratsu, K.; Ohba, T.; Karatsu, T.; Hollamby, M. J.; Shimizu, N.; Takagi, H.; Haruki, R.; Adachi, S.; Yagai, S. Light-induced unfolding and refolding of supramolecular polymer nanofibers. Nat. Commun. 2017, 8, 15254.
17. Yagai, S.; Yamauchi, M.; Kobayashi, A.; Karatsu, T.; Kitamura, A.; Ohba, T.; Kikkawa, Y. Control over Hierarchy Levels in the Self-Assembly of Stackable Nanotoroids. J. Am. Chem. Soc. 2012, 134,44, 18205–18208.
18. Prabhu, D. D.; Aratsu, K.; Kitamoto, Y.; Ouchi, H.; Ohba, T.; Hol-lamby, M. J.; Shimizu, N.; Takagi, H.; Haruki, R.; Adachi, S.; Yagai, S. Self-folding of supramolecular polymers into bioinspired topology. Sci. Adv. 2018, 4, [9], 8466.
19. Huang, Z.; Lee, E.; Kim, H.-J.; Lee, M. Aqueous Nanofibers with Switchable Chirality Formed of Self-Assembled Dumbbell-Shaped Rod Amphiphiles. Chem. Commun. 2009, 44, 6819–6821.
20. Feijter, I.; Besenius, P.; Albertazzi, L.; Meijer, E. W.; Palmans, A. R. A.; and Voets, I. K. Mechanistic control over morphology: self-assembly of a discotic amphiphile in water. Soft Matter. 2013, 9 [42], 10025–10030.
21. Alemán García, M. Á.; Magdalena Estirado, E.; Milroy, L.-G.; Brunsveld, L. Dual-Input Regulation and Positional Control in Hybrid Oligonucleotide/Discotic Supramolecular Wires. Angew. Chem. Int. Ed. 2018, 57 [18], 4976–4980.
22. Kumar, M.; Brocorens, P.; Tonnelé, C.; Beljonne, D.; Surin, M.; George, S. J. A Dynamic Supramolecular Polymer with Stimuli-Responsive Handedness for in Situ Probing of Enzymatic ATP Hydrolysis. Nat. Commun. 2014, 5, 5793.

23. Mishra, A.; Korlepara, D. B.; Balasubramanian S. and S. J. George. Bioinspired, ATP-driven co-operative supramolecular polymerization and its pathway dependence. Chem. Commun. 2020,56, 1505-1508.
24. Albertazzi, L.; Veeken, N. van der; Baker, M. B.; Palmans, A. R. A.; Meijer, E. W. Supramolecular Copolymers with Stimuli-Responsive Sequence Control. Chem. Commun. 2015, 51 [90], 16166–16168.
25. Molla, M. R.; Prasad, P.; Thayumanavan, S. Protein-Induced Supramolecular Disassembly of Amphiphilic Polypeptide Nanoassemblies. J. Am. Chem. Soc. 2015, 137 [23], 7286–7289.
26. Dun, S.; Ottmann, C.; Milroy, L. and Brunsveld, L. Supramolecular Chemistry Targeting Proteins. J Am Chem Soc. 2017 Oct 11; 139(40): 13960–13968.
27. Guo, J.; Zhuang, J.; Wang, F.; Raghupathi, K. R.; Thayumanavan, S. Protein AND Enzyme Gated Supramolecular Disassembly. J. Am. Chem. Soc. 2014, 136 [6], 2220–2223.
28. Erbas-Cakmak, S.; Kolemen, S.; Sedgwick, A. C.; Gunnlaugsson, T.; James, T. D.; Yoon J. and Akkaya, E. U. Molecular logic gates: the past, present and future. Chem. Soc. Rev. 2018, 47, 2228.
29. Gao, J.; Wu, P.; Fernandez, A.; Zhuang J. and S. Thayumanavan. Cellular AND Gates: Synergistic Recognition to Boost Selective Up-take of Polymeric Nanoassemblies. Angew. Chem. Int. Ed. 2020, 59, 1 – 6.
30. Spitzer, D.; Rodrigues, L. L.; Straßburger, D.; Mezger, M.; Besenius, P. Tuneable Transient Thermogels Mediated by a pH- and Redox-Regulated Supramolecular Polymerization. Angew. Chem. Int. Ed. 2017, 56 (48), 15461–15465.
31. Goskulwad, S.; La, D. D.; Kobaisi, M. A.; Bhosale, S. V.; Bansal, V.; Vinu, A.; Ariga, K.; Bhosale, S. V. Dynamic multistimuli-responsive reversible chiral transformation in supramolecular helices. Sci. Rep. 2018, 8, 1, 1–11.
32. Liu, X.; Hu, D.; Jiang, Z.; Zhuang, J.; Xu, Y.; Guo, X.; Thayumanavan, S. Multi-Stimuli-Responsive Amphiphilic Assemblies through Simple Post-polymerization Modifications. Macromolecules. 2016, 49 [17], 6186–6192.
33. Chen, J.; Zhang, S.; Sun, F.; Li , N.; Cui, K.; He, J.; Niu, D.; Li, Y. Multi-stimuli responsive supramolecular polymers and their electrospun nanofibers. Polym. Chem. 2016, 7 [17], 2947–2954.
34. Cantekin, S.; Nakano, Y.; Everts, J. C.; Schoot, P. van der; Meijer, E. W.; Palmans, A. R. A. A Stereoselectively Deuterated Supramolecular Motif to Probe the Role of Solvent during Self-Assembly Processes. Chem. Commun. 2012, 48 [32], 3803–3805.
35. Pianowski, Z. L. Recent Implementations of Molecular Photoswitches into Smart Materials and Biological Systems. Chem. – Eur. J. 2019, 25 [20], 5128–5144.
36. Szymański, W.; Beierle, J. M.; Kistemaker, H. A. V.; Velema, W. A.; Feringa, B. L. Reversible Photocontrol of Biological Systems by the Incorporation of Molecular Photoswitches. Chem. Rev. 2013, 113 [8], 6114–6178.
37. Ishikawa, M.; Ohzono, T.; Yamaguchi, T.; Norikane, Y. Photo-Enhanced Aqueous Solubilization of an Azo-Compound. Sci. Rep. 2017, 7 [1], 1–6.
38. Vancoillie, G.; Frank, D.; Hoogenboom, R. Thermoresponsive Poly(oligo Ethylene Glycol Acrylates). Prog. Polym. Sci. 2014, 39 [6], 1074–1095.
39. Lüsse, S.; Arnold, K. The Interaction of Poly(ethylene Glycol) with Water Studied by 1H and 2H NMR Relaxation Time Measurements. Macromolecules. 1996, 29 [12], 4251–4257.

40. Chandler, D. Interfaces and the Driving Force of Hydrophobic Assembly. Nature. 2005, 437 [7059], 640–647.
41. Smith, G. D.; Bedrov, D. Roles of Enthalpy, Entropy, and Hydrogen Bonding in the Lower Critical Solution Temperature Behaviour of Poly(ethylene oxide)/Water Solutions. J. Phys. Chem. B. 2003, 107 [14], 3095–3097.
42. Besenius, P.; Goedegebure, Y.; Driesse, M.; Koay, M.; Bomans, P.; Palmans, A. R. A.; Dankers, P. Y. W.; Meijer, E. W. Peptide functionalised discotic amphiphiles and their self-assembly into supramolecular nanofibres. Soft Matter. 2011, 7 [18], 7980–7983.
43. Volgraf, M.; Gorostiza, P.; Szobota, S.; Helix, M. R.; Isacoff, E. Y. and D. Trauner. Reversibly Caged Glutamate: A Photochromic Agonist of Ionotropic Glutamate Receptors. J. Am. Chem. Soc. 2007, 129, 260-261.
44. Riefolo, F.; Matera, C.; Garrido-Charles, A.; Gomila, A. M. J.; Sortino, R.; Agnetta, L.; Claro, E.; Masgrau, R.; Holzgrabe, U.; Batlle, M.; Decker, M.; Guasch E. and Gorostiza, P. Optical Control of Cardiac Function with a Photoswitchable Muscarinic Agonist. J. Am. Chem. Soc. 2019, 141, 7628−7636.
45. Bandara, H. M. D.; Burdette, S. C. Photoisomerization in Different Classes of Azobenzene. Chem. Soc. Rev. 2012, 41 [5], 1809–1825.
46. Titov, E.; Granucci, G.; Götze, J. P.; Persico, M.; Saalfrank, P. Dynamics of Azobenzene Dimer Photoisomerization: Electronic and Steric Effects. J. Phys. Chem. Lett. 2016, 7 [18], 3591–3596.
47. Cocchi, C.; Draxl, C. Understanding the Effects of Packing and Chemical Terminations on the Optical Excitations of Azobenzene-Functionalized Self-Assembled Monolayers. J. Phys. Condens. Matter. 2017, 29 [39], 394005.
48. Galanti, A.; Diez-Cabanes, V.; Santoro, J.; Valašek, M.; Minoia, ˇA.; Mayor, M.; Cornil, J.; Samorì, P. Electronic Decoupling in C3-Symmetrical Light-Responsive Tris(Azobenzene) Scaffolds: Self-Assembly and Multiphotochromism. J. Am. Chem. Soc. 2018, 140 [47], 16062–16070.
49. Tong, X.; Wang, G.; Soldera, A.; Zhao, Y. How Can Azobenzene Block Copolymer Vesicles Be Dissociated and Reformed by Light? J. Phys. Chem. B 2005, 109 [43], 20281–20287.
50. Liu, M.; Zhang, L.; Wang, T. Supramolecular Chirality in Self-Assembled Systems. Chem. Rev. 2015, 115 [15], 7304–7397.
51. Casellas, N. M.; Pujals, S.; Bochicchio, D.; Pavan, G. M.; Torres, T.; Albertazzi, L.; García-Iglesias, M. From isodesmic to highly cooperative: reverting the supramolecular polymerization mechanism in water by fine monomer design. Chem. Commun. 2018, 54 [33], 4112–4115.
52. Hamley, I. W.; Cheng, G.; Castelletto, V. A. Thermoresponsive Hydrogel Based on Telechelic PEG End-Capped with Hydrophobic Dipeptides. Macromol. Biosci. 2011, 11 [8], 1068–1078.
53. Fuller, J. M.; Raghupathi, K. R.; Ramireddy, R. R.; Subrahmanyam, A. V.; Yesilyurt, V.; Thayumanavan, S. Temperature-Sensitive Transitions below LCST in Amphiphilic Dendritic Assemblies: Host–Guest Implications. J. Am. Chem. Soc. 2013, 135 [24], 8947–8954.
54. Engel, S.; Spitzer, D.; Rodrigues, L. L.; Fritz, E.; Straßburger, D.; Schönhoff, M.; Ravoo, B. J.; Besenius, P. Kinetic control in the temperature-dependent sequential growth of surface-confined supramolecular copolymers. Faraday Discuss. 2017, 204 [0], 53–67.

55. Frisch, H.; Fritz, E.; Stricker, F.; Schmüser, L.; Spitzer, D.; Weidner, T.; Ravoo, B. J.; Besenius, P. Kinetically Controlled Sequential Growth of Surface-Grafted Chiral Supramolecular Copolymers. Angew. Chem. Int. Ed. 2016, 55 [25], 7242–7246.
56. Besenius, P.; Portale, G.; Bomans, P.; Janssen, H. M.; Palmans, A. R. A.; Meijer, E. W. Controlling the Growth and Shape of Chiral Supramolecular Polymers in Water. Proc. Natl. Acad. Sci. 2010, 107 [42], 17888–17893.
57. Calculator Plugins were used for pKa and microspecies calculation, MarvinSketch 16.9.26, 2016, ChemAxon (http://www.chemaxon.com).
58. M. Bose, D. Groff, J. Xie, E. Brustad, and P. G. Schultz. The Incorporation of a Photoisomerizable Amino Acid into Proteins in E. coli, J. Am. Chem. Soc. 2006, 128 (2), 388-389.
59. W. Li, I. Park, S.-K. Kang, and M. Lee,. Smart hydrogels from laterally-grafted peptide assembly, Chem. Commun., 2012, 48 (70), 8796-8798.
60. Podewin, T.; Rampp, M. S.; Turkanovic, I.; Karaghiosoff, K. L.; Zinth, W. and Hoffmann-Röder A. Photocontrolled chignolin-derived β-hairpin peptidomimetics. Chem. Commun. 2015, 51 [19], 4001–4004.

# Chapter 3 | Supramolecular robustness and stability in the biological media

## 3.1 Introduction

In **chapter 2** the adaptive nature of supramolecular materials was exploited to create a new supramolecular system, responsive to multiple cues *in vitro*. Other authors have contributed enormously to this field even in complex scenarios.[1] Stupp and co-workers remarkably designed a fibrous supramolecular network based on peptide amphiphiles, able to reversibly switch between distinct hierarchical architectures.[2] Meijer and co-workers showed spatio-temporal control on supramolecular polymers using ssDNA to cluster reversibly specific monomers.[3] The groups of Gianneschi, Amir and Thayumanavan independently reported interesting stimuli responsive micelles, using light, pH or biomolecules to modulate their response.[4–7] Recently, Choi et al. have shown polymeric micelles responsive to light and enzymes, obtaining a dual control over the assemblies.[8] Besenius lab showed supramolecular polymers responsive to pH and reactive oxygen species, used together with temperature to control the hydrogelation and properties of the material.[9]

However, and despite these remarkable advances, there are still many challenges to tackle before the final application. One of these challenges revolves around the supramolecular integrity in complex environments, where multiple biomolecular interactions can impact the assembled structure.

In the nanomedicine world, in which the temperature window is very narrow, the supramolecular destabilization usually comes from the decrease of the free monomer availability (sequestering, dilution, degradation). This effect is alleviated when using supramolecular bulk materials (e.g. hydrogels), given the huge concentration of monomer, the limited diffusion within and the low surface/volume ratio.[10] However, other applications specifically require the use of discrete structures.

Targeted drug delivery aims to use discrete nanostructures to carry drugs through the bloodstream and deliver them selectively at the destination. This means facing a massive dilution along with a variety of serum proteins and the potential side-interactions.[11] These circumstances contribute to the decrease of the monomer availability, promoting the carrier disruption before reaching the target. Supramolecular drug delivery systems require at the same time a high robustness to resist the journey and the ability to respond to stimuli to deliver the drug.

Even though it is a crucial issue, this destabilization is not very well understood. A thorough understanding about this phenomenon could lead to improved supramolecules for drug delivery. Few pioneering examples can be found in literature. Together with the group of Roey Amir, our group thoroughly studied the integrity of enzyme responsive micelles when facing a biological environment or even biological barriers. [12,13] These works show how the presence of proteins impact differently depending on the stability-responsiveness balance. Furthermore, it was proven that extravasation and even the internalization by cells is affected by the supramolecular stability.

Interestingly, a recent article of Pavan, Palmans and Meijer demonstrated the interaction of specific benzene-1,3,5-tricarboxamide (BTA) fibres and monomers with serum proteins.[14] These results suggest that BTA stacked systems could be destabilized when used as biomaterials. There is a need for rationalizing the factors influencing supramolecular stability in a complex media. This could allow to improve the designs and push forward the field.

It is known that the intrinsic supramolecular stability is related to the CAC values, the lower CAC the higher the intrinsic stability. However, it is difficult to relate CAC values with stabilities or to correlate these values with stabilities in the biological environment. For this reason, and as the stability and responsiveness are inversely related, we believe a more complete view must evaluate the responsive abilities. The stability-responsiveness trade-off defines better the intrinsic robustness of the system.

In **Chapter 2**, the first supramolecular polymer based on BTA-azobenzene is studied in terms of self-assembly and responsiveness. However, little information could be extracted regarding the robustness of the material and its stability in the biological environment. For this reason, in this chapter we have expanded the family of the BTA-Azobenzenes with monomers exhibiting different hydrophobic/hydrophilic ratios and we have interrogated their stability/photo-responsive abilities.

Studying the stability-responsiveness trade-off unveiled two well separated regimes in vitro, one with low stability and high responsivity, and a second of high stability and low responsivity. Relating these regimes with the behaviour upon a hypothetical intravenous injection is of great significance. Förster resonance energy transfer emerged as a powerful quantitative tool to monitor the assembly state of the supramolecular polymers in a complex environment. Remarkably, response to dilution matches perfectly with the two stability/responsiveness regimes; the high stability/low responsiveness being translated into high resistance to dilution. However, when proteins were present, the difference between the two regimes blurred, implying that supramolecular stability in the biological environment goes beyond a high stability/responsiveness balance. These results give insights on the key parameters to be optimized to achieve complete supramolecular stability upon intravenous injection.

## 3.2 Results

### 3.2.1 Molecular design and synthesis:

In Chapter 2, C0 was synthesised and studied, yielding a highly responsive polymer to multiple stimuli in water.[15] In this chapter, and starting from C0, we have designed two new monomers in search of a change in stability/responsiveness, trying to maintain as many common features as possible. To do so, we extended the hydrophobic core with a 4-aminobutanoic acid or an 8-aminooctanoic acid (creating respectively C4 and C8 monomers, Fig. 3.1 a). This approach allowed us to apply the same synthetic route used for C0, consisting of growing the bearing wedges first by solid phase synthesis, and coupling them to the core in solution. (see methods section).

Altogether, the three molecules should allow to determine the relationship between stability and responsiveness in aqueous stacked systems and relate it with their performance in the biological environment. This is possible because the different hydrophobic/hydrophilic balances lead to changes in the supramolecular stability. At the same time, it affects equally the responsive capabilities, given the trade-off relation between supramolecular stability and responsiveness, in which increasing one decreases the other. How this defined trade-off for each molecule affects the stability in a biological environment is of high value. The newly designed monomers allow to keep the key common features required for this study: ability to self-assemble, responsiveness to light, and the same surface identity.

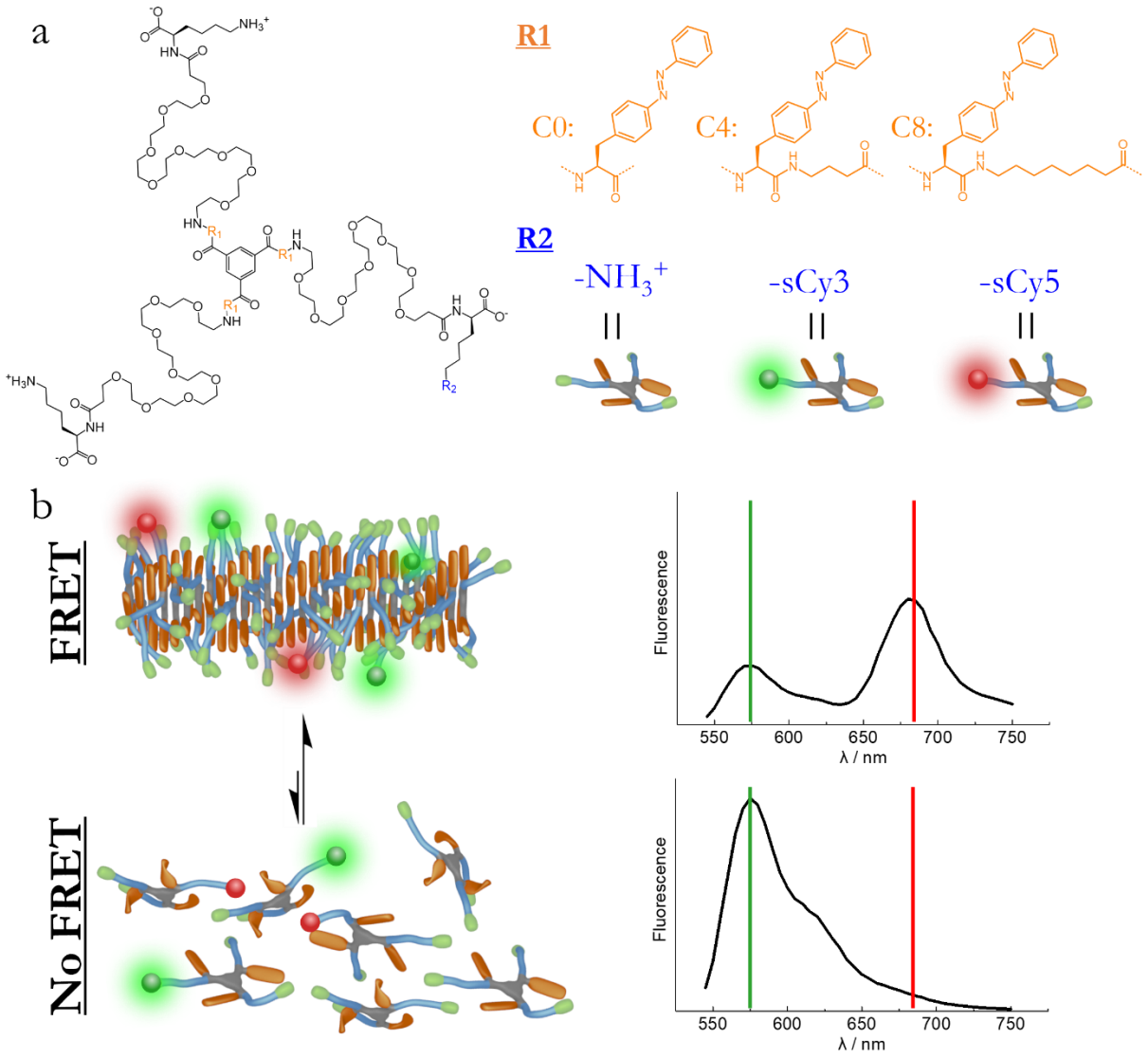


Figure 3.1 Molecular structure of C0, C4 and C8 monomers (a). Cartoon representing the FRET monitoring of self-assembly (b). Green and red lines were added to illustrate the peaks used to monitor the assembly %. An increase in green signal and decrease in red signal is translated into fibre disassembly and FRET loss.

To monitor the self-assembly, each molecule was also post-functionalized at the R2 position with a single sulfo-Cyanine3 (sCy3) or sulfo-Cyanine5 (sCy5), a well-studied FRET pair of dyes.[16–18] This FRET pair operates in the range of 550-750 nm, well separated from the azobenzene

absorption window (250-500 nm) to avoid any kind of crosstalk. Pristine monomers can be mixed with sCy3 and sCy5 labelled monomers in DMSO, achieving a well-mixed monomerically dissolved solution. Next, we inject the solution in Phosphate Buffer Saline (PBS) at 25 μM in order to trigger the self-assembly into fibres. The amount of labelled monomers, when needed, were kept at 10 mol% for an optimal FRET signal. In figure 3.1 b, we can observe schematically how we can use FRET to assess stability. Only assembled monomers produce a powerful FRET signal, while upon disassembly monomers are physically separated and FRET is lost. This allows monitoring the self-assembly process.[3,19]

### 4.2.2 Self-assembly characterization

First, the self-assembly of the samples at 25 μM was studied using TEM, CD and FRET (Fig. 3.2).

TEM showed fibrillar aggregates for the three monomers. Interestingly, C0 and C4 present a similar morphology, apparently single fibres of ~6.5 nm in width but different lengths, ~300 nm and few μm, respectively (Fig. 3.2 a). Instead, monomer C8 seems to self-assemble more into tight bundles of ~300 nm in length and ~8.3 nm in width. Increasing hydrophobicity of C0 to C4 increased the length of the fibres. However, increasing the hydrophobicity from C4 to C8 resulted in shorter fibres and apparent changes in thickness/bundling.

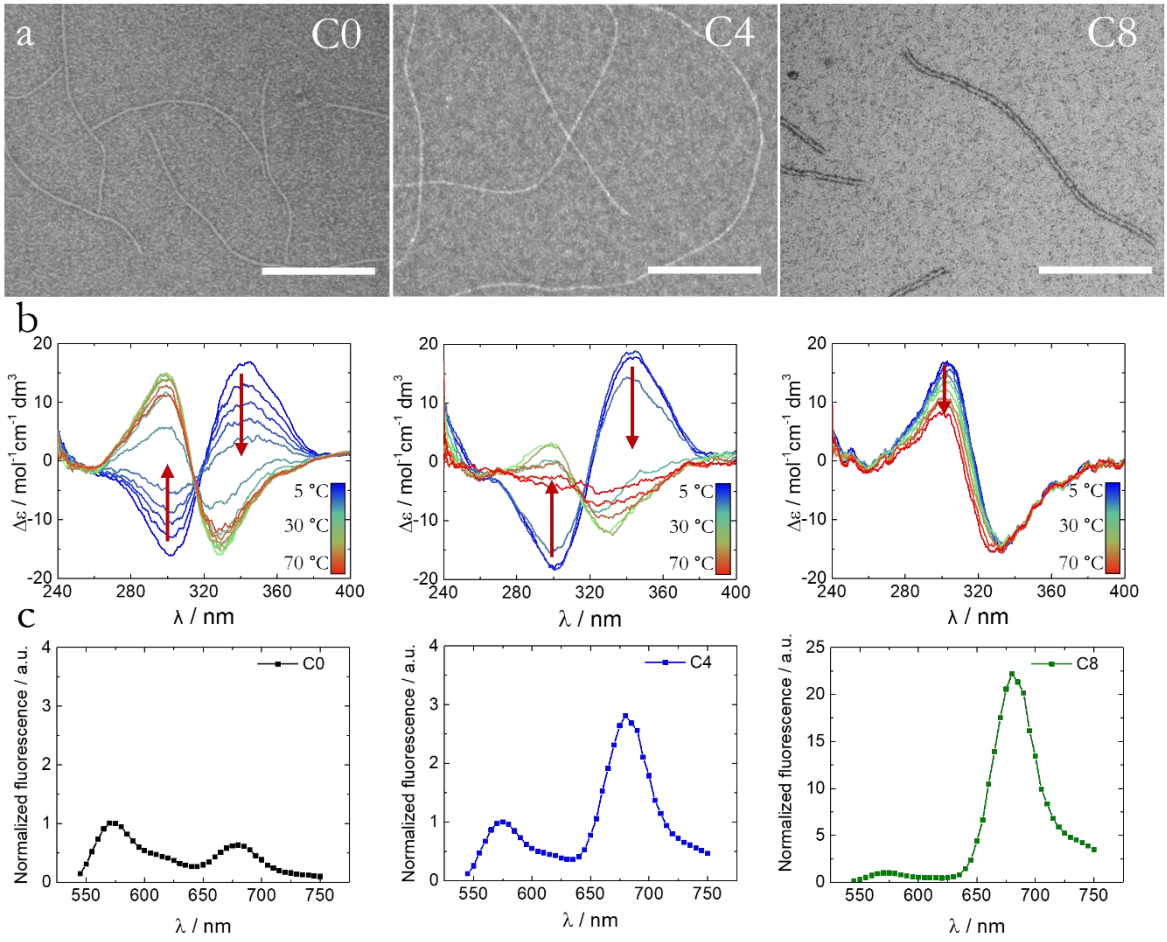


Figure 3.2 (a) TEM images of C0, C4 and C8 (from left to right). Scale bar: 200nm. (b) CD spectra vs T of C0, C4 and C8 (from left to right), at 25 μM. (c) FRET spectra of C0, C4 and C8 (from left to right), at 25 μM, 10 % labelling and 37 °C. (Line was added to guide the eye).

4A temperature ramped CD, measured on the inner azobenzene range, provides interesting insights into the fibre stacking and its temperature dependency (Fig. 3.2 b). C0 and C4 share the same temperature response, a positive Cotton effect can be observed at low temperatures that inverts reversibly to a negative Cotton effect at high temperatures. This behaviour was previously associated to an azobenzene stacking rearrangement and an increased stability state. It is originated from the loss of solvation water of the OEG at high temperatures, increasing hydrophobicity and reducing steric hindrance.[20,21] On the other hand, C8 shows a permanent negative Cotton effect at all temperatures, suggesting a different azobenzene arrangement and a superior stability. C8 only shows a CD signal decrease, probably deriving from partial depolymerization at higher temperatures. C0 and C4 start showing a decrease in CD intensity above 50 °C, however none of them disassemble completely.

FRET experiments, performed at 37 °C, also shows differences between the molecules under the same conditions (Fig. 3.2 c). C0 shows the lower FRET signal (~0.5 a.u.), C4 a moderate signal (~2.5 a.u.), and C8 a surprisingly high signal (~23 a.u.). This trend matches the hydrophobic-hydrophilic balance trend of the molecules, and it is explained by a combination of two parameters: the distance and the number of the FRET pair of dyes. Higher hydrophobic-hydrophilic balances translate into lower critical aggregation concentration. As C0 has lower hydrophobic forces, the free monomer concentration is higher, meaning that less labelled monomer is assembled and hence, less FRET is obtained. However, C8 signal seems extraordinarily high to be generated only by this effect. Probably, the bundled nature of the fibres put dyes in clos-er proximity leading to the increased energy transfer, since it scales with $R^{-6}$.

Overall, the three monomers self-assemble into fibres. C0 and C4 fibres are morphologically similar and the azobenzene moieties reorganize at high temperatures. C8 fibres are thicker and are not responsive to temperature. Finally, C0, C4 and C8 exhibit FRET ratio with quantitative differences that match their respective degree of aggregation.

### 3.2.3 Light-responsiveness

For the sake of establishing the stability-responsiveness balance of our systems in vitro, the light-responsive abilities must be tested. It is of interest to understand if fibres of increasing hydrophobic blocks can be disassembled by the azobenzene photoisomerization. We studied the samples before and after UV irradiation by UV-Vis and CD spectroscopy, FRET and TEM.

The absorption spectra show that the azobenzene moieties in all three cases are initially in E configuration (330 nm peak), and then isomerize to Z configuration (450 nm peak) after irradiation with UV light (360 nm). It is interesting to mention that C8 presents few differences. The absorption band attributed to the E isomer (~330 nm) is blue shifted by ~5nm, the population of initial Z isomers is slightly lower, and the kinetics of photoisomerization is slower.

CD and FRET give insights about the self-assembly state of the monomers (Fig. 3.3). Before irradiation, each monomer shows its own characteristic CD signal. After irradiation, CD signal reaches noise levels for C0 and C4, suggesting depolymerisation of the supramolecular fibres. For C8, the signal is reduced but it is still present. FRET experiments match CD results and follow the

same trend: C0 and C4 signal decrease to minimum levels, while C8 decreases partially. This shows that FRET is an excellent technique to monitor self-assembly.

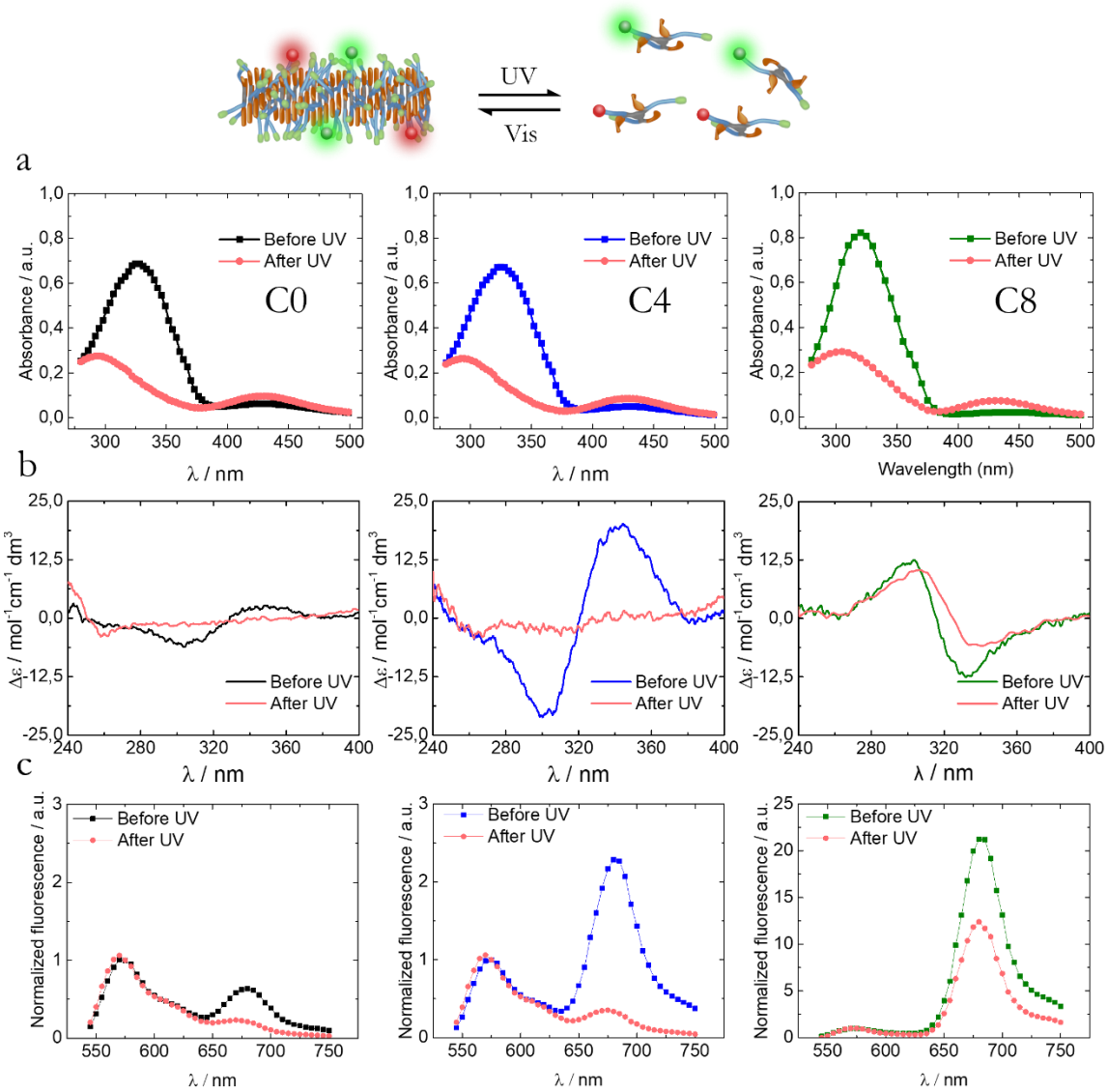


Figure 3.3 (a) E-Z photoisomerization at 25 μM in water. (b) CD spectra of samples before and after irradiation at 25 μM in water. C) FRET spectra before and after irradiation, matching the CD results. (C0, left column; C4, middle column; C8, right column.) (Line was added to guide the eye). Irradiation conditions: 365 nm, 1000 mA at 100% of the LED intensity, where irradiation time was modified in each case to reach plateau: UV-Vis/CD (cuvette): 8s for C0, 10s and C4 and 93s for C8. FRET (microplate): 30s for C0 and C4, 360s for C8.

These results have been further confirmed by TEM (Fig 3.4), where irradiated C0 (reported in chapter 2) and C4 did not show fibres, while irradiated C8 showed a shortening of the fibres, reaching lengths of ~35 nm. Interestingly, the fibres could assemble back after irradiation with blue light (455 nm), because azobenzenes isomerize back to the *E* state.

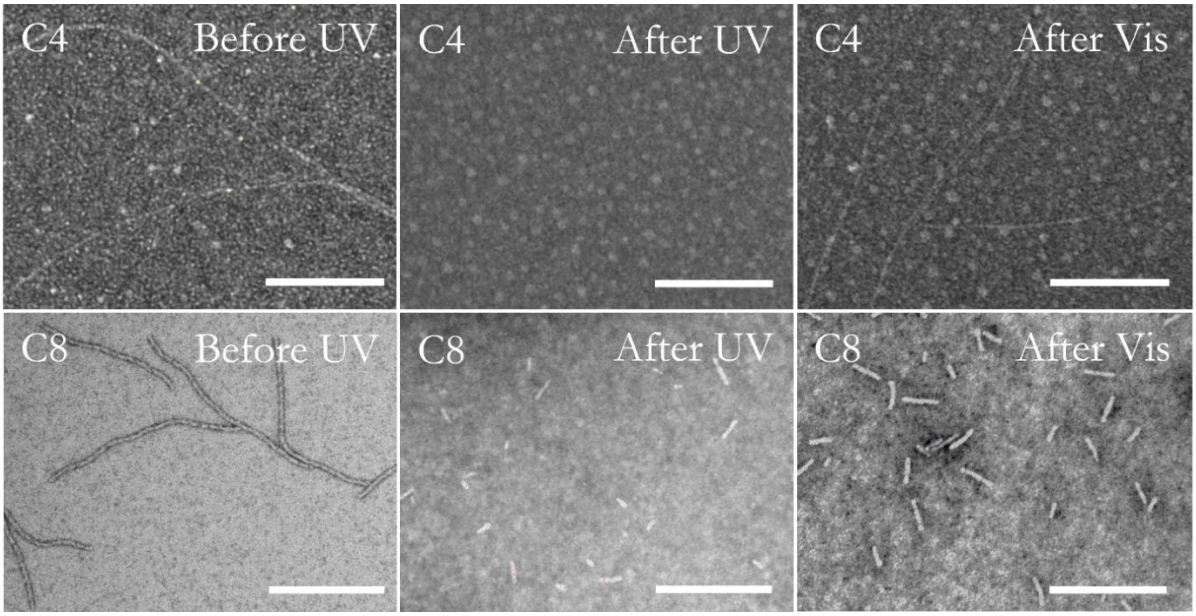


Figure 3.4 TEM images of C4 (above) and C8 (below) under different irradiations conditions. Scale bar: 200 nm.

Additionally, *E* to *Z* photoisomerization kinetics was compared in the assembled (water) and molecularly dissolved states (DMSO). Samples of each polymer were prepared in water and DMSO and irradiated with UV with consecutive irradiations of 5 s. The three monomers in DMSO displayed an identical and fast isomerization kinetics (~10 s) because they are monomerically dissolved. In water, C0 and C4 showed very similar results, indicating the assembly has a minimal impact in the photoisomerization. However, C8 clearly showed a decrease in the photoisomerization rate in water (+80 s). This can happen due to a stronger monomer binding, a higher steric hindrance in C8 fibres because of the different azobenzene packing or a combination of both.

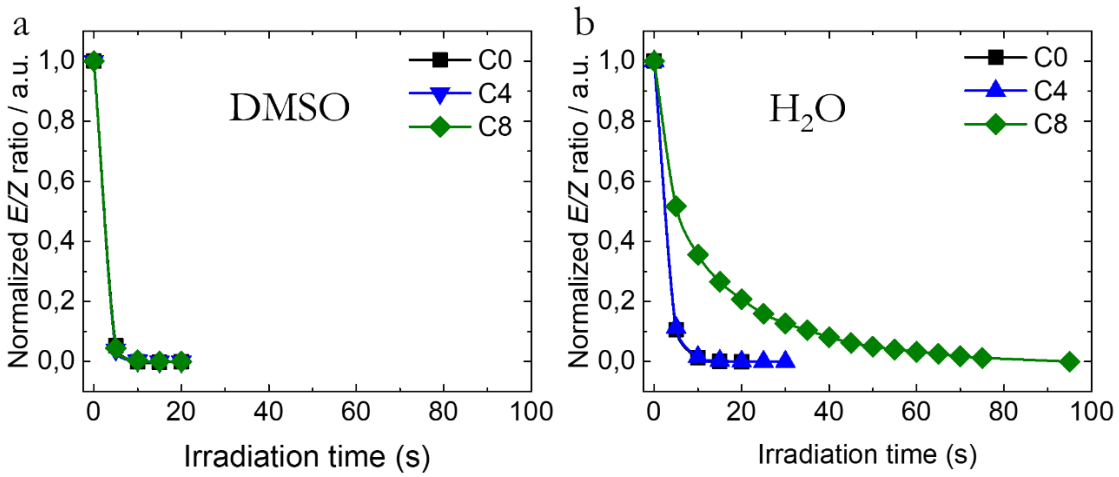


Figure 3.5 *E-Z* isomerization kinetics, comparison between DMSO (a) and $H_2O$ (b) for monomers at 25 μM. Notice that C0 and C4 curves are overlapped in both situations.

We can conclude that C0 and C4 are fully responsive to irradiation with UV light, disassembling completely, while C8 is partially responsive. C8 needed higher irradiation times to isomerize, and still short assemblies remain. The azobenzene isomerization represents a massive change for a

stacked system in terms of space, orientation and symmetry. For this reason, it is an adequate approach to trigger disassembly even in very hydrophobic systems that can show insensitivity to other external cues. Hence, it is a convenient strategy to define the stability/responsiveness trade-off of the system, before evaluating the robustness in the biological environment.

### 3.2.4 Supramolecular dynamics

The dynamics of supramolecular polymers can be assessed by the velocity of exchange between assembled and free monomers. Mixing fibres labelled with different fluorophores (out of equilibrium), and letting it equilibrate to homogeneously labelled fibres (equilibrium) give an idea of how fast assembled monomers exchange with the solvent, or if they exchange at all. Two solutions of fibres were prepared, the first containing only sCy3 labelled monomer and the second containing only sCy5 labelled monomer. After mixing the solutions together, FRET was monitored over time (Fig. 3.6).

Once again, for C0 and C4 the results are similar. FRET shows maximum values immediately after mixing. After that, they present a slight decrease with time, but it does not seem significant. On the other side, C8 presents an extremely slow increase. These results suggest that C8 is governed by kinetics, displaying a very slow monomer exchange (low $k_{off}$).[10,22] This indicates a sort of insensitivity to any change in the free monomer concentration, a key property to maintain monomers assembled in the biological environment, facing dilution and unspecific interactions with biomolecules.

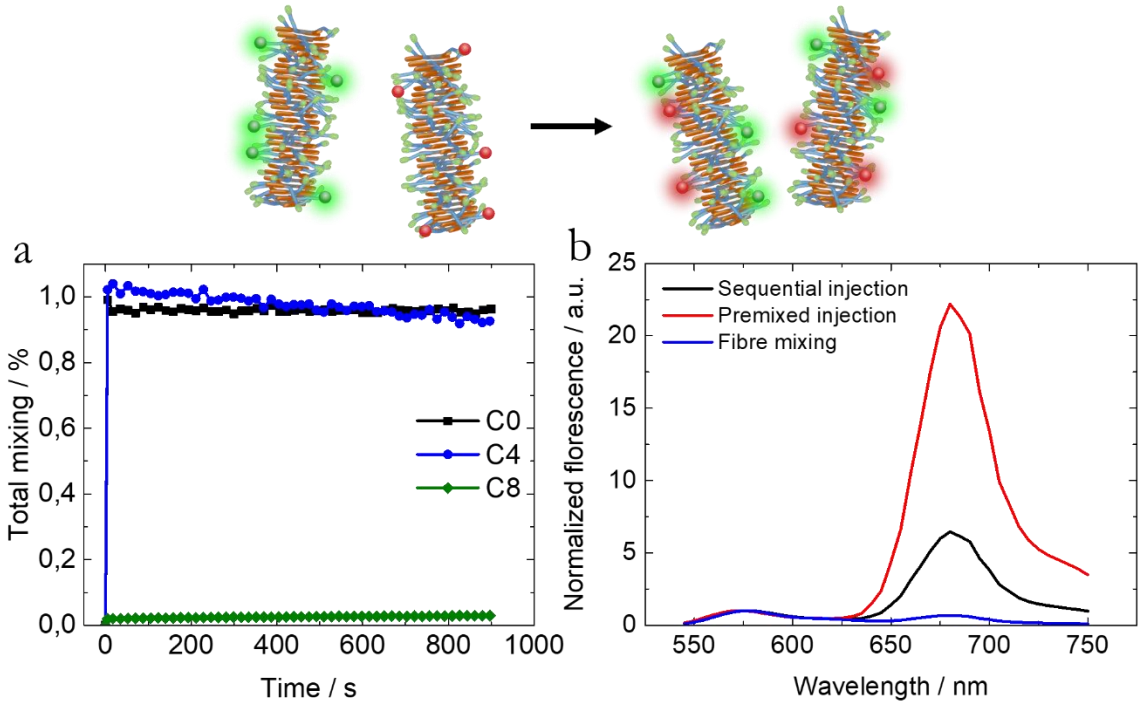


Figure 3.6 (a) Mixing of 25 μM 10% sCy3 labelled fibres with 25 μM 10% sCy5 fibres at and 37°C in water, monitored in time. Line was added to guide the eye. Total mixing was defined relatively to analogous FRET experiments, where the components were formulated together from the beginning and not mixed after formulation. (b) Comparison of FRET spectra of three different preparation methods for labelled fibres. In black, sequential addition of labelled monomers in PBS. In red, single injection in PBS of premixed

monomers in DMSO. In blue, mixture of sCy3 labelled fibre with sCy5 labelled fibre. All samples were prepared at a concentration of 25 μM and 10% of labelling.

Additionally, and as a consequence of its high hydrophobicity, C8 mixing is strongly affected by the sample preparation method. If instead of mixing the labelled monomers in DMSO, we inject them subsequently in water, one after the other, the resulting FRET is around half of the initial value. This is a sort of intermediate step between the well-mixed sample (premix in DMSO) and the phase-separated sample (separately preformed fibres). Probably, the first labelled monomer injected in water self-assembles fast, and by the time we inject the second one (seconds) This indicates the assembly in water is fast, corroborates the extremely low monomer exchange rates of C8, because once the labelled monomers are assembled, they do not disassemble and reassemble again on another fibre.

### 3.2.5 Behaviour in biological media

Supramolecular drug delivery carriers must resist harsh conditions upon intravenous injection.[23] 5000-fold dilutions are faced on top of potential side interactions with serum proteins in a large excess. Thus, understanding the self-assembly dependencies on dilution and protein concentration is of major importance.

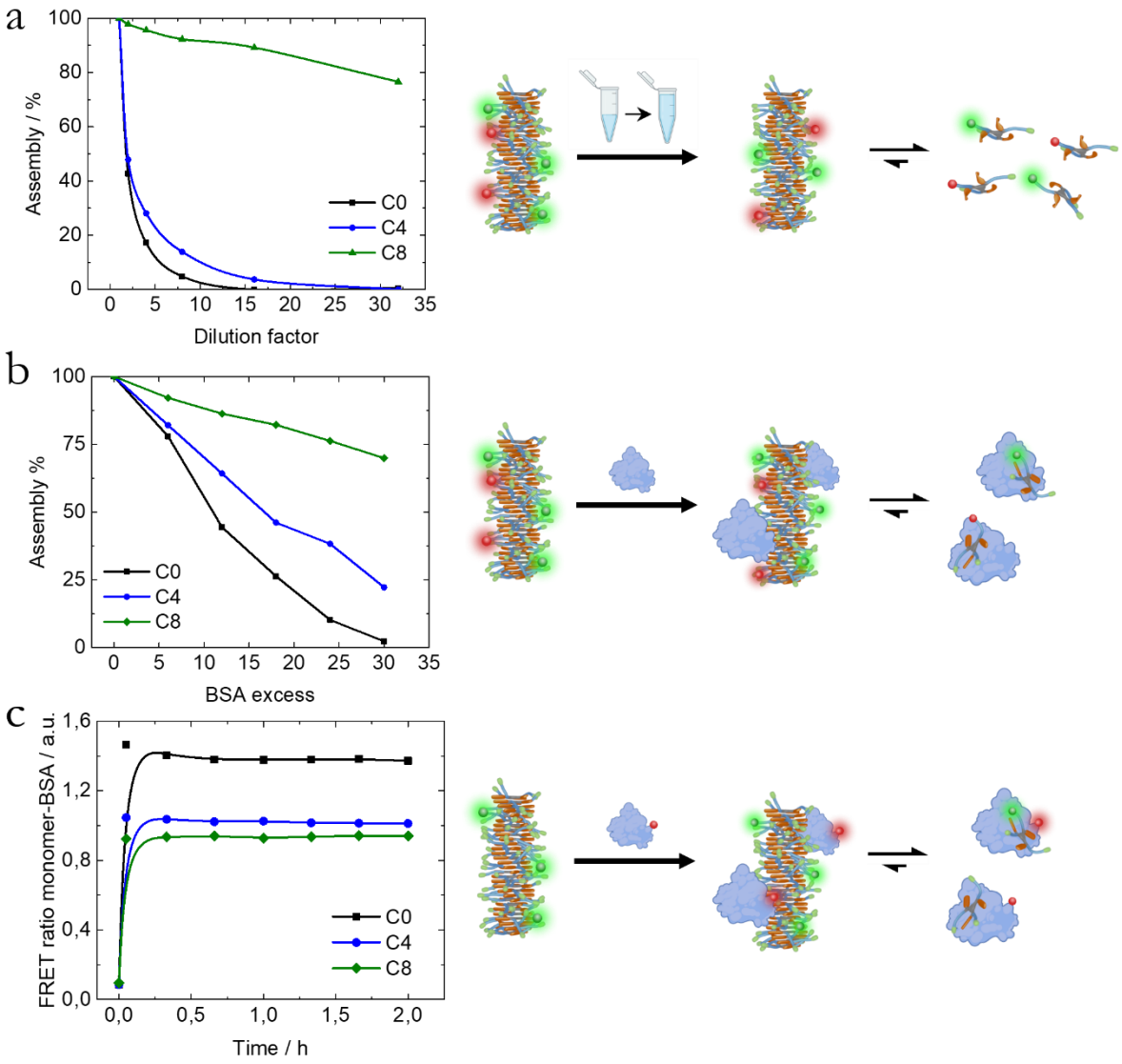


Figure 3.7 (a) Supramolecular stability along a ½ serial dilution experiment from 100 μM samples. (b) Supramolecular stability vs [BSA] of samples at 25 μM. (c) FRET ratio of the polymer-BSA interaction vs time, at a concentration of 25 μM, 10 mg/ml of BSA and 10% labelled. (Line was added to guide the eye).

Using FRET, we assessed the assembly degree of the systems and compared the behaviour of a 1/2 serial dilution in PBS and with an increasing concentration of Bovine Serum Albumin (BSA) assay. We aim to understand how these two factors promote disassembly of fibres of different stability.

Dilution experiments showed two different results, matching the stability/responsiveness balance (Fig. 3.7, a). On one side, C0 and C4 showed a dramatic decrease in the population of self-assembled structures upon dilution. On the other side, C8 showed a very mild decrease. The results show that C0 and C4 cannot remain assembled upon dilution, while C8 is mildly affected in this range. The limit of detection of the technique (concentration below 5 μM) impedes the analysis at higher dilutions. Interestingly, FRET decreased rapidly in time in all the cases, even for C8. This effect on C8 seems opposite to the dynamic's experiments in vitro (Fig. 3.6), in which we could see a very slow monomer exchange. As release of the monomer from the fibre does not seem a

likely explanation, other concentration dependent phenomenon like fibre bundling could be happening. Altogether, we observe two well-differentiated regimes, a low stability and high responsiveness, and a high stability and low responsiveness.

Then, polymers were incubated with an increasing concentration of BSA, mimicking a hypothetical intravenous injection. Results showed the same C0-C8 trend as before, however with important differences (Fig. 3.7 b). Here, the protein clearly destabilized all the monomers, being the C0 the most affected due to the low robustness and C8 being the less affected thanks to its outstanding robustness. This destabilization occurs via monomer sequestration by BSA.[12] We demonstrated it experimentally by labelling BSA with Cy5 dye and mixing it with supramolecular polymers loaded only with sCy3. FRET was obtained for the three molecules, proving the interaction (Fig. 3.7 c). This time, the FRET ratio is lower for C8 (less disassembly caused by BSA), and higher for the C0 (higher disassembly caused by BSA). In addition, we irradiated the samples with UV to disassemble the polymers and observe whether the BSA is interacting with monomers or fibres. In figure 3.8 we can observe a slight decrease in the signal of C0 and C4 after UV irradiation (fibre disassembly), and the recovery after Vis irradiation (fibre re-assembly). This result indicates the signal is primarily coming from BSA bound to monomers and little fibre-BSA interaction. Interestingly, C8 displays a similar behaviour, but increasing the signal after UV and decreasing after Vis. The exact mechanism causing this effect is very challenging to predict however we can hypothesise it is related to the reduced free monomer concentration.

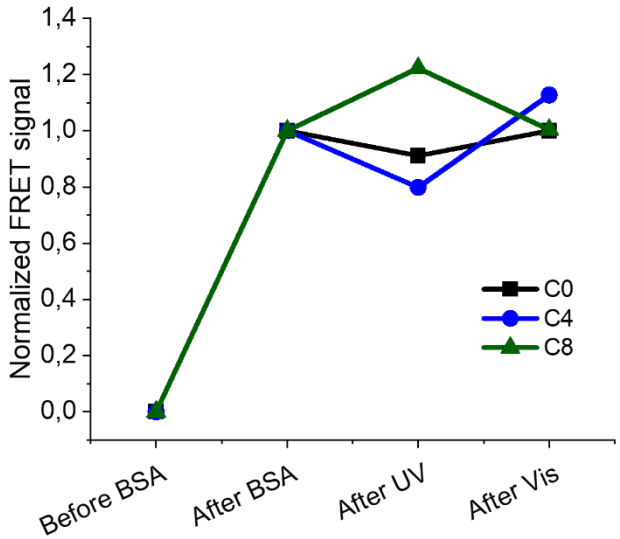


3.8 Normalized polymer-BSA FRET signal before and after UV, and after Vis irradiation.

Although demonstrating the scavenging effect of BSA over monomers, it remains unknown which route of disassembly it takes.

As demonstrated by a recent work of the group of Meijer, BSA can interact with both free and assembled BTA monomers.[14] They demonstrated using simulations that monomers can diffuse towards the protein when fibre and protein are in contact, and it requires less energy than doing it as free monomers. However, this depends deeply on the strength of the BSA-monomer interaction. In the end, two possibilities exist for our destabilization (Fig. 3.9):

1. BSA depletes the free monomers in solution, forcing the monomer release from the fibres to maintain concentration. The destabilization is governed by the $k_{off}$ of the monomers.
2. BSA scavenges monomers from the fibres, after direct contact. The disassembly is governed by the $K_d$ of the BSA-fibre.

The first situation just requires a very robust structure (low CAC, kinetic effects), to remain stable under out-of-equilibrium conditions (depleted free monomer). The stability in the second situation is insensitive to the monomer-fibre equilibrium.

Our results give clear insights regarding this point. The disassembly of C8 for both dilution and BSA experiments is similar in absolute terms, however not in relative terms compared to C0/C4. The effect of proteins on C8 relative to C0 and C4 is much higher than the dilution effect. In other words, the difference between C0/C4 and C8 is dramatic for dilution and quite mild for proteins. Where before we had a clear difference between the two stability/responsiveness regimes, now the difference is very diffuse. This necessarily implies that C8 is more sensitive to the presence of proteins than to dilution. Very importantly, C8 does not exchange monomers at a significant rate as observed in the mixing experiment (Fig. 3.6). BSA must then scavenge monomers directly from the fibres, route 2 (Fig. 3.9).

### 3.2.6 Discussion

We demonstrated experimentally that the assembled monomer state and the monomer-BSA state are connected through two different routes, rather than being connected only through the free monomer. Even though it is not clear whether low stability polymers can lose monomers using both routes or not, high stability polymers can exclusively be destabilized by the direct interaction with proteins. This implies that stability in the biological environment is not only achieved by high supramolecular robustness, but also by absence of scavenging effects. For hence, the protein-supramolecule interaction is decisive for the stability. When it is high, proteins would interact longer, eventually allowing the monomer diffusion towards the BSA.[14] Once bound, BSA could detach from the fibre depleting the monomer from fibre, leaving the stability-responsiveness balance in a second plane. If, just for sake of speculation, we assume a linear trend for the C8 assembly vs BSA excess graph (Fig. 3.7 b), we can extrapolate that complete disassembly would happen at 95-fold excess of protein. Upon a hypothetical intravenous injection, this would represent only around the 0.7% of the actual albumin in the blood. Proteins are in vast number, if they can bind fibres, they will eventually deplete all the monomers, independently of the CAC. These results have profounds implications because CAC has been largely used as a key performance indicator for in-blood circulations stability.[24,25]

For this reason, and because proteins in the blood outnumber monomers by several orders of magnitude, the key factor for in-blood stability falls on reducing protein interaction rather than increasing the stability-responsiveness balance.

In the scenarios where the protein-supramolecule interaction is low, proteins interact only with free monomers, and the only requirement for in-blood stability is high supramolecular stabilities, typically associated to low CAC values and kinetic effects. This reveals the importance of studying the protein-supramolecule interactions.

Overall, works on micelles have shown a result in accordance with our observation. Robust micelles with low CMC from the Thayumanavan group containing inner enzyme cleavable groups have shown cleavage ONLY when the protein specifically binds to a ligand on the surface.[6] Analogous micelles from the Amir group containing inner enzyme cleavable groups have shown no cleavage in presence of proteins.[12] Both examples show how high stability hampers the release of monomers to re-equilibrate for replacing the cleaved free monomer (route 1). However, in presence of proteins that specifically bind to the surface, the cleavage is possible. Proteins can bind and scavenge monomers that get exposed to the enzyme (route 2). When this interaction appears to be weak, the presence of proteins has a minimal effect.

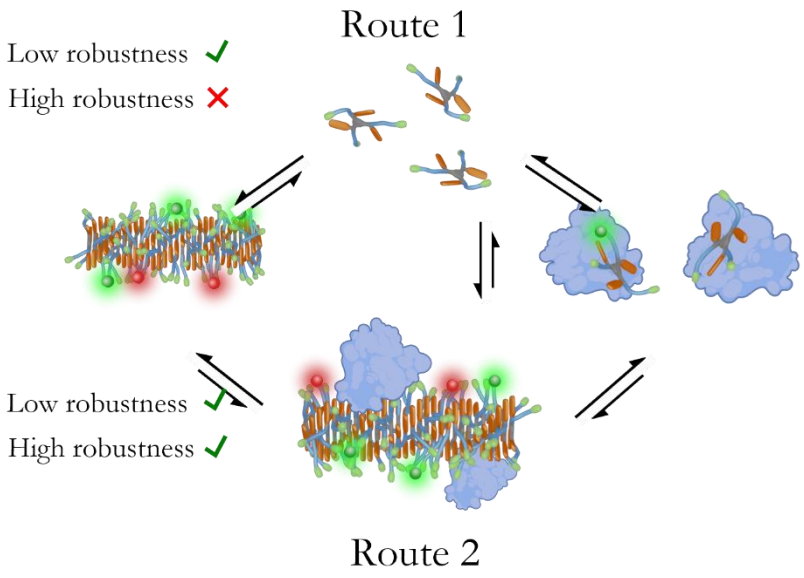


Figure 3.9 Cartoon representing the possible disassembling pathways. Route 1, protein scavenging from free monomer, at the top. Route 2, protein scavenging from fibre, at the bottom. Route 1 is forbidden for highly stable assemblies.

## 3.3 Conclusions

We have synthesised three BTA based discotic amphiphiles, with three different hydrophobic-hydrophilic balances. The evaluation of their stability-responsiveness trade-off allowed to separate them into two well differentiated regimes, low stability-high responsivity for C0 and C4, and high stability-low responsivity for C8.

In a hypothetical intravenous injection, C0 and C4 clearly showed a very low stability. Dilution seems critical for these structures, and protein scavenging monomers leads also to disassembly.

C8 seems extraordinarily robust against dilution. However, proteins seem to be able to destabilize the structures. This is possible only because proteins can scavenge monomers directly from fibres and not only from solution. Then, we demonstrate that designing supramolecules for drug delivery requires inevitably a high stability-responsiveness trade-off to resist dilution and a weak BSA-supramolecule interaction to minimize scavenging effects.

## 3.4 Materials and methods

### 3.4.1 Materials

All solvents, unless stated otherwise, were obtained from commercial sources in at least analytical quality (a.r.) and were used without further purification. Ultrapure water was obtained from a Milli Pore system from Merck. Lysine and 2-Chlorotrityl chloride resin were obtained from Iris biotech. Fmoc-$PEG_8$-OH and PyBOP were purchased from Chempep. DIEA, piperidine, formic acid benzene tricarbonyl chloride, Fmoc-GABA and Fmoc-8-Aoc-OHwere obtained from Sigma-Aldrich.

L-Phenylalanine-4'-azobenzene was synthesised following the procedure reported before.[28, 29] Synthesis performed by Dr. José Augusto Berrocal.

### 3.4.2 Instrumentation

**UV-Vis**

Measurements were performed with a Tecan infinite M200Pro microplate reader using a quartz cuvette of 0.5 mL and 1 cm of pathlength. Spectra were taken from 280 nm to 500 nm at every 5 nm.

**Reverse Phase-High Performance Liquid Chromatography**

During synthesis and characterization of the monomers, measurements were recorded on a HPLC Waters e2695 separation module equipped with Photodiode Array detector Waters 2998 and Mass spectrometer QDA detector Acquity. A XSelect CSH C183.5 µm 4.6x50mm was used. Water 0.1% HCOOH and ACN 0.1% HCOOH were used as eluents. A gradient of 25-45% ACN in water was applied in 3.5 min. The elution speed was kept at 1.6 ml·min−1 and the temperature was maintained at 50 °C. The injection volume was 10 µl.

**Transmission Electron Microscopy**

Images were taken with Jeol JEM 1010 MT electron microscope (Japan), operating at 80 kV. Images were obtained on a CCD camera Megaview III (ISIS), MNnster, Germany.

**Negative staining**

Samples were deposited onto C-only grids (pre-treated with glow discharge for 30 s) for 1.5 min. The solution was washed with water for 30 s, and finally it was negatively stained with uranyl acetate 2% during 1.5 min. The excess of solution was blotted with a filtering paper and the grids were stored in the desiccator.

**Circular Dichroism**

Spectra was recorded on a Jasco J815 spectrometer, equipped with a JASCO Peltier PFD-425S/15 with a range of 263–383 K. A sealable quartz cell with a pathlength of 5 mm was used. The spectra were recorded continuously between 500-240 nm at every 0.1 nm, with a sensitivity of 100 mdeg, at 100 nm/min. The response time was set to 0.25s. The temperature dependent spectra were recorded at an interval of 10 °C between 5-75 °C at a temperature ramp of 1 °C/min. During photoirradiation measurements the sample was kept isothermal at 20 °C.

**$^1$H-NMR**

$^1$H NMR spectra were recorded on a Varian Mercury Vx 400 MHz. Chemical shifts are given in ppm (δ) values relative to tetramethylsilane (TMS).

**MALDI-TOF**

Spectra were recorded on a Applied Biosystems - 4800 Plus MALDI TOF/TOF™ Analyzer. α-Cyano-4-hydroxycinnamic acid was used as a matrix.

## 3.4.3 Methods

**Chemical synthesis**

The synthetic strategy and protocols are the same as described in the methods section of chapter 2. It consisted of growing the wedge by Solid Phase Peptide Synthesis, the subsequent cleavage from the solid support and the final convergent coupling to the core in solution.

**4-(Fmoc-amino)butanoic acid and 8-(Fmoc-amino)octanoic acid coupling**

1.5 eq Fmoc protected building block was preactivated in DCM:DMF 9:1 with 1.5 eq PyBOP and 4.5 eq. DIEA. The mixture was transferred to the syringe, rocked for 15 h and shaken for 5 min every hour during the first three hours. Then, the syringe was filtered and washed with DCM 15 mL x 3, DMF 15 mL x 3 and DCM 15 mL x 3.

C4 wedge

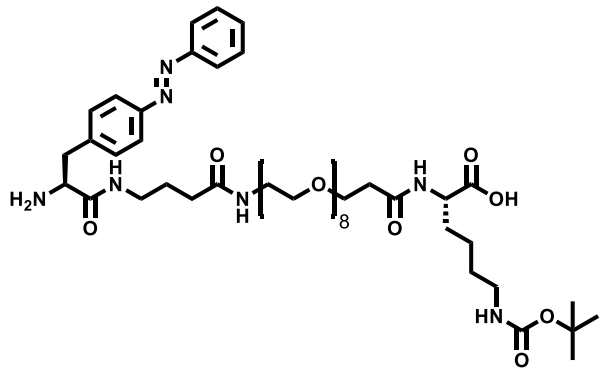


3.8 Molecular structure of C4 wedge.

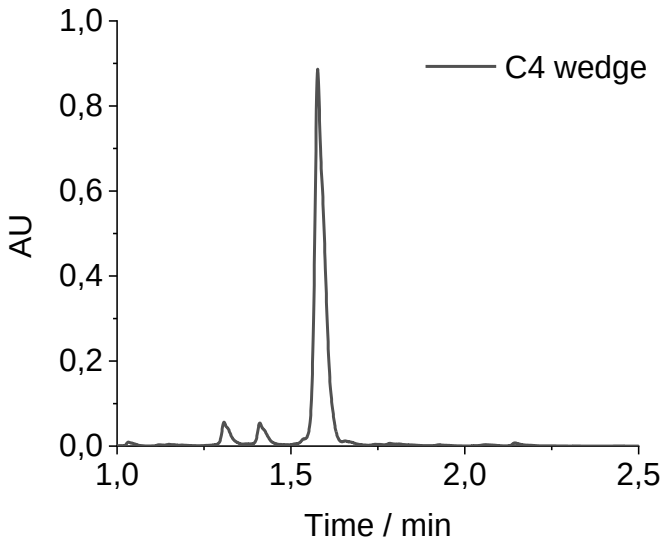


3.9 Chromatogram of C4 wedge. Peak at 1.6 min corresponds to E-isomer, peak at 1.4 corresponds to the Z-isomer. ESI(+) of wedge 1. m/z: $[M+H]^+$= 1007.0, $[M+2H]^{2+}$= 504.0. Calculated: m/z: $[M+H]^+$=1007,21, $[M+2H]^{2+}$= 504.1

C8 wedge

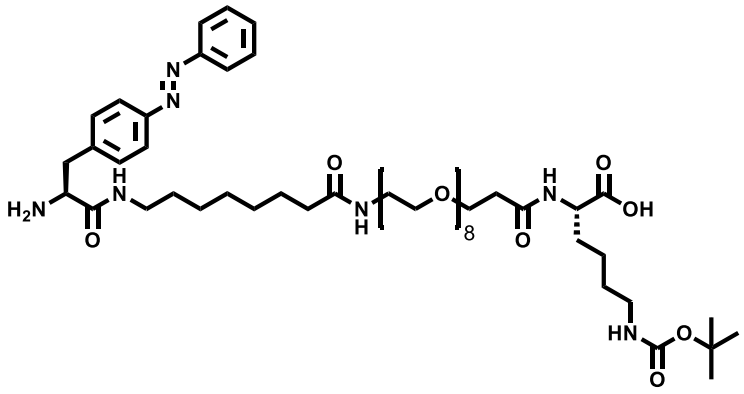


3.10 Molecular structure of C8 wedge.

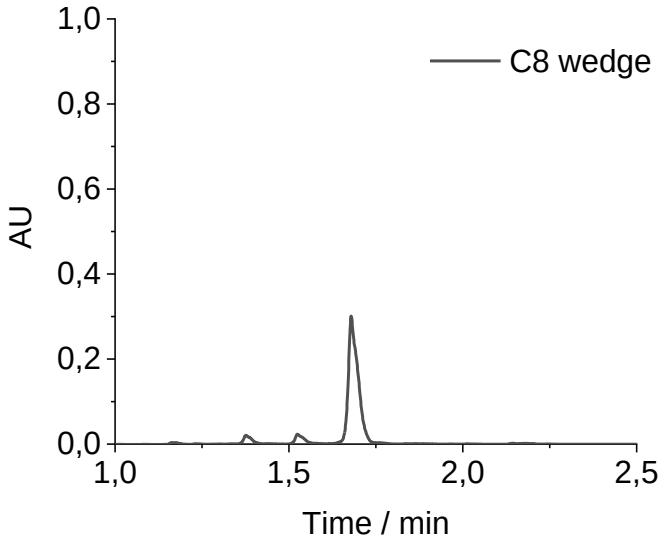


3.11 Chromatogram of C8 wedge. The peak at 1.55 min corresponds to the Z-isomer, the peak at 1.7 min corresponds to the E-isomer. ESI(+) of C4. m/z: $[M+H]^+$= 1063.1 $[M+2H]^{2+}$= 532.0 m/z Calculated: m/z: $[M+H]^+$=1063.3, $[M+2H]^{2+}$= 532.15.

- Solution synthesis of C3-symmetric monomers

Monomers C4 and C8 were synthesised by reacting the corresponding wedge with 1,3,5-benzenetricarbonyl trichloride. The wedges (1 eq. 150.0 mg wedge 1, 217.2 mg wedge) and 3 eq of triethylamine were dissolved in $CHCl_3$ (0.5 mL) and cooled to 0 °C. 1,3,5-benzenetricarbonyl trichloride (13 mg for C4 wedge and 15.7 mg for C8 wedge, 0.33 eq) was dissolved in 0.5 mL of $CHCl_3$ and added dropwise to the reaction mixture under stirring at 0 °C. After 15 min at 0 °C, the mixture was stirred another 12 hrs at rt. The mixture was subsequently concentrated in vacuo and the resulting oil was dissolved in $H_2O$:ACN 1:1 and dried in vacuo. Boc cleavage was performed by treating the product with TFA 95% and 5% TIPS (Triisopropyl Silane) for 1 h. The product was then dried by a gentle stream of $N_2$, dissolved in $H_2O$:ACN 1:1, purified by reversed-phase HPLC and dried in vacuo yielding monomer C4 and C8. (C4: Yield: 23.9% / Purity: 95.4% // C8: Yield: 33.1% / Purity: 97.6% )

C4 monomer

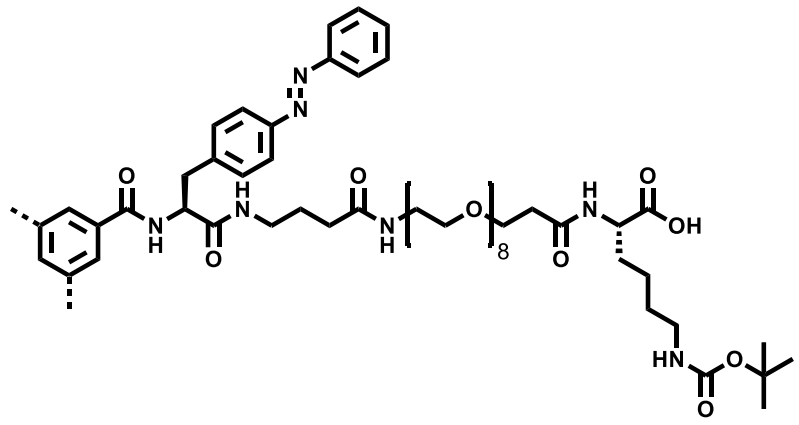

3.12 Molecular structure of C4 monomer. MW: 2874.04.

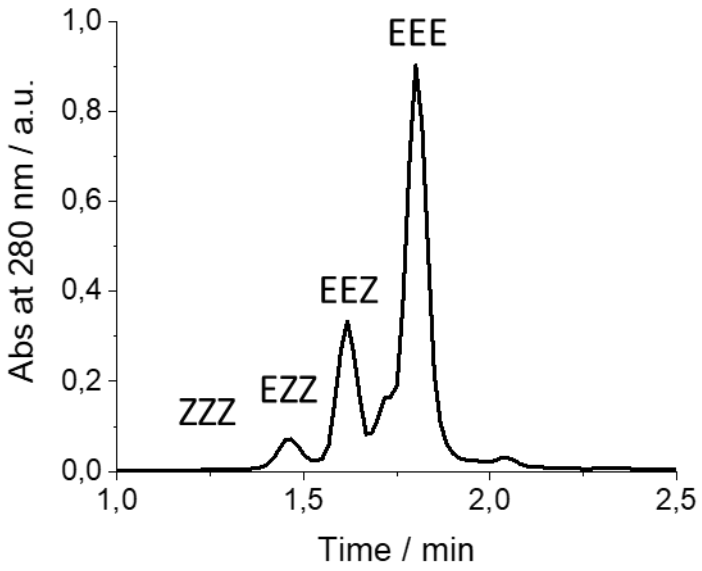


3.13 RP-HPLC at 280 nm of C4 monomer.

MS-C4: ESI-MS deconvoluted (+): 2873.1. Calculated mass: 2874.4.

MALDI-TOF-MS (α-Cyano-4-hydroxycinnamic acid was used as a matrix): m/z: $[M+H]^+$= 2874.04 (Isotopic distribution can be observed).

$^1$H NMR (400 MHz, DMSO-d6, *E*/*Z* mixture, signals of the main isomer)

δ /ppm = 9.02 (s, 3H), 8.38 (m, 3H), 8.32 (m, 3H), 7.88 (m, 3H), 7.82 (m, 9H), 7.77 (m, 6H), 7.55 (m, 15), 4.78 (m, 3H), 4.04 (m, 3H), 3.57 (m, 12H), 3.48 (m, 87H) partially hidden by water signal), 3.17 (m, 15H), 2.72 (m, 6H), 2.35 (m, 6H), 2.06 (m, 6H), 1.70-1.45 (m, 24H), 1.30 (m, 6H).

C8 monomer

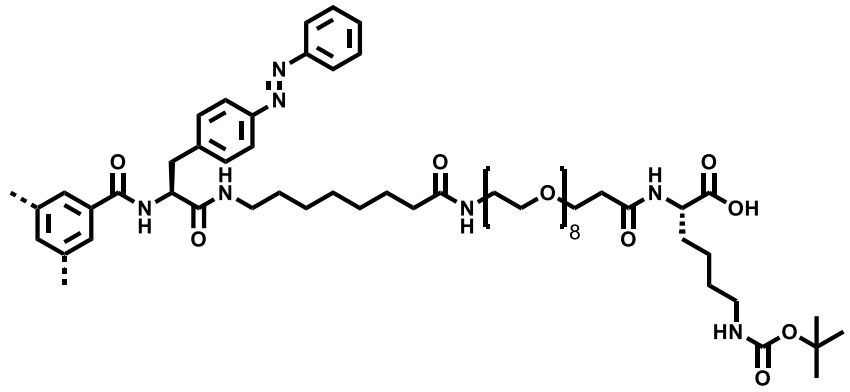


3.14 Molecular structure of C8 monomer. MW: 3042.7.

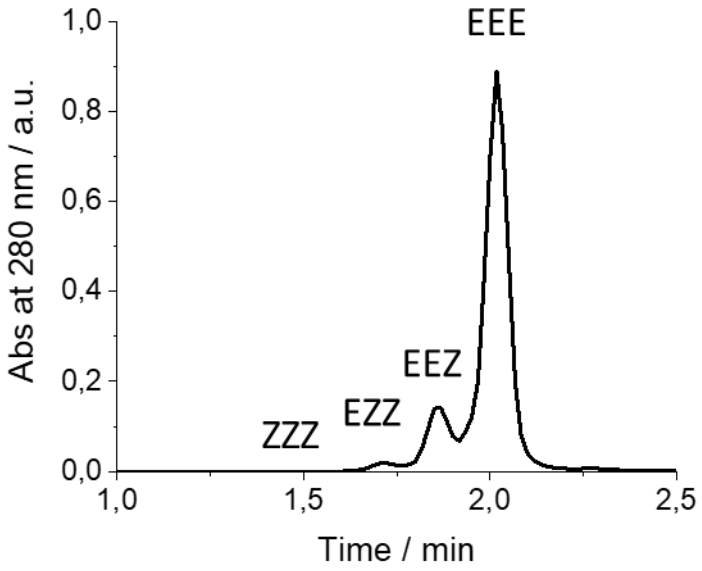


3.15 RP-HPLC at 280nm of C8.

MS-C8: ESI-MS deconvoluted (+): 3041.9. Calculated mass: 3042.7

MALDI-TOF-MS (α-Cyano-4-hydroxycinnamic acid was used as a matrix): m/z: $[M+H]^+$= 3043.0 (Isotopic distribution can be observed).

$^1$H NMR (400 MHz, DMSO-d6, *E*/*Z* mixture, signals of the main isomer)

δ /ppm = 8.97 (s, 3H), 8.35 (m, 3H), 8.22 (m, 3H), 7.85-7.76 (m, 18H), 7.60-7.51 (m, 15H), 4.79 (m, 3H), 4.04 (m, 3H), 3.54-3.61 (m, 12H), 3.49 (m, 87H) partially hidden by water signal), 3.20-3.12 (m, 15H), 2.73 (m, 6H), 2.37 (m, 6H), 2.01 (m, 6H), 1.67 (m, 3H), 1.52 (m, 9H), 1.42 (m, 6H), 1.32 (m, 12H), 1.18 (m, 24H).

- Monomer labelling protocol

Monomers were labelled by reacting the monomers with sulfo-Cyanine 3 and sulfo-Cyanine 5 NHS ester. C4 and C8 (5 mg , 1 eq) were dissolved in 1mL DMSO at room temperature and put under stirring. 3 eq of TEA were added dropwise. The corresponding NHS-Ester dye, previously dissolved in DMSO (10 mM for sCy3 and 15 mM for sCy5, 1 eq), was added dropwise to the corresponding monomers solution. The reaction was stirred for 20 h under stirring at room temperature. Excess of dye was removed by dialysis. Products were lyophilized, dissolved in $H_2O$:ACN 1:1 and purified by reversed-phase HPLC and dried in vacuo yielding monomer C4-sCy3, C4-sCy5, C8-sCy3 and C8-sCy5. Products were analysed by RP-HPLC-MS.

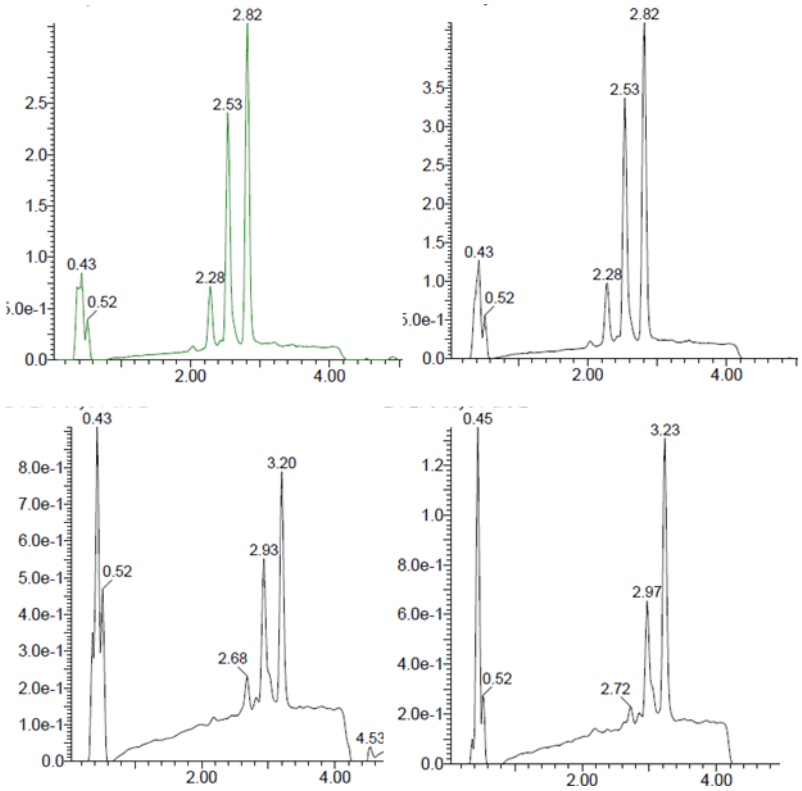


3.16 (Top Left) RP-HPLC of C4-sCy3. (Top right) RP-HPLC of C4-sCy5. (Bottom Left) RP-HPLC of C8-sCy3. (Bottom right) RP-HPLC of C8-sCy5.

MS- C4-sCy3: ESI-MS deconvoluted (+): 3485.8. Calculated mass: 3486.1

MS- C4-sCy5: ESI-MS deconvoluted (+): 3512.3. Calculated mass: 3512.2.

MS- C8-sCy3: ESI-MS deconvoluted (+): 3653.64. Calculated mass: 3654.4

MS- C8-sCy5: ESI-MS deconvoluted (+): 3679.97. Calculated mass: 3680.5

## 4. Self-assembly and UV-response

Irradiation set up: Thorlabs M365LP1 was used as UV source at 365 nm, and Thorlabs M455L4 was used as blue source at 455 nm. Irradiations were performed inside a custom-made black box. For the absorbance experiments, irradiations were performed on the cuvette, at a distance of 10 cm. For the rest, the irradiation was performed on a 96-well plate at a distance of 10 cm.

Photofatigue experiment: Several photoisomerization cycles were performed in order to observe the reversibility of the system. The three monomers showed the same complete reversibility.

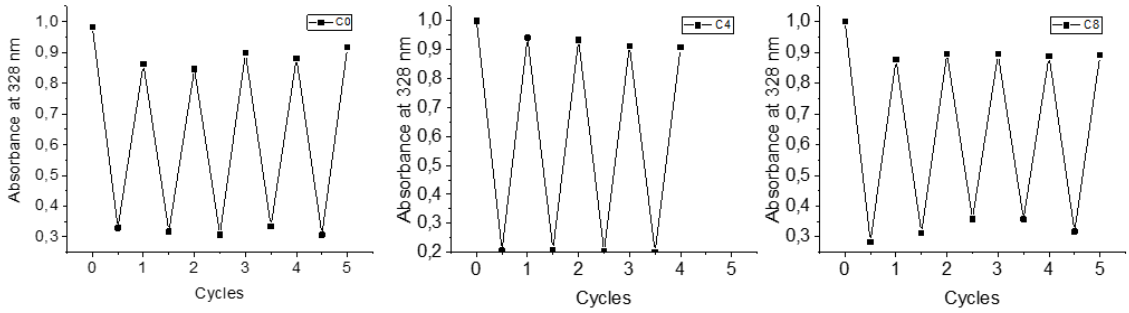


3.17 Photofatigue experiment on monomers at 25 μM. Samples were consecutively irradiated at 360nm and 455 nm and measure before each irradiation. No signs of photofatigue were observed for the molecules.

## 5. Stability in biological-like conditions experiments

Irradiation set up: For CD experiments and HPLC of Figure 3.3, two LED light sources were used, a Thorlabs M365LP1-C5 was used as UV source at 365 nm (irradiation steps of 1s, 100% at 1000 mA of the LED intensity), and a Thorlabs M455L3-C5 was used as blue source at 455 nm (irradiation steps of 10 s, 100% at 1000 mA of the LED intensity). Irradiation occurred on the bench top at rt, with approximately 15 cm distance between the sample and the LED.

Sample preparation:

- Dilution: samples were prepared initially at 100 μM, and ½ diluted directly in the 96 well plate before recording FRET.
- BSA: Polymer samples were prepared at a concentration of 37 μM. Specific amounts of BSA were added to each well and well mixed to reach a final concentration of 25 μM of polymer. The final concentrations of BSA were 0, 10, 20, 30, 40 and 50 mg/ml, that were expressed in terms of BSA excess (0 to 30 fold relative to polymer concentration). FRET signal was measured before and after addition of BSA.
- Fibre-BSA FRET: BSA was added at a final concentration of 10 mg/ml (6 fold) and 10% Cy5 labelled. Sample preparation was identical to the previous experiment with BSA.

Kinetics of disassembly of supramolecular polymers

The disassembly caused by dilution and BSA addition was also evaluated in time. Figure 3.18 shows the temporal evolution of the FRET signal in time. In all the cases, for all monomers, the signal showed the major signal decrease from the first measure. Dilution experiment results are in accordance to the behaviour observed for C0 and C4, but apparently not for C8. We expected seeing kinetic effects here due to the high robustness observed. We hypothesise that other effects could interfere, like for example fibre bundling. This could explain a very slow monomer exchange while experimenting some dilution effects. Protein experiments also show a fast equilibration, what indicates a very fast interaction with BSA.

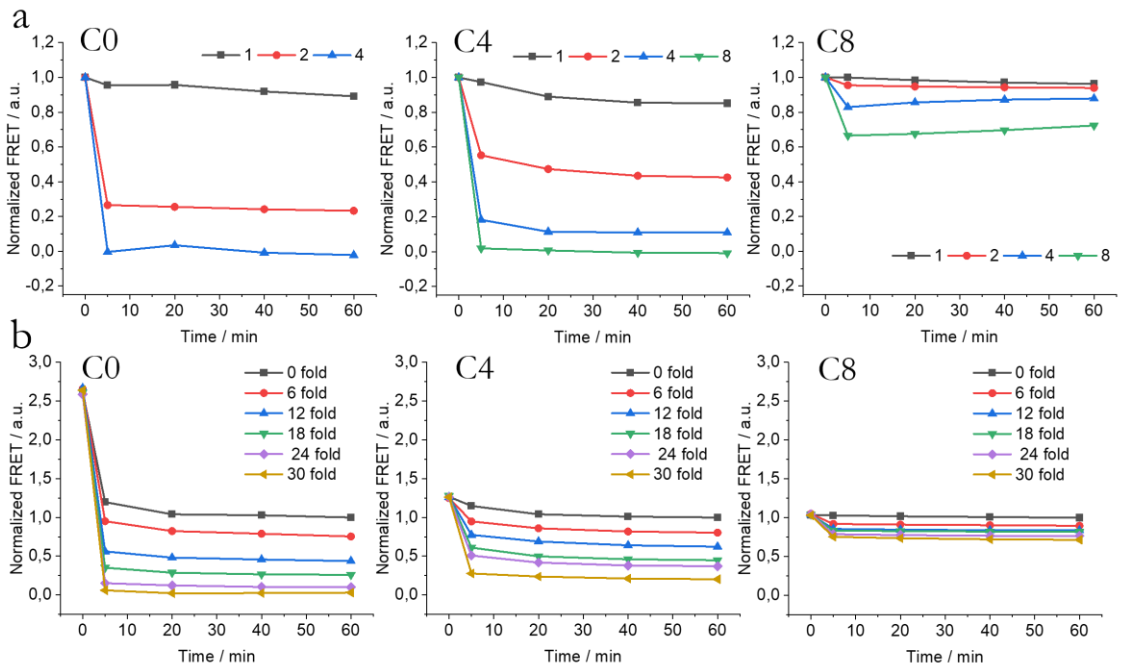


3.18 Normalized FRET signal vs. time after ½ serial dilution (a) and after protein addition (b).

## 4.5 References


1. Ma, X.; Tian, H. Stimuli-Responsive Supramolecular Polymers in Aqueous Solution. Acc. Chem. Res. 2014, 47 (7), 1971–1981.
2. Freeman, R.; Han, M.; Álvarez, Z.; Lewis, J. A.; Wester, J. R.; Stephanopoulos, N.; McClendon, M. T.; Lynsky, C.; Godbe, J. M.; Sangji, H.; Luijten, E.; Stupp, S. I. Reversible Self-Assembly of Superstructured Networks. Science 2018, 362 (6416), 808–813.
3. Albertazzi, L.; Martinez-Veracoechea, F. J.; Leenders, C. M. A.; Voets, I. K.; Frenkel, D.; Meijer, E. W. Spatiotemporal Control and Superselectivity in Supramolecular Polymers Using Multivalency. PNAS 2013, 110 (30), 12203–12208.
4. Proetto, M. T.; Callmann, C. E.; Cliff, J.; Szymanski, C. J.; Hu, D.; Howell, S. B.; Evans, J. E.; Orr, G.; Gianneschi, N. C. Tumor Retention of Enzyme-Responsive Pt(II) Drug-Loaded Nanoparticles Imaged by Nanoscale Secondary Ion Mass Spectrometry and Fluorescence Microscopy. ACS Cent. Sci. 2018, 4 (11), 1477–1484.
5. Harnoy, A. J.; Slor, G.; Tirosh, E.; Amir, R. J. The Effect of Photoisomerization on the Enzymatic Hydrolysis of Polymeric Micelles Bearing Photo-Responsive Azobenzene Groups at Their Cores. Org. Biomol. Chem. 2016, 14 (24), 5813–5819.
6. Guo, J.; Zhuang, J.; Wang, F.; Raghupathi, K. R.; Thayumanavan, S. Protein AND Enzyme Gated Supramolecular Disassembly. J. Am. Chem. Soc. 2014, 136 (6), 2220–2223.
7. Liu, B.; Thayumanavan, S. Substituent Effects on the PH Sensitivity of Acetals and Ketals and Their Correlation with Encapsulation Stability in Polymeric Nanogels. J. Am. Chem. Soc. 2017, 139 (6), 2306–2317.

8. Choi, W.; Battistella, C.; Gianneschi, N. C. High Efficiency Loading of Micellar Nanoparticles with a Light Switch for Enzyme-Induced Rapid Release of Cargo. Biomater. Sci. 2021, 9 (3), 653–657.
9. Spitzer, D.; Rodrigues, L. L.; Straßburger, D.; Mezger, M.; Besenius, P. Tuneable Transient Thermogels Mediated by a PH- and Redox-Regulated Supramolecular Polymerization. Angewandte Chemie International Edition 2017, 56 (48), 15461–15465.
10. Krieg, E.; Rybtchinski, B. Noncovalent Water-Based Materials: Robust yet Adaptive. Chemistry – A European Journal 2011, 17 (33), 9016–9026.
11. Othman, Z.; Cillero Pastor, B.; van Rijt, S.; Habibovic, P. Understanding Interactions between Biomaterials and Biological Systems Using Proteomics. Biomaterials 2018, 167, 191–204.
12. Feiner-Gracia, N.; Buzhor, M.; Fuentes, E.; Pujals, S.; Amir, R. J.; Albertazzi, L. Micellar Stability in Biological Media Dictates Internalization in Living Cells. J. Am. Chem. Soc. 2017, 139 (46), 16677–16687.
13. Feiner-Gracia, N.; Glinkowska Mares, A.; Buzhor, M.; Rodriguez-Trujillo, R.; Samitier Marti, J.; Amir, R. J.; Pujals, S.; Albertazzi, L. Real-Time Ratiometric Imaging of Micelles Assembly State in a Microfluidic Cancer-on-a-Chip. ACS Appl. Bio Mater. 2021, 4 (1), 669–681.
14. Varela-Aramburu, S.; Morgese, G.; Su, L.; Schoenmakers, S. M. C.; Perrone, M.; Leanza, L.; Perego, C.; Pavan, G. M.; Palmans, A. R. A.; Meijer, E. W. Exploring the Potential of Benzene-1,3,5-Tricarboxamide Supramolecular Polymers as Biomaterials. Biomacromolecules 2020, 21 (10), 4105–4115.
15. Besenius, P.; Portale, G.; Bomans, P. H. H.; Janssen, H. M.; Palmans, A. R. A.; Meijer, E. W. Controlling the Growth and Shape of Chiral Supramolecular Polymers in Water. Proceedings of the National Academy of Sciences 2010, 107 (42), 17888–17893.
16. Leenders, C. M. A.; Albertazzi, L.; Mes, T.; Koenigs, M. M. E.; Palmans, A. R. A.; Meijer, E. W. Supramolecular Polymerization in Water Harnessing Both Hydrophobic Effects and Hydrogen Bond Formation. Chem. Commun. 2013, 49 (19), 1963–1965.
17. Fuentes, E.; Gerth, M.; Berrocal, J. A.; Matera, C.; Gorostiza, P.; Voets, I. K.; Pujals, S.; Albertazzi, L. An Azobenzene-Based Single-Component Supramolecular Polymer Responsive to Multiple Stimuli in Water. J. Am. Chem. Soc. 2020, 142 (22), 10069–10078.
18. Rajdev, P.; Ghosh, S. Fluorescence Resonance Energy Transfer (FRET): A Powerful Tool for Probing Amphiphilic Polymer Aggregates and Supramolecular Polymers. J. Phys. Chem. B 2019, 123 (2), 327–342.
19. Roy, R.; Hohng, S.; Ha, T. A Practical Guide to Single Molecule FRET. Nat Methods 2008, 5 (6), 507–516.
20. Algar, W. R.; Hildebrandt, N.; Vogel, S. S.; Medintz, I. L. FRET as a Biomolecular Research Tool — Understanding Its Potential While Avoiding Pitfalls. Nat Methods 2019, 16 (9), 815–829.
21. Baker, M. B.; Albertazzi, L.; Voets, I. K.; Leenders, C. M. A.; Palmans, A. R. A.; Pavan, G. M.; Meijer, E. W. Consequences of Chirality on the Dynamics of a Water-Soluble Supramolecular Polymer. Nat Commun 2015, 6.
22. Smith, G. D.; Bedrov, D. Roles of Enthalpy, Entropy, and Hydrogen Bonding in the Lower Critical Solution Temperature Behavior of Poly(Ethylene Oxide)/Water Solutions. J. Phys. Chem. B 2003, 107 (14), 3095–3097.

23. Lüsse, S.; Arnold, K. The Interaction of Poly(Ethylene Glycol) with Water Studied by $^{1}H$ and 2H NMR Relaxation Time Measurements. Macromolecules 1996, 29 (12), 4251–4257.
24. Cui, H.; Chen, Z.; Zhong, S.; Wooley, K. L.; Pochan, D. J. Block Copolymer Assembly via Kinetic Control. Science 2007, 317 (5838), 647–650.
25. Chenthamara, D.; Subramaniam, S.; Ramakrishnan, S. G.; Krishnaswamy, S.; Essa, M. M.; Lin, F.-H.; Qoronfleh, M. W. Therapeutic Efficacy of Nanoparticles and Routes of Administration. Biomaterials Research 2019, 23 (1), 20.
26. Su, H.; Wang, F.; Ran, W.; Zhang, W.; Dai, W.; Wang, H.; Anderson, C. F.; Wang, Z.; Zheng, C.; Zhang, P.; Li, Y.; Cui, H. The Role of Critical Micellization Concentration in Efficacy and Toxicity of Supramolecular Polymers. Proceedings of the National Academy of Sciences 2020, 117 (9), 4518–4526.
27. Ma, S.; Zhou, J.; Zhang, Y.; He, Y.; Jiang, Q.; Yue, D.; Xu, X.; Gu, Z. Highly Stable Fluorinated Nanocarriers with iRGD for Overcoming the Stability Dilemma and Enhancing Tumor Penetration in an Orthotopic Breast Cancer. ACS Appl. Mater. Interfaces 2016, 8, 42, 28468–28479
28. M. Bose, D. Groff, J. Xie, E. Brustad, and P. G. Schultz. The Incorporation of a Photoisomerizable Amino Acid into Proteins in E. coli, J. Am. Chem. Soc. 2006, 128 (2), 388-389.
29. W. Li, I. Park, S.-K. Kang, and M. Lee,. Smart hydrogels from laterally-grafted peptide assembly, Chem. Commun., 2012, 48 (70), 8796-8798.

# Chapter 4 | Strategies for drug entrapment into supramolecular polymers

## 4.1 Introduction

As shown in the previous chapters, the self-assembly of our discotic designs can be switch on/off using light. Owing this great external control that we can exert on the assembly, we wanted to explore the use of supramolecular polymers as drug carriers.

Many examples can be found for nanoparticles such as gold or silica nanoparticles, vesicles or micelles, among others.[1-6] However, little attention have been paid to supramolecular polymers and discotic amphiphiles in particular.

The Stupp lab have extensively explored the use of peptide amphiphiles for different purposes. Matson and Stupp demonstrated the possibility to conjugate peptide amphiphiles with a small drug through a hydrazone linker. The conjugate demonstrated to self-assemble into fibres with the ability to gradually release the drug under physiological conditions.[7] They also reported the direct encapsulation of camptothecin into supramolecular polymer and demonstrated its release.[8]

Other labs have smartly implemented the one component strategy,[9,10] an approach that uses drugs as hydrophobic moieties of amphiphilic conjugates, to prepare drug-loaded fibres. Lu et. al. demonstrated the self-assembly of camptothecin-tocopherol conjugate stabilized by polyethylene glycol and demonstrating its antitumor efficacy.[11] Other works by Cui, Yang and Xui demonstrated the potential of drug-peptide conjugates to build supramolecular nanofibres.[12,13] They achieved an absolute control over drug loading, great release rates, and even control over assemblies' morphology.[14-23]

In a pioneering work of Albertazzi lab, Bakker et al.,[24] explored the possibility of using discotic amphiphiles for intracellular release. They demonstrated the encapsulation of NileRed and the complexation of siRNA using multicomponent discotic fibres and achieved the intracellular release of the cargoes.

Inspired by this work, we explored two load-and-release strategies of biologically active molecules with our discotic amphiphiles. We exploited the light responsiveness of our system to control the release of the cargo.

The first strategy (strategy 1, Fig. 4.1 a), is designed for hydrophilic ligands, consisting of a co-assembly approach in which two similar discotic monomers stack together forming the fibres. One of them will carry the molecule attached at the hydrophilic side while the other will serve as scaffold, mainly building the fibre and hiding the ligand from the receptor. Even though this approach is complex, it also brings high advantages like high loading control together with a higher loading capacity due to the C3-symmetric nature of discs (3 ligands/monomer). However, it may introduce some disadvantages, like unexpected changes in the self-assembly.

The second strategy (strategy 2, Fig. 4.1 b) is designed for hydrophobic drugs, consisting of its direct encapsulation in the discotic hydrophobic pocket. Even though it is simpler approach, the total loaded ligand is difficult to quantify.

We believe the selection of the ligands and monomers is of key importance and must be personalized to maximize the entrapping efficiency and minimize the impact on self-assembly. For strategy 1, C4 is paired to a BTA-Azo-Glutamate (C4g), a BTA-Azo derivative that contains a glutamate as the biologically active molecule (Fig. 4.1 a). C4 and C4g are paired because of higher resemblances. In C4g, the hydrophobic BTA core is maintained to maximize the co-assembly between the two monomers, however the hydrophilic part of C4 is substituted in C4g by a modified glutamate. It will act as the hydrophilic part given the multiple charges present at physiological pH but being shorter than the octaethylene counterpart. Glutamate is the primary excitatory neurotransmitter in mammalian brain, and it plays a key role as neuromodulator in many neural circuits. Its dysregulation is related with many neurological diseases like epilepsy, depression, Alzheimer disease, Parkinson disease or unpaired vision.[25,26] Additionally, it has been used successfully to study photopharmacological activity of glutamate derivates.[27]

Using our strategy, C4 and C4g can coassemble into the same structure, carrying the C4g the biologically active glutamate and C4 hiding it, forbidding any interaction until disassembly.

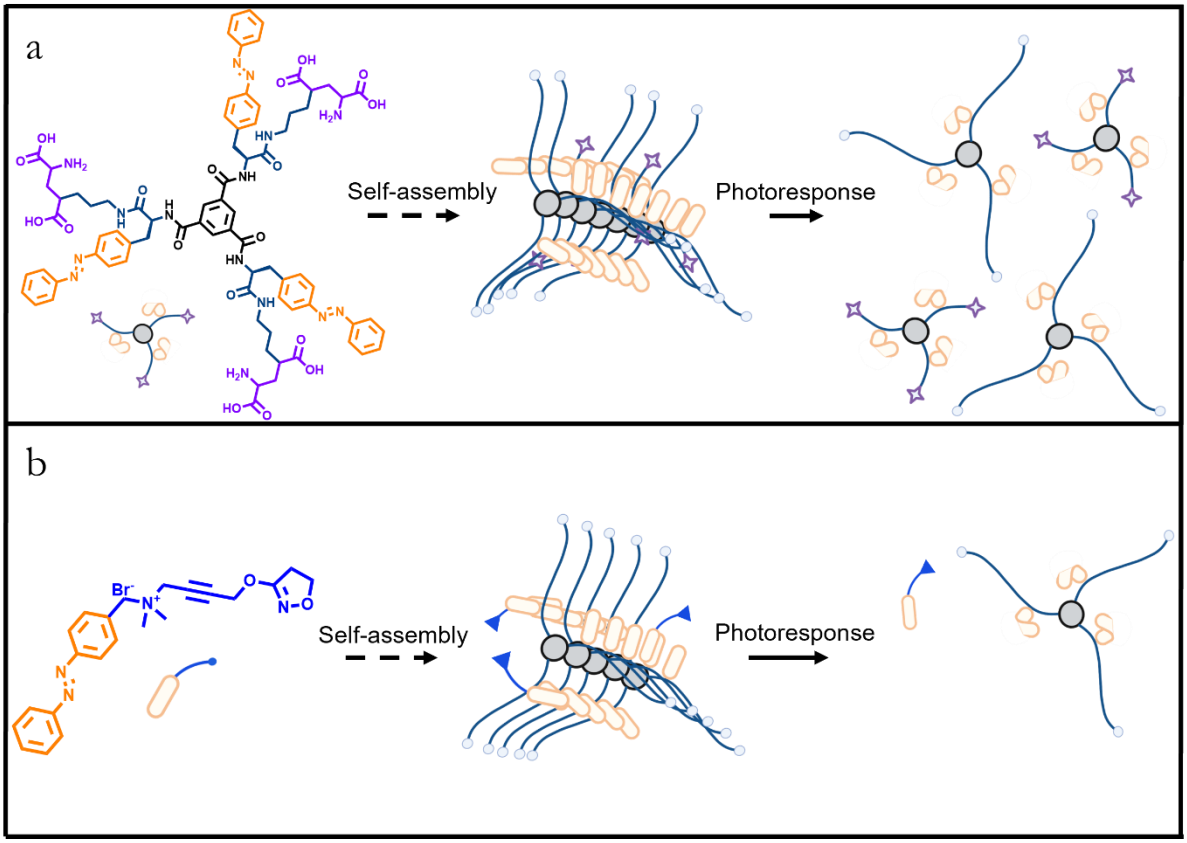


Figure 4.1 Molecular structure of ligands and representation of strategy 1 (a), and strategy 2 (b).

For strategy 2, C8 is paired to the already reported Iperoxoazo (IA).[28] Iperoxoazo is a photoswitchable derivative of the potent muscarinic acetylcholine receptor (M1AChRs) agonist, Iperoxo, and here is used as our drug model. Additionally, it is chosen because of its small size, its

light hydrophobicity and its azobenzene. This is particularly interesting because it can potentially interact with C8's azobenzenes, it can photoisomerize and the activity of *E* and *Z* isomers is equal. (Fig. 4.1 b). C8 is chosen because it has a larger hydrophobic pocket than C4, it is more hydrophobic and more stable.

## 4.2 Results and discussion

Molecules C4 and C8 were synthesised in the previous chapter, while IA was previously synthesised and reported.[28] C4g was newly designed and was newly synthesized. In this case, the synthesis was performed completely in solution (Fig. 4.2), and it consisted first of the coupling between a protected glutamate derivative (1) and Fmoc-L-phenylalanine-4 azobenzene (2) to yield molecule 3. After proper Fmoc-deprotection (3), it was coupled to the 1,3,5-benzenetricarbonyl trichloride in a convergent fashion, forming the C3-symmetric shape. Finally, Boc groups were removed in acid conditions (5). Detailed description of the synthesis can be found in the methods section.

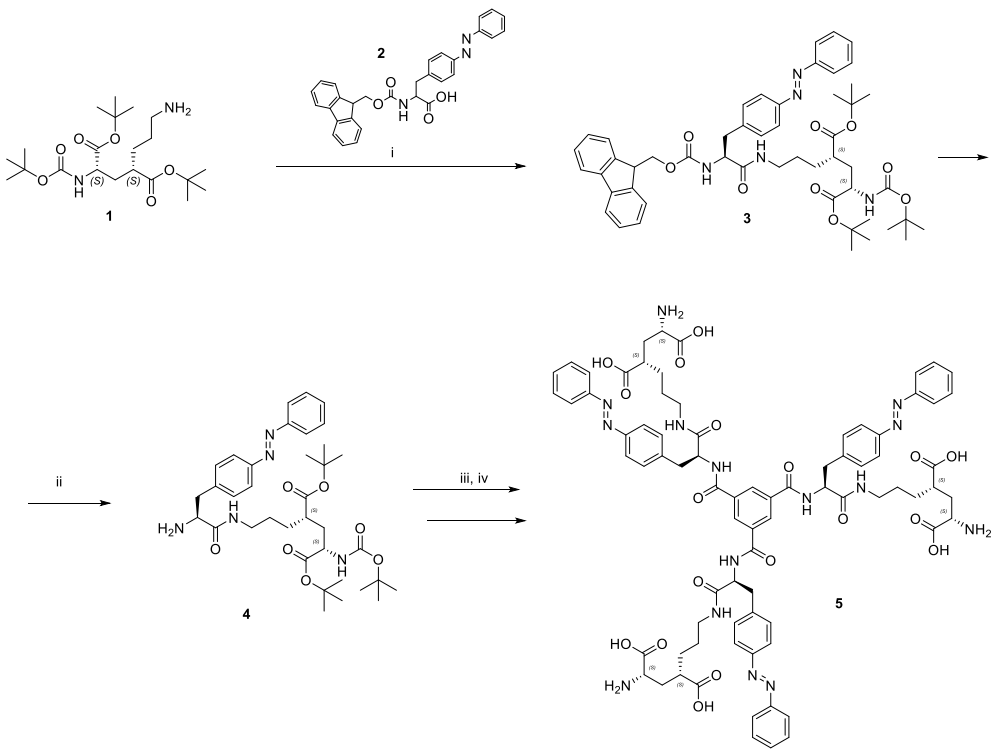


Figure 4.2 Synthetic route of BTA-azo-glutamate. i) PyBOP, DIEA, DCM:DMF; ii) 20% piperidine in $CH_3CN$; iii) Trimesoyl chloride, DCM; vi) TFA, $Et_3SiH$, DCM

### 4.2.1 Co-assembly investigation

Once the molecules are synthesized, the first step consists of evaluating the co-assembly and stacking abilities of the drugs. In order to promote the highest entrapment, monomers and drugs

were dissolved in DMSO at high concentration (C4: 20 mM, C4g: 1mM, C8: 10 mM, IA: 10 mM), mixed in DMSO at the desired ratio, and injected in a specific buffer. Strategy 1 used Neurobasal media as buffer, supplemented with B-27 (5%), penstrep (5 UI/ml), glutaMAX (0,5x) and glucose (15mM), while strategy 2 used an Hepes buffer (150 mM NaCl, 3 mM KCl, 2 $MgCl_2$ mM, 10 mM HEPES, 10 mM D-glucose and 2 mM $CaCl_2$; pH adjusted to 7.4 with NaOH.).

As exposed in chapter 1 and 2, biomolecules and salts can impact the self-assembly, so it is of major importance to perform all the experiments under the diluting buffer

TEM was initially performed on both systems to prove the internalization of the drug models. In figure 4.3 we can observe electron microscopy images of the polymers alone, the cargoes alone, the polymers and cargoes formulated together and the UV response of the later. Interestingly, system 1 started showing a higher degree of entanglement above 30% of co-assembly. Below this amount, morphology cannot be distinguished from C4 alone. This is a result of the internalization of the more hydrophobic C4g. A clear indication of the internalization is evident when C4g is assembled alone and imaged by TEM. The images show heavily aggregated structures, displaying high degrees of entanglements and coiling. These features are not observable in the co-assembled samples. If the molecules could not assemble together, they would do separately and then we should observe supramolecular polymers of both shapes. We can conclude the C4 and C4g indeed co-assemble.

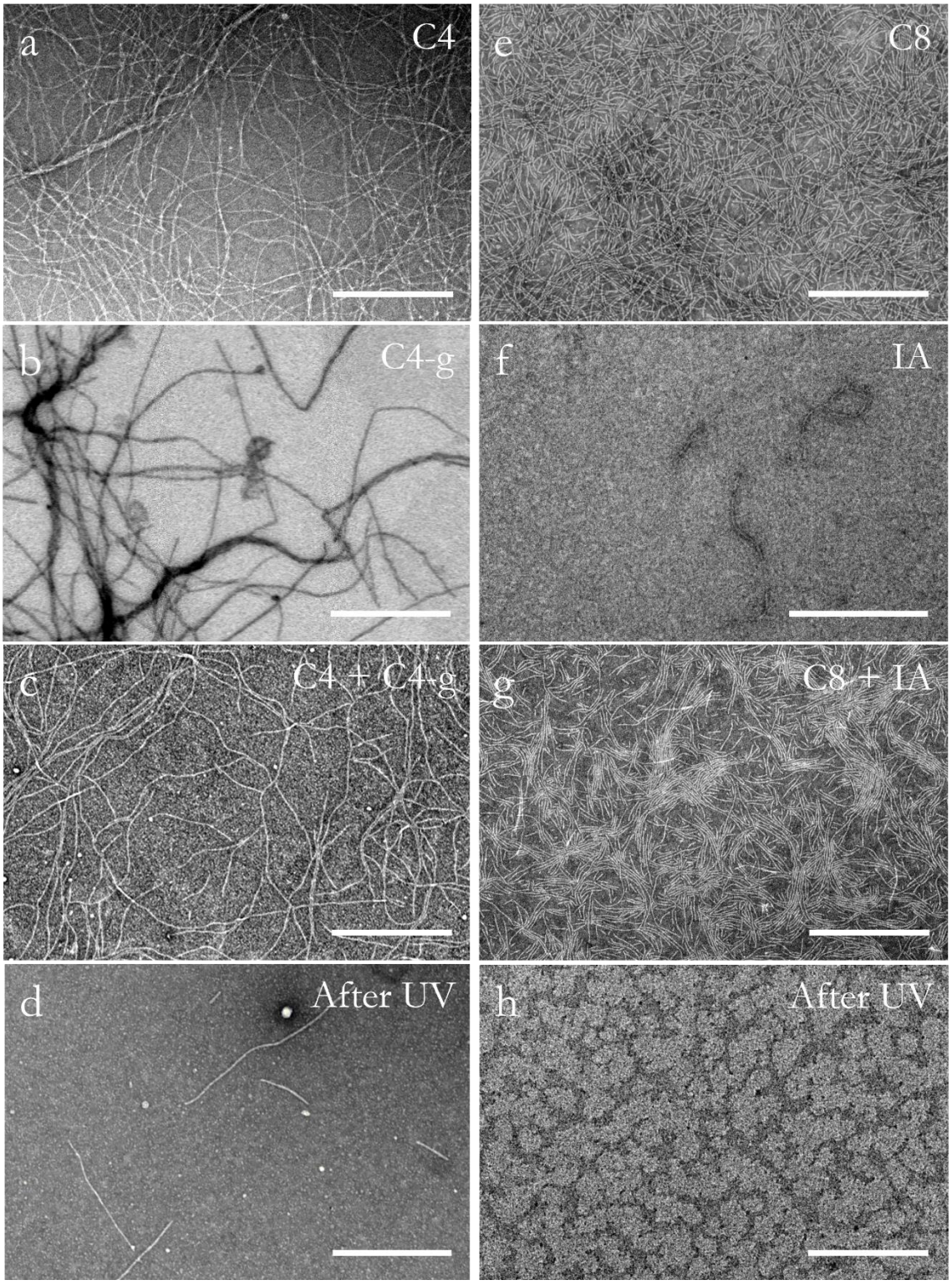


Figure 4.3 TEMS of strategy 1 (C4 & C4g) and strategy 2 (C8 & IA). TEM images correspond to formulations: C4 at 400 μM (a), C4g at 100 μM (b), C4+C4g at 400 μM and 100 μM respectively (c), C4+C4g at 400 μM and 100 μM respectively after UV irradiation (d), C8 at 18 μM €, IA at 2 μM (f), C8+IA at 18 μM and 2 μM respectively (g) and C8+IA at 18 μM and 2 μM respectively after UV irradiation at (h). Scale bar: 500 nm. Irradiation conditions: 365 nm, 1000 mA at 100% of the LED intensity for 5 min.

In strategy 2, IA alone formed few thick fibres in comparison to C8 alone. These thicker fibres were not observed when formulated together with C8, and C8 showed no difference in morphology. These results possibly suggest the innocuous entrapping of the drug inside C8 polymers. Additionally, samples were illuminated by UV light to trigger the disassembly of the fibres. In the case of the C4 + C4g, most of the fibres disappeared, remaining only few fibres and few spherical aggregates. These remaining aggregates could be formed by C4g, given that it demonstrated to be poorly soluble both in DMSO and water. In the case of C8 and IA, the disassembly seemed to be complete under the irradiation conditions, no aggregates were observable. Thus, indicating the *Z* monomers are soluble in water and could potentially lead to IA release and efficient biological trigger.

To elucidate if this co-assemblies produced internal changes, CD signal at 275 nm (azobenzene signal) was measured at different loading % (Fig. 4.4). Interestingly, system 2 showed a decrease in the azobenzene stacking signal, probably produced by the internalization of the Iperoxoazo moiety. Even though this is a good indication of internalization, cell studies will elucidate confirm these internalization studies.

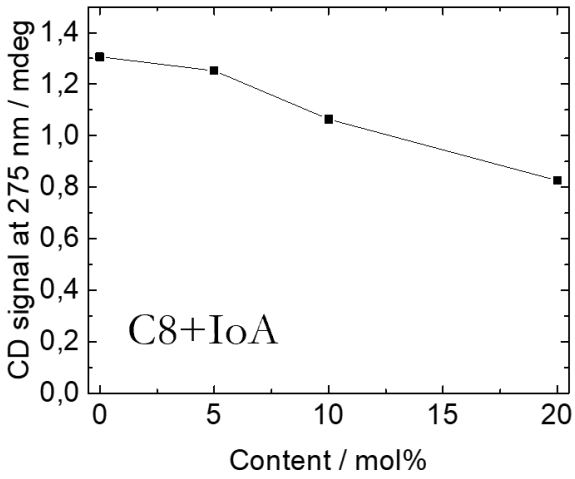


Figure 4.4 CD signal at 275 nm of system 2 (C8 & IA) from 0 to 20 % of IA content during formulation.

From these data we can conclude that C4 and C4g indeed co-assemble, because when assembled separately at the same concentration, we can observe very different morphologies (discrete fibres vs heavily entangled fibres). However, when C4 and C4g are formulated together, only the morphology of C4 is visualized. For C8 and IA the differences are more subtle by TEM, and CD results reinforced the hypothesis of the encapsulation. After UV irradiation, higher degrees of fibre disassembly were observable, even though C4 + C4g presented still few fibres and spherical aggregates. With these positive results, we proceeded to the evaluation of the activity in cells.

### 4.2.2 Release studies

Once demonstrated the entrapping of the drug into the supramolecular fibres, the ability to release the drug must be evaluated. For this purpose, the two strategies were evaluated separately. Strategy 1 involving C4 and C4g derivative was tested on hippocampal neurons culture. Unfortunately, no appreciable change in the signal was observed in this experimental set up after application of the irradiated or non-irradiated fibres. It is possible that C4g does not interact with the receptor, even though it seems unlikely because modified glutamates with similar shapes have been used before. Our hypothesis is that the low solubility of C4g in DMSO and the strong bundling/entanglement and aggregation in water, disturbs any possible recognition with the receptor. Probably, the few fibres (and some small spherical aggregates) that can be observed by TEM after UV irradiation (figure 4.3 d), are formed by C4glut.

Strategy 2 involving C8 and IA was tested on TSA 201 cells overexpressing M1AChRs and calcium sensor R-GECO1. Calcium mediated signals were recorded using customised epifluorescence microscopy setup. A C8 at 500 μM concentration loaded at 10 % of IA was applied onto cells in a specific sequence, and the calcium response was recorded for each cell in different condition to minimize the cell-to-cell response variability (figure 4.4 a). When the sample was irradiated with UV light before application to the cells we have observed a statistically significant increase in R-GECO 1 fluorescence (preillum step, figure 4.4 a, b). This increase is due to UV-triggered release of IA from C fibres and activation of the M1 AChRs, which led to the elevation of the intracellular concentration of $Ca^{+2}$. It was followed by a wash to remove the sample from cells, causing the signal decrease. Then, cells were exposed to a sample of the same composition (same batch) and concentration but without applying the UV irradiation (nonillum step). As fibres are still assembled, and IA is not released, only minor (yet statistically significant) increase in $Ca^{2+}$ mediated fluorescence was observed during this step. After cells were bathed in nonilluminated fibres for some time we applied UV light of low intensity (to not produce imaging artefacts), to trigger the *in-situ* release of the IA. Unfortunately, only several cells have responded with elevation of R-GECO1 fluorescence, which evidence for low efficiency of AI release in these conditions. And finally, in order to confirm expression and functionality of the receptors, Iperoxo (ipx) was applied causing a potent elevation of $Ca^{+2}$ mediated signal.

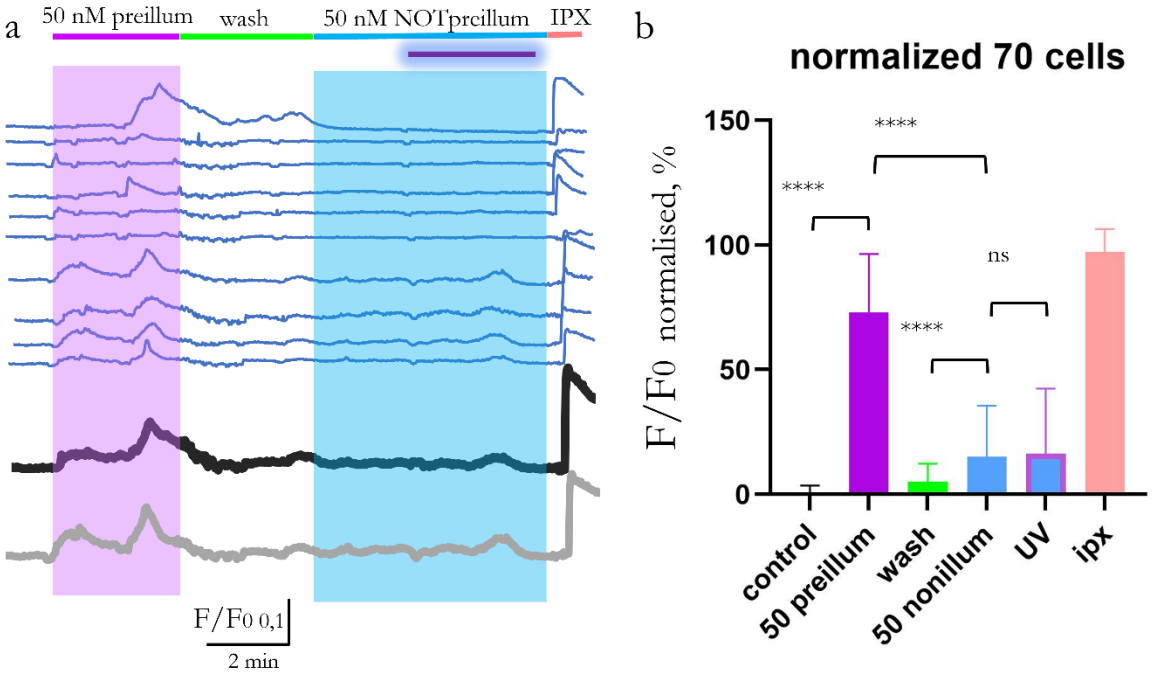


Figure 4.4 UV-induced photorelease of entrapped IA ligand. a. Representative traces of real-time calcium imaging responses of TSA201 cells expressing M1 AChRs and R-GECO1 sensor to the photorelease of entrapped IA. Violet rectangle indicates duration of the application of preilluminated C8 fibres with IA (released), blue rectangle indicates duration of the application of the non-illuminated C8 fibres with IA (encapsulated). Application of the IPX (20 pM) is indicated by red bar. b. Cumulative graph that demonstrates the mean fluorescence increase induced by the application of the preirradiatedor non-irradiated mixture of C8 fibres with IA ligand compared to Iperoxo effect. Mean ± SD, n = 70 cells, **** - P < 0,0001; ns – not significant according to paired t-test.

In figure 4.4 b, the cumulative graph of the mean normalized fluorescence of 70 cells in different conditions. It demonstrates the mean response of cells to irradiated and non-irradiated samples of C8 fibres with IA and it shows the statistically significant difference in the amplitude of fluorescence increase between the conditions. These results evidence that we have achieved a successful IA entrapment and release from C8 fibres. Finally, iperoxo applications demonstrate a comparable effect to the pre-illuminated sample.

In summary, the co-assembly strategy (strategy 1) proved useful to control the drug loading, at the expense of changing the physicochemical properties of fibres (higher bundling and hydrophobicity, less responsiveness). Unfortunately, the monomer resulted to be extremely hydrophobic and hampered its effective use in cells. More work has to be done in order to use this strategy, which could consist of the preparation of a modified C4g, including a short hydrophilic tail before the modified glutamate. Strategy 2 proved the possibility of encapsulating small molecules in stacked aggregates without changing fibres properties and proved useful to deliver them efficiently into cells.

## 4.3 Conclusions and outlook

In this work, two strategies have been explored to internalize bioactive molecules inside the discotic supramolecular polymers. The first consisted of the design of a glutamate containing monomer and co-assemble it with C4. The co-assembly demonstrated to be effective, however, the glutamate containing monomer did not display any activity. Or glutamate could not interact with the receptor or glutamate remained aggregated after fibre disassembly.

A second generation of C4g was started but could not be finished. The monomer was extended with a $PEG_2$ (8-amino-3,6-dioxaoctanoic acid) right between the azobenzene and the glutamate. The molecule was successfully synthesised until the last deprotections step, in which an unusual reaction took place, reducing drastically the yield. Unfortunately, this made the purification step very challenging, and no pure molecule could be isolated.

The second strategy consisted of the classical encapsulation in the hydrophobic pocket of the supramolecular polymer. Encapsulation was proved as well, even though the indications were more subtle than with strategy 1. Finally, light triggered release was proven. Only when fibres were exposed to UV-light, bioactivity was observed.

Even though these strategies are interesting for making drug delivery systems with supramolecular polymers, and could potentially be applicable, there is a need for a higher drug loading and higher control on the drug content. The next step towards this goal could consist of designing a self-assembling prodrug with BTA.

## 4.4 Materials and methods

### 4.4.1 Materials

All reagents and solvents were purchased from Sigma-Aldrich and Activate Scientific and were used without any further purification.

Compound 8 (L-Phenylalanine-4'-azobenzene) was synthesised following the procedure reported before.[29,30] Synthesis performed by Dr. José Augusto Berrocal.

Compound 7 was synthesised following the procedure reported before.[31] Synthesis performed by Ramona Santini.

### 4.4.2 Instrumentation

**Nuclear magnetic resonance spectrometry**

Spectra were registered with a Varian Mercury 400 MHz instrument. Chemical shifts (δ) are reported in parts per million (ppm) against the reference compound tetramethylsilane using the signal of the residual non-deuterated solvent (CDCl3 δ = 7.26 ppm (1H), δ = 77.16 ppm (13C). Spectra were analysed using MestreNova v14.2.0-26256.

**High-performance Liquid Chromatography**

For synthesis and characterization of intermediates: dmf 2-12, measurements were recorded on Waters Alliance 2795 Separation module coupled with a Waters 996 Photodiode Array Detector and a QDA Detector Acquity. Column used: XSelect CSH C18 (3.5 μm, 4.6x50mm). Column temperature was kept at 50 °C. Mobile phase: Water w/0.1% HCOOH (solvent A) and ACN w/0.1% HCOOH (solvent B). Elution method: flow of 1.6 mL/min, runtime of 5 min; 0-3.5min 5%B; 3.5-4.5min 100% B; 4.55-5min 5%B.

The final purification of the compound 12 was carried out using a Waters Alliance 2695 Separation module coupled with a Waters 2996 Photodiode Array Detector. Column used: XSelect CSH C18 OBD Prep Column (130 Å, 5 μm, 10x150mm). Column temperature was kept at 50 °C. Mobile phase: Water w/0.1% HCOOH (solvent A) and ACN w/0.1% HCOOH (solvent B). Elution method: flow of 3 mL/min, runtime of 10 min; 0-0.5min 20%B; 0.5-0.8min 40% B; 0.8-8min 70%; 8-8.10min 100%B; 8.10-9.60 100%B; 9.60-10min 20% B.

**Transmission Electron Microscopy**

Images were taken with Jeol JEM 1010 MT electron microscope (Japan), operating at 80 kV. Images were obtained on a CCD camera Megaview III (ISIS), MNnster, Germany. Samples were negatively stained with Uranyl acetate 2%. Samples were deposited onto C-only grids (pre-treated with glow discharge for 30 s) for 1 min. Then the solution was washed with water for 30 s, and finally it was negatively stained with uranyl acetate 2% during 1 min. The excess of solution was blotted with a filtering paper and the grids were stored in the desiccator.

**Circular Dichroism**

Spectra was recorded on a Jasco J815 spectrometer, equipped with a PTC-423s/5 Peltier cell holder. A sealable quartz cell with a pathlength of 1 cm was used. The spectra were recorded continuously between 500-230 nm at 20 °C every 1 nm, with a sensitivity of 100 mdeg, at 100 $nm \cdot min^{-1}$. The response time was set to 0.25s. The average of 3 accumulations is reported.

**MALDI-TOF**

Spectra were recorded on an Applied Biosystems - 4800 Plus MALDI TOF/TOF™ Analyzer. α-Cyano4-hydroxycinnamic acid was used as a matrix.

**Microscope**

Calcium imaging experiment were performed using inverted IX71 Olympus microscope (Japan) with XLUMPLFLN 20X Olympus water immersion objective (Japan). Polychrome V (Till Photonics, USA) with Xenon Short-Arc lamp (Ushio, Japan) was used as a light source. For OGB-1 AM calcium sensor excitation 505 nm dichroic beam splitter (Chroma Technology, USA) was used, emitted light was filtered by D535/40 nm emission filter. For R-GECO1 calcium sensor excitation 585 nm dichroic beam splitter (Chroma Technology, USA) was used, emitted light was

filtered by ET630/75 nm emission filter (Chroma Technology, USA) and collected by C9100-13 EM-CCD Hamamatsu camera (Japan).

### 4.4.3 Methods

## Chemical synthesis

BTA-AZO-GLUTAMATE (compound 12) was obtained by coupling compound 7 (protected glutamate derivative) with compound 8 followed by the final convergent coupling to 1,3,5-benzenetricarbonyl trichloride.

The synthesis of compound 7 is described in Scheme 4.2, was carried out by Ramona Santini and was already reported in literature.[31]

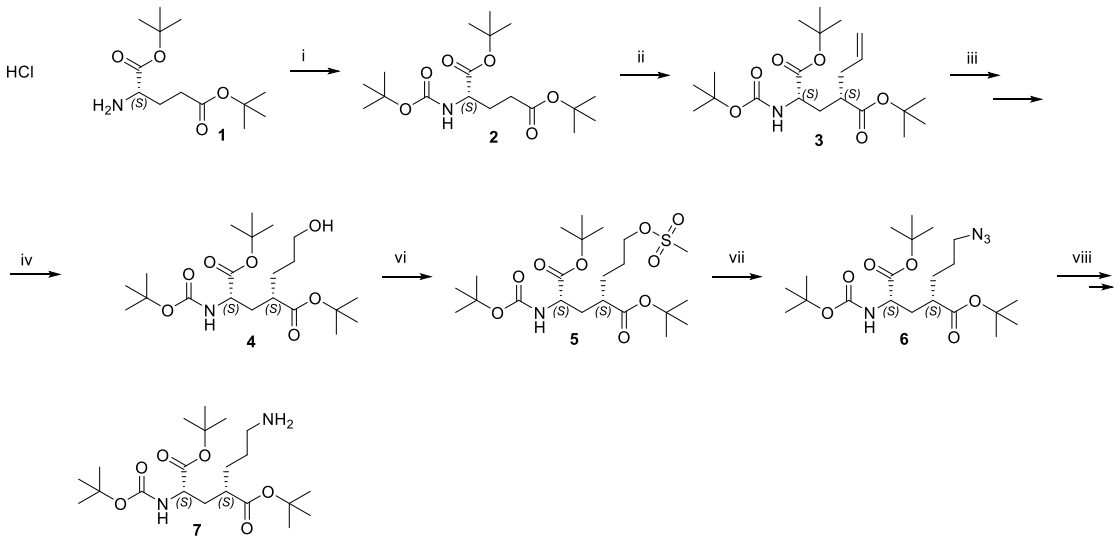


Scheme 4.2 Synthesis of the protected glutamate derivative 7. i) $Boc_2O$, DCM, O °C; ii) allyl bromide, LiHMDS, THF, -78 °C, inert atmosphere; iii) diboran/tetrahydrofuran, THF, inert atmosphere; iv) NaOH, $H_2O_2$, 0 °C; vi) MeCl, TEA, 0 °C, inert atmosphere; vii) $NaN_3$, DMF, 60 °C, inert atmosphere; viii) PPh3, Dioxane/MeOH 5:1, inert atmosphere.

The synthetic strategy that leads to BTA-AZO GLUTAMATE starts with the coupling between the protected glutamate unit 7 and scaffold 8, followed by the FMOC-group removal and the final convergent coupling to the core. The final step consists in removing Boc- and Tert-butyl- groups by acidic treatment.

Synthesis of Di-tert-butyl (4S)-2-(3-((S)-2-((((9H-fluoren-9-yl)methoxy)carbonyl)amino)-3-(4-((E) phenyldiazenyl)phenyl)propanamido)propyl)-4-((tert-butoxycarbonyl)amino)pentanedioate (9)

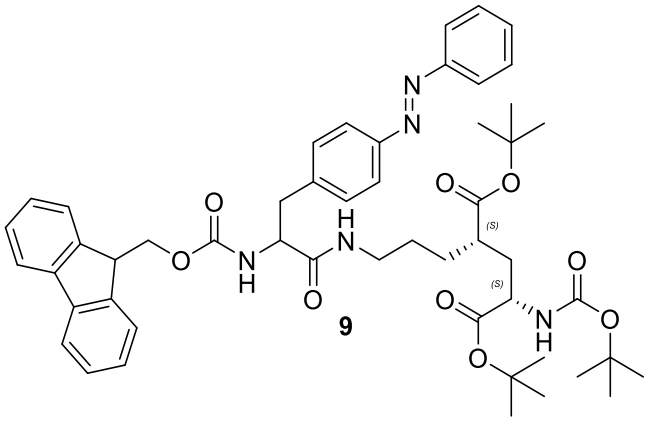

**9**

In a vial, compound 8 (40.12 mg, 81.62 μmol) and PyBOP (42.23 mg, 81.62 μmol) were dissolved in DCM (3 mL) and DMF (1.5 mL). The mixture was transferred into a flask and DIEA (42.65 μL, 244,63 μmol) was added.

Successively, compound 7 (34 mg, 81,62 μM) was dissolved in DCM (3 mL) and added to the mixture, which was left stirring at room temperature for one hour.

Then, the mixture was added with water, the organic phase was separated off, dried over $MgSO_4$ and evaporated, affording an orange oil.

The crude was purified over silica gel chromatography with a DCM /MeOH gradient (0à10%, TLCs in DCM/MeOH 95:5, Rf=0.7) to give an orange paste in 67% yield (48.4 mg, 54.38μmol).

HPLC-MS: 891 [M+H+]

Tr: 3.98

$^{1}$H NMR (400 MHz, CDCl3) δ 7.90 (d, J = 8.5 Hz, 2H), 7.85 (d, J = 8.3 Hz, 2H), 7.75 (d, 2H), 7.55 (dd, 2H), 7.50 (d, 2H), 7.49 – 7.46 (m, 1H), 7.42 – 7.34 (m, 4H), 7.30 (td, J = 7.5, 1.2 Hz, 3H), 6.55 (s, 1H), 5.53 (d, 1H), 5.04 (d, 1H), 4.54 – 4.46 (m, 1H), 4.42 (dd, J = 10.5, 7.0 Hz, 1H), 4.37 – 4.29 (m, 1H), 4.19 (t, J = 7.0 Hz, 1H), 4.15 – 4.09 (m, 1H), 3.37 (s, 1H), 3.18 (s, 2H), 3.01 (s, 1H), 2.27 (s, 1H), 1.81 – 1.69 (m, 2H), 1.46 – 1.43 (m, 5H), 1.43 – 1.39 (m, 27H).

$^{13}$C NMR (101 MHz, CDCl3) δ 174.73, 171.74, 156.10, 155.67, 152.82, 151.87, 143.98, 141.28, 131.08, 130.20, 129.57, 129.20, 128.87, 127.76, 127.23, 125.18, 123.22, 122.97, 120.54, 120.12, 81.03, 67.11, 56.24, 52.38, 51.05, 47.32, 41.64, 39.12, 37.94, 35.83, 28.48, 28.21, 28.11, 26.57.

Synthesis of Di-tert-butyl (4S)-2-(3-((S)-2-amino-3-(4-((E)-phenyldiazenyl)phenyl)propanamido) propyl)-4-((tert-butoxycarbonyl)amino)pentanedioate (10)

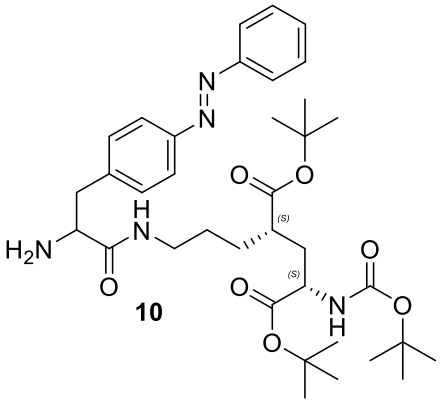

10

Into a nitrogen purged flask, compound 9 (48 mg, 53.93 µmol) was dissolved at 0° C in 6 mL CH3CN/piperidine 3:1 and the mixture was left stirring for one hour.

The solvent was evaporated under vacuum and the crude was taken up in water/DCM, the organic phase was separated off and washed three times with water. The organic phases was dried over MgSO4 and evaporated under vacuum.

The crude (orange powder) was purified over silica gel chromatography with a DCM/MeOH gradient (0à10%, TLCs in DCM/MeOH 95:5, Rf: 0.7) affording compound 10 in quantitative yield.

HPLC-MS: 668 ($M+H^+$)

Tr: 2.44 (cis) 2.62 (trans)

1H NMR (400 MHz, CDCl3) δ 7.92 – 7.89 (m, 2H), 7.87 (d, 2H), 7.54 – 7.46 (m, 3H), 7.38 (d, 2H), 4.94 (d, J = 9.1 Hz, 1H), 4.32 – 4.21 (m, 2H), 4.19 – 4.09 (m, 1H), 3.66 (dd, J = 9.2, 4.2 Hz, 1H), 3.34 (dd, J = 13.6, 4.4 Hz, 2H), 3.23 – 3.11 (m, 1H), 2.80 (dd, J = 13.7, 9.2 Hz, 1H), 2.38 – 2.27 (m, 1H), 1.87 – 1.79 (m, 2H), 1.72 (h, J = 6.2 Hz, 1H), 1.60 – 1.51 (m, 6H), 1.46 – 1.44 (m, 18H), 1.42 (s, 9H).

C13 recorded but not clear – ADD!

Synthesis of BTA-AZO-GLUTAMATE (12)

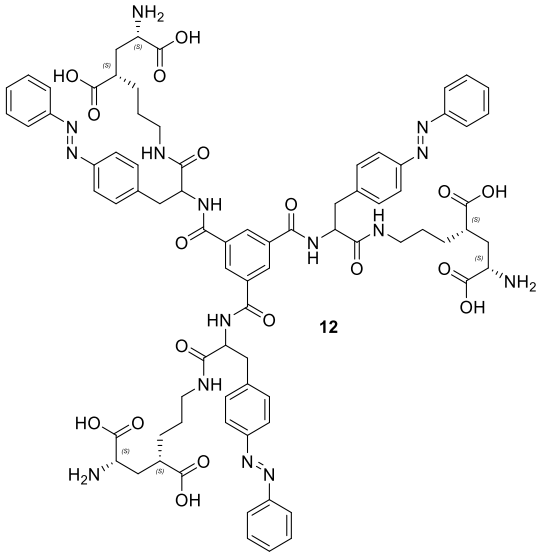

12

Compound 10 (37.3 mg, 55.85 µmol) was dissolved in 3 mL of $CHCl_3$ and stirred at 0° C. Triethylamine (23.35 µL, 167.55 µmol) was added dropwise and the mixture was left stirring for 3 minutes. 1,3,5-benzene-triacetyl chloride (3.71 mg, 13.96 µmol) was added dropwise and the reaction was left stirring overnight. The solvent was evaporated under vacuum and the crude was purified by silica gel chromatography over a DCM/MeOH gradient (0à10%, TLCs in DCM/MeOH 95:5, Rf:), affording an orange oil (27 mg, 12.50µmol, 90% yield).

Crude 11 (17.7 mg, 8.2 µmol) was dissolved in 1 mL of DCM, added with 3 mL of trifluoroacetic acid and diisopropylsilane (100 µL, 8.20 µmol). The reaction was stirred for 4 hours and monitored by HPLC-MS. TFA was removed by bubbling nitrogen over the mixture, that was subsequentially dried under vacuum.

The crude was purified by HPLC affording BTA-AZO-GLUTAMATE (12) into two fractions with two different retention times: 5.30 (0.7 mg) and 6.77 (1.7 mg). The two fractions were evaporated separately and collected into two vials.

Overall yield: 2.4 mg, 1.58 µmol, 19%.

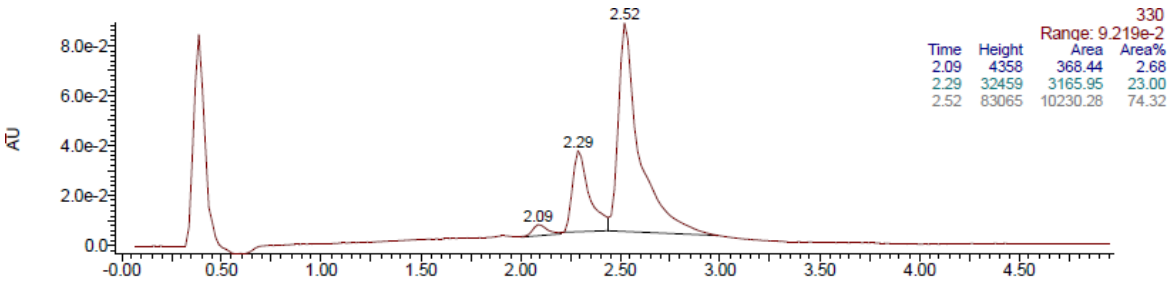

5.6 Chromatogram of BTA-AZO-GLUTAMATE wedge. Peak at 2.6 min corresponds to *E*-isomer, peak at 2.3 corresponds to the *Z*-isomer. ESI(+) of GFLG wedge. m/z: $[M+H]^+$= 1296.0

MALDI-TOF-MS (α-Cyano-4-hydroxycinnamic acid was used as a matrix): m/z: $[M+H]^+$= 1520,4 (Isotopic distribution can be observed). Calculated: $[M+H]^+$= 2521.

**Primary hippocampal cultures**

Procedures were performed in accordance with the European guidelines for animal care and use in research and were approved by the Animal Experimentation Ethics Committee at the University of Barcelona.

Sprague-Dawley rat pups (P 1-5) were sacrificed by decapitation, hippocampi were isolated and treated with 0,1% trypsin in HBSS (10 min, 37ºC). Neurons were plated on Poly-D-Lysine (PDL)-coated 16 mm coverslips (0.5-1 x $10^5$ cells) and incubated at 37ºC, 5% $CO_2$ for 1,5 hours (to allow cells adhesion) in MEM supplemented with heat-inactivated FBS (5%), heat-inactivated HS (5%), penstrep (10 UI/ml), L-glutamine (2mM) and glucose (20mM). Cells were cultured in Neurobasal A medium, supplemented with B-27 (5%), penstrep (5 UI/ml), glutaMAX (0,5x) and glucose (15mM). On DIV 3 cultured cells were treated with 1 μM of Ara-C to prevent proliferation of non-neuronal cells. 50% of the maintenance medium was exchanged every 4 days.

Before each experiment neurons were incubated in PBS solution containing 10 μM of OGB-1 AM calcium indicator (Thermofisher, USA) for 30 min at 37ºC and 5% $CO_2$. During imaging experiment neurons were maintained in the solution containing: 150 mM NaCl, 3 mM KCl, 1 mM $MgCl_2$, 2 mM $CaCl_2$, 10 mM HEPES, 10 mM D-glucose; pH 7.40-7.42. OGB-1 was excited with 488 nm light during 100 ms every 2 s.

**TSA201 cells culturing and transfection**

HEK TSA201 cells were maintained in Dulbecco´s Modified Eagle Medium: Nutrient Mixture F12 (DMEM/F12, 1:1, Life Technologies) with 10% Fetal Bovine Serum (FBS, Life Technologies) and 1% antibiotics (Pen/Strep, Sigma-Aldrich), at 37ºC and 5% $CO_2$ humidified atmosphere in the cell incubator. Cells were harvested using acutase (Sigma-Aldrich) and plated on 15 mm borosilicate glass coverslips (Fisher Scientific) pre-treated with Poly-L-Lysine (Sugma-Aldrich) to allow cell adhesion. Next day X-treme GENE 9 DNA Transfection Reagent (Roche Applied Science) was used to obtain cells transiently expressing M1 mAChRs and R-GECO1 calcium sensor. According to the manufacturer´s protocol total of 1 μg of cDNA and 3 μl of X-treme GENE 9 were mixed in a volume of 100 μl in culture medium free from FBS and P/S, and incubated during 20 min at RT. Calcium imaging experiments were held 48-55 hours after the transfection.

## 4.5 References

1. Mitchell, M. J.; Billingsley, M. M.; Haley, R. M.; Wechsler, M. E.; Peppas, N. A.; Langer, R. Engineering Precision Nanoparticles for Drug Delivery. Nat. Rev. Drug Discov. 2021, 20 (2), 101–124.

2. Farokhzad, O. C.; Langer, R. Impact of Nanotechnology on Drug Delivery. ACS Nano 2009, 3 (1), 16–20.
3. Hadinoto, K.; Sundaresan, A.; Cheow, W. S. Lipid–Polymer Hybrid Nanoparticles as a New Generation Therapeutic Delivery Platform: A Review. Eur. J. Pharm. Biopharm. 2013, 85 (3, Part A), 427–443.
4. Yao, Y.; Zhou, Y.; Liu, L.; Xu, Y.; Chen, Q.; Wang, Y.; Wu, S.; Deng, Y.; Zhang, J.; Shao, A. Nanoparticle-Based Drug Delivery in Cancer Therapy and Its Role in Overcoming Drug Resistance. Front. Mol. Biosci. 2020, 7.
5. Bao, G.; Mitragotri, S.; Tong, S. Multifunctional Nanoparticles for Drug Delivery and Molecular Imaging. Annu. Rev. Biomed. Eng. 2013, 15, 253–282.
6. Raemdonck, K.; Braeckmans, K.; Demeester, J.; Smedt, S. C. D. Merging the Best of Both Worlds: Hybrid Lipid-Enveloped Matrix Nanocomposites in Drug Delivery. Chem. Soc. Rev. 2013, 43 (1), 444–472.
7. Matson, J. B.; Stupp, S. I. Drug Release from Hydrazone-Containing Peptide Amphiphiles. Chem. Commun. 2011, 47 (28), 7962–7964.
8. Moyer, T. J.; Finbloom, J. A.; Chen, F.; Toft, D. J.; Cryns, V. L.; Stupp, S. I. PH and Amphiphilic Structure Direct Supramolecular Behavior in Biofunctional Assemblies. J. Am. Chem. Soc. 2014, 136 (42), 14746–14752.
9. Su, H.; Koo, J. M.; Cui, H. One-Component Nanomedicine. J. Control. Release Off. J. Control. Release Soc. 2015, 219, 383–395.
10. Cheetham, A. G.; Chakroun, R. W.; Ma, W.; Cui, H. Self-Assembling Prodrugs. Chem. Soc. Rev. 2017, 46 (21), 6638–6663.
11. Lu, J.; Liu, C.; Wang, P.; Ghazwani, M.; Xu, J.; Huang, Y.; Ma, X.; Zhang, P.; Li, S. The Self-Assembling Camptothecin-Tocopherol Prodrug: An Effective Approach for Formulating Camptothecin. Biomaterials 2015, 62, 176–187.
12. Wang, Y.; Cheetham, A. G.; Angacian, G.; Su, H.; Xie, L.; Cui, H. Peptide–Drug Conjugates as Effective Prodrug Strategies for Targeted Delivery. Adv. Drug Deliv. Rev. 2017, 110–111, 112–126.
13. Wang, F.; Porter, M.; Konstantopoulos, A.; Zhang, P.; Cui, H. Preclinical Development of Drug Delivery Systems for Paclitaxel-Based Cancer Chemotherapy. J. Controlled Release 2017, 267, 100–118.
14. Cheetham, A. G.; Zhang, P.; Lin, Y.-A.; Lin, R.; Cui, H. Synthesis and Self-Assembly of a Mikto-Arm Star Dual Drug Amphiphile Containing Both Paclitaxel and Camptothecin. J. Mater. Chem. B 2014, 2 (42), 7316–7326.
15. Zhang, P.; Cheetham, A. G.; Lin, Y.; Cui, H. Self-Assembled Tat Nanofibers as Effective Drug Carrier and Transporter. ACS Nano 2013, 7 (7), 5965–5977.
16. Wang, H.; Wei, J.; Yang, C.; Zhao, H.; Li, D.; Yin, Z.; Yang, Z. The Inhibition of Tumor Growth and Metastasis by Self-Assembled Nanofibers of Taxol. Biomaterials 2012, 33 (24), 5848–5853.
17. Gao, Y.; Kuang, Y.; Guo, Z.-F.; Guo, Z.; Krauss, I. J.; Xu, B. Enzyme-Instructed Molecular Self-Assembly Confers Nanofibers and a Supramolecular Hydrogel of Taxol Derivative. J. Am. Chem. Soc. 2009, 131 (38), 13576–13577.
18. Su, H.; Zhang, W.; Wang, H.; Wang, F.; Cui, H. Paclitaxel-Promoted Supramolecular Polymerization of Peptide Conjugates. J. Am. Chem. Soc. 2019, 141 (30), 11997–12004.

19. Ma, W.; Su, H.; Cheetham, A. G.; Zhang, W.; Wang, Y.; Kan, Q.; Cui, H. Synergistic Antitumor Activity of a Self-Assembling Camptothecin and Capecitabine Hybrid Prodrug for Improved Efficacy. J. Controlled Release 2017, 263, 102–111.
20. Mao, L.; Wang, H.; Tan, M.; Ou, L.; Kong, D.; Yang, Z. Conjugation of Two Complementary Anti-Cancer Drugs Confers Molecular Hydrogels as a Co-Delivery System. Chem. Commun. 2011, 48 (3), 395–397.
21. Vemula, P. K.; Cruikshank, G. A.; Karp, J. M.; John, G. Self-Assembled Prodrugs: An Enzymatically Triggered Drug-Delivery Platform. Biomaterials 2009, 30 (3), 383–393.
22. Yang, C.; Li, D.; FengZhao, Q.; Wang, L.; Wang, L.; Yang, Z. Disulfide Bond Reduction-Triggered Molecular Hydrogels of Folic Acid–Taxol Conjugates. Org. Biomol. Chem. 2013, 11 (40), 6946–6951.
23. Cheetham, A. G.; Ou, Y.-C.; Zhang, P.; Cui, H. Linker-Determined Drug Release Mechanism of Free Camptothecin from Self-Assembling Drug Amphiphiles. Chem. Commun. 2014, 50 (45), 6039–6042.
24. Bakker, M. H.; Lee, C. C.; Meijer, E. W.; Dankers, P. Y. W.; Albertazzi, L. Multicomponent Supramolecular Polymers as a Modular Platform for Intracellular Delivery. ACS Nano 2016, 10 (2), 1845–1852.
25. Hansen, K. B.; Wollmuth, L. P.; Bowie, D.; Furukawa, H.; Menniti, F. S.; Sobolevsky, A. I.; Swanson, G. T.; Swanger, S. A.; Greger, I. H.; Nakagawa, T.; McBain, C. J.; Jayaraman, V.; Low, C.-M.; Dell'Acqua, M. L.; Diamond, J. S.; Camp, C. R.; Perszyk, R. E.; Yuan, H.; Traynelis, S. F. Structure, Function, and Pharmacology of Glutamate Receptor Ion Channels. Pharmacol. Rev. 2021, 73 (4), 1469–1658.
26. Meldrum, B. S. Glutamate as a Neurotransmitter in the Brain: Review of Physiology and Pathology. J. Nutr. 2000, 130 (4), 1007S-1015S.
27. Volgraf, M.; Gorostiza, P.; Szobota, S.; Helix, M. R.; Isacoff, E. Y.; Trauner, D. Reversibly Caged Glutamate: A Photochromic Agonist of Ionotropic Glutamate Receptors. J. Am. Chem. Soc. 2007, 129 (2), 260–261.
28. Agnetta, L.; Bermudez, M.; Riefolo, F.; Matera, C.; Claro, E.; Messerer, R.; Littmann, T.; Wolber, G.; Holzgrabe, U.; Decker, M. Fluorination of Photoswitchable Muscarinic Agonists Tunes Receptor Pharmacology and Photochromic Properties. J. Med. Chem. 2019, 62 (6), 3009–3020.
29. M. Bose, D. Groff, J. Xie, E. Brustad, and P. G. Schultz. The Incorporation of a Photoisomerizable Amino Acid into Proteins in E. coli, J. Am. Chem. Soc. 2006, 128 (2), 388-389.
30. W. Li, I. Park, S.-K. Kang, and M. Lee,. Smart hydrogels from laterally-grafted peptide assembly, Chem. Commun., 2012, 48 (70), 8796-8798.
31. EP 2 322 171 A2

.

# Chapter 5 | Creating specificity towards cancer: Enzyme responsive discotic amphiphiles

## 5.1 Introduction

So far, we developed a system that exhibits responsiveness to different stimuli and whose robustness can be tuned. In **chapter 4** we demonstrate that our system can internalize biologically active molecules and release them employing UV light. This is a relevant proof-of-concept for discotic amphiphiles, however its practical application for cancer drug delivery is quite challenging because of the high light power required for release, the low light penetration in tissues (useful only for superficial areas) and the complexity of the proceedings which require specific instrumentation.[1-4]

Another possibility to achieve local activation consists of modifying the system to make it reactive to cancer. Cancer tissues are known to develop an anomalous metabolism, growth and expansion regime, that is possible because of an abnormal regulation of specific proteins, like membrane receptors.[5] As these biomolecules are found in higher concentrations than in healthy tissues, they sometimes can be used to direct the therapeutic action.[6-8] Here, two approaches can be envisioned:

- Targeting surface proteins: It involves the recognition and interaction between the therapeutic and the protein, leading to an accumulation or internalization. The most investigated proteins include transferrin receptor, EGFR, glycoproteins and folate receptor.[9]
- Targeting enzymes: It requires to design a protherapeutic to become a substrate for an overexpressed enzyme.[10] After hydrolytic action, the protherapeutic is locally activated increasing the local concentration of the drug. The same strategy has been combined with self-assembly, just by synthesising a monomer that includes a group or sequence reactive to an overexpressed enzyme in cancer.

Interestingly, the location of the sequence inside the assembly is critical to define the supramolecular response to the enzyme. Depending on where the responsive sequence is placed and its role in self-assembly, the output will change dramatically. We can distinguish two approaches:

- Sequence as hydrophilic part: the loss of a hydrophilic part provokes an enhanced self-assembly, structure growth or uncontrolled aggregation. Which it has been reported to promote an increased aggregation, accumulation and retention.[11-15] This strategy is sometimes called assembly-induced retention.
- Sequence in hydrophobic part: Cleavage disrupts completely the self-assembly of the supramolecular structure.[16,17]

As long as the field was growing, it encountered a major challenge. Enzyme activity on supramolecules depends on supramolecular stability. Again, making a system robust and yet responsive is not trivial and a most wanted in the field. The Amir group thoroughly studied the

enzymatic degradation of micelles of different hydrophilic-hydrophobic ratios, molecular weights and shapes.[18-21] They systematically showed hoe high stability is inversely related with lower or inexistant enzymatic degradation. Interestingly, they show that monomers in the aggregated state are not accessible for enzymes, enzymatic cleavage happens in solution and degradation depends on monomer re-equilibration.[22] This is very interesting because enzymes can only interact with the surface of the micelles or with free monomers.

From this perspective, two approaches have appeared to overcome the situation. Departing from the self-immolative polymers concept, a depolymerization mechanisms of hydrophobic domains from hydrophilic group cleavage have been envisioned. This mechanism have been called chain unzipping, and it requires a very specific molecular design that undergoes an electronic cascade upon a single bond cleavage.[23-25] Another strategy, proposed by the Amir group, consist of a multi responsive approach in which micelles possess two states, the first in which monomers are free to exchange with the medium and hence are cleavable by enzymes, and a second in which monomers cannot exchange so freely. They achieved this second state either by introducing an entropic penalty either by dimerizing the monomers or by isomerizing to a more hydrophobic configuration.[26,27] Even though the potential applicability of this strategy, new alternatives are also very appealing to explore.

Apparently, one of the inconveniences of micelles, vesicles or even worm-like micelles is their intrinsic surface isotropy. On this regard, discotic fibres have "sharper" ends and could potentially have a different interaction with enzymes. According to recent findings, BTA based fibres are formed by the coiling of two individual fibres, each one formed by the stacking of individual monomers.[28] Even though it is still unknown how the ends of the fibres are, it is possible that the ends of the fibres are quite abrupt, making the monomers more accessible to enzymes. These make fibres very appealing for enzymatic degradation even if the self-assembly is very strong.

For these reasons, we adapted our previous systems to explore the potential enzyme responsiveness of discotic fibres. To do so, we have designed a discotic amphiphile that contains an enzyme degradable peptide as part of the hydrophobic domain.

## 5.2 Results and discussion

### 5.2.1 Molecular design and synthesis

For this project, our previous system must be adapted to include an enzyme responsive moiety, that upon cleavage will trigger a major change in self-assembly. For this reason, we decided to use the well-known GFLG sequence, a hydrophobic tetrapeptide substrate of Cathepsin B.

Cathepsin B is a lysosomal cysteine protease known to be upregulated in different types of cancer and have been correlated with invasion and metastasis.[29,30] Even though cathepsin B is a lysosomal enzyme, in cancer tissue it is excreted, by a still unknown mechanism, and accumulated in the extracellular matrix (ECM). Here, cathepsin B can hydrolyse specific ECM proteins in addition to

promote the activity of some other ECM proteases like matrix-metalloproteinases by inactivating their inhibitors.[31]

The sequence GLFG (Gly-Phe-Leu-Gly) is a known substrate for Cathepsin B and it have been successfully used under different scenarios to trigger a response to the enzyme.[10,32] So, it appears as an ideal candidate to be implemented in our discotic design to confer responsiveness to enzymes.

As GFLG is a small and hydrophobic, we could place it in the backbone of our previous C0 design at junction between the hydrophobic and hydrophilic parts (Fig. 5.1). By these means, we obtain a monomer keeping the BTA and azobenzene moieties to drive self-assembly and introduce light responsiveness. The hydrophobic peptide GFLG would reinforce self-assembly and give responsiveness to Cathepsin B. Finally, octaethylene glycol and lysine would offer great water solubility and an anchoring point for posterior functionalizations.

This monomer was designed with the intention to obtain photocontrol on the self-assembly and responsiveness against Cathepsin B. By this means we can study the difference in the enzymatic activity of the *E* and *Z* configurations (presumably, in the assembled and non-assembled state).

Additionally, this design offers the possibility to co-assemble it with a monomer-drug conjugate, having the drug internalized within the structure when assembled and expose the drug upon enzymatic cleavage.

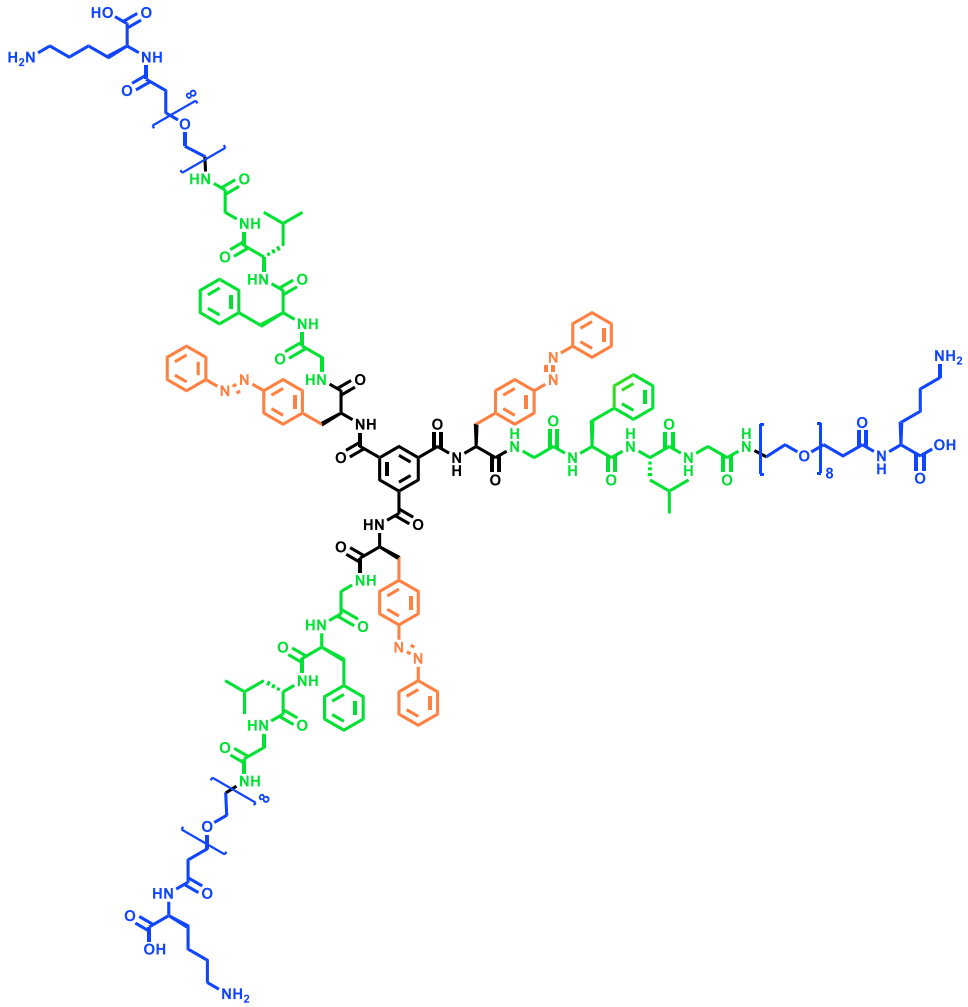

Figure 5.1 Molecular structure of BTA-GFLG. The GFLG sequence is highlighted in green.

The peptidic nature of the monomer allowed to use the same strategy of previous chapters. The amphiphilic wedge is grown by solid phase peptide synthesis, and then is coupled to the core in solution. However, this time the purification was more challenging. The crude of the final reaction was formed by a mixture of the target monomer (trimer) and the uncomplete trimer (dimer), and other minor impurities. This crude was first purified using a semipreparative HPLC, obtaining a mixture of dimer and trimer. After some optimization, the crude was then purified using an analytical HPLC to achieve better separation. Even though the time and the effort put, the crude still contained a large fraction of dimer. The fraction of monomer corresponded to 67.56% of the crude, while the dimer forms the remaining 32.44%.

The purification methods must be improved in order to obtain pure fraction of the molecule. One possibility that will be tested in the future is direct phase silica gel. It is likely that the different amount of charges of the dimer comparing with the trimer make them separate better in a direct phase chromatography.

Another challenge is the chemical stability. Along the purification, that lasted few months, we could observe a shift in the mass of both the molecule and the impurity. Initially, after the first

purification we observed the calculated mass (3746.4 Da), but after few months the observed mass increased by +52 Da, both of the monomer and dimer. The origin of this change is still unknown and will have to be addressed.

Despite all these drawbacks and hypothesising the molecules could maintain some of the original properties they were designed for, we performed some preliminary experiments with this mixture.

### 5.2.2 Self-assembly characterization

We started with a set of TEM assays, in which the self-assembly and the responsiveness to light was tested. Extraordinarily, we could observe μm long fibres of around 12 nm in thickness (Fig. 5.2). Interesting, fibres are thicker than C8, longer and present some degree of entanglement.

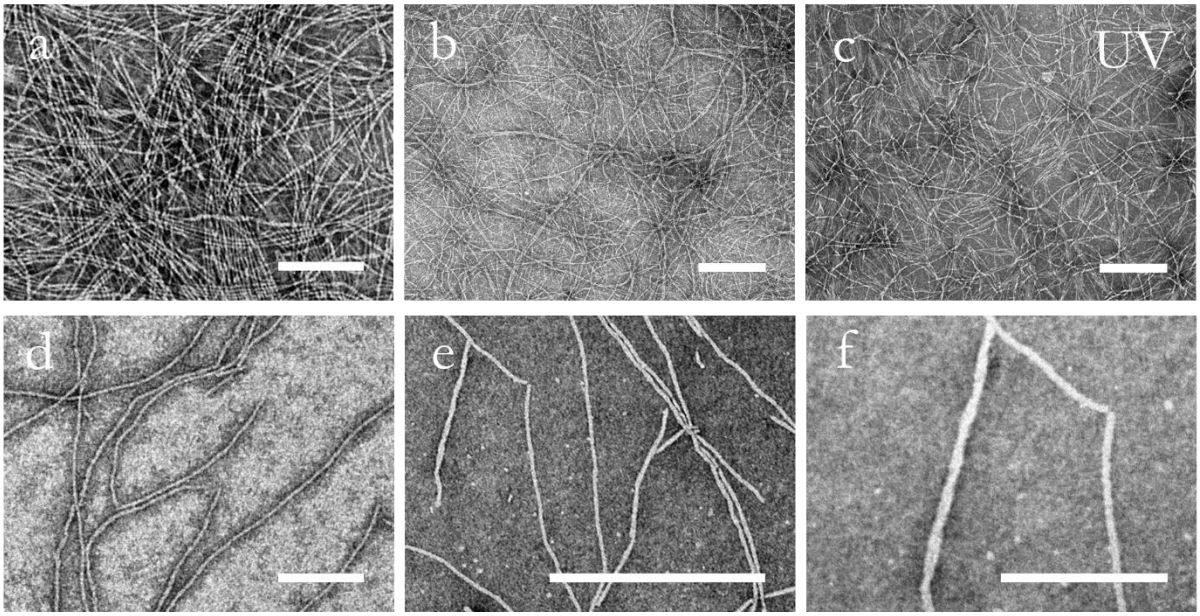


Figure 5.2 TEM of sample in water at 200 μM (a), 100 μM (b), 100 μM UV irradiated (c) and 25 μM (d, e and f). Scale bar: 200 nm for a, d, e and f. 500 nm for b and c. Irradiation conditions: 365 nm, 1000 mA at 100% of the LED intensity for 5 min.

After irradiation with UV light, we could observe a mild decrease in the number of fibres. This result indicates a high stability of the supramolecular polymer, comparable o even higher to the one displayed by C8. It is interesting to mention that at the tested concentrations we could not observe a big difference between irradiated and non-irradiated samples.

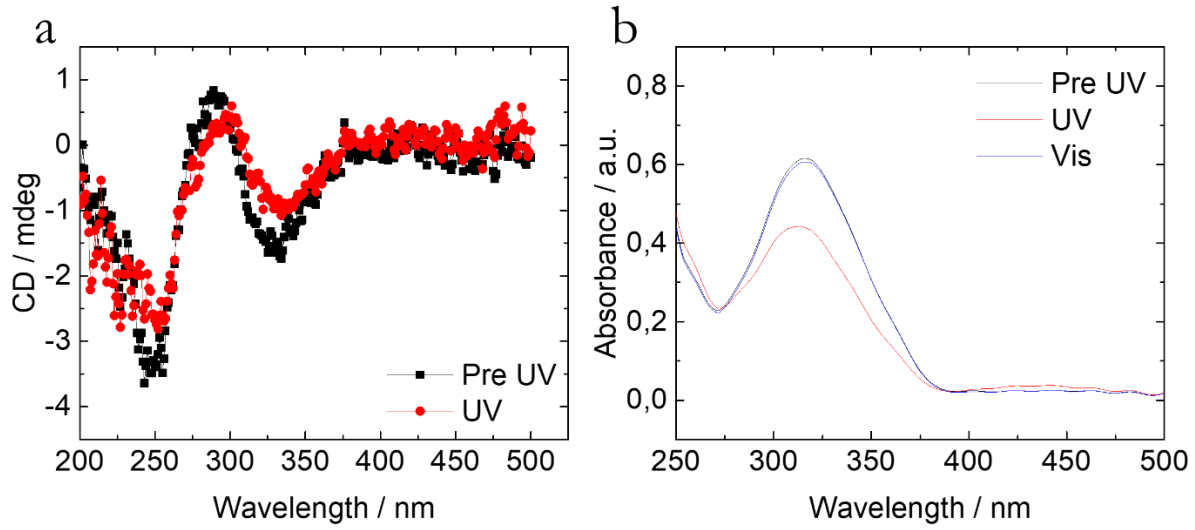


Figure 5.3 CD spectra (a) and absorbance spectra (b) of sample at 25 μM in water before and after irradiation with UV. Irradiation conditions: 365 nm, 1000 mA at 100% of the LED intensity for 5 min.

CD and UV-Vis spectroscopies are performed to observe the stacking signal of the monomer and its responsiveness to light (Fig. 5.3). CD shows a negative cotton effect, like the observed for C8 at room temperature or C0/C4 at high temperatures, that in both cases we assigned to a high stability state. Interestingly, this time we observed a strong negative band at 250 nm, that we could see before. After irradiation with UV light, only a very mild reduction in the signal is observed, reinforcing the low response to light obtained by TEM. Absorbance shows results in accordance to CD, very low isomerization by UV irradiation, but additionally it shows some reversibility.

Altogether, these preliminary results show thick fibres, of high stability and very low responsiveness to light.

### 5.2.3 Enzymatic degradability

Finally, we tested the enzymatic degradability of the crude using Cathepsin B. Two samples of BTA-GFLG at 200 μM, being the first UV irradiated while the second not, before being mixed with a solution of cathepsin B. The assay was analysed by HPLC, showing in both cases a similar behaviour. Apparently, enzymatic degradability happened exclusively on the dimer but not on the trimer. This could have very interesting implications, that at this point can only be speculative. Dimer being cleaved by the Cathepsin B is exposing that the GFLG sequence is a good substrate even if it's found in the monomer backbone. The lack of responsiveness of the trimer, which is probably the fraction in charge of self-assembly, leaves open very interesting questions. Is the trimer a good substrate for cathepsin B? If so, is cathepsin B cleaving the free monomer but it cannot access the assembled monomers from the ends?

These two questions could be answered easily performing more experiments. The firsts question could be answered by disassembling the fibres. Unfortunately, these polymers do not seem responsive to the azobenzene isomerization, and we could not study the enzymatic degradation of

disassembled monomers. However, this question could be answered with few FRET experiments yielding information about the monomer exchange.

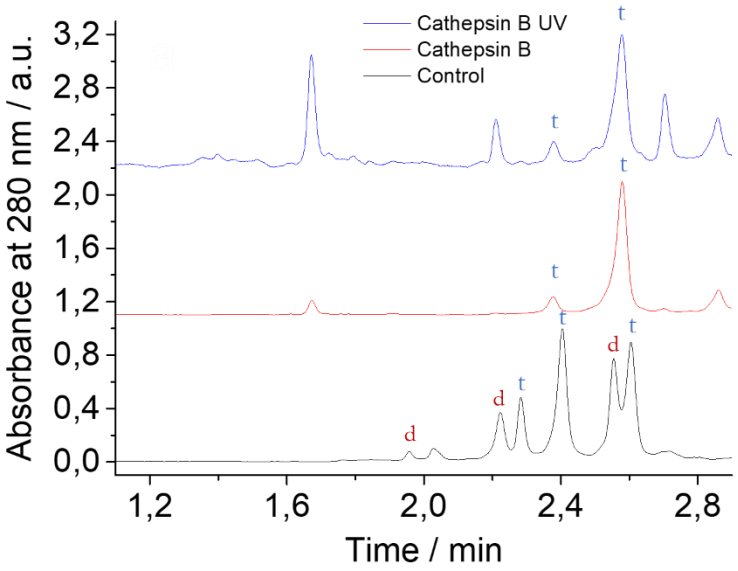


Figure 5.4. Enzymatic degradation of BTA-GFLG. HPLC traces of BTA-GFLG (black), BTA-GFLG in the presence of Cathepsin B at 0.5 u/mL without UV pre-irradiation (red) and with UV pre-irradiation (blue). Irradiation conditions: 365 nm, 1000 mA at 100% of the LED intensity for 5 min. Trimer is indicate with a t, and dimer is indicated with a d. Remaining peaks could not be identified.

If monomer is exchanged, like in the case of C0, then it implies that free monomer is not a good substrate for cathepsin B. However, if monomer does not exchange, like in the case of C8, and the low UV responsiveness points towards this option, then two options remain open: or trimer is not a good substrate or the enzyme only cleaves free monomer (no re-equilibration) without being able to access the assembled monomer, even at the ends. It is worth to remember that these fibres are thicker than their predecessors, what could indicate that the fibres are formed by several fibres bundled/twisted, and this could have an impact on the end morphology.

Nevertheless, it must be reiterated that even though these experiments are very exciting, they are very preliminary and should be repeated and expanded with a pure fraction of the monomer to be valid.

## 5.3 Conclusions

The synthesis of BTA-GFLG monomer is feasible, but purification methods must be improved to remove dimer impurities or synthetic route must be changed to avoid the formation of the dimer impurities.

Interestingly, the final crude mixture showed a strong self-assembly into fibres of around 12 nm in thickness and -µm in length. CD displayed a similar signal for stacked azobenzene comparing to C8, suggesting a strong self-assembly. Likewise, UV response seems comparable to the one of C8.

Finally, assays with cathepsin B showed degradation of dimer, but not of trimer. Whether the trimer is a good substrate for cathepsin B, or if BTA-GFLG is a dynamic supramolecular fibre is still unknown. These preliminary assays must be repeated and expanded with a pure fraction in order to extract robust conclusions

## 5.4 Materials and methods

### 5.4.1 Materials

All solvents, unless stated otherwise, were obtained from commercial sources in at least analytical quality (a.r.) and were used without further purification. Ultrapure water was obtained from a Milli Pore system from Merck. Lysine and 2-Chlorotrityl chloride resin were obtained from Iris biotech. Fmoc-$PEG_8$-OH and PyBOP were purchased from Chempep. DIEA, piperidine, formic acid and benzene tricarbonyl trichloride were obtained from Sigma-Aldrich.

L-Phenylalanine-4'-azobenzene was synthesised following the procedure reported before.[35,36] Synthesis performed by Dr. José Augusto Berrocal.

### 5.4.2 Instrumentation

**UV-Vis**

Measurements were performed with a Tecan infinite M200Pro microplate reader using a quartz cuvette of 1 cm of pathlength. Spectra were taken from 250 nm to 500 nm at every 3 nm.

**Reverse Phase-High Performance Liquid Chromatography**

During synthesis and characterization of the monomers, measurements were recorded on a HPLC Waters e2695 separation module equipped with Photodiode Array detector Waters 2998 and Mass spectrometer QDA detector Acquity. A XSelect CSH C183.5 µm 4.6x50mm was used. Water 0.1% HCOOH and ACN 0.1% HCOOH were used as eluents. A gradient of 25-45% ACN in water was applied in 3.5 min. The elution speed was kept at 1.6 $ml \cdot min^{-1}$ and the temperature was maintained at 50 °C. The injection volume was 10 µl.

**Transmission Electron Microscopy**

Images were taken with Jeol JEM 1010 MT electron microscope (Japan), operating at 80 kV. Images were obtained on a CCD camera Megaview III (ISIS), MNnster, Germany.

**Negative staining**

Samples were deposited onto C-only grids (pre-treated with glow discharge for 30 s) for 1.5 min. The solution was washed with water for 30 s, and finally it was negatively stained with uranyl acetate 2% during 1.5 min. The excess of solution was blotted with a filtering paper and the grids were stored in the desiccator.

**Circular Dichroism**

Spectra was recorded on a Jasco J815 spectrometer, equipped with a JASCO Peltier PFD-425S/15 with a range of 263–383 K. A sealable quartz cell with a pathlength of 10 mm was used. The spectra were recorded continuously between 500-200 nm at every 0.1 nm, with a sensitivity of 100 mdeg, at 100 nm/min. The response time was set to 0.25s. The temperature was kept at 20 °C

**$^1$H-NMR**

$^1$H NMR spectra were recorded on a Varian Mercury Vx 400 MHz. Chemical shifts are given in ppm (δ) values relative to tetramethylsilane (TMS).

## 5.4.3 Methods

**Chemical synthesis**

The synthetic strategy and protocols are the same as described in the methods section of chapter 2. It consisted of growing the wedge on a polymeric support (Solid Phase Peptide Synthesis), the subsequent cleavage from the solid and the final convergent coupling to the core in solution.

**GFLG wedge**

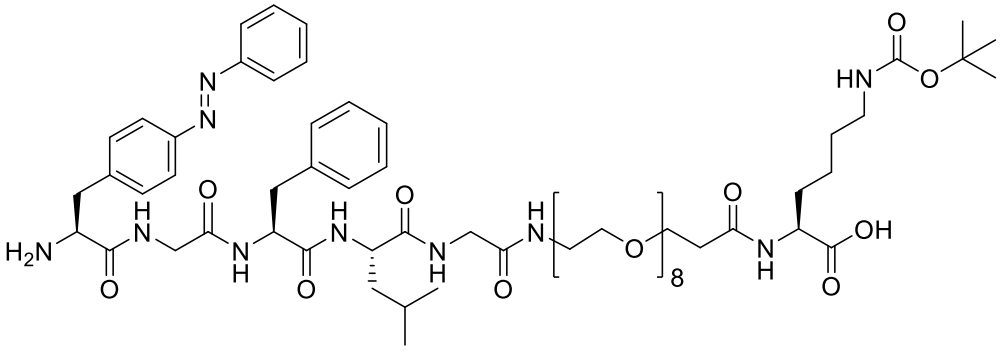


5.5 Molecular structure of BTA-GFLG wedge. MW: 1295.5

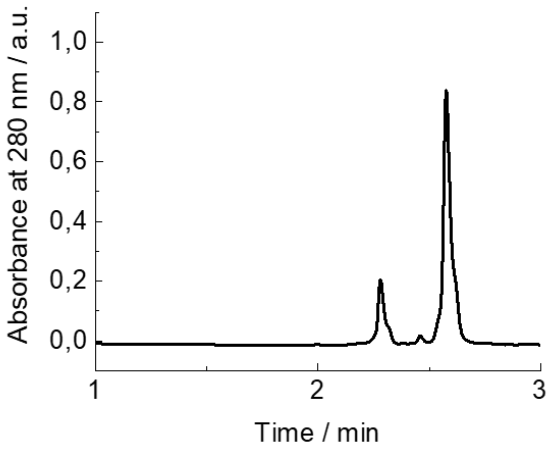


5.6 Chromatogram of BTA-GFLG wedge. Peak at 2.6 min corresponds to *E*-isomer, peak at 2.3 corresponds to the *Z*-isomer. ESI(+) of GFLG wedge. m/z: $[M+H]^+$= 1296.0, $[M+2H]^{2+}$= 648.6. Calculated: m/z: $[M+H]^+$=1296.5, $[M+2H]^{2+}$= 648.75.

**BTA-GFLG monomer**

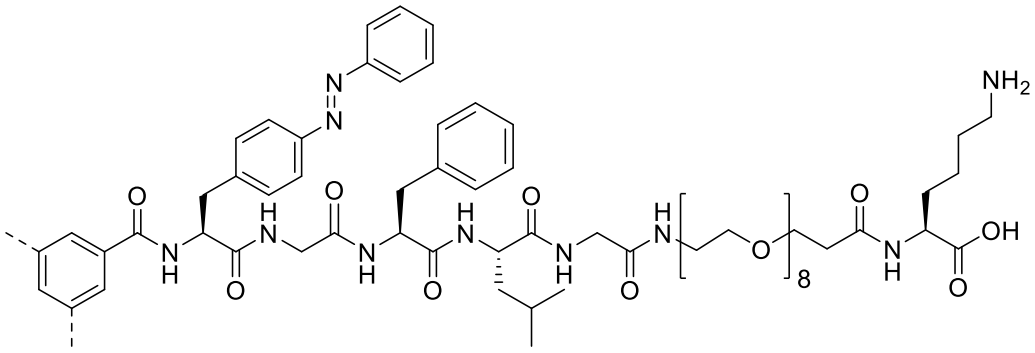


5.7 Molecular structure of BTA-GFLG monomer. MW: 3742.4.

**Enzymatic cleavage assay**

The solvent used for the preparation of the sample and Cathepsin B was a buffer of 50 mM Sodium Acetate, 30 mM Ditiotreitol, 1 mM EDTA dissolved in Milli Q. pH was adjusted to 5.[33,34] Samples of BTA-GFLG prepared at 200 μM were preheated at 37 ºC and mixed with a Cathepsin B solution to a final concentration of 0.5 u/mL. then, mixtures were incubated overnight at 37 ºC. Controls consisted on the same procedure but without the addition of Cathepsin B. UV sample was irradiated right before the mixture with Cathepsin B.

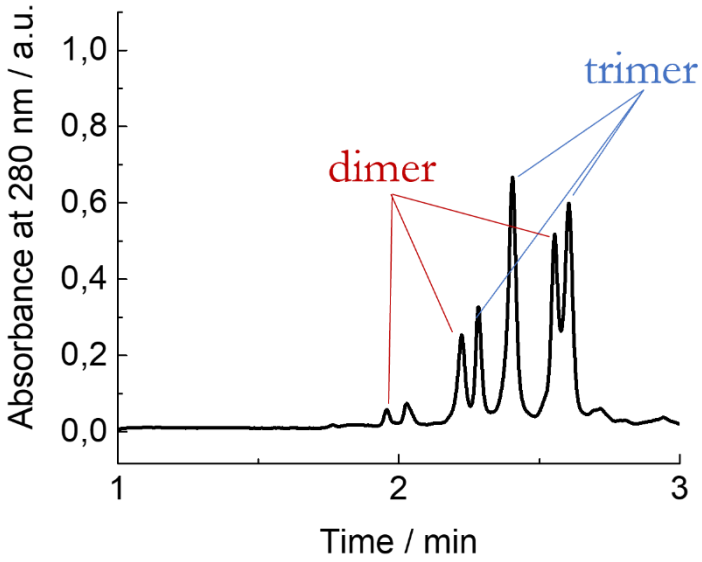


5.8 RP-HPLC at 280 nm of BTA-GFLG after second purification.

ESI-MS deconvoluted for monomer(+): 3794.4. Calculated mass: 3742.4.

ESI-MS deconvoluted for dimer(+): 2616.4. Calculated mass: 2564.9.

## 5.5 References


1. Correia, J. H.; Rodrigues, J. A.; Pimenta, S.; Dong, T.; Yang, Z. Photodynamic Therapy Review: Principles, Photosensitizers, Applications, and Future Directions. Pharmaceutics 2021, 13 (9), 1332.
2. Meinhardt, M.; Krebs, R.; Anders, A.; Heinrich, U.; Tronnier, H. Wavelength-Dependent Penetration Depths of Ultraviolet Radiation in Human Skin. J. Biomed. Opt. 2008, 13 (4), 044030.
3. Velema, W. A.; Szymanski, W.; Feringa, B. L. Photopharmacology: Beyond Proof of Principle. J. Am. Chem. Soc. 2014, 136 (6), 2178–2191.
4. Zhang, Y.; Xu, C.; Yang, X.; Pu, K. Photoactivatable Protherapeutic Nanomedicine for Cancer. Adv. Mater. 2020, 32 (34), 2002661.
5. Martínez-Reyes, I.; Chandel, N. S. Cancer Metabolism: Looking Forward. Nat. Rev. Cancer 2021, 21 (10), 669–680.
6. Bertrand, N.; Wu, J.; Xu, X.; Kamaly, N.; Farokhzad, O. C. Cancer Nanotechnology: The Impact of Passive and Active Targeting in the Era of Modern Cancer Biology. Adv. Drug Deliv. Rev. 2014, 66, 2–25.
7. Peer, D.; Karp, J. M.; Hong, S.; Farokhzad, O. C.; Margalit, R.; Langer, R. Nanocarriers as an Emerging Platform for Cancer Therapy. Nat. Nanotechnol. 2007, 2 (12), 751–760.

8. Manzari, M. T.; Shamay, Y.; Kiguchi, H.; Rosen, N.; Scaltriti, M.; Heller, D. A. Targeted Drug Delivery Strategies for Precision Medicines. Nat. Rev. Mater. 2021, 6 (4), 351–370.
9. Bazak, R.; Houri, M.; El Achy, S.; Kamel, S.; Refaat, T. Cancer Active Targeting by Nanoparticles: A Comprehensive Review of Literature. J. Cancer Res. Clin. Oncol. 2015, 141 (5), 769–784.
10. Sun, I.-C.; Yoon, H. Y.; Lim, D.-K.; Kim, K. Recent Trends in In Situ Enzyme-Activatable Prodrugs for Targeted Cancer Therapy. Bioconjug. Chem. 2020, 31 (4), 1012–1024.
11. Yang, P.-P.; Luo, Q.; Qi, G.-B.; Gao, Y.-J.; Li, B.-N.; Zhang, J.-P.; Wang, L.; Wang, H. Host Materials Transformable in Tumor Microenvironment for Homing Theranostics. Adv. Mater. 2017, 29 (15), 1605869.
12. Nguyen, M. M.; Carlini, A. S.; Chien, M.-P.; Sonnenberg, S.; Luo, C.; Braden, R. L.; Osborn, K. G.; Li, Y.; Gianneschi, N. C.; Christman, K. L. Enzyme-Responsive Nanoparticles for Targeted Accumulation and Prolonged Retention in Heart Tissue after Myocardial Infarction. Adv. Mater. 2015, 27 (37), 5547–5552.
13. Cheng, D.-B.; Wang, D.; Gao, Y.-J.; Wang, L.; Qiao, Z.-Y.; Wang, H. Autocatalytic Morphology Transformation Platform for Targeted Drug Accumulation. J. Am. Chem. Soc. 2019, 141 (10), 4406–4411.
14. Zhang, D.; Qi, G.-B.; Zhao, Y.-X.; Qiao, S.-L.; Yang, C.; Wang, H. In Situ Formation of Nanofibers from Purpurin18-Peptide Conjugates and the Assembly Induced Retention Effect in Tumor Sites. Adv. Mater. 2015, 27 (40), 6125–6130.
15. Feng, Z.; Wang, H.; Zhou, R.; Li, J.; Xu, B. Enzyme-Instructed Assembly and Disassembly Processes for Targeting Downregulation in Cancer Cells. J. Am. Chem. Soc. 2017, 139 (11), 3950–3953.
16. Shahriari, M.; Zahiri, M.; Abnous, K.; Taghdisi, S. M.; Ramezani, M.; Alibolandi, M. Enzyme Responsive Drug Delivery Systems in Cancer Treatment. J. Controlled Release 2019, 308, 172–189.
17. Kumar, V.; Koyasseril-Yehiya, T. M.; Thayumanavan, S. Enzyme-Triggered Nanomaterials and Their Applications. In Molecular Assemblies: Characterization and Applications; ACS Symposium Series; American Chemical Society, 2020; Vol. 1355, pp 95–107.
18. Slor, G.; Papo, N.; Hananel, U.; Amir, R. J. Tuning the Molecular Weight of Polymeric Amphiphiles as a Tool to Access Micelles with a Wide Range of Enzymatic Degradation Rates. Chem. Commun. 2018, 54 (50), 6875–6878.
19. Segal, M.; Ozery, L.; Slor, G.; Wagle, S. S.; Ehm, T.; Beck, R.; Amir, R. J. Architectural Change of the Shell-Forming Block from Linear to V-Shaped Accelerates Micellar Disassembly, but Slows the Complete Enzymatic Degradation of the Amphiphiles. Biomacromolecules 2020, 21 (10), 4076–4086.
20. Segal, M.; Avinery, R.; Buzhor, M.; Shaharabani, R.; Harnoy, A. J.; Tirosh, E.; Beck, R.; Amir, R. J. Molecular Precision and Enzymatic Degradation: From Readily to Undegradable Polymeric Micelles by Minor Structural Changes. J. Am. Chem. Soc. 2017, 139 (2), 803–810.
21. Harnoy, A. J.; Buzhor, M.; Tirosh, E.; Shaharabani, R.; Beck, R.; Amir, R. J. Modular Synthetic Approach for Adjusting the Disassembly Rates of Enzyme-Responsive Polymeric Micelles. Biomacromolecules 2017, 18 (4), 1218–1228.

22. Slor, G.; Amir, R. J. Using High Molecular Precision to Study Enzymatically Induced Disassembly of Polymeric Nanocarriers: Direct Enzymatic Activation or Equilibrium-Based Degradation? Macromolecules 2021, 54 (4), 1577–1588.
23. Phillips, S. T.; DiLauro, A. M. Continuous Head-to-Tail Depolymerization: An Emerging Concept for Imparting Amplified Responses to Stimuli-Responsive Materials. ACS Macro Lett. 2014, 3 (4), 298–304.
24. Addy, P. S.; Shivrayan, M.; Cencer, M.; Zhuang, J.; Moore, J. S.; Thayumanavan, S. Polymer with Competing Depolymerization Pathways: Chain Unzipping versus Chain Scission. ACS Macro Lett. 2020, 9 (6), 855–859.
25. Kumar, V.; Munkhbat, O.; Secinti, H.; Thayumanavan, S. Disassembly of Polymeric Nanoparticles with Enzyme-Triggered Polymer Unzipping: Polyelectrolyte Complexes vs. Amphiphilic Nanoassemblies. Chem. Commun. 2020, 56 (60), 8456–8459.
26. Slor, G.; Tevet, S.; Amir, R. J. Stimuli-Induced Architectural Transition as a Tool for Controlling the Enzymatic Degradability of Polymeric Micelles. ACS Polym. Au 2022.
27. Harnoy, A. J.; Slor, G.; Tirosh, E.; Amir, R. J. The Effect of Photoisomerization on the Enzymatic Hydrolysis of Polymeric Micelles Bearing Photo-Responsive Azobenzene Groups at Their Cores. Org. Biomol. Chem. 2016, 14 (24), 5813–5819.
28. Lafleur, R. P. M.; Herziger, S.; Schoenmakers, S. M. C.; Keizer, A. D. A.; Jahzerah, J.; Thota, B. N. S.; Su, L.; Bomans, P. H. H.; Sommerdijk, N. A. J. M.; Palmans, A. R. A.; Haag, R.; Friedrich, H.; Böttcher, C.; Meijer, E. W. Supramolecular Double Helices from Small C3-Symmetrical Molecules Aggregated in Water. J. Am. Chem. Soc. 2020, 142 (41), 17644–17652.
29. Gondi, C. S.; Rao, J. S. Cathepsin B as a Cancer Target. Expert Opin. Ther. Targets 2013, 17 (3), 281–291.
30. Aggarwal, N.; Sloane, B. F. Cathepsin B: Multiple Roles in Cancer. PROTEOMICS – Clin. Appl. 2014, 8 (5–6), 427–437.
31. Mason, S. D.; Joyce, J. A. Proteolytic Networks in Cancer. Trends Cell Biol. 2011, 21 (4), 10.
32. Dheer, D.; Nicolas, J.; Shankar, R. Cathepsin-Sensitive Nanoscale Drug Delivery Systems for Cancer Therapy and Other Diseases. Adv. Drug Deliv. Rev. 2019, 151–152, 130–151.
33. Jin, X.; Zhang, J.; Jin, X.; Liu, L.; Tian, X. Folate Receptor Targeting and Cathepsin B-Sensitive Drug Delivery System for Selective Cancer Cell Death and Imaging. ACS Med. Chem. Lett. 2020, 11 (8), 1514–1520.
34. Lock, L. L.; Tang, Z.; Keith, D.; Reyes, C.; Cui, H. Enzyme-Specific Doxorubicin Drug Beacon as Drug-Resistant Theranostic Molecular Probes. ACS Macro Lett. 2015, 4 (5), 552–555.
35. M. Bose, D. Groff, J. Xie, E. Brustad, and P. G. Schultz. The Incorporation of a Photoisomerizable Amino Acid into Proteins in E. coli, J. Am. Chem. Soc. 2006, 128 (2), 388-389.
36. W. Li, I. Park, S.-K. Kang, and M. Lee,. Smart hydrogels from laterally-grafted peptide assembly, Chem. Commun., 2012, 48 (70), 8796-8798.

# Chapter 6 | Advanced optical microscopy for supramolecular materials

## 6.1 Imaging BTA-azo supramolecular polymers by fluorescence microscopy

### 6.1.1 Introduction

Supramolecular materials can be characterized by a wide variety of techniques, that mainly measures bulk properties. However, in the recent years it has been exposed the need for a more in-depth analysis, in which individual nanostructures must be visualized and where variability particle to particle is taken into account.[1-3]

The main approach to tackle this challenge is microscopy, allowing the direct visualization of the material, discriminating individual structures. As most of the supramolecular materials are fundamentally nanosized, special techniques or methods must be used to study them. Typically, nanosized structures are studied either by electron microscopy or scanning probe microscopies.[4-6]. Even though being very powerful techniques to measure sizes, composition, mechanical or electrical properties among others, they are difficult to use in native conditions and its challenging to do dynamic studies discriminating between multiple components.

For these reason, fluorescence optical microscopy has emerged as an outstanding tool to image and understand nanosized systems, not only from the morphology side but also from the fundamental side. Fluorescence optical microscopy allows for distinguishing specific structures due to the fluorophore labelling and its multicolour imaging capabilities.[7,8] However, it comes with a limit of resolution of around 250 nm, above the size of most of the supramolecular structures, for that reason researchers make use of two approaches.

The first consists of studying the system at low resolution, when the structures are immobilized on a surface and can be individually identified. This approach is useful for particle by particle qualitatively spectroscopic studies, measuring polydispersion of spectroscopic parameters.

The second strategy consists of using super-resolution microscopies, that has emerged as extraordinarily powerful tool for the study of nanosized materials.[1] For example, in 2014, Albertazzi et al developed a methodology to probe monomer exchange pathways in supramolecular fibres, by identifying individual components in a multicomponent system.[9]

Super-resolution optical microscopies can be divided in three main methods, according to their strategy (Fig. 6.1.1):

- Structured illumination: This method relies on the excitation of the sample using a high-spatial-frequency pattern. This generates an interference pattern (Moiré fringes) that can be mathematically deconvoluted into a better resolved image. Depending on the specific method used, resolutions can change from 125 nm down to 50 nm. The speed of acquisition is the best advantage of this technique, what allow life cell imaging.[10-13]
- Stimulated emission depletion: This method uses two light beams simultaneously, the first is in charge of exciting the fluorophores (in blue in the figure), and the second has a

doughnut shape, centred with the prior beam, that depletes the fluorophore emission. By using both beams simultaneously the size of the point spread function is reduced and hence, the resolution improved. This method improves resolution to 50-80 nm, or even below.[16]

- Single molecule localization: strategy based on the individual localization of fluorophores as single emission spots (~200 nm) and calculation of the emission centre (~20 nm). There are different strategies to achieve the individual localization of fluorophores, but essentially all are focused on maintaining most of the dyes in an off state while few dyes randomly activate and can be localized while isolated. After some time imaging, sufficient dyes activated to allow a full reconstruction of the structure. Different strategies can be used for the activation of a small portion of dyes, like for example direct Stochastic Optical Reconstruction Microscopy (dSTORM)[17-19] or Point Accumulation Imaging in Nanoscale Topography (PAINT).[20-22] In dSTORM structures are permanently labelled with photoswitchable dyes, that remain most of the time in the dormant state and are stochastically activated for a short period of time. This switch between on and off states is normally achieved by a reversible photochemical reaction, that can be controlled with the reactant concentration in the buffer and laser power. Dyes typically photobleach during acquisition. In PAINT, structures are not permanently labelled. Instead, a dye-labelled probe is designed to have a weak interaction with the structures of interest. The probe is found in solution (undetectable) and it can be localized just upon a transient binding with the structure. In this case, imaging is not affected by photobleaching of the dyes, due to the huge reservoir of dyes in solution.

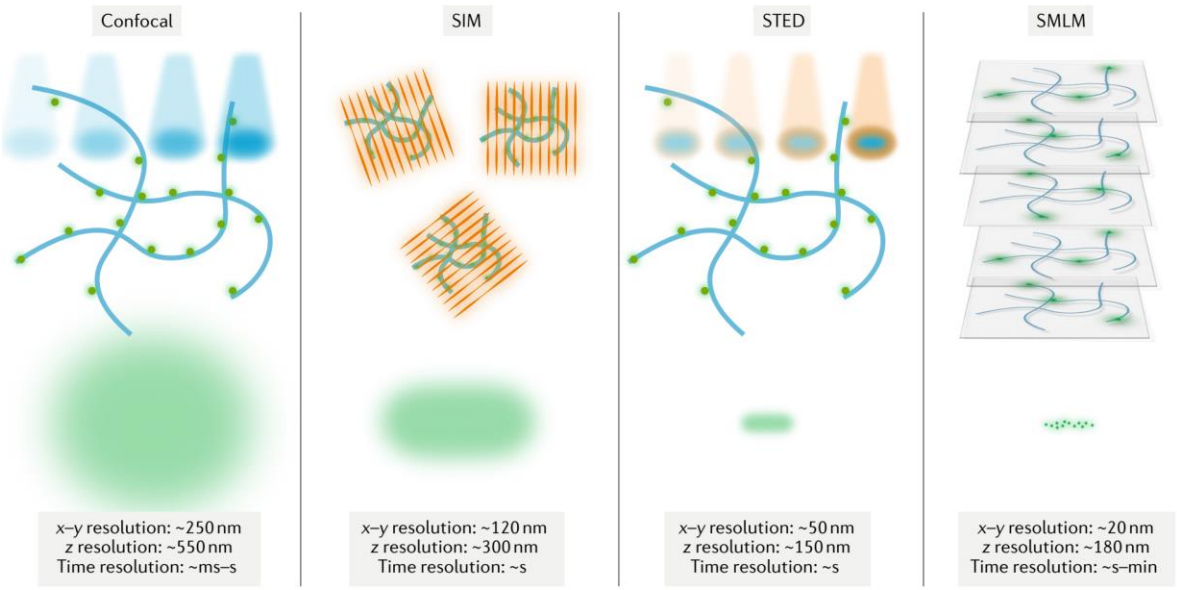


Figure 6.1.1 Comparison between confocal microscopy and the three main types of super-resolution microscopy.

In this chapter, we show the first steps towards the imaging of supramolecular BTA-azo by fluorescence microscopy. Fibres were visualized in solution, immobilized on a coverslip surface and even in the presence of cells.

## 6.1.2 Results and discussion

First, we studied the possibility to qualitatively assess the assembly states of BTA-azo monomers with highly inclined thin illumination (HILO). C0 samples were prepared at 100 μM containing 5% of labelled monomer with Cy3, diluted to 25 μM and flown into a flow-chamber glass slide. The focal point was set above the surface, the incident angle of the laser adjusted at around 50°, reduce the background but enough to illuminate the focal plane. Under these settings, many fibre-like objects were observed, still, with high background. These fibres were in continuous movement due to the Brownian motion, moving laterally and in and out of focus. In figure 6.1.2, we can observe a series of consecutive snapshots extracted from a video, tracing the movement of a single fibre.

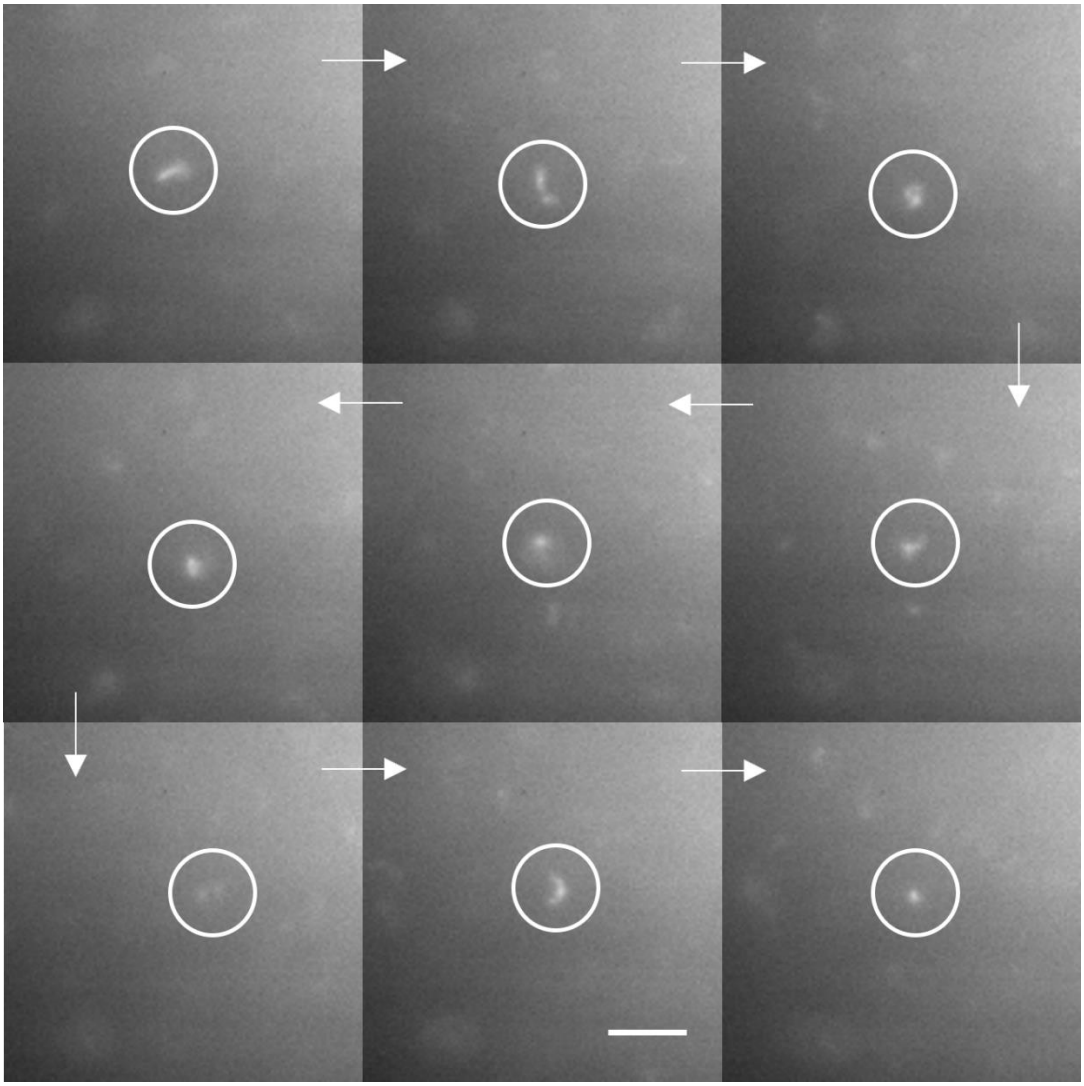

Figure 6.1.2 Snapshots from a video tracking a single C0 fibre moving in solution. Laser power was kept at 2.5 %. Scale bar: 10 μm.

Many small objects were observed moving the in the field of view, however only few were big enough to be identify as fibres. Additionally, background levels were quite high, probably due to a high number of small fibres, free and *Z*-configured monomers.

Additionally, we performed the same procedure for C8 samples, preparing the sample at 25 μM and diluting to 2.5 μM prior imaging. In this case, the results show a slight lower background and an improved signal-to-noise ratio. In this case, to reduce the background we could make a partial wash with Milli Q to remove most of the floating fibres and monomers but keeping enough of them to be visualized (Fig. 6.1.3). Presumably, it worked for C8 because we can dilute without affecting the fibre integrity and because C8 has less free monomer that C0.

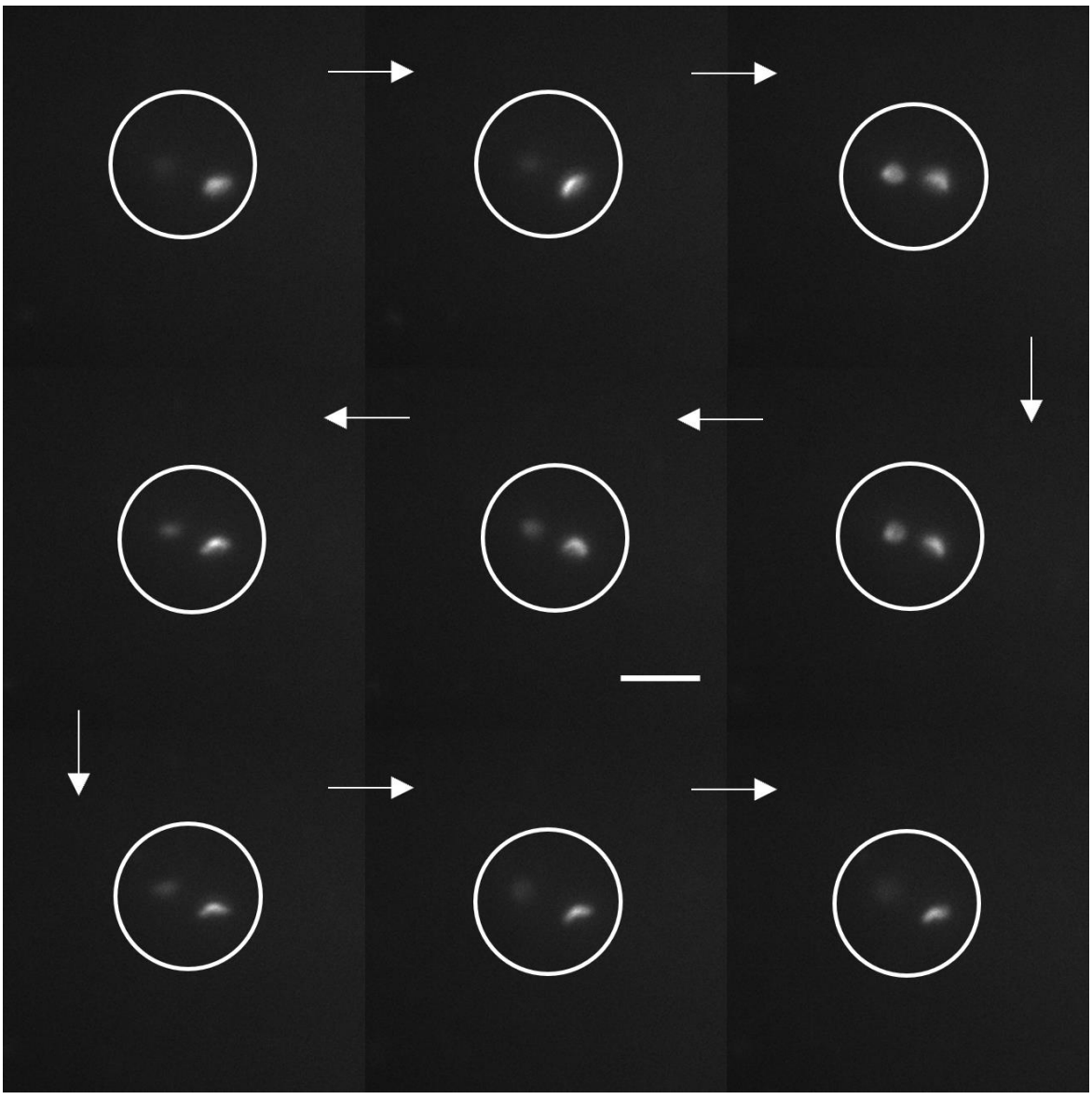

Figure 6.1.3 Snapshots from a video tracking a single C8 fibre moving in solution. Laser power was kept at 2.5 %. Scale bar: 10 μm.

Interestingly, when samples are irradiated with UV light, no fibres are observed for C0, and small and fast aggregates are observed for C8. Under this irradiation conditions, C0 is completely

disassembled and C8 is partially disassembled, dissolving all the big fibres that were visualized before.

In second place, we wanted to visualize the fibre when immobilized on a surface. For that reason, we proceeded as explained previously but washing out the sample after 1 min in the chamber. That time is enough to allow some fibre attachment on the coverslip. In figure 6.1.4 we can observe some typical low-res images of C0 and C8 fibres. This time, we changed the configuration to a Total Internal Reflection Fluorescence (TIRF).

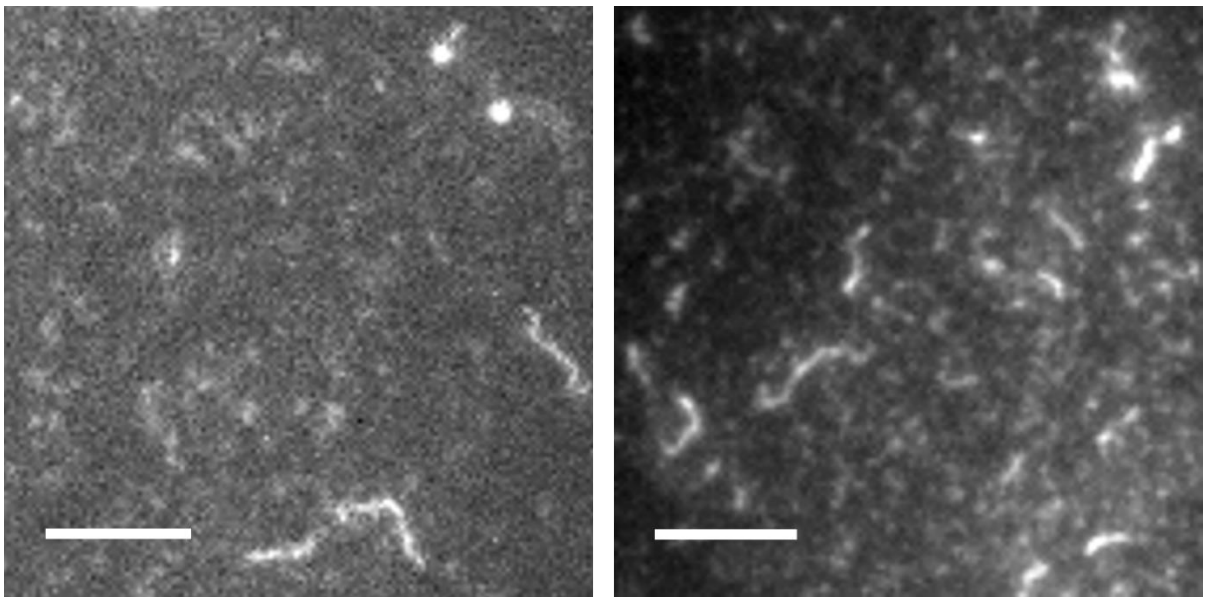

Figure 6.1.4 Images of C0 (left) and C8 (right) were obtained by TIRF microscopy. Laser power was kept at 2.5 %. Scale bar: 5 μm.

Surprisingly, we could observe few very long fibres attached on the coverslip, of around 2-5 μm in length. However, previous TEMs showed that fibres length was around 300 nm when prepared at the same concentration, showing also some dispersion in length and occasionally showing lengths longer than 1 μm.

As expected by TEM, the field of view is plenty of shorter fibres attached, some of them are even visible having a closer look in Figure 6.1.4 (specially for C8). These smaller fibres that are still visible are still very long (ca. 1 μm). These fibres are clearly less bright that the very long ones, and this together with the fact that are extremely long makes us hypothesise that correspond to several fibres entangled together, forming a much longer and brighter structure.

In any case, fibres matching the mean size (300 nm) will look more like dots than fibres due to the limit of resolution of conventional fluorescence microscopy. For that reason, and aiming to visualize single fibres, we perform also STORM microscopy.

Samples were then washed with STORM buffer, required to achieve fluorophore blinking. However, during image aquision and reconstruction it could be observed the very fast fluorescence bleaching and the very poor reconstruction of original image. Single fibres were not possible to be imaged, dyes photobleached before sufficient events were collected.

Only in some cases, considerably big fibres were imaged. To corroborate if the imaged structures corresponded to single or multiple fibres, we chose to optimize a dSTORM-TEM correlative method. It consisted of the imaging of the same filed-of-view with fluorescence light microscopy and electron microscopy, and then overlap the images. By this means, we can correlate the spectral information with the morphological information.

Given the complexity of the methods, we decided to use C8 given its increased robustness, labelled with a Cy3 dye for microscopy purposes. Fibres formulated in water were first attached to a nickel-hexagonal 200 mesh TEM grid coated with a formvar-carbon layer. The grid choice is particularly important, because dSTORM buffer can oxidize other metals such as copper (very typical in electron microscopy), leading to peeling of the supportive layer. Next, the grid was imaged by dSTORM, thoroughly washed and imaged by TEM (see methods section).

We first obtained a dSTORM image of C8 fibre (Figure 6.1.5 a, left), and then a TEM image of the same field-of-view (Figure 6.1.5 a, middle panel), and overlapped the respective images to create the correlative dSTORM-TEM image of supramolecular polymers (Figure 6.1.5 a, right panel). Initially, dSTORM showed fibres of greater lengths (> 3 μm) compared to previously reported sizes (250-1000 nm). Then, we acquired higher resolution images by TEM of the same fibre and carried out the dSTORM-TEM correlation on a smaller area (Figure 6.1.5 b). The results demonstrated that the fibres were in fact polymer bundles (~ 80 nm) made of much smaller fibres, roughly 8 nm in diameter. Since the resolution of dSTORM is ~ 20 nm, molecules with a smaller size will not be distinguished from one another when closer to each other by less than 20 nm. For this reason, dSTORM alone was unable to show the true structure of these fibres.

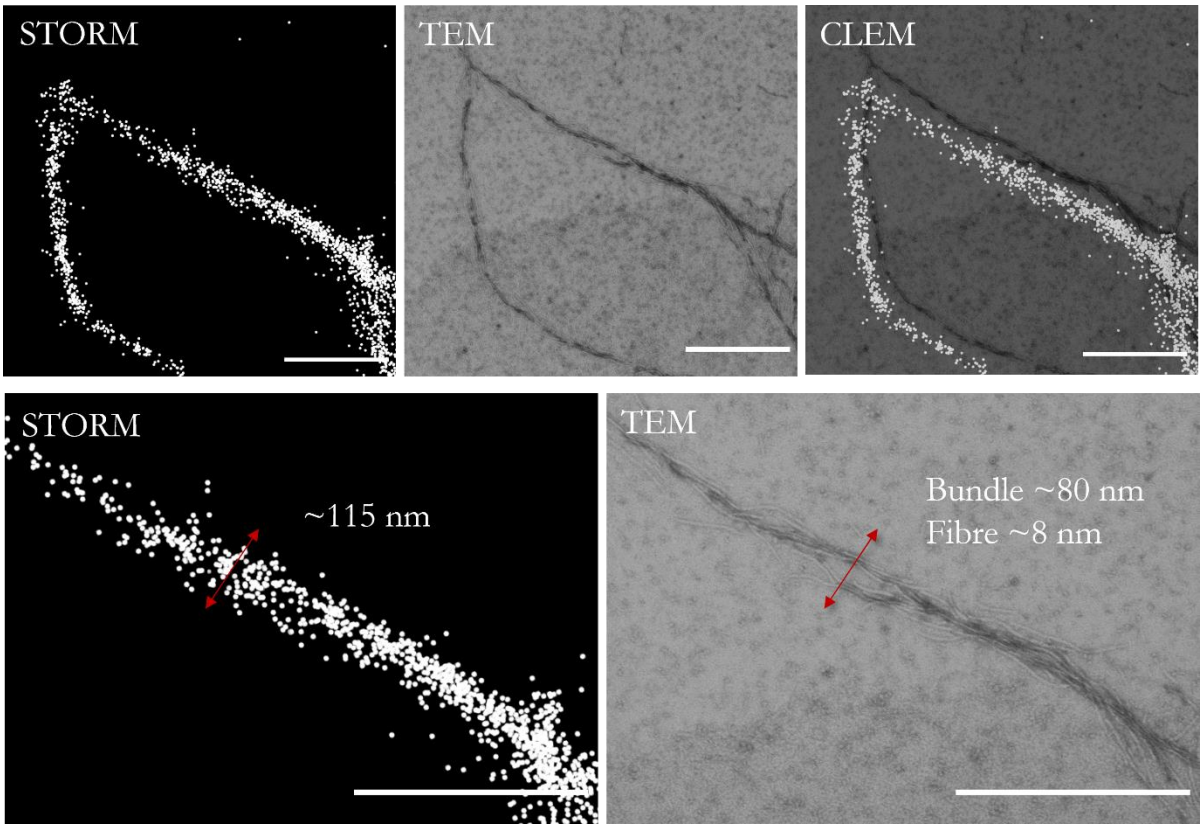


Figure 6.1.5 CLEM images. a) Large field views of BTA-AZO-C8 supramolecular fibres by dSTORM, TEM and by correlative STORM-TEM, of the same area. b) Zoom-in images of the area highlighted with the

lined red box in A), showing that the single fibre observed by dSTORM is a bundle of smaller fibres. Scale bars = 500 nm.

This method demonstrated extremely powerful here and in other systems,[23] however in this case we are limited by the dSTORM imaging performance. Following experiments, should be focused on the dSTORM imaging, changing buffer composition to reduce the photobleaching. After, it would be interesting to study the monomer exchange of the different polymers, like in chapter 3, observing a fast monomer exchange when mixing different colour fibres for C0 and C4, but not for C8. Additionally, it will be interesting to corroborate the monomer exchange pathways observed before by Albertazzi et. al.[9] identifying if the exchange occurs along the fibre (monomer intercalation) or localized at the ends (monomer addition).

Finally, we explored the imaging of fibres in presence of live HeLa cells. Cells were seeded on a 8-well glassbottom labtek, at 37 ºC and kept in cell medium. A C0 sample at 100 μM and 5% Cy5 loaded monomer was introduced in the well and washed out with PBS after 5 min. HILO illumination was used for the imaging. Surprisingly, fibres were very clearly observable on the cell membrane (Fig. 6.1.6), especially on the sides and at the junction with other cells. Fibres were also observed attached along the whole membrane at all different z-planes. Hella cells were verified by transmission optical microscopy.

Interestingly, we could detect many fibres attached only with one end to the cell surface, having the other end free, floating in solution. Additionally, even though no signal was observed inside the cells, this technique could be useful to make kinetic internalization studies.

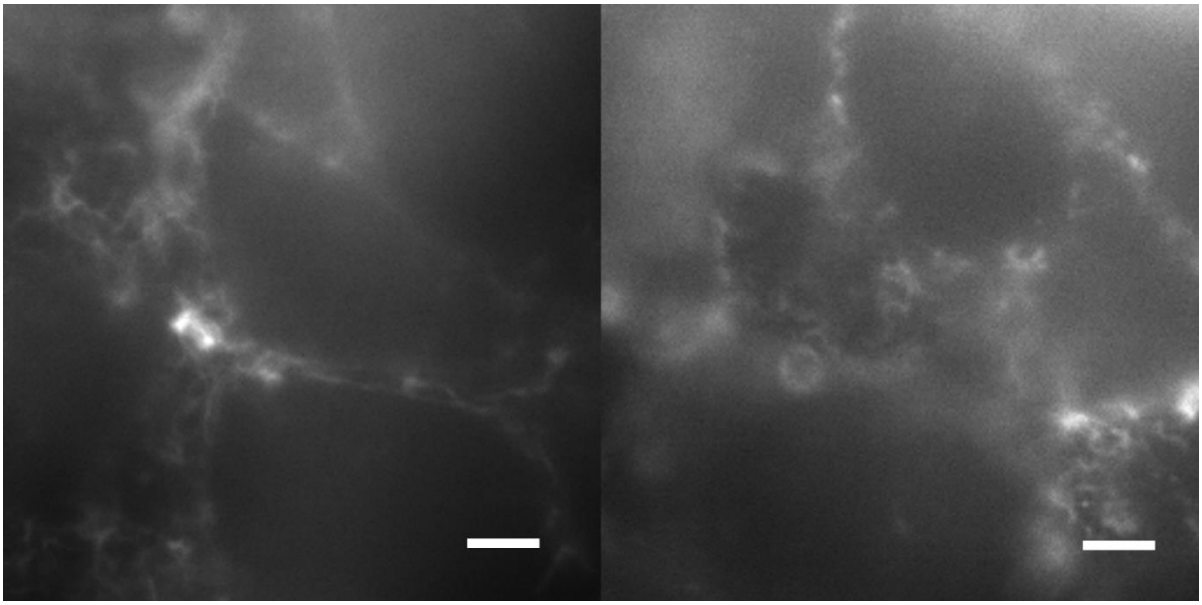

Figure 6.1.6 Frames of live cell imaging videos of C0 and HeLa cells. HILO illumination was used, temperature was kept at 37º C. Laser power was kept at 2.5 %. Scale bar: 5 μm.

Fluorescence microscopy with HiLo illumination could be good enough to image fluorescent nanofibres on cells, designing more systematic experiments at different times, concentrations, media or temperatures.

### 6.1.3 Conclusions

Optical fluorescence microscopy is a powerful tool for the characterization of supramolecular fibres based on BTA-azo. Supramolecular fibres in solution can be visualized and studied under HILO and TIRF configurations. These techniques can provide additional qualitative information regarding the assembly state in solution and immobilized in a coverslip. Additionally, even though STORM imaging is very challenging, low resolution optical microscopy could be enough for some studies of the interaction between polymers and cells.

### 6.1.4 Materials and methods

**Instruments**

Nikon N-STORM microscope was used for the BTA-azo imaging, configured as HILO or TIRF. Laser was chosen as a function of the dye imaged, 647 nm (160 mW) for Cy5 and 561 nm (80 mW) for Cy3. Fluorescence was collected by a 100× 1.49 NA oil immersion objective; it passed through a quad-band dichroic mirror (97335 Nikon) and was collected by a Hamamatsu ORCA Flash 4.0 CMOS camera (pixel size 160 nm). The acquisition time was modified from 20 to 50 ms.

**Methods**

The flow chambers (35 μl) were assembled from a glass slide and a coverslip separated by double-sided tape. Samples were flown in from the side with a micropipette. Washings were performed flowing in the washing solution allowing the initial sample to flow out from the other side using a dust free tissue.

STORM buffer consisted of 100 mM mercaptoethylamine (MEA), an oxygen scavenger system consisting of 5% glucose (wt/vol) and 0.5 mg/mL glucose oxidase, 40 mg/mL catalase, and 15% glycerol, in PBS at pH 8.5.

HeLa cells were cultured in Dulbecco's Modified Eagle Medium (DMEM, as received with L-Glutamine, 4.5 g/L D-glucose and pyruvate, Gibco) supplemented with FBS 5% (Gibco) and penicillin/streptomycin 1% (Biowest). HeLa cells were seeded on a 8-well glassbottom Nunc labtek, in DMEM, 24h before the experiment to reach a confluency around 0.7-0.8. After, cells were placed at 37ºC and 5% $CO_2$.

C0 sample was prepared at 100 μM in PBS and heated up to 37ºC for 1h. DMEM in the wells was replaced by the PBS solution with the fibres and started imaging. As fluorescence background was too high, after 5 min the solution was replaced by fresh PBS. All the solutions used were kept at 37ºC.

dSTORM-TEM correlative microscopy method: C8 monomers 10% Cy3 labelled, with a final concentration of 50 μM in milliQ water were prepared. The polymers were allowed to reach equilibrium at rt for 24 h, then annealed at 70°C for 1 h and allowed to settle at rt for a further 24 h. Polymer was further diluted to 25 μM and heated up to 50°C.

The nickel-hexagonal 200 mesh grids with formvar-carbon coating were treated with glow discharge for 30 sec at 5 mA, to improve fibre attachment. Fibres were then diluted to 1 μM in milliQ water, attached for 1 min onto the TEM grid and washed 30 seconds by milliQ water to remove unattached polymers.

The grid was placed into a microscopy chamber as previously described, and a STORM buffer was flown in. Fibres were imaged by STORM using the 561 nm laser at 20 ms exposure for 10 000 frames. The grid was then removed from the chamber and washed on a milliQ water drop for 30 sec before negative staining for 1 min using 2% uranyl acetate. The same region was later imaged by TEM, and correlation was carried out manually using Adobe Photoshop CS9.

### 6.1.5 References


1. Pujals, S.; Feiner-Gracia, N.; Delcanale, P.; Voets, I.; Albertazzi, L. Super-Resolution Microscopy as a Powerful Tool to Study Complex Synthetic Materials. Nat. Rev. Chem. 2019, 3 (2), 68–84.
2. Habuchi, S. Super-Resolution Molecular and Functional Imaging of Nanoscale Architectures in Life and Materials Science. Front. Bioeng. Biotechnol. 2014, 2.
3. Feiner-Gracia, N.; Beck, M.; Pujals, S.; Tosi, S.; Mandal, T.; Buske, C.; Linden, M.; Albertazzi, L. Super-Resolution Microscopy Unveils Dynamic Heterogeneities in Nanoparticle Protein Corona. Small 2017, 13 (41), 1701631.
4. Franken, L. E.; Boekema, E. J.; Stuart, M. C. A. Transmission Electron Microscopy as a Tool for the Characterization of Soft Materials: Application and Interpretation. Adv. Sci. 2017, 4 (5), 1600476.
5. Zhong, S.; Pochan, D. J. Cryogenic Transmission Electron Microscopy for Direct Observation of Polymer and Small-Molecule Materials and Structures in Solution. Polym. Rev. 2010, 50 (3), 287–320.
6. Huey, B. D.; Luria, J.; Bonnell, D. A. Scanning Probe Microscopy in Materials Science. In Springer Handbook of Microscopy; Springer Handbooks; 2019.
7. Kubota, R.; Nakamura, K.; Torigoe, S.; Hamachi, I. The Power of Confocal Laser Scanning Microscopy in Supramolecular Chemistry: In Situ Real-Time Imaging of Stimuli-Responsive Multicomponent Supramolecular Hydrogels. ChemistryOpen 2020, 9 (1), 67–79.
8. Lakowicz, J. R., Principles of Fluorescence Spectroscopy; Springer, 2011.
9. Albertazzi, L.; Zwaag, D. van der; Leenders, C. M. A.; Fitzner, R.; Hofstad, R. W. van der; Meijer, E. W. Probing Exchange Pathways in One-Dimensional Aggregates with Super-Resolution Microscopy. Science 2014.
10. Gustafsson, M. G. L. Surpassing the Lateral Resolution Limit by a Factor of Two Using Structured Illumination Microscopy. J. Microsc. 2000, 198 (2), 82–87.

11. Gustafsson, M. G. L. Nonlinear Structured-Illumination Microscopy: Wide-Field Fluorescence Imaging with Theoretically Unlimited Resolution. Proc. Natl. Acad. Sci. 2005, 102 (37), 13081–13086.
12. Instant Super-Resolution Imaging in Live Cells and Embryos via Analog Image Processing. Nat. Methods 2013, 10 (11), 1122–1126.
13. Godin, A. G.; Lounis, B.; Cognet, L. Super-Resolution Microscopy Approaches for Live Cell Imaging. Biophys. J. 2014, 107 (8), 1777–1784.
14. Klar, T. A.; Jakobs, S.; Dyba, M.; Egner, A.; Hell, S. W. Fluorescence Microscopy with Diffraction Resolution Barrier Broken by Stimulated Emission. Proc. Natl. Acad. Sci. 2000, 97 (15), 8206–8210.
15. Gustafsson, M. G. L.; Shao, L.; Carlton, P. M.; Wang, C. J. R.; Golubovskaya, I. N.; Cande, W. Z.; Agard, D. A.; Sedat, J. W. Three-Dimensional Resolution Doubling in Wide-Field Fluorescence Microscopy by Structured Illumination. Biophys. J. 2008, 94 (12), 4957–4970.
16. Dyba, M.; Hell, S. W. Focal Spots of Size λ/23 Open Up Far-Field Florescence Microscopy at 33 Nm Axial Resolution. Phys. Rev. Lett. 2002, 88 (16), 163901.
17. Rust, M. J.; Bates, M.; Zhuang, X. Sub-Diffraction-Limit Imaging by Stochastic Optical Reconstruction Microscopy (STORM). Nat. Methods 2006, 3 (10), 793–796.
18. Heilemann, M.; van de Linde, S.; Schüttpelz, M.; Kasper, R.; Seefeldt, B.; Mukherjee, A.; Tinnefeld, P.; Sauer, M. Subdiffraction-Resolution Fluorescence Imaging with Conventional Fluorescent Probes. Angew. Chem. Int. Ed. 2008, 47 (33), 6172–6176.
19. Huang, B.; Wang, W.; Bates, M.; Zhuang, X. Three-Dimensional Super-Resolution Imaging by Stochastic Optical Reconstruction Microscopy. Science 2008, 319 (5864), 810–813.
20. Spahn, C. K.; Glaesmann, M.; Grimm, J. B.; Ayala, A. X.; Lavis, L. D.; Heilemann, M. A Toolbox for Multiplexed Super-Resolution Imaging of the E. Coli Nucleoid and Membrane Using Novel PAINT Labels. Sci. Rep. 2018, 8 (1), 14768.
21. Lin, C.; Jungmann, R.; Leifer, A. M.; Li, C.; Levner, D.; Church, G. M.; Shih, W. M.; Yin, P. Submicrometre Geometrically Encoded Fluorescent Barcodes Self-Assembled from DNA. Nat. Chem. 2012, 4 (10), 832–839.
22. Aloi, A.; Vilanova, N.; Albertazzi, L.; Voets, I. K. IPAINT: A General Approach Tailored to Image the Topology of Interfaces with Nanometer Resolution. Nanoscale 2016, 8 (16), 8712–8716.
23. Andrian T, Pujals S, Albertazzi L. Quantifying the effect of PEG architecture on nanoparticle ligand availability using DNA-PAINT. Nanoscale Adv. 2021, 3, 6876-6881.

## 6.2 PAINT-ing Fluorenylmethoxycarbonyl-Diphenylalanine Hydrogels

*This chapter reproduces almost literally the findings reported in Fuentes, E.; Boháčová, K.; Fuentes-Caparrós, A. M.; Schweins R.; Draper E. R.; Adams D. J.; Pujals S.; Albertazzi, L. PAINT-ing Fluorenylmethoxycarbonyl-Diphenylalanine Hydrogels. Chem. – Eur. J., 2020, 26, 9869–9873.*

### 6.2.1 Introduction

Gels formed by the self-assembly of small molecules are of considerable interest in a range of fields.[1-5] Such gels are formed by the self-assembly of the gelator molecules into nanostructures such as fibres, nanotubes or helical fibres.[1] At a suitable concentration, these structures entangle or otherwise cross-link to form a network. In practice, assuming the gelator is stable, it is relatively easy to prepare gels using approaches such as heating and cooling, adjusting the pH of the solution or the addition of a salt. In all cases, these methods work by providing one regime where the gelator is solubilised or dispersed and then a second regime where the solubility is much lower and hence the self-assembly is favoured.

The mechanical and chemical properties of the gels that are formed depend on many parameters of the underlining network structure such as fibre persistence length, type and number of crosslinks and the network geometry.[6,7] Being able to measure these parameters is crucial in understanding gel formation and it is key for the rational design of improved structures.

Typically, many aspects of these gels are determined by microscopy techniques such as transmission electron microscopy (TEM), scanning electron microscopy (SEM) or atomic force microscopy (AFM). Whilst powerful, there are some limitations related to these techniques. Drying of the gels is needed in most cases, which typically means that at best a 2D representation of the 3D network is imaged. On top of this, it is known that drying the gels can lead to changes to the self-assembled structures and networks, meaning that the images do not represent the native gels.[5,8] Methods such as freeze-drying have been used to remove the solvent(s) in a less invasive manner, but still result in the perturbation of the native structure. Cryo-TEM can be used without the need for drying, but sample preparation requires that thin films are used (typically 300 nm or less),[9] which again means that it is hard to be sure that the 3D structure of the gel has not been perturbed.

Spectroscopic techniques such as small angle X-ray scattering (SAXS) and small angle neutron scattering (SANS) can be used to probe the self-assembled structures without the need for drying.[10] These methods allow the structures that underpin the gels to be determined, typically by fitting the scattering profile to a model. Whilst effective, the length scale probed (typically <100 nm) represents a limitation in obtaining a full picture of the gel structure. Longer length scales can be accessed by moving to ultra-small angle scattering (USAXS or USANS), but there is little information available currently and limited models to understand how the observed scattering links to a particular type of network. Moreover, these techniques are ensemble methods and fail to provide information about structure spatial heterogeneity.

Confocal microscopy can overcome several of these issues.[11] This technique allows the microstructure to be determined, and it can show how the properties of different gels correlate

with how the self-assembled nanofibres are organized in space (the microstructure).[12] One of the main issues here is the spatial resolution that hampers the observations of features below 250–300 nm. Super-resolution microscopy techniques are becoming progressively accessible and allow an increase in resolution whilst maintaining some of the advantages of confocal imaging. Recently, several reports show the potential of super-resolution imaging to unveil the nanoscale structural and functional features of materials.8 In the hydrogels field, these techniques are very appealing allowing to measure gel nanostructure in the solvated state.[13-18] For example, Hamachi and co-workers used Stimulated Emission Depletion (STED) microscopy for in situ visualization of self-sorted supramolecular fibres.[19] STED allows for fast and multicolour imaging; however, structures must be pre-labelled which potentially affects the supramolecular structure and the very high illumination power needed can create artefacts due to local heating or photo-crosslinking.

In the present chapter, we develop a single molecule localization microscopy (SMLM) method based on Points Accumulation for Imaging in Nanoscale Topography (PAINT) for hydrogels imaging. Our method allows us to image hydrogels with a resolution down to tens of nanometres without the need of direct labelling (e.g. without needing to synthesize a dye-modified hydrogelator). We show here the potential to measure the geometry and organization in 2D and 3D of the hydrogels and to obtain key parameters such as mesh size and fibre diameter. As a first proof-of-principle, we applied PAINT to a widely used family of hydrogelators, Fmoc-protected short peptides.

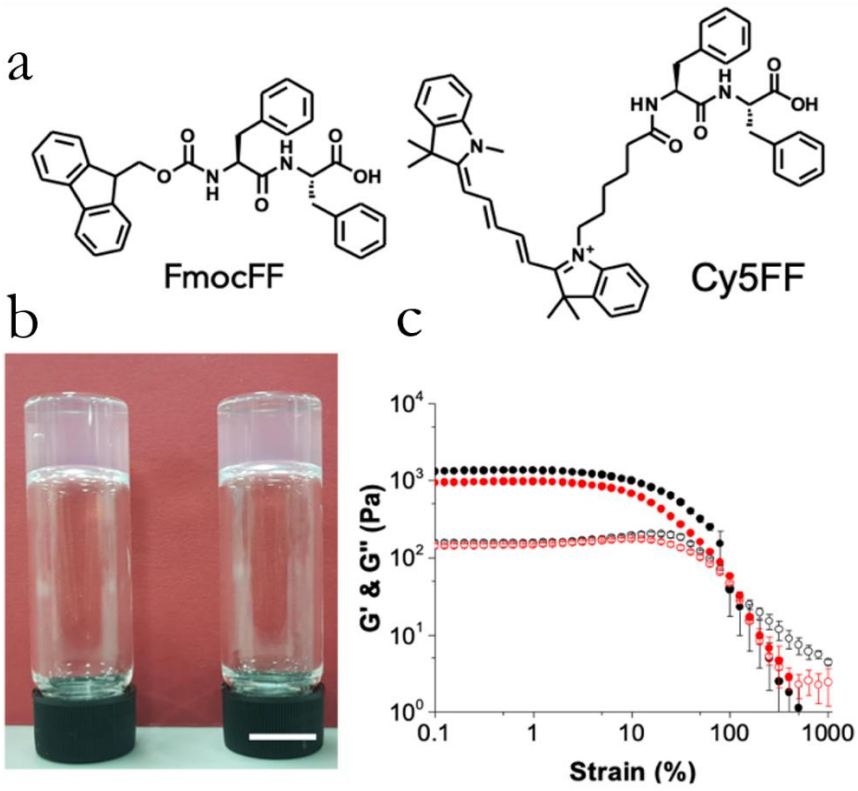


Figure 6.2.1 (a) Chemical structures of (left) FmocFF and (right) Cy5FF; (b) Photographs of gels formed at (left) 20% DMSO and (right) 40% DMSO. The scale bar is 1 cm; (c) Strain sweeps for gels formed in 20% DMSO (black data) and 40% DMSO (red data). In both cases, G¢ is shown by full symbols and G″ by empty symbols. Error bars calculated from standard deviation of three measurements at 25°C.

## 6.2.2 Results and discussion

Gels formed by the self-assembly of short peptides are a thriving field.[20,21] Hydrogels can be formed from a wide range of different oligopeptides, including dipeptides.[21-23] Perhaps the most widely known dipeptide can form hydrogels is diphenylalanine protected at the *N-terminus* with the fluorenylmethoxycarbonyl group (FmocFF, Fig. 6.2.1 a).[24-26] Gels can be formed from FmocFF in a variety of ways, including adding water to a solution of FmocFF in a solvent such as DMSO or hexafluoroisopropanol,[25] adjusting the pH of a solution from around 10 to around 4,[27] or adding a calcium salt to a solution at pH 10.[28] Gels formed from FmocFF have been used for many applications including 3D cell culturing,[27,29,30] controlled release,[25] in biocatalysis[31] and for biomineralization.[32] Despite the interest in this material, there is a limited understanding as to how the gel properties are related to the underlying network. Here, we report the first super-resolution microscopy study of this important material. Gels were prepared by adding water to a solution of FmocFF in DMSO.[25,33] Using this approach, gels were prepared at final ratios of DMSO to water of 20:80 (i.e. 20 % DMSO), 30:70 (30 % DMSO) and 40:60 (40 % DMSO) and a final concentration of FmocFF of 1-1.5 mg mL$^{-1}$ (Fig. 6.2.1 b). These gels showed rheological data typical of such low molecular weight gels. The storage modulus (G') and the loss modulus (G") are relatively independent of frequency. The gels break at <10 % strain as is typical, with the gels formed at 20 % DMSO being slightly stiffer than those formed at 40 % DMSO (Fig. 6.2.1 c).

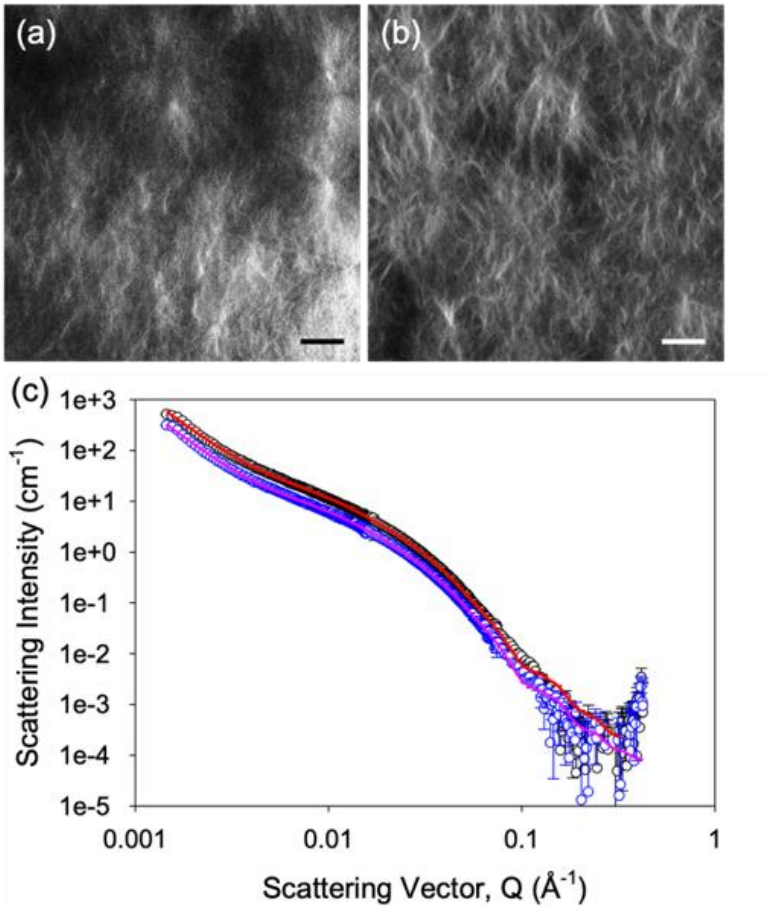

Figure 6.2.2 (a) Confocal microscope image of a gel formed at 20 % DMSO; (b) Confocal microscope image of a gel formed at 40 % DMSO; (c) Scattering pattern (open circles) and fit (solid lines) for gels formed at 20 % DMSO (black and red data) and 40 % DMSO (blue and pink data). For (a) and (b), the scale bar represents 20 μm.

Next, gels were imaged by confocal microscopy by incorporating Nile Blue as a staining agent as previously described (Fig. 6.2.2 a and b).[33] The gels are formed by domains of fibrous structures as can qualitatively visualised by diffraction-limited microscopy. Such spherulitic domains are expected from previous data.[33,34]

Moreover, the nature of the fibrous structures making up the domains was probed using small angle neutron scattering (Fig. 6.2.2 c). The scattering data fit best to a flexible elliptical cylinder model combined with a power law to take into account the scattering at low Q (see methods section for full fitting parameters). The scattering from gels at both ratios of DMSO:water give very similar parameters from the fits to the data, implying that the underlying structures are the same in both cases. The fits imply that the flexible elliptical cylinders have a radius of 3.3 nm, an axis ratio of 2.2, a Kuhn length of 8.9 nm, and lengths of >100 nm. The scattering at low Q can be interpreted as being due to the scattering from the network. The data can also be fitted to a flexible cylinder with a power law, but in this case, it is necessary to include a significant polydispersity in the radius (0.3) to access a reasonable fit and, even then, the fit is not as good as to the flexible elliptical cylinder model.

The SANS data are informative as to the primary underlying structures that lead to the gel network. However, it is very difficult to understand the network from these data, with there simply being a contribution from the network that we take into account using a power law. To better understand the network, we turned to super-resolution microscopy. Here, we used PAINT, a single molecule localization technique where free probes bind reversibly to the structure of study, allowing for the precise localization of the binding events (Fig. 6.2.3 a).[35] We chose Cy5FF (Fig. 6.2.1 a) as a PAINT probe as it had been reported to reversibly bind and unbind from the FF assemblies.[36] By this means, we avoided labelling permanently the monomers, eliminating a potential impact in the final network structure as well as avoiding photobleaching effects during acquisition. Notably the choice of a PAINT probe is crucial as the binding and unbinding kinetic constant have to be finely tuned to allow the probe to bind long enough to accumulate significant signal but to achieve individual emitters localization without signal overload. Figure 6.2.3 b shows a representative image of the FmocFF gel structure imaged by PAINT.

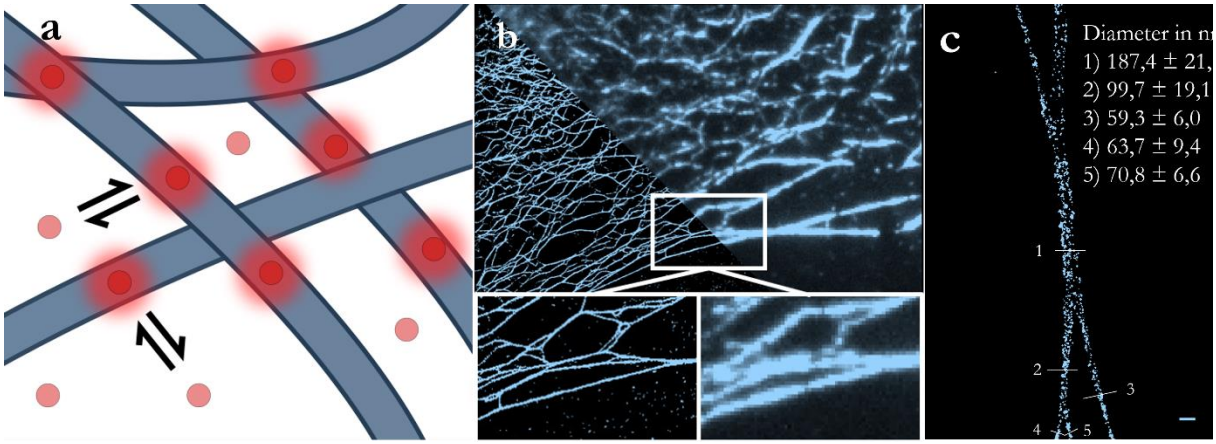


Figure 6.2.3 (a) A cartoon showing how PAINT works. The probe (red circle) can reversibly bind to the fibres (blue shapes). When they are bound, they fluoresce and can be imaged; (b) low resolution (right) vs. PAINT image (left). Scale bar top image represents 5 μm. Scale bar bottom image represents 2.5 μm; (c) Magnification of a crossed fibre. Scale bar represents 200 nm. Image corresponds to FmocFF 1.5 mg mL−1, 40 % DMSO, 20 nm Cy5FF representing the 1.78×10−4 mol %. The numbers represent the different points at which the diameter of the fibre was measured.

In figure 6.2.3 b, we compare a low-resolution image where the gel features remain unresolved with a PAINT image of the same field. The improved resolution allows for a better direct visualization of the fibre network, showing the potential of this technique to study some key features of gels. The thinner fibres observed by PAINT have a diameter of ≈50 nm, that is close to the limit of resolution of this technique in ideal cases (≈10 nm). The drift during the imaging process (movement of imaging stage or sample holder) and the movement of gel scaffold (vibration) are the most challenging concerns lowering the resolution. We applied a drift correction to minimize the first effect, while it is not possible to correct inner movements of the gel. This explains the larger diameter observed in comparison with SANS measurements. Figure 6.2.3 c shows a zoom in of three separated fibres converging together and separating again after. The diameter of the fibres 3, 4 and 5 is 59.3±6.0, 63.7±9.4 and 70.8±6.6 nm in diameter while the cross-link or entanglement diameter of 1 is 187.4±21.3 nm. Interestingly, the sum of the three diameters (3+4+5), 193.8 nm, is very close to the measured value of the cross-link/entanglement. This may indicate that the fibres entangle or bundle together, summing the diameters of the fibres. If instead we had a single fibre branching, the diameter should remain essentially constant. Fibres bundling and separating again is a feature that only microscopy can discriminate, although a better fitting of small angle scattering techniques could complement it.

Another parameter that can be obtained with our method is the mesh size, one of the factors affecting the physical properties of the gel. Indirect methods have been developed to determine mesh size, for example using diffusion measurements by Fluorescence Recovery After Photobleaching (FRAP),[37] NMR spectroscopy[38] or diffusion measurements.[39] The mesh size can also be determined from rheological properties assuming key information such as fibre persistence length are known.[40] However, in all of these cases, it is common to assume that the mesh size is relatively uniform. PAINT is the only technique able to directly image hole units of the network. In figure 6.2.4 a, we show how PAINT images can be processed to obtain the size distribution of the mesh holes. With a partially automated image analysis routine (see methods section), we

measured the areas between the fibres, summing a total of 5,608 meshes, and plotting a histogram (see Fig. 6.2.4 c). The histogram shows two populations, one more frequent of very small mesh sizes (between 20–40 $nm^2$), and another one very broad representing larger areas. Interestingly, the small size population has been reported before by other techniques like micro-rheology,[37,38,41] however it is not the case for the big size population. Generally, a single mesh size is assumed for hydrogels, although in such entangled fibre systems it would be expected that the mesh size is polydisperse.

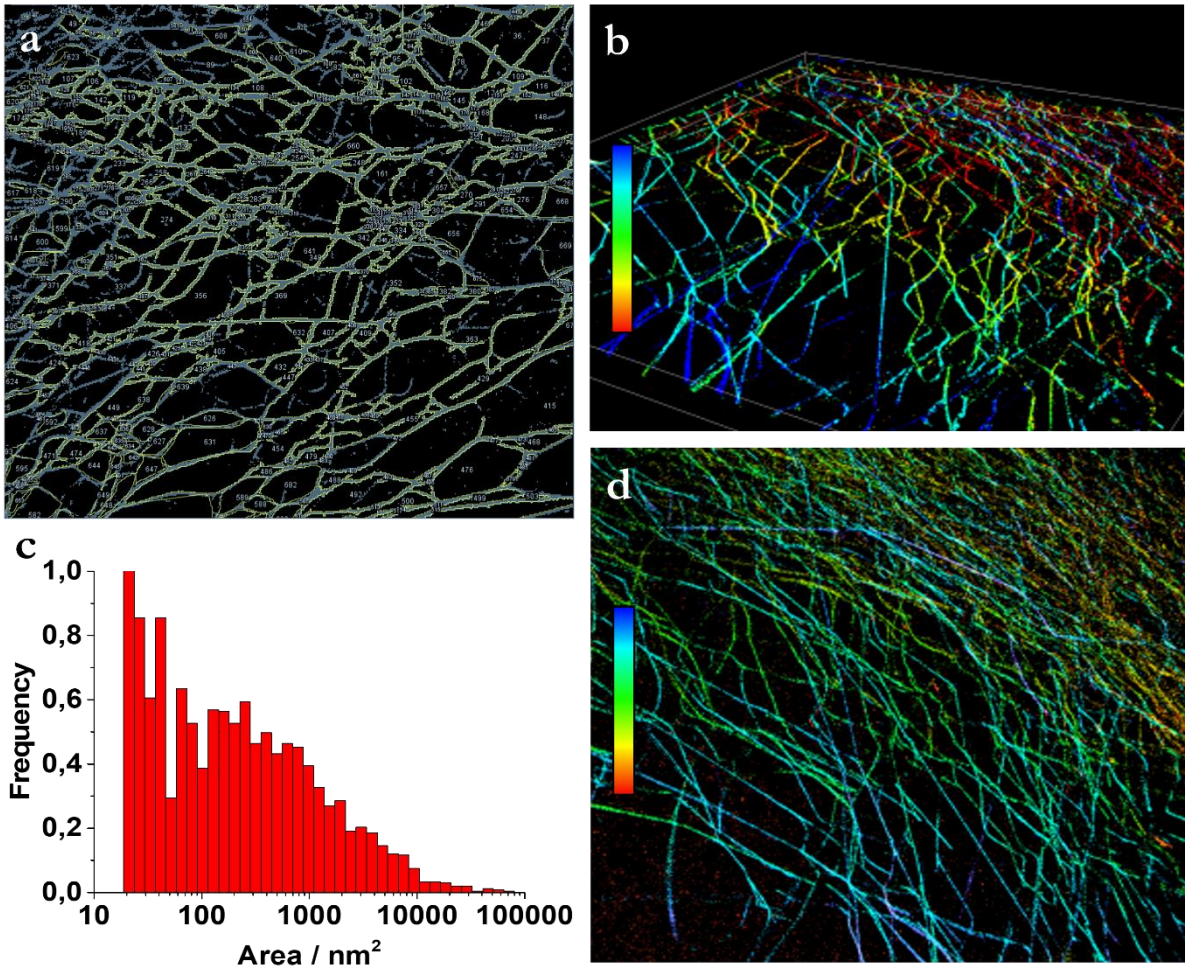


Figure 6.2.4 (a) Mesh size identification of FmocFF hydrogel (1.5 mg mL−1, 40 % DMSO); (b) 3D imaging of hydrogels (1 mg mL−1, 30 % DMSO, 20 nm Cy5FF representing the 2.67×10−4 mol %. Imaged in layers of 120 nm from the glass (red) up to 1.85 μm (blue). The x−y region corresponds to 41 μm x 41 μm; (c) histogram of mesh size; (d) Further 3D imaging of hydrogels (same conditions as (b)).

As a bulk material, it is of real interest not only to study the 2D characteristics, but also the 3D properties. For these reasons, we performed 3D super-resolution images of these networks using astigmatism Point Spread Function (PSF) shaping. In Figures 6.2.4 b and d, 3D images of the hydrogel surface can be observed. Fibres in different planes can be perfectly observed in a region of 41 μm×41 μm×1.85 μm. Notably imaging the bulk of the gel in depth is difficult with this method. First, imaging in depth is limited with HiLo illumination to few microns. Moreover, the limited diffusion of the Cy5FF makes very slow the imaging of the less accessible areas of the gel.

Improved optics solutions (e.g. adaptive optics) and more efficient probes (that better balance gel diffusion with binding) represents future improvements of the technique.

### 6.2.3 Conclusions

In conclusion, we have developed a PAINT method to image hydrogels in native conditions both in 2D and 3D. Due to the improvement in resolution of this method, we were able to quantify fibre diameter, distribution and the mesh size of the hydrogels network. This work paves the way towards the use of super-resolution imaging for gel characterization offering a powerful tool to complement the existing analysis methods. In particular we envision super-resolution microscopy to be very useful in combination with scattering methods. Where the ensemble scattering techniques can obtain quantitative data on the gel features, methods like PAINT will offer a direct visualization of the network and provide information of the spatial heterogeneity of important feature such as mesh size. The combination of multiple techniques, with their own advantages and disadvantages, will be key to achieve a complete understanding of hydrogels networks and formation and their impact in their mechanical properties.

### 6.2.4 Materials and methods

**Materials**

FmocFF was prepared as described previously.

DMSO, $d_6$-DMSO and $D_2O$ were purchased from Sigma-Aldrich. For the microscopy, gels were directly prepared in Labtek 8-well and Ibidi µ-Slide 8-well (Cat. No. 80826, Ibidi GmbH, Germany). Gels for small angle scattering were prepared in Hellma cuvettes.

**Methods**

**Preparation of Gels.** Milli-Q water was transferred into the well and a FmocFF solution in DMSO was injected into the water drop (total 60 µL) and homogenized. Gelation took place immediately and a change of state could be observed; the solution went initially turbid, then quickly became transparent. The prepared gel was left in a humidity case overnight to ensure consistency. One hour before imaging, 150 µL of a solution with the probe at a concentration of 20-50 nM was added, maintaining the DMSO:$H_2O$ ratio.

This procedure allowed a gel to be created with variable thickness for better imaging, but with sufficient consistency to remain assembled and attached to the glass after addition of the probe solution.

**pH measurements.** pH measurements of gels were assessed using a calibrated FC2020 pH probe (Hanna Instruments). The accuracy of the pH measurements is stated as ± 0.1

**Confocal Microscopy.** The microstructure of the gel was visualised by using a Zeiss LSM 710 confocal microscope. The sample was prepared in a CELLviewTM 35 mm plastic cell culture dish with a borosilicate glass bottom purchased from Greiner Bio-One. Nile blue A was used as fluorochrome in a concentration of 2 $\mu L \cdot mL^{-1}$ of a 0.1 w% stock solution and excited at 634 nm using a He-Ne laser (Zeiss). The objective used was a LD EC Epiplan NEUFLUAR 50x (0,55 DIC). The gel was prepared by dissolving the required amount of FmocFF (1.5 mg/mL) in DMSO in a vial, then the solution was transferred into the culture dish. Next water was added as the antisolvent to trigger gelation. The ratios of DMSO:$H_2O$ used were 20:80 and 40:60 and the gel was prepared at a total volume of 400 μL. The gel was kept in a humid environment to prevent evaporation issues by wrapping humid tissue inside the culture dish without touching the gel and sealing it using parafilm and left overnight to gel.

**Small angle neutron scattering.** The gels were prepared as described above in UV spectrophotometer grade, quartz cuvettes (Hellma) with a 2 mm path length. The cuvettes were placed in a temperature-controlled sample rack during the measurements. SANS measurements were performed using the D11 instrument (Institut Laue Langevin, Grenoble, France). A neutron beam, with a fixed wavelength of 6 Å and divergence of $\Delta\lambda/\lambda$ = 9%, was used, allowing measurements over a large range in Q [$Q = 4\pi\sin(\theta/2)/\lambda$] range of 0.001 to 0.3 $Å^{-1}$, by using three sample-detector distances of 1.5 m, 8m, and 39 m.

The data were reduced to 1D scattering curves of intensity vs. Q using the facility provided software. The electronic background was subtracted, the full detector images for all data were normalized and scattering from the empty cell was subtracted. The scattering from the solvent mixture prepared using $D_2O$ and $d_6$-DMSO was also measured and subtracted from the data. Most of the data were radially averaged to produce the 1D curves for each detector position. The instrument-independent data were then fitted to models using the SasView software package version.[42]

**Rheology.** Rheological measurements were undertaken on an Anton Paar MCR 301 rheometer. A cup and vane geometry, with a measuring gap of 1.8 mm, was used throughout to perform strain and frequency sweeps. In all cases, 2 mL gels were prepared in 7 mL Sterilin vials and left to stand overnight at room temperature before measurements. Frequency sweeps were collected at a range of frequencies varying between 1 rad $s^{-1}$ to 100 rad $s^{-1}$, at a constant strain of 0.5 %. Strain sweeps were performed from 0.1 % to 1000 % at a frequency of 10 rad $s^{-1}$. All the measurements were carried out at room temperature.

**Super-resolution microscopy: Optical Setup.** PAINT imaging was carried out with a Nikon N-STORM microscope configured for total internal reflection (TIR), using a Perfect Focus System. Irradiation under TIR conditions allowed to avoid illumination of out of focus structures, reducing background contributions and allowing for single event localizations. After laser excitation (647 nm), fluorescence was collected by a 100× 1.49 NA oil immersion objective; it passed through a quad-band dichroic mirror (97335 Nikon) and was collected by a Hamamatsu ORCA Flash 4.0 CMOS camera (pixel size 160 nm). A movie was produced where blinking generated by molecule emission appears like circular spots lasting a few acquisition frames. Three-dimensional measurements were carried out with the astigmatism method: a cylindrical lens was introduced in

the light path, producing optical aberrations (elongation and inclination) of the detected fluorescence spots depending on the z-position of the emitter.

2D images were acquired at 30 ms 20-30k frames. 3D images were acquired at 30 ms, 6-10k frames, 20 stacks of 120 nm, total of 1.85 μm high.

The NIS elements Nikon software generates a list of localizations by Gaussian fitting the fluorescence spots of binding dyes in the acquired movie of diffraction-limited images. To avoid overcounting, bindings detected in consecutive frames are counted as single by the software. For 3D imaging, the z-coordinate of the localization is retrieved from the ellipticity and the inclination of the elongated spots.

**Mesh quantification:** ImageJ was used to analyse and measure the mesh size of the gel. The threshold of the images was adjusted so the background pixels corresponded to black pixels and fibre pixels corresponded to white pixels. The scale was set and the function "analyse particles" was run. This software basically clusters the black pixels surrounded by white pixels. Visual inspection was carried out to ensure the correct recognition of the mesh, and manual selection was also applied to include the non-recognized ones. The number of pixels/clusters are counted and transformed into area, sitting a threshold of 4 pixels to minimize the wrong identifications by the software.

**Resolution calculation.** Resolution Calculations STORM module in the Nikon NIS-software is able to automatically calculate the localization precision distribution for each image. As can be seen below (Fig. 6.2.5), the maximum of the distribution is 9.25 nm, with most of the localizations below 9.25 nm and decreasing sharply from 9.25 nm to 11 nm.

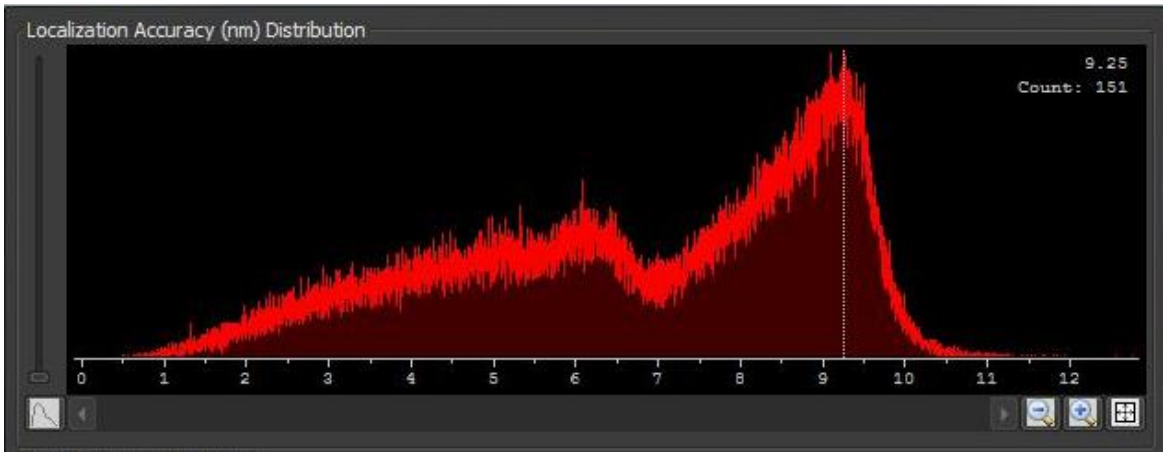


Figure 6.2.5. Localization accuracy distribution extracted from a PAINT image with the Nikon NIS-software.

These numbers are well in agreement with our calculations. The localization precision is defined as:

$$\sigma^2 = \frac{S^2 + \frac{a}{12}}{N} + \frac{8\pi^2 s^4 b^2}{a^2 N^2}$$

s is the width of the PFS

N is the number of detected photons

a is the size of pixels on the camera

b is the background intensity

This can be simplified to:[2]

$$\sigma_x \geq \frac{s}{\sqrt{N}}$$

The average s for one of the images was calculated to be 246.81 ± 10.67 nm (for 218581 localizations). Also, the average for the number of photons for the same image is 606.6, with a significant population above that value. Therefore, as the average s= 246.81 nm and the average N=606.6 photons, $\sigma_x \geq 10.02$ nm, resulting in the claimed 20 nm resolution. Single molecule localization and fitting was performed using the STORM module of NIS Elements by performing a Gaussian fitting based on the following parameters:

Minimum and maximum height: We selected the darkest bright point to be identified as a molecule and its brightness minus the background intensity was the minimum height. In our case it was set to 250. The maximum height for the used system with a sCMOS camera is 65000 and the baseline was set to 100. For the PSF, the initial fit width was set to 300, with a minimum with of 200 and a maximum width of 400. The average for an image was calculated to be 246.81±10.67 nm (based on 218581 localizations). This parameter was tested on different frames and optimized using all frames selected. This analysis yielded a molecule list in binary format from which multiple emitters are automatically discarded prior to analysis. STORM NIS-software renders a molecule list in binary format whose coordinates are translated into an image. STORM images are shown in cross or gaussian display mode in Nikon software. Cross takes into account directly the localizations while Gaussian, the one used in our case, is a Gaussian rendering of the localizations considering lateral localization accuracy (with an average of 17.9 ± 4.6) for each localization.

**Imaging the gel**: During acquisition few signals coming from the free (non-attached) Cy5FF are localized. This noise signal is much weaker than the signal coming from binding events because in this case the probe is immobilized for a long period. For this reason, we set a intensity threshold of the signal to reconstruct the image with the brighter events minimizing the noise.

Also, we obtained better results in apparent lower density areas, especially in the borders of the gel. Imaging the inner parts of the gel by PAINT was not possible even though we were able to image by low resolution TIRF microscopy. We attribute this behaviour to the very low diffusion of the probes inside the gel.

**Width measure:** in order to emphasise the differences, we performed the same kind of fibre width measurement made in figure 6.2.3 c, but using the low res image. First of all, we can only differentiate three fibres, instead of 5. The width measured for fibre 1, 2 and 3 are 488 nm ±46 nm, 505 nm ±37 nm and 411 nm ±50 nm. The results yielded from analysing the low-resolution image show an increase in both size and standard deviation. Also, we want to highlight that like this we observe no difference among fibres width, while using the high-resolution image we could observe those differences.

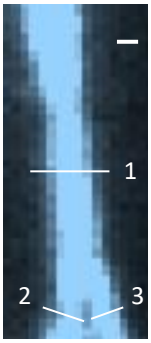


Figure 6.2.6 Zoom in of a low-resolution image, corresponding to the same field as in Fig 6.2.3 c. Scale bar: 200 nm.

**Small Angle Neutron Scattering**

To fit the SANS data, the following scattering length densities (SLDs) were used:

FmocFF: 2.757 x $10^{-6}$ $Å^{-2}$

$D_2O$: 6.393 x $10^{-6}$ $Å^{-2}$

$d_6$-DMSO: 5.278 x $10^{-6}$ $Å^{-2}$

The SLDs were calculated using the software available from NIST.[44] An assumed density of 1.58 g/mL was used for FmocFF.

The scattering data fit best to a flexible elliptical cylinder model combined with a power law to take into account the scattering at low Q; this combined model was generated in SASView.[42] The data can also be fitted to a flexible cylinder with a power law, but in this case, it is necessary to include a significant polydispersity in the radius (0.3) to access a reasonable fit and, even then, the fit is not as good as to the flexible elliptical cylinder model. As such, the flexible elliptical cylinder and power law model was used. The parameters from this fit are shown in Table 6.1.

Table 6.1 Fit parameters obtained from a fit to the SANS data using a flexible elliptical cylinder model combined with a power law. * indicates the value was fixed for the fitting procedure.

| | **20:80 DMSO: $D_2O$** | **40:60 DMSO: $D_2O$** |
|---|---|---|
| Background ($cm^{-1}$) | 0.00005* | 0.00005* |
| Scale (power law) | $5.18x10^{-6}\pm 5.24x10^{-7}$ | $1.80x10^{-6}\pm 4.21x10^{-7}$ |
| Power Law | $2.83 \pm 0.01$ | $2.90\pm 0.01$ |
| Scale (flexible elliptical cylinder) | $6.69x10^{-4}\pm 5.23x10^{-5}$ | $4.35x10^{-4}\pm 1.58x10^{-5}$ |

| | | |
|---|---|---|
| Length (Å) | 1448±16 | 1458±16 |
| Kuhn Length (Å) | 89±1.3 | 85±1.8 |
| Radius (Å) | 33.5±0.1 | 33.1±0.2 |
| Axis Ratio | 2.24±0.01 | 2.26±0.02 |
| c2 | 3.5674 | 1.777 |

### 6.2.5 References


1. Terech, P.; Weiss, R. G. Low Molecular Mass Gelators of Organic Liquids and the Properties of Their Gels. Chem. Rev. 1997, 97 (8), 3133–3160.
2. Hirst, A. R.; Escuder, B.; Miravet, J. F.; Smith, D. K. High-Tech Applications of Self-Assembling Supramolecular Nanostructured Gel-Phase Materials: From Regenerative Medicine to Electronic Devices. Angew. Chem. Int. Ed. 2008, 47 (42), 8002–8018.
3. Estroff, L. A.; Hamilton, A. D. Water Gelation by Small Organic Molecules. Chem. Rev. 2004, 104 (3), 1201–1218.
4. Weiss, R. G. The Past, Present, and Future of Molecular Gels. What Is the Status of the Field, and Where Is It Going? J. Am. Chem. Soc. 2014, 136 (21), 7519–7530.
5. Weiss, R. G. Controlling Variables in Molecular Gel Science: How Can We Improve the State of the Art? Gels 2018, 4 (2), 25.
6. Yan, C.; Pochan, D. J. Rheological Properties of Peptide-Based Hydrogels for Biomedical and Other Applications. Chem. Soc. Rev. 2010, 39 (9), 3528–3540.
7. Sathaye, S.; Mbi, A.; Sonmez, C.; Chen, Y.; Blair, D. L.; Schneider, J. P.; Pochan, D. J. Rheology of Peptide- and Protein-Based Physical Hydrogels: Are Everyday Measurements Just Scratching the Surface? WIREs Nanomedicine Nanobiotechnology 2015, 7 (1), 34–68.
8. Mears, L. L. E.; Draper, E. R.; Castilla, A. M.; Su, H.; Zhuola; Dietrich, B.; Nolan, M. C.; Smith, G. N.; Doutch, J.; Rogers, S.; Akhtar, R.; Cui, H.; Adams, D. J. Drying Affects the Fiber Network in Low Molecular Weight Hydrogels. Biomacromolecules 2017, 18 (11), 3531–3540.
9. Zhong, S.; Pochan, D. J. Cryogenic Transmission Electron Microscopy for Direct Observation of Polymer and Small-Molecule Materials and Structures in Solution. Polym. Rev. 2010, 50 (3), 287–320.
10. Guilbaud, J.-B.; Saiani, A. Using Small Angle Scattering ( SAS ) to Structurally Characterise Peptide and Protein Self-Assembled Materials. Chem. Soc. Rev. 2011, 40 (3), 1200–1210.
11. Kubota, R.; Nakamura, K.; Torigoe, S.; Hamachi, I. The Power of Confocal Laser Scanning Microscopy in Supramolecular Chemistry: In Situ Real-Time Imaging of Stimuli-Responsive Multicomponent Supramolecular Hydrogels. ChemistryOpen 2020, 9 (1), 67–79.

12. Colquhoun, C.; Draper, E. R.; Schweins, R.; Marcello, M.; Vadukul, D.; Serpell, L. C.; Adams, D. J. Controlling the Network Type in Self-Assembled Dipeptide Hydrogels. Soft Matter 2017, 13 (9), 1914–1919.
13. Pujals, S.; Feiner-Gracia, N.; Delcanale, P.; Voets, I.; Albertazzi, L. Super-Resolution Microscopy as a Powerful Tool to Study Complex Synthetic Materials. Nat. Rev. Chem. 2019, 3 (2), 68–84.
14. Wöll, D.; Flors, C. Super-Resolution Fluorescence Imaging for Materials Science. Small Methods 2017, 1 (10), 1700191.
15. Post, R. a. J.; van der Zwaag, D.; Bet, G.; Wijnands, S. P. W.; Albertazzi, L.; Meijer, E. W.; van der Hofstad, R. W. A Stochastic View on Surface Inhomogeneity of Nanoparticles. Nat. Commun. 2019, 10 (1), 1663.
16. Delcanale, P.; Miret-Ontiveros, B.; Arista-Romero, M.; Pujals, S.; Albertazzi, L. Nanoscale Mapping Functional Sites on Nanoparticles by Points Accumulation for Imaging in Nanoscale Topography (PAINT). ACS Nano 2018, 12 (8), 7629–7637.
17. Feiner-Gracia, N.; Beck, M.; Pujals, S.; Tosi, S.; Mandal, T.; Buske, C.; Linden, M.; Albertazzi, L. Super-Resolution Microscopy Unveils Dynamic Heterogeneities in Nanoparticle Protein Corona. Small 2017, 13 (41), 1701631.
18. Habuchi, S. Super-Resolution Molecular and Functional Imaging of Nanoscale Architectures in Life and Materials Science. Front. Bioeng. Biotechnol. 2014, 2.
19. Onogi, S.; Shigemitsu, H.; Yoshii, T.; Tanida, T.; Ikeda, M.; Kubota, R.; Hamachi, I. In Situ Real-Time Imaging of Self-Sorted Supramolecular Nanofibres. Nat. Chem. 2016, 8 (8), 743–752.
20. Hu, X.; Liao, M.; Gong, H.; Zhang, L.; Cox, H.; Waigh, T. A.; Lu, J. R. Recent Advances in Short Peptide Self-Assembly: From Rational Design to Novel Applications. Curr. Opin. Colloid Interface Sci. 2020, 45, 1–13.
21. Du, X.; Zhou, J.; Shi, J.; Xu, B. Supramolecular Hydrogelators and Hydrogels: From Soft Matter to Molecular Biomaterials. Chem. Rev. 2015, 115 (24), 13165–13307.
22. Draper, E. R.; Adams, D. J. Controlling the Assembly and Properties of Low-Molecular-Weight Hydrogelators. Langmuir 2019, 35 (20), 6506–6521.
23. D. Martin, A.; Thordarson, P. Beyond Fmoc: A Review of Aromatic Peptide Capping Groups. J. Mater. Chem. B 2020, 8 (5), 863–877. https://doi.org/10.1039/C9TB02539A.
24. Makam, P.; Gazit, E. Minimalistic Peptide Supramolecular Co-Assembly: Expanding the Conformational Space for Nanotechnology. Chem. Soc. Rev. 2018, 47 (10), 3406–3420.
25. Mahler, A.; Reches, M.; Rechter, M.; Cohen, S.; Gazit, E. Rigid, Self-Assembled Hydrogel Composed of a Modified Aromatic Dipeptide. Adv. Mater. 2006, 18 (11), 1365–1370.
26. Diaferia, C.; Morelli, G.; Accardo, A. Fmoc-Diphenylalanine as a Suitable Building Block for the Preparation of Hybrid Materials and Their Potential Applications. J. Mater. Chem. B 2019, 7 (34), 5142–5155.
27. Jayawarna, V.; Richardson, S. M.; Hirst, A. R.; Hodson, N. W.; Saiani, A.; Gough, J. E.; Ulijn, R. V. Introducing Chemical Functionality in Fmoc-Peptide Gels for Cell Culture. Acta Biomater. 2009, 5 (3), 934–943.
28. Chen, L.; Pont, G.; Morris, K.; Lotze, G.; Squires, A.; Serpell, L. C.; Adams, D. J. Salt-Induced Hydrogelation of Functionalised-Dipeptides at High PH. Chem. Commun. 2011, 47 (44), 12071–12073.

29. Jayawarna, V.; Ali, M.; Jowitt, T. A.; Miller, A. F.; Saiani, A.; Gough, J. E.; Ulijn, R. V. Nanostructured Hydrogels for Three-Dimensional Cell Culture Through Self-Assembly of Fluorenylmethoxycarbonyl–Dipeptides. Adv. Mater. 2006, 18 (5), 611–614.
30. Ryan, D. M.; Nilsson, B. L. Self-Assembled Amino Acids and Dipeptides as Noncovalent Hydrogels for Tissue Engineering. Polym. Chem. 2011, 3 (1), 18–33.
31. Scott, G.; Roy, S.; Abul-Haija, Y. M.; Fleming, S.; Bai, S.; Ulijn, R. V. Pickering Stabilized Peptide Gel Particles as Tunable Microenvironments for Biocatalysis. Langmuir 2013, 29 (46), 14321–14327.
32. Ryu, J.; Kim, S.-W.; Kang, K.; Park, C. B. Mineralization of Self-Assembled Peptide Nanofibers for Rechargeable Lithium Ion Batteries. Adv. Mater. 2010, 22 (48), 5537–5541.
33. Raeburn, J.; Mendoza-Cuenca, C.; Cattoz, B. N.; Little, M. A.; Terry, A. E.; Cardoso, A. Z.; Griffiths, P. C.; Adams, D. J. The Effect of Solvent Choice on the Gelation and Final Hydrogel Properties of Fmoc–Diphenylalanine. Soft Matter 2015, 11 (5), 927–935.
34. Dudukovic, N. A.; Zukoski, C. F. Mechanical Properties of Self-Assembled Fmoc-Diphenylalanine Molecular Gels. Langmuir 2014, 30 (15), 4493–4500.
35. Sharonov, A.; Hochstrasser, R. M. Wide-Field Subdiffraction Imaging by Accumulated Binding of Diffusing Probes. Proc. Natl. Acad. Sci. 2006, 103 (50), 18911–18916.
36. Pujals, S.; Tao, K.; Terradellas, A.; Gazit, E.; Albertazzi, L. Studying Structure and Dynamics of Self-Assembled Peptide Nanostructures Using Fluorescence and Super Resolution Microscopy. Chem. Commun. 2017, 53 (53), 7294–7297.
37. Branco, M. C.; Pochan, D. J.; Wagner, N. J.; Schneider, J. P. Macromolecular Diffusion and Release from Self-Assembled β-Hairpin Peptide Hydrogels. Biomaterials 2009, 30 (7), 1339–1347.
38. Wallace, M.; Adams, D. J.; Iggo, J. A. Analysis of the Mesh Size in a Supramolecular Hydrogel by PFG-NMR Spectroscopy. Soft Matter 2013, 9 (22), 5483–5491.
39. Sutton, S.; Campbell, N. L.; Cooper, A. I.; Kirkland, M.; Frith, W. J.; Adams, D. J. Controlled Release from Modified Amino Acid Hydrogels Governed by Molecular Size or Network Dynamics. Langmuir 2009, 25 (17), 10285–10291.
40. Ozbas, B.; Rajagopal, K.; Schneider, J. P.; Pochan, D. J. Semiflexible Chain Networks Formed via Self-Assembly of β-Hairpin Molecules. Phys. Rev. Lett. 2004, 93 (26), 268106.
41. Aufderhorst-Roberts, A.; Frith, W. J.; Kirkland, M.; Donald, A. M. Microrheology and Microstructure of Fmoc-Derivative Hydrogels. Langmuir 2014, 30 (15), 4483–4492.
42. www.sasview.org.
43. H. Deschout, F. C. Zanacchi, M. Mlodzianoski, A. Diaspro, J. Bewersdorf, S. T. Hess and K. Braeckmans. Precisely and accurately localizing single emitters in fluorescence microscopy. Nature Methods, 2014, 11, 253-266.
44. https://www.ncnr.nist.gov/resources/activation/)

## 6.3 Mapping the optical properties of highly fluorophore loaded vesicles

*This chapter reproduces almost literally the findings reported in Ultrabright Föster Resonance Energy Transfer Nanovesicles: The Role of Dye Diffusion. J. Morla-Folch, G. Vargas-Nadal, E. Fuentes, S. Illa-Tuset, M. Köber, C. Sissa, S. Pujals, A. Painelli, J. Veciana, J. Faraudo, K. D. Belfield, L. Albertazzi, and N. Ventosa*. Chem. Mater. 2022, in press.*

### 6.3.1 Introduction

Molecular imaging plays a vital role in the healthcare sector since abnormal conditions and diseases are often diagnosed through imaging, and relevant therapeutic approaches are often guided by imaging.[1] Optical imaging is a highly sensitive technique, easier and less expensive than other imaging techniques, including tomography, magnetic resonance imaging (MRI), or ultrasound imaging.[2] Moreover, optical imaging offers the possibility of employing multiple probes with different spectral features for multichannel imaging. The main drawback of optical imaging is the restricted tissue penetration, limited by the strong scattering and absorption of the various tissue components. Moreover, in the optical detection of single molecules, the brightness of organic dyes is limited by molar absorption coefficients lower than 300,000 $M^{-1}$ $cm^{-1}$ and quantum yields below unity.[3] In this perspective, fluorescent organic nanoparticles (FONs) offer a promising alternative.

Engineering FONs exploits the flexibility offered by supramolecular synthesis and molecular self-assembly, opening the way to multifunctional probes. Moreover, FONs can harbor hundreds of fluorescent dyes to achieve enhanced brightness. FONs have proven successful in molecular imaging methods and are therefore gaining popularity in the medical imaging community.[4,5] This spurred the recent development of several approaches to synthesize bright FONs, notably based on the direct assembly of small organic dyes into nanoparticles, [6,7] the entrapment of fluorophores in dendrimer-like structures,[8–10] or encapsulation of dyes in lipidic[11,12] or polymer[13–15] particles. However, the design of bright FONs of small diameters remains challenging mainly because the number of fluorophores per particle is limited due to fluorescence self-quenching at high dye loading, which compromises the FON brightness.[16,17] The paradigm is even more challenging if we want to exploit Förster resonance energy transfer (FRET) at the organic nanostructure since FRET requires interchromophore distances of 1–10 nm.[18] In FRET-based FONs, the emission signature can be fine-tuned by changing the nature, amount, and ratio of the fluorescence entities (FRET donor and acceptor). FRET FONs also allow ratiometric measurements, providing built-in self-calibration for signal correction, enabling more sensitive and reliable detection.[19] Moreover, FRET ensures large Stokes shifts, thereby reducing background noise, and represents an attractive tool to monitor nanoparticle stability for theranostic applications. Nonetheless, there are few published works on FONs showing FRET, [20–24] but no information regarding the optical properties heterogeneity, studied particle-by-particle.

In previous works, novel FONs built from quatsomes (QSs) we reported, where they were loaded with lipophilic dyes.[25,26] QSs are innovative nanovesicles made by the self-assembly of quaternary ammonium surfactants and sterols. These nanovesicles are unilamellar with a fluid-like membrane

and high colloidal stability.[27] QSs are produced through the green technology DELOS-susp, a sustainable process, which allows a high control of the molecular self-assembling process and yields nanovesicular formulations with a high degree of nanovesicle homogeneity.[28,29] Taking into account the challenge that represents for soft materials to achieve long-term stability, QSs, which have demonstrated >3 years of colloidal stability,[30] have aroused considerable interest in biomedical applications (i.e., as bioimaging nanoprobes).[31−34] More recently, QSs loaded with a FRET pair composed of DiI (1,1'-dioctadecyl-3,3,3'3'-tetramethylindocarbocyanine perchlorate) and DiD (1,1'-dioctadecyl-3,3,3',3'-tetramethylindodicarbo-cyanine perchlorate), the amphiphilic analogs of Cy3 and Cy5, respectively, were described as promising nanoprobes.[34] Bulk spectroscopic measurements demonstrated FRET in the colloidal QS formulations, with DiI and DiD corresponding to the energy donor and acceptor, respectively.

Herein, we study and describe for the first time the impact of different dye loadings on the vesicle-to-vesicle homogeneity in brightness and FRET. A set of QSs with different DiI–DiD loadings is investigated through direct and individual observation by total internal reflection fluorescence (TIRF) microscopy and stochastic optical reconstruction microscopy (STORM). Characterization with conventional fluorescence spectroscopy is sufficient to allow the relative estimation of FRET efficiency and brightness at the nanoparticle level. Through this detailed inspection of the colloidal formulation, we validate the high vesicle-to-vesicle homogeneity in terms of physicochemical properties as well as spectral properties.

## 6.3.2 Results and discussion

Four different colloidal formulations of QS nanovesicles, composed of hexadecyltrimethyl-ammonium bromide surfactant (CTAB) and cholesterol, loaded with different amounts of DiI and DiD dyes were prepared (Fig. 6.3.1 a). These formulations (hereafter referred to as QS-I,D), were prepared following DELOS-susp methodology that yielded QS with equimolar relationship between the dyes (see methods section). DELOS-susp is a method based on the use of green compressed $CO_2$, that ensures a robust and reproducible molecular self-assembly of the nanovesicle membrane components.[25,28,29] The final nanoformulations in aqueous media showed low morphology and size dispersity, as well as dye loading homogeneity (see Table 6.3.1). In the quatsome formulation, the carbocyanine dyes are concentrated at the nanovesicle membrane compartment,[25] which represents 22% of the total volume of the nanovesicle (methods section, table 6.3.3). To calculate the dye concentration per nanovesicle, the group of Ventosa considered the number of fluorophores per nanovesicle and the membrane volume of the QS. Notably, the dye concentration per quatsome is not affected by dilution since the dyes stay entrapped in the QS membrane (dilution reduces the number of nanovesicles per unit volume, but not the number of dyes in the nanovesicle, see Fig. 6.3.1 b). Hence, four QS-I,D formulations were prepared, varying the total dye concentration (2 to 143 mM), keeping constant the concentration of the membrane components and keeping the dye combination equimolar (Table 6.3.1).

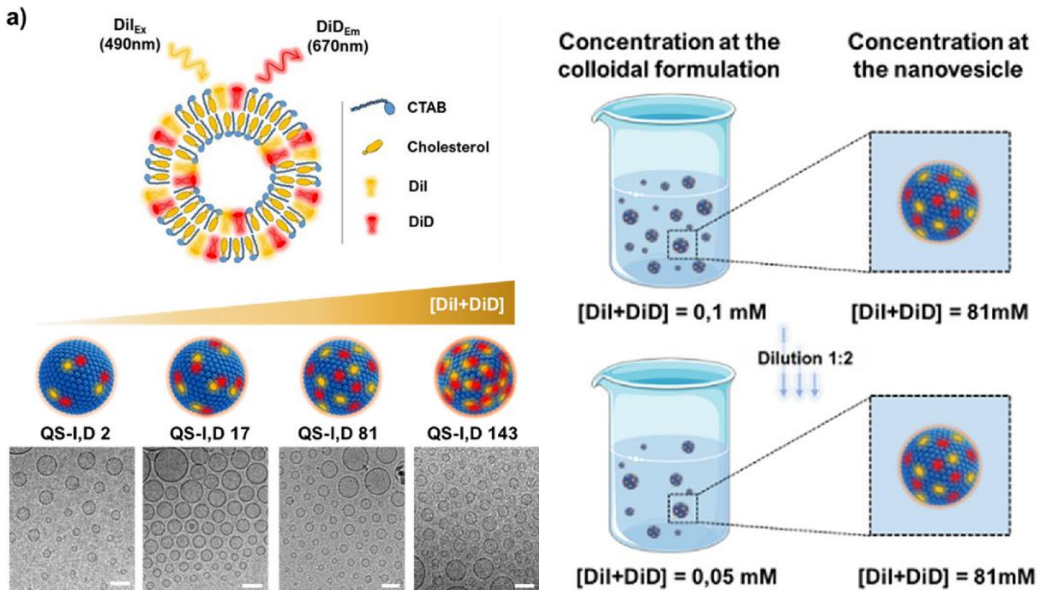


Figure 6.3.1 Schematic representation and characterization of the FRET QS nanovesicles under study. (a) Schematic representation of QS loaded with different amounts of DiI and DiD dyes, at an equimolar relationship between both dyes, and the representation of its components. Cryo-TEM images are displayed for each sample (scale bar = 100 nm). (b) Representation of the different impacts of dilution process over dye concentration in the bulk colloidal formulation and over dye concentration at the nanostructure.

Table 6.3.1 Fluorophore concentration per QS

| | concentration per nanovesicle (mM)[a] | | |
|---|---|---|---|
| sample | DiI | DiD | total |
| QS-I,D 2 | 1 | 0.9 | 1.9 |
| QS-I,D 17 | 9 | 7.8 | 16.8 |
| QS-I,D 81 | 41 | 40 | 81 |
| QS-I,D 143 | 73 | 70 | 143 |

[a]Calculated as mol dye/QS membrane volume (see Table S5), error ± 5%.

Physicochemical Characterization of FRET Nanoprobes at the Nanoscale

The size and morphology of the fluorescent nanovesicles were previously characterized by nanoparticle tracking analysis (NTA) and cryo-transmission electron microscopy (cryo-TEM). Cryo-TEM microscopy revealed spherical and unilamellar vesicles with high homogeneity in terms of morphology and membrane lamellarity (Fig. 6.3.1 a). NTA showed a mean hydrodynamic diameter of ca. 141 nm for all four systems (Fig. 6.3.2), and a fairly narrow size distribution for a nanovesicle. Importantly, the different dye concentration at the nanovesicles affects neither the size or morphology of the nanostructures nor the vesicle-to-vesicle homogeneity.[28]

After, we evaluated the size by stochastic optical reconstruction microscopy (STORM). Our results showed spherical fluorescents dots of very similar sizes, ca. 155 nm, taking into account the lower resolution of the technique. Even though being able to image the QS using long image acquisition

times, we observed a qualitative reduced dye blinking compared to other systems, maybe related with the local concentration of dye and the confinement into the dense vesicle membrane.

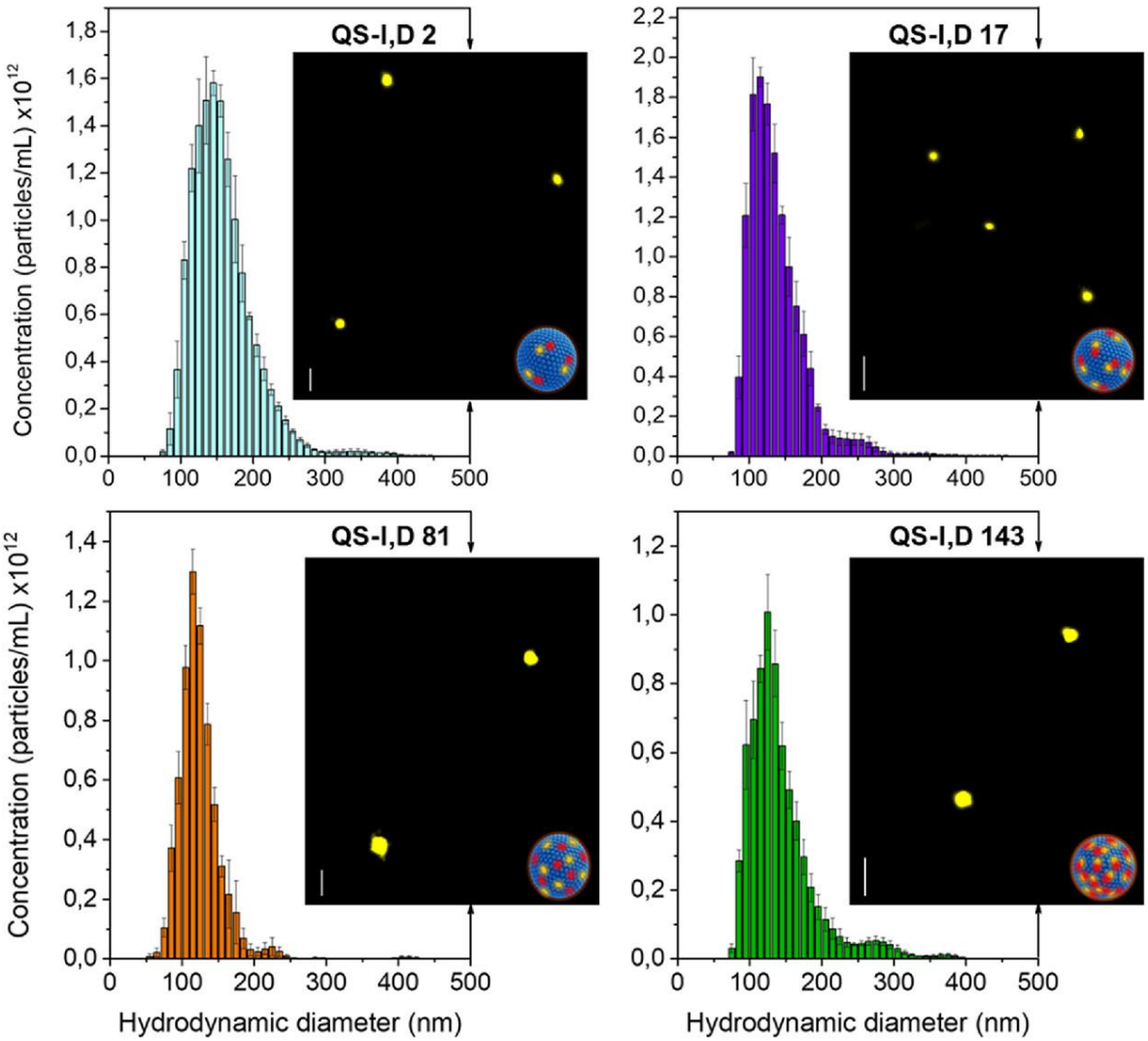


Figure 6.3.2 NTA and STORM of FRET QS nanovesicles. Hydrodynamic diameter distribution obtained by NTA and STORM images of four QS-I,D colloidal formulations with increasing dye concentration per nanovesicle (2, 17, 81, and 143 mM; 300 nm scale bar).

The controlled morphology and size of the nanoprobes at different nanoconcentrations (from 2 to 143 mM) demonstrate significant versatility of the QS nanoplatforms. Specifically, they can be loaded with different molecules[26] in a large range of dye concentrations without compromising the size, homogeneity, or stability at the nanoscale.

Brightness and FRET efficiency measurement in bulk

On one side, FRET efficiency corresponds the amount of energy transferred from donor to acceptor, and it is proportional to the inverse sixth power of the distance between fluorophores.[18] In bulk FRET efficiency was evaluated by conventional fluorescence spectroscopy, comparing

absorption with excitation spectras) together with the theoretical brightness. In figure 6.3.3, we can observe the FRET efficiency values obtained for each formulation.

On the other side, the brightness of fluorescent probes constitutes an important attribute for fluorescence imaging since a particle with high brightness improves the signal-to-noise ratio, resulting in a better quality of the image and allowing for higher scanning speed.[3,35] Brightness per particle is defined by the product of quantum yield and the extinction coefficient. The quantum yield was measured with a quantum yield spectrometer (Quantaurus), and the extinction coefficient extracted from Lambert-Beer law. In figure 6.3.3, the measured brightness is reported.

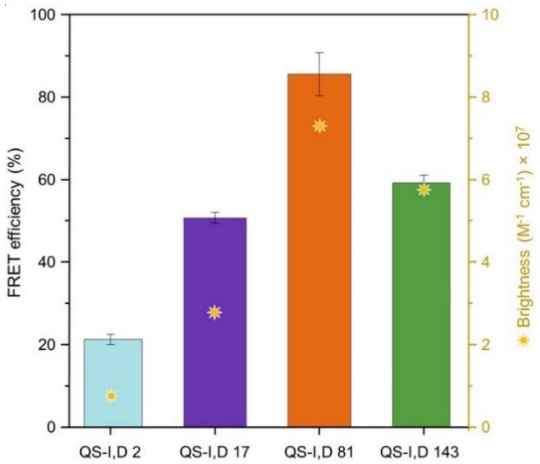


Figure 6.3.3 Steady-state fluorescence acquired from colloidal formulations of FRET QS nanovesicles. FRET efficiency calculated from the spectroscopic measurements (absorption in comparison to excitation) together with the theoretical brightness per vesicle.

These results showed that QS-I,D samples are exceptionally bright nanoparticles, with QS-I,D 81 being the best performing one. The high brightness of QS-I,D 81, was ten-fold brighter than QDots 655, what can be categorized as an ultrabright nanoparticle. As described by Sokolov and colleagues, "ultrabrightness" applies to systems whose brightness is at least one order of magnitude larger than QDs. [16,36,37]

Both FRET efficiency and brightness showed the same trend. Interestingly, from 2 to 81 mM, FRET brightness increased with loading. However, the formulation with higher concentration of dyes (143 mM) displayed less brightness and FRET efficiency than the 81 mM, suggesting that there is a maximum brightness achievable by increasing the dyes concentration. At these high concentrations dyes can probably self-quench fluorescence or even aggregate.[38]

Optical microscopy characterization of single QS

Next, we aimed to understand better how brightness and FRET values are distributed along the vesicles. For this reason, TIRF microscopy was then exploited to assess the vesicle-to-vesicle variability of brightness and FRET ratio. Relative values of brightness and FRET ratio were obtained simultaneously from single QS by TIRF microscopy for each QS-I,D formulation.

TIRF microscopy images obtained both collecting donor and acceptor emissions together and only acceptor emission. These images were then processed obtain the FRET ratio images (Fig.

6.3.4 a–d and methods section). After, all images were carefully analysed to measure particle by particle the relative brightness (photon counts) and FRET ratio values.

A box plot constructed from the FRET ratio per particle is shown in Figure 6.3.4 e. The results are in agreement with the bulk measurements, being the QS-I,D 81 the formulation with the highest mean value of the FRET ratio. More interestingly, ratiometric images provided information regarding the dispersity in FRET. It is clear that QS-I,D 2, 17 and 81 display low vesicle-to-vesicle FRET variability (65% of all QS-I,D 81 particles (n = 211) show deviations ≤10% of the mean value). Again, QS-I,D 143 shows a lower mean value than QS-I,D 81, however this time we can see a big variability that could not be observed before. 84% of all QS-I,D 143 nanovesicles show deviations >10%, clearly point to its unstable photophysical behavior. It is interesting to know that not only the mean but also the FRET distribution is affected by high dye concentrations, probably due to aggregation effects as mention before.

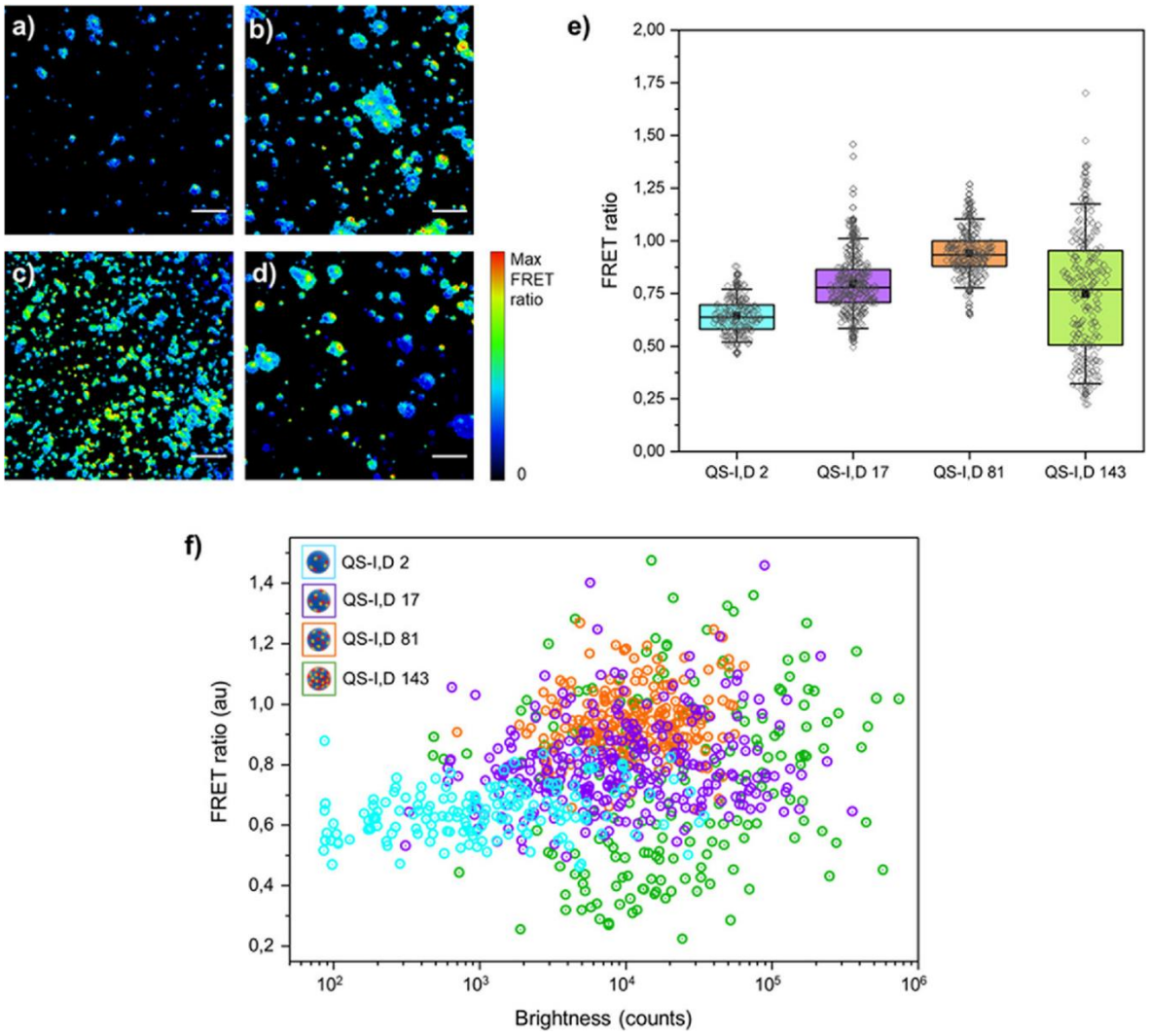


Figure 6.3.4 Brightness and FRET ratio studied at the single-particle level with TIRF microscopy. (a–d) FRET ratio represented from the TIRF images of QS-I,D 2, QS-I,D 17, QS-I,D 81, and QS-I,D 143, respectively (scale bar = 5 µm). (e) Box and whisker plots (indicating the 25–75 percentile and 1 SD) of the FRET ratio of individual nanoprobes, obtained from TIRF maps. Measured values are represented as empty black diamonds (n > 150) and mean values as filled black squares. (f) FRET ratio vs brightness of individual nanoprobes obtained by TIRF microscopy for different dye loadings.

Since with TIRF microscopy, FRET ratio and brightness were obtained from the same QS, we could simultaneously plot in Figure 6.3.4 f the dispersion of these two variables for each formulation. In this map, each dot represents a single quatsome and the position depends brightness and FRET ratio values. QS-I,D 2, QS-I,D 17, and QS-I,D 81 followed the same trend of increasing brightness and FRET ratio at higher dye concentration in the QS nanovesicle membrane. Interestingly, we can visualize how the centre of mass of the formulations moves towards higher FRET and brightness with increasing concentration, indicating the relation between these two parameters. Also, it can be visualized how polydisperse is QS-I,D 143 not only in FRET, but also in brightness.

Finally, QS-I,D 81 is the formulation with higher FRET and brightness, and it displays a great vesicle-to-vesicle homogeneity, which is an important attribute for fluorescent nanoprobes.

### 6.3.3 Conclusions

This chapter reports the characterization of FRET-based organic nanoparticles (quatsomes) specially designed as nanoprobes for imaging. Quatsomes at different dye loadings are investigated individually by TIRF microscopy and visualized by super-resolution microscopy. This detailed inspection of the colloidal formulation allowed to report a high vesicle-to-vesicle homogeneity in terms of physicochemical properties but also regarding optical emission, a crucial attribute for fluorescent nanoprobes. FRET ratio and brightness has been estimated in bulk by fluorescence spectroscopy and also particle-by-particle with TIRF microscopy, reporting FRET efficiencies >80%.

The optical characterization at the nanoscale demonstrates a good compositional homogeneity of the nanoparticles and discriminated the best local dye concentration in the nanovesicle for maximizing FRET and brightness. QS-I,D 81 represented the formulation with highest brightness and FRET efficiency. In this system, the dyes are located in the nanovesicle membrane, which represents 22% of the total volume of the nanovesicle. This tight localization represents an advantage in nanoparticle design with respect to other common organic nanoparticles where such a large local concentration is more challenging to achieve.

### 6.3.4 Materials and methods

Materials

5-Cholesten-3β-ol (purity 95%) was purchased from Panreac (Barcelona, Spain). Hexadecyltrimethylammonium bromide (CTAB, BioUltra for molecular biology, purity ≥99.0%) was obtained from Sigma-Aldrich. 1,1'-dioctadecyl-3,3,3',3'-tetramethyl-indocarbocyanine perchlorate (DiI) and 1,1'-dioctadecyl-3,3,3',3'-tetramethyl-indodicarbocyanine perchlorate (DiD) were purchased from Life Technologies (Carlsbad, USA). MilliQ water was used for all the sample preparation (Millipore Ibérica, Madrid, Spain). Ethanol (EtOH) was from Teknocroma (Sant Cugat del Vallès, Spain). Carbon dioxide ($CO_2$, 99.9% purity) was purchased from Carburos

Metálicos S.A. (Barcelona, Spain). All reagents and solvents purchased from commercial suppliers were used without further purification.

Quatsomes were made and kindly provided by Dr. Judit Morla and Guillem Vargas, under the supervision of Prf. Nora Ventosa.

Methods:

Sample preparation: Formulations were diluted 1/2, prior the addition to a flow chamber, made with glass slide, double sided tape and a coverslip on top. Once in the chamber, the sample was left for 1 min prior washing with Milli Q buffer.

Table S2. Characteristics of the dye-loaded nanoformulations.

| SAMPLE | [a] Dye concentration in bulk (μM) | | Ratio DiI:DiD | [b] Total dye loading ($x10^{-3}$) | [c] Dye encapsulation efficiency (%) | | [d] QS concentration (particle/mL) $x10^{11}$ | [d] Hydrodynamic diameter (nm) *NTA* | Mean diameter (nm) *STORM* |
|---|---|---|---|---|---|---|---|---|---|
| | DiI | DiD | | | DiI | DiD | | | |
| QS-I,D 2 | 2.5 | 2.2 | 1.00 : 0.95 | 1.0 | 100 | 88 | 141 ± 5 | 144 ± 1 | 141 ± 44 |
| QS-I,D 17 | 24.4 | 21.1 | 1.00 : 0.89 | 8.8 | 98 | 84 | 137 ± 9 | 156 ± 2 | 159 ± 49 |
| QS-I,D 81 | 55 | 53 | 1.00 : 0.88 | 25.0 | 100 | 96 | 68 ± 2 | 138 ± 3 | 156 ± 58 |
| QS-I,D 143 | 104 | 99 | 1.00 : 0.98 | 49.0 | 95 | 90 | 72 ± 4 | 125 ± 2 | 164 ± 49 |

[a] The final concentration of dyes was determined measuring the absorbance of the diafiltrated fluorescent Quatsomes in ethanol and applying the Lambert-Beer Law (see Experimental Section). [b] The dye loading indicates the relation in composition between the content of dye vs membrane components. It is calculated as [(mg dye/mL solution) / (mg membrane components CTAB+Chol /mL solution)]. The final concentration of membrane components was estimated lyophilizing the fluorescent Quatsomes after the diafiltration. [c] The dye encapsulation efficiency is defined as the ratio between the amount of dye present in the final formulation of QS-I,D and the initial amount of dye loaded into the reactor. final dye concentration in bulk and the initial dye concentration in bulk. [d] QS concentration and size distribution were measured by Nanoparticle Tracking Analysis (NTA). The averaged results are obtained from n ≥ 3 (error ± 7%)

DELOS-susp formulation technology:

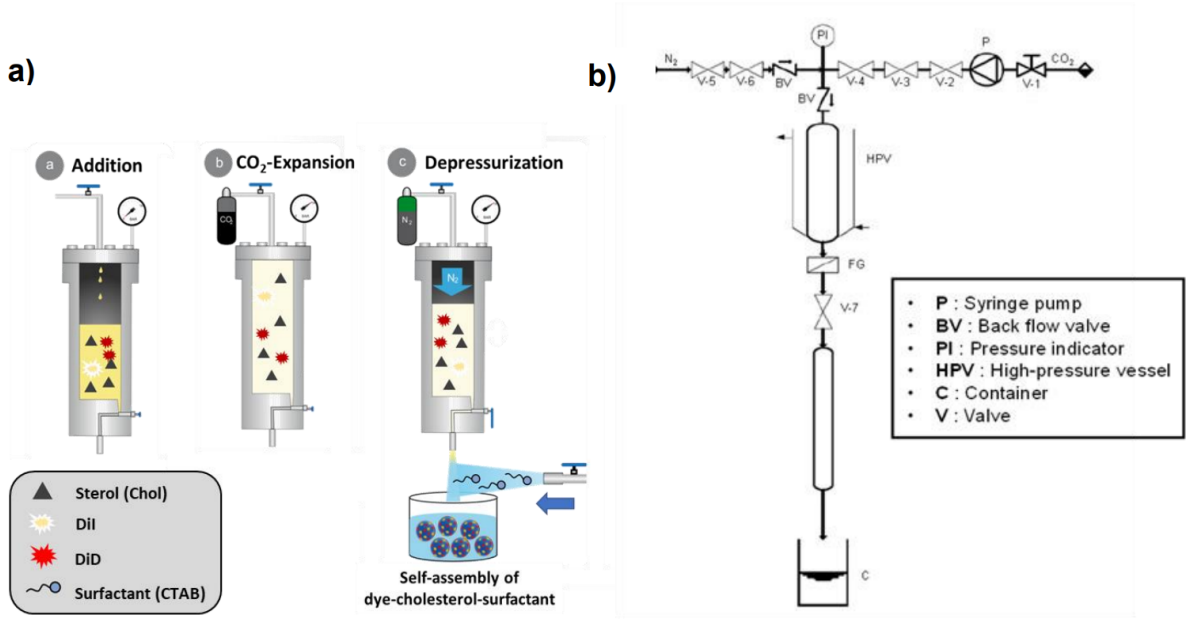


Figure 6.3.5. Equipment configuration of the small-scale reactor DELOS-susp (depressurization of an expanded liquid organic solution–suspension). This method has been previously described[39] and includes the depressurization of a $CO_2$- expanded organic liquid solution into an aqueous phase containing a solution or dispersion of a polar compound using mild conditions of temperature (308 K) and pressure (10 MPa). a) The general procedure includes: (a) Loading of the organic solution containing the membrane components (cholesterol and dyes); (b) Addition of liquid compressed $CO_2$ and formation of a $CO_2$ - expanded solution with all the membrane components dissolved; (c) Depressurization of the $CO_2$ - expanded solution into an aqueous solution containing the free surfactant (CTAB). b) The configuration comprises a 7.3 mL high-pressure vessel (HPV), whose temperature is controlled by an external thermostatic bath; a syringe pump (model 260D, ISCO Inc, USA) (P) to introduce $CO_2$ inside the HPV through valve V-4; a depressurization valve (V-7) from which the expanded liquid solution is depressurized into the aqueous phase placed in a collector (C) located after V-7, $N_2$ is pumped into the vessel through V-6. A one-way valve is located after V6 to prevent contamination of $CO_2$ in the $N_2$ line. V-2, V-3, and V-5 are dividing the $CO_2$ and $N_2$ pipelines. There is also a pressure indicator (PI) and another one-way valve before the vessel to prevent the backflow from HPV, which could lead to contamination of the gas lines.

Ratiometric FRET images:

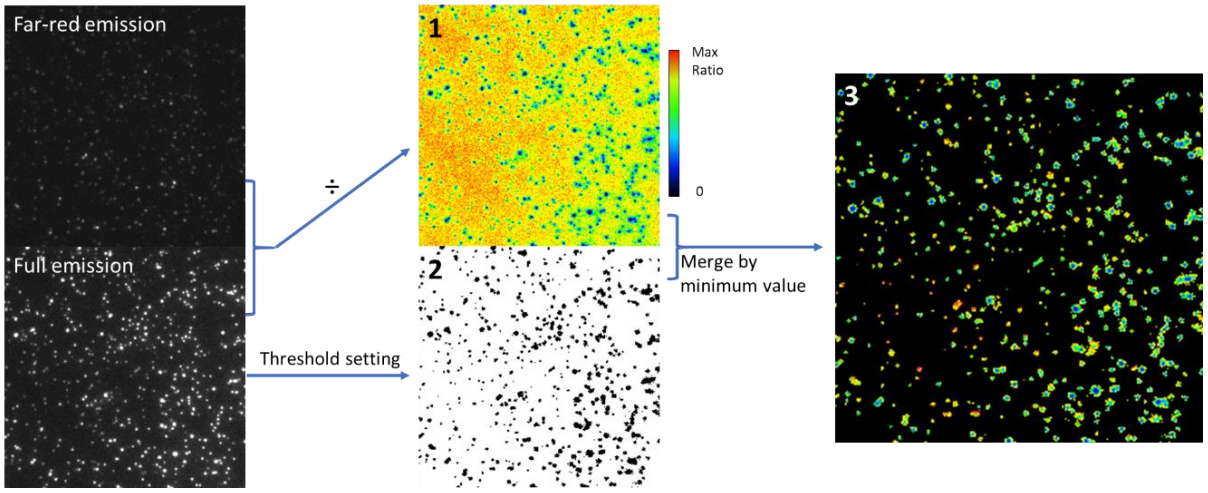


Figure 6.3.6 Procedure for FRET Ratio estimation through TIRF-microscopy. Schematic representation of the procedure for the calculation of FRET ratio through TIRF-microscopy.

The TIRF-images were analysed following the next steps for all the formulations:

1. Subtract background from original images. Divide the far-red emission image by the full-emission image to obtain a ratiometric image.
2. Threshold the full-emission image to obtain a mask (QS=1, Background=NAN).
3. Multiply the ratiometric image by the mask. (FRET ratio information)
4. Multiply the full-emission image by the mask. (Brightness Information)
5. Stack both masked images and measure both parameters in each QS. Individual QS were easily identified in the full-emission image (output of step 4), defining the delimiting area. This same area was used to measure the Brightness (output of step 4) and the FRET ratio (output of step 3).

Table 6.3.2 In the Table are presented the averaged values obtained per N nanovesicles studied (N=total number of nanoprobes interrogated, SD = Standard Deviation).

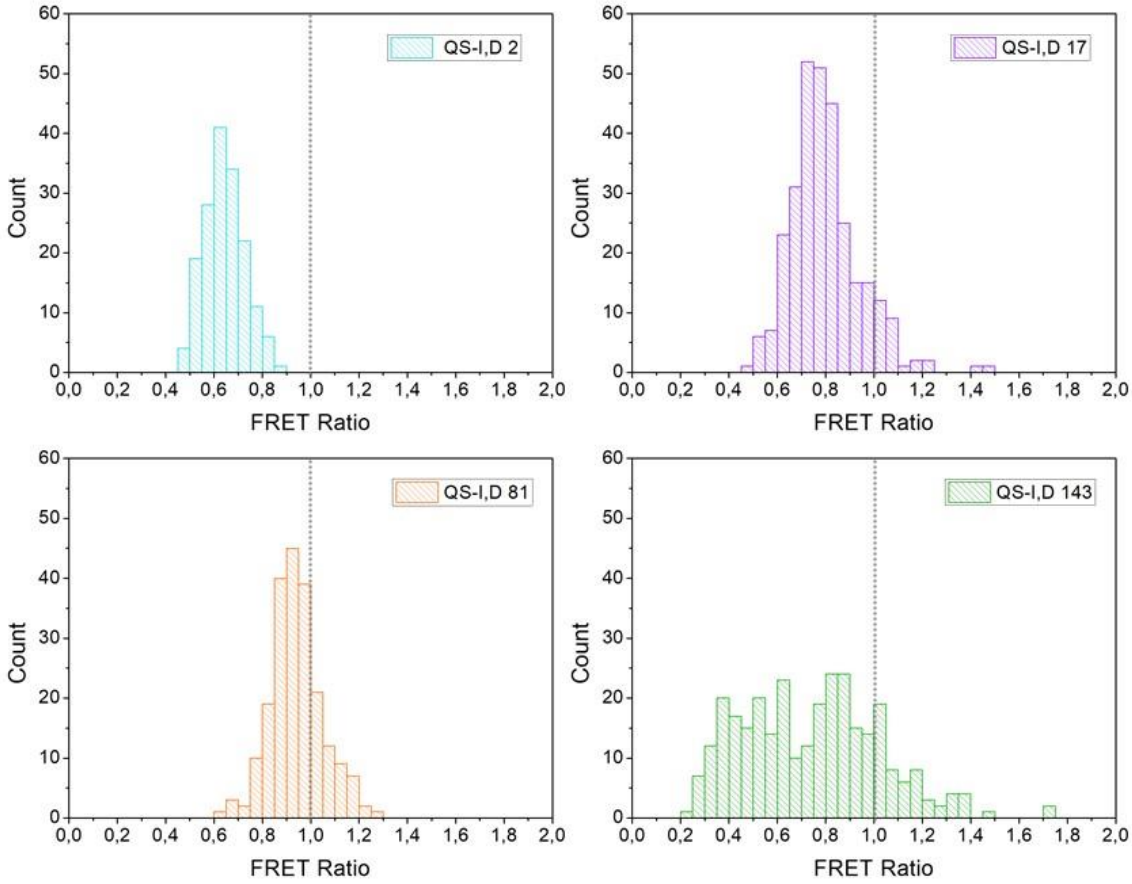


Figure 6.3.7 FRET ratio histograms represented for each nanoprobe.

Table 6.3.3 FRET ratio histogram averaged values, obtained per N nanovesicles studied (N=total number of nanoprobes interrogated, SD = Standard Deviation).

| Sample | N | Mean | SD | Median |
|---|---|---|---|---|
| **QS-I,D 2** | 166 | 0,645 | 0,083 | 0,638 |
| **QS-I,D 17** | 299 | 0,798 | 0,142 | 0,778 |
| **QS-I,D 81** | 211 | 0,941 | 0,109 | 0,933 |
| **QS-I,D 143** | 202 | 0,748 | 0,284 | 0,770 |

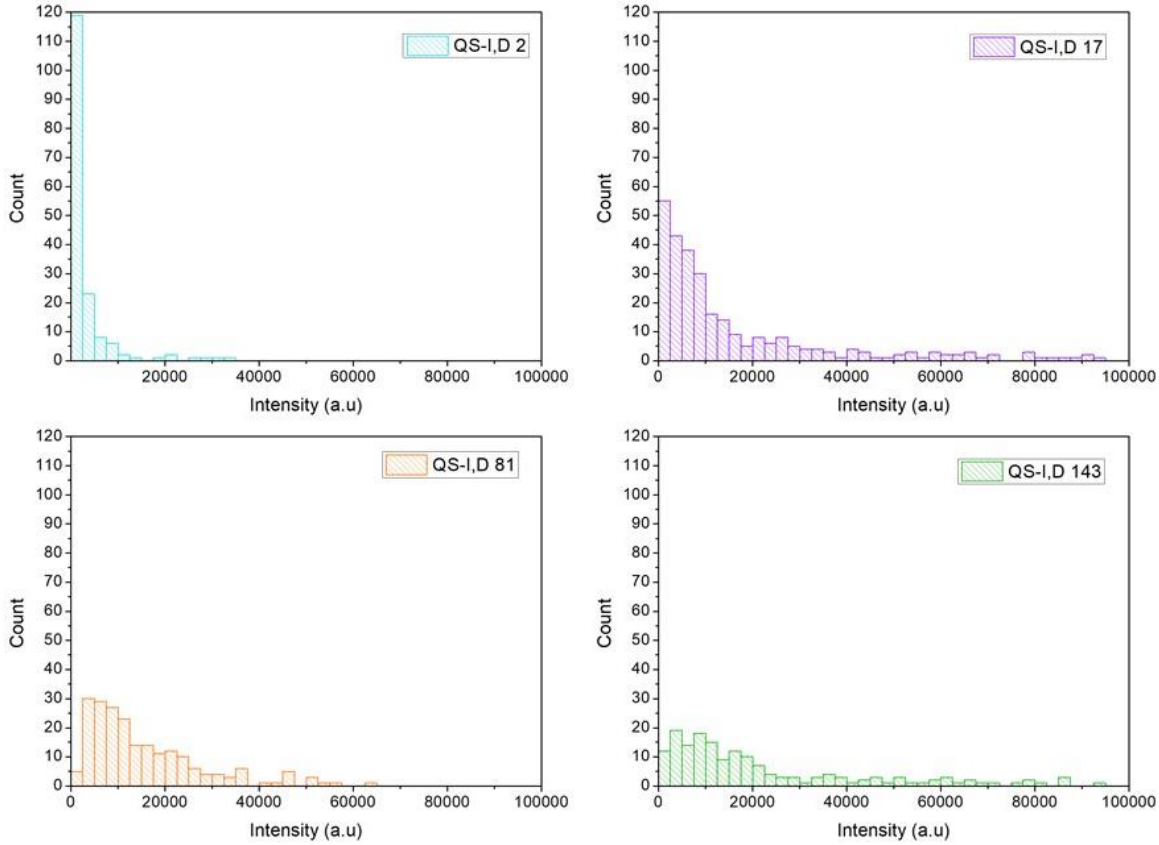


Figure 6.3.8 Brightness histogram calculated from TIRF-microscopy.

Table 6.3.4 Brightness (photon counts) histogram averaged values, obtained per N nanovesicles studied (N=total number of nanoprobes interrogated, SD = Standard Deviation).

| Sample | N | Mean | SD | Median |
|---|---|---|---|---|
| **QS-I,D 2** | 166 | 3.004,6 | 5.556,1 | 1.035 |
| **QS-I,D 17** | 299 | 22.742,0 | 38.326,5 | 8.432 |
| **QS-I,D 81** | 211 | 15.489,9 | 12.360,3 | 11.441 |
| **QS-I,D 143** | 202 | 59.289,5 | 104.758,1 | 17.909,5 |

## 6.3.5 References

1. Chen, F.; Ma, K.; Madajewski, B.; Zhuang, L.; Zhang, L.; Rickert, K.; Marelli, M.; Yoo, B.; Turker, M. Z.; Overholtzer, M. Ultrasmall Targeted Nanoparticles with Engineered Antibody Fragments for Imaging Detection of HER2-Overexpressing Breast Cancer. Nat. Commun. 2018, 9, 4141.

2. Mulder, W. J. M.; Jaffer, F. A.; Fayad, Z. A.; Nahrendorf, M. Imaging and Nanomedicine in Inflammatory Atherosclerosis. Sci. Transl. Med. 2014, 6, 1– 25.
3. Dempsey, G. T.; Vaughan, J. C.; Chen, K. H.; Bates, M.; Zhuang, X. Evaluation of Fluorophores for Optimal Performance in Localization-Based Super-Resolution Imaging. Nat. Methods 2011, 8, 1027– 1036.
4. Sofias, A. M.; Toner, Y. C.; Meerwaldt, A. E.; van Leent, M. M. T.; Soultanidis, G.; Elschot, M.; Gonai, H.; Grendstad, K.; Flobak, Å.; Neckmann, U.; Wolowczyk, C.; Fisher, E. L.; Reiner, T.; Davies, C. . L.; Bjørkøy, G.; Teunissen, A. J. P.; Ochando, J.; Pérez-Medina, C.; Mulder, W. J. M.; Hak, S. Tumor Targeting by Avβ3-Integrin-Specific Lipid Nanoparticles Occurs via Phagocyte Hitchhiking. ACS Nano 2020, 14, 7832– 7846.
5. Senders, M. L.; Meerwaldt, A. E.; van Leent, M. M. T.; Sanchez-Gaytan, B. L.; van de Voort, J. C.; Toner, Y. C.; Maier, A.; Klein, E. D.; Sullivan, N. A. T.; Sofias, A. M. Probing Myeloid Cell Dynamics in Ischaemic Heart Disease by Nanotracer Hot-Spot Imaging. Nat. Nanotechnol. 2020, 15, 398– 405.
6. Mastrodonato, C.; Pagano, P.; Daniel, J.; Vaultier, M.; Blanchard-Desce, M. Molecular-Based Fluorescent Nanoparticles Built from Dedicated Dipolar Thienothiophene Dyes as Ultra-Bright Green to NIR Nanoemitters. Molecules 2016, 21, 1227.
7. Daniel, J.; Godin, A. G.; Palayret, M.; Lounis, B.; Cognet, L.; Blanchard-Desce, M. Innovative Molecular-Based Fluorescent Nanoparticles for Multicolor Single Particle Tracking in Cells. J. Phys. D: Appl. Phys. 2016, 49, 84002.
8. Sourdon, A.; Gary-Bobo, M.; Maynadier, M.; Garcia, M.; Majoral, J.-P.; Caminade, A.-M.; Mongin, O.; Blanchard-Desce, M. Dendrimeric Nanoparticles for Two-Photon Photodynamic Therapy and Imaging: Synthesis, Photophysical Properties, Innocuousness in Daylight and Cytotoxicity under Two-Photon Irradiation in the NIR. Chem. – Eur. J. 2019, 25, 3637– 3649.
9. Mongin, O.; Krishna, T. R.; Werts, M. H.; Caminade, A. M.; Majoral, J. P.; Blanchard-Desce, M. A Modular Approach to Two-Photon Absorbing Organic Nanodots: Brilliant Dendrimers as an Alternative to Semiconductor Quantum Dots?. Chem. Commun. 2006, 8, 915– 917.
10. Caminade, A.-M.; Hameau, A.; Majoral, J.-P. Multicharged and/or Water-Soluble Fluorescent Dendrimers: Properties and Uses. Chem. – Eur. J. 2009, 15, 9270– 9285.
11. Wang, X.; Anton, N.; Ashokkumar, P.; Anton, H.; Fam, T. K.; Vandamme, T.; Klymchenko, A. S.; Collot, M. Optimizing the Fluorescence Properties of Nanoemulsions for Single Particle Tracking in Live Cells. ACS Appl. Mater. Interfaces 2019, 11, 13079– 13090.
12. Kilin, V. N.; Anton, H.; Anton, N.; Steed, E.; Vermot, J.; Vandamme, T. F.; Mely, Y.; Klymchenko, A. S. Counterion-Enhanced Cyanine Dye Loading into Lipid Nano-Droplets for Single-Particle Tracking in Zebrafish. Biomaterials 2014, 35, 4950– 4957.
13. Reisch, A.; Klymchenko, A. S. Fluorescent Polymer Nanoparticles Based on Dyes: Seeking Brighter Tools for Bioimaging. Small 2016, 12, 1968– 1992.
14. Chen, J.; Zhang, P.; Yu, X.; Li, X.; Tao, H.; Yi, P. Fabrication of Novel Polymer Nanoparticle-Based Fluorescence Resonance Energy Transfer Systems and Their Tunable Fluorescence Properties. J. Macromol. Sci. Part A 2011, 48, 219– 226.
15. Cabral, H.; Matsumoto, Y.; Mizuno, K.; Chen, Q.; Murakami, M.; Kimura, M.; Terada, Y.; Kano, M. R.; Miyazono, K.; Uesaka, M.Accumulation of Sub-100 Nm Polymeric Micelles in Poorly Permeable Tumours Depends on Size. Nat. Nanotechnol. 2011, 6, 815.

16. Kalaparthi, V.; Palantavida, S.; Sokolov, I. The Nature of Ultrabrightness of Nanoporous Fluorescent Particles with Physically Encapsulated Fluorescent Dyes. J. Mater. Chem. C 2016, 4, 2197– 2210.
17. Larson, D. R.; Ow, H.; Vishwasrao, H. D.; Heikal, A. A.; Wiesner, U.; Webb, W. W. Silica Nanoparticle Architecture Determines Radiative Properties of Encapsulated Fluorophores. Chem. Mater. 2008, 20, 2677– 2684.
18. Lakowicz, J. R. Principles of Fluorescence Spectroscopy, 3rd Ed, 3rd ed.; Springer US, 2006.
19. Huang, X.; Song, J.; Yung, B. C.; Huang, X.; Xiong, Y.; Chen, X. Ratiometric Optical Nanoprobes Enable Accurate Molecular Detection and Imaging. Chem. Soc. Rev. 2018, 47, 2873– 2920.
20. Sun, X.; Wang, G.; Zhang, H.; Hu, S.; Liu, X.; Tang, J.; Shen, Y. The Blood Clearance Kinetics and Pathway of Polymeric Micelles in Cancer Drug Delivery. ACS Nano 2018, 12, 6179– 6192.
21. Anil, W.; Faidat, J.; Sanku, M.; Steven, Q.; Estelle, L.; Benedict, L. Polymeric Nanoparticles with Sequential and Multiple FRET Cascade Mechanisms for Multicolor and Multiplexed Imaging. Small 2013, 9, 2129– 2139.
22. Wagh, A.; Qian, S. Y.; Law, B. Development of Biocompatible Polymeric Nanoparticles for in Vivo NIR and FRET Imaging. Bioconjugate Chem. 2012, 23, 981– 992.
23. Mulder, W. J. M.; van Leent, M. M. T.; Lameijer, M.; Fisher, E. A.; Fayad, Z. A.; Pérez-Medina, C. High-Density Lipoprotein Nanobiologics for Precision Medicine. Acc. Chem. Res. 2018, 51, 127– 137.
24. Rossetti, M.; Stella, L.; Morlà-Folch, J.; Bobone, S.; Boloix, A.; Baranda, L.; Moscone, D.; Roldán, M.; Veciana, J.; Segura, M. F.Engineering DNA-Grafted Quatsomes as Stable Nucleic Acid-Responsive Fluorescent Nanovesicles. Adv. Funct. Mater. 2021, n/a, 2103511.
25. Ardizzone, A.; Kurhuzenkau, S.; Illa-Tuset, S.; Faraudo, J.; Bondar, M.; Hagan, D.; Van Stryland, E. W.; Painelli, A.; Sissa, C.; Feiner, N.Nanostructuring Lipophilic Dyes in Water Using Stable Vesicles, Quatsomes, as Scaffolds and Their Use as Probes for Bioimaging. Small 2018, 14, 1703851.
26. Ardizzone, A.; Blasi, D.; Vona, D.; Rosspeintner, A.; Punzi, A.; Altamura, E.; Grimaldi, N.; Sala, S.; Vauthey, E.; Farinola, G. M. Highly Stable and Red-Emitting Nanovesicles Incorporating Lipophilic Diketopyrrolopyrroles for Cell Imaging. Chem. – Eur. J. 2018, 24, 11386– 11392.
27. Gumí-Audenis, B.; Illa-Tuset, S.; Grimaldi, N.; Pasquina-Lemonche, L.; Ferrer-Tasies, L.; Sanz, F.; Veciana, J.; Ratera, I.; Faraudo, J.; Ventosa, N.Insights into the Structure and Nanomechanics of a Quatsome Membrane by Force Spectroscopy Measurements and Molecular Simulations. Nanoscale 2018, 10, 23001– 23011.
28. Elizondo, E.; Larsen, J.; Hatzakis, N. S.; Cabrera, I.; Bjørnholm, T.; Veciana, J.; Stamou, D.; Ventosa, N. Influence of the Preparation Route on the Supramolecular Organization of Lipids in a Vesicular System. J. Am. Chem. Soc. 2012, 134, 1918– 1921.
29. Grimaldi, N.; Andrade, F.; Segovia, N.; Ferrer-Tasies, L.; Sala, S.; Veciana, J.; Ventosa, N. Lipid-Based Nanovesicles for Nanomedicine. Chem. Soc. Rev. 2016, 45, 6520– 6545.
30. Ferrer-Tasies, L.; Moreno-Calvo, E.; Cano-Sarabia, M.; Aguilella-Arzo, M.; Angelova, A.; Lesieur, S.; Ricart, S.; Faraudo, J.; Ventosa, N.; Veciana, J. Quatsomes: Vesicles Formed by Self-Assembly of Sterols and Quaternary Ammonium Surfactants. Langmuir 2013, 29, 6519– 6528.

31. Vargas-Nadal, G.; Muñoz-Ubeda, M.; Alamo, P.; Arnal, M. M.; Céspedes, V.; Köber, M.; Gonzalez, E.; Ferrer-Tasies, L.; Vinardell, M. P.; Mangues, R.MKC-Quatsomes: A Stable Nanovesicle Platform for Bio-Imaging and Drug-Delivery Applications. Nanomedicine 2020, 24, 102136.
32. Segura Ginard, F.M.; Gallego Melcon, S.; Sánchez de Toledo Codina, J.; Soriano Fernánez, A.; Ventosa Rull, N.; Veciana Miró, J.; Boloix Amenós, A.; Segovia Ramos, N. V. Nanovesicles and Its Use for Nucleic Acid Delivery. Patent Appl. EP19382372, 2019.
33. Ferrer-Tasies, L.; Santana, H.; Cabrera-Puig, I.; González-Mira, E.; Ballell-Hosa, L.; Castellar-Álvarez, C.; Córdoba, A.; Merlo-Mas, J.; Gerónimo, H.; Chinea, G.Recombinant Human Epidermal Growth Factor/Quatsome Nanoconjugates: A Robust Topical Delivery System for Complex Wound Healing. Adv. Ther. 2021, 2000260.
34. Morla-Folch, J.; Vargas-Nadal, G.; Zhao, T.; Sissa, C.; Ardizzone, A.; Kurhuzenkau, S.; Köber, M.; Uddin, M.; Painelli, A.; Veciana, J.Dye-Loaded Quatsomes Exhibiting FRET as Nanoprobes for Bioimaging. ACS Appl. Mater. Interfaces 2020, 12, 20253– 20262.
35. McKinney, S. A.; Murphy, C. S.; Hazelwood, K. L.; Davidson, M. W.; Looger, L. L. A Bright and Photostable Photoconvertible Fluorescent Protein. Nat. Methods 2009, 6, 131– 133.
36. Cho, E.-B.; Volkov, D. O.; Sokolov, I. Ultrabright Fluorescent Mesoporous Silica Nanoparticles. Small 2010, 6, 2314– 2319.
37. Palantavida, S.; Tang, R.; Sudlow, G. P.; Akers, W. J.; Achilefu, S.; Sokolov, I. Ultrabright NIR Fluorescent Mesoporous Silica Nanoparticles. J. Mater. Chem. B 2014, 2, 3107– 3114.
38. v. Berlepsch, H.; Böttcher, C. H-Aggregates of an Indocyanine Cy5 Dye: Transition from Strong to Weak Molecular Coupling. J. Phys. Chem. B 2015, 119, 11900– 11909.
39. Cabrera, I.; Elizondo, E.; Esteban, O.; Corchero, J. L.; Melgarejo, M.; Pulido, D.; Córdoba, A.; Moreno, E.; Unzueta, U.; Vazquez, E.; et al. Multifunctional Nanovesicle-Bioactive Conjugates Prepared by a One-Step Scalable Method Using $CO_2$-Expanded Solvents. Nano Lett. 2013, 13, (8), 3766–3774.

# Discussion and future perspectives

Drug delivery using supramolecular carriers is a challenging task. The complexity of self-assembly makes it an empirical field, in which most of the times the physicochemical properties of assemblies are difficult predict. For this reason, achieving supramolecular polymers displaying the desired properties for drug delivery often requires of screening molecular structures until finding the ideal properties. This thesis is an effort towards the exploration of discotic supramolecular polymers as drug delivery carriers, evaluating the required properties for drug delivery.

This work has been carried out by synthesising a new family of multi-responsive polymers, characterizing them in vitro, understanding their stability, exploring strategies for the drug encapsulation and exploring how to modify the system to obtain responsiveness against cancer tissue.

For this reason, our polymers were designed to be synthesised in a straight-forward manner. Most part of the monomer was built by amino acid building blocks to allow its synthesis mainly by solid phase peptide synthesis, reducing the preparation time and allowing for a faster screening of molecular structures. In this thesis, standard solid phase synthesis procedures have been used, however, the synthesis route is susceptible to be improved, applying faster methods like automated peptide synthesisers or microwave-assisted syntheses in high efficiency methods. This would allow for a very fast wedge synthesis and screening, being the purification of the final discotic monomer the most challenging step.

Once synthesised, our monomers were formulated by hand, this is, dissolving the polymer in a good solvent and diluting in a bad solvent. Even though this method is quite reproducible, the quality of the formulation (e.g. polydispersity) is sensitive to small variations in volume, temperatures and mixing speed. In the recent years it appeared the possibility to formulate them using microfluidic technologies. This is a very precise method to control the process by confining the mixing in micrometre sized channels, being able to tune the diffusion and rate of mixing of the good and bad solvents. For example, flow-focusing devices have been successfully used to formulate PLGA nanoparticles, tuning their size by changing the flow rate of the solvents. For this reason, microfluidic technologies appear as a very precise tool to control the polymerization and growth of supramolecular polymers.

In chapter 2, we explored the self-assembly and the responsiveness mechanisms to stimuli of the first BTA-Azo monomer. The highest control over self-assembly was achieved by using light as stimuli, thanks to the azobenzene moieties. *E* configuration demonstrated to be strongly related with the self-assembly, while *Z* configuration did not. Light allowed to externally control the concentration of the *E* configuration, hence, fine control the assembly degree. However, it is still unclear, and very challenging to study, which isomers out of *EEE*, *EEZ*, *EZZ* form part of the self-assembly. Computational simulations could introduce some valuable information on this regard.

In chapter 3, we extended the BTA-Azo family to understand the relation between supramolecular robustness and responsiveness to stimuli, as well as understanding the factors impacting the supramolecular stability upon a hypothetical intravenous injection. Our results demonstrate that

C0 and C4 possess low stability characteristics. They disassemble quickly upon UV irradiation and additionally they monomer exchange between polymers and solution remains intact. On the other side, C8 have high stability characteristics like reduced light responsiveness and minimal monomer exchange. Overall, this fact makes C0 and C4 less stable upon a hypothetical intravenous injection than C8. However, due to the direct BSA scavenging of monomers from fibres, C8 would eventually disassemble.

For achieving supramolecular polymers with enough stability, two requirements are essential, if not more. First, supramolecular polymers must be static, with very low monomer exchange rates. This is necessary to resist dilution. On the other side, fibres should not interact with BSA to avoid the scavenging effect. Here, multiple polymers displaying different hydrophilic cues should be explored. Possibly, the use of saccharides could help on this regard. Additionally, it would be interesting to study more hydrophobic monomers. Would they present the same behaviour as C8 or would they keep increasing in stability. Of course, further increasing the stability of fibres would also affect their capacity to release any drug inside, so their applicability for drug delivery would be limited.

Next steps should be focused on understanding the fibre-cell interaction. If possible, different lengths should be tested displaying the same surface chemistry for determining the ideal size for interaction and/or internalization.

In chapter 4, two strategies for the encapsulation and delivery of biologically active molecule are explored. The co-assembly strategy showed a great potential given that we demonstrated the co-assembling possibility of C4 monomer with C4-glutamate. This approach would allow for a better control on the drug loading. However, the co-assembly of two monomers and the posterior photo-disassembly was not enough to trigger a biological response. In order to assess whether this strategy would be effective or not, a second generation of C4g should be synthesised and tested. This second generation should contain a short hydrophilic spacer between the azobenzene and the glutamate to increase the separation and the water solubility. The strategy encapsulating the IperoxoAzo on C8 demonstrated functional, however this classical strategy suffers of low encapsulation efficiencies and lacks control over loading.

For all these reasons, a very appealing strategy that should be explored for BTA based systems is the one component nanomedicine. Or in order words, create self-assembling prodrugs from BTA monomers. This strategy would incorporate a small hydrophobic drug as a part of the hydrophobic domains of the monomers, actively contributing to self-assembly. This drug should not disturb the monomer stacking and at the same time should be releasable. One possibility could be the linkage of the small and highly cytotoxic 5-Fluorouracil-1-acetic acid to an amino acid like serine through an ester bond. This building block could be easily implemented in the solid phase synthesis of the molecule, allowing to incorporate as many units as needed. By these means, a potent drug can be incorporated in our peptide like wedges, achieving high and controlled loadings. Also, 5-Fu could be easily released under reduced pH environments due to the ester link.

In chapter 5, a new monomer was design with the intention to explore the enzymatic degradability of peptide sequences placed in the hydrophobics domains of the monomer. Even though the molecule synthesis was challenging, some interesting results could be obtained. Impure product showed self-assembly into long fibrillar aggregates. These aggregates showed very little response

to light (if any) and dimer but not trimer showed response to Cathepsin B. However, molecule must be obtained pure and experiments performed again to consolidate these results.

After, FRET experiments should be performed to evaluate exactly the monomer exchange capabilities of the supramolecular polymers. If monomers exchange like C0 or C4, then the results indicate the monomer is not a good substrate for the enzyme. If the supramolecular polymers are static like C8, then new generations must be synthesised to elucidate better the enzyme responsive behaviour.

Light responsive polymers or even dynamic polymers must be synthesised to understand better this enzyme responsive polymers. They can be achieved by introducing more hydrophilic domains, or introducing net charges in the structure, creating some electrostatic repulsion between monomers, and increasing their solubility in water.

Another very interesting possibility consists of the use of hydrophilic cleavable peptides. Instead of the hydrophobic GFLG, we could use the more hydrophilic FRRG (also substrate of cathepsin B) and place it as the hydrophilic segment of the wedge. The cleavage of this sequence should lead towards an increased hydrophobic-hydrophilic ratio, an enhanced self-assembly and the consequent accumulation in the tumour site. In this case, even though the sequence is clearly more exposed than for hydrophobic sequences, the accessibility of the enzyme when monomers are assembled should also be evaluated.

# Conclusions

In **chapter 2**, we synthesised C0 for the first time, proving the possibility to condensate different response mechanisms in single-component supramolecular polymers through a rational monomer design. Following a modular synthesis, we incorporate moieties in the monomer design which, simultaneously, drive the self-assembly and introduce responsiveness to different stimuli. The synthesis introduces advantages in light of structure optimization as well as for the generation of libraries of compounds.

Our system responds in a controlled and reversible fashion to light, temperature, pH and ionic strength modulating the assembly-disassembly equilibrium. By these means, we describe a system with multiple equilibria in which each state is accessible through different pathways, applying the stimuli either orthogonally or in combination, thereby facilitating a sophisticated degree of control.

Our results pave the way towards effective and highly controllable supramolecular materials in which the responsiveness is fully imprinted in a single monomer. This is especially interesting for biological applications, such as drug delivery or tissue engineering, where controlling the material performance in a complex environment is challenging.

In **chapter 3**, we extended the BTA-Azo family including two new monomers of increasing hydrophobicity. The evaluation of their stability-responsiveness trade-off allowed to separate them into two well differentiated regimes, low stability-high responsivity for C0 and C4, and high stability-low responsivity for C8. Upon a hypothetical intravenous injection, C0 and C4 clearly showed a very low stability. Dilution seems critical for these structures, and protein scavenging monomers leads also to disassembly.

C8 seems extraordinarily robust against dilution. However, proteins seem to destabilize the structures. This is possible only because proteins can scavenge monomers directly from fibres and not only from solution. Then, we demonstrate that designing supramolecules for drug delivery requires inevitably a high stability-responsiveness trade-off to resist dilution and a weak BSA-supramolecule interaction to minimize scavenging effects.

In **chapter 4**, two strategies have been explored to internalize bioactive molecules inside the discotic supramolecular polymers. The first consisted of the design of a glutamate containing monomer and co-assemble it with C4. The co-assembly demonstrated to be effective, however, the glutamate containing monomer did not display any activity. Or glutamate could not interact with the receptor or glutamate remained aggregated after fibre disassembly.

The second strategy consisted of the classical encapsulation in the hydrophobic pocket of the supramolecular polymer. Encapsulation was proved as well, even though the indications were more subtle than with strategy 1. Finally, light triggered release was proven. Only when fibres were exposed to UV-light, bioactivity was observed.

In **chapter 5**, **t**he synthesis of BTA-GFLG monomer is feasible, but purification methods must be improved to remove dimer impurities or synthetic route must be changed to avoid the formation of the dimer impurities.

Interestingly, the final crude mixture showed a strong self-assembly into fibres of around 12 nm in thickness and -μm in length. CD displayed a similar signal for stacked azobenzene comparing to C8, suggesting a strong self-assembly. Likewise, UV response seems comparable to the one of C8.

Assays with cathepsin B showed degradation of dimer, but not of trimer. Whether the trimer is a good substrate for cathepsin B, or if BTA-GFLG is a dynamic supramolecular fibre is still unknown. These preliminary assays must be repeated and expanded with a pure fraction in order to extract robust conclusions

In **chapter 6**, optical microscopy is a powerful tool for the characterization of supramolecular materials. Supramolecular fibres in solution can be visualized and studied by HiLo, and TIRF. These techniques can provide additional qualitative information like assembly state and can visualize the fibres in presence of cells.

Supramolecular Fmoc-FF hydrogels can be imaged by PAINT microscopy. By using a FF-cy5 probe, the hydrogel network close to the surface was imaged under native conditions, with a resolution of ~10 nm. The mesh size was evaluated, and first steps towards 3D hydrogel imaging were performed.

Dye loaded quatsomes were successfully imaged by TIRF microscopy, what allowed a simultaneous multiparametric analysis particle by particle. Relative brightness and FRET ratio was measured for individual particles of different formulation. Increasing the dye loading during the formulation lead to an increase in the brightness and FRET ratio up to 81 mM. After this point, increasing dye loading decrease the FRET and brightness, and increase the polydispersion of these two parameters, probably caused by dye aggregation.